The University Of Sheffield.

Feasibility study on the current AMRC process monitoring capability during grinding & investigating the repeatability of using AE response features; AE RMS, Skew, MVD, CFAR and ROP for process monitoring grinding of IN718

Felix Johnson Mundanmany

A thesis submitted in partial fulfilment of the requirements for the degree of Master of Philosophy

The University of Sheffield
Faculty of Engineering
Department of Mechanical Engineering

15 October 2022

Executive Summary

This thesis investigates the application of Acoustic Emission (AE) monitoring to enhance the reliability and efficiency of grinding processes, specifically focusing on IN718 superalloy using aluminium oxide grinding wheels. The primary objective of this research was to develop a robust methodology for capturing and analysing AE signals to improve process monitoring, fault diagnosis, and predictive maintenance in industrial grinding operations.

An advanced data acquisition system was implemented to capture synchronous signals from various sensors at high sampling rates. This system facilitated the comprehensive analysis of AE features, including AE RMS, Skew, MVD, CFAR, and ROP, across different grinding regimes: roughing, semi-finishing, and finishing. The study involved multiple grinding trials with varying grinding wheel diameters, enabling the assessment of AE signal repeatability and reliability.

Key findings from the research include:

AE RMS and MVD Values: Demonstrated high repeatability across different grinding regimes and wheel diameters, indicating their robustness for continuous process monitoring. The AE RMS values were particularly higher in the roughing regime due to increased material removal rates and grinding forces.

Skew: Showed consistent patterns in roughing and semi-finishing regimes but exhibited variability in the finishing regime due to sensitivity to lower magnitude AE responses. This sensitivity highlighted the need for careful consideration of grinding parameters when using Skew as a diagnostic feature.

CFAR: Maintained stable values across all grinding regimes and wheel diameters, reflecting the consistency of AE event frequency. The roughing regime had the highest CFAR values, indicating more intense interactions between the grinding wheel and the workpiece.

ROP: The prominent frequency bands were in the 100–150 kHz range, consistent across all grinding regimes. This consistency suggests the potential for using ROP values in predictive modeling of grinding wheel wear.

In addition, significant work was done on developing wavelet de-noising techniques to enhance AE signal quality by reducing machine noise. Parameters for the wavelet de-noising process were optimized to ensure maximum signal clarity without compromising the integrity of the data. This development was crucial for improving the accuracy of AE feature extraction and overall signal analysis.

The novelty of this work lies in the comprehensive application of AE monitoring to different grinding regimes and the integration of advanced signal processing techniques. The study's approach to understanding the correlation between AE features and grinding parameters provides valuable insights that can be leveraged for predictive maintenance and improved process control in industrial settings.

In conclusion, this thesis contributes significantly to the field of process monitoring and fault diagnosis in grinding operations. The methodologies and insights developed herein provide a solid foundation for future research and industrial application, driving innovation and continuous improvement in the manufacturing sector.

Table of Contents

Declaration

I, Felix Johnson Mundanmany, confirm that the Thesis is my own work. I am aware of the University's Guidance on the Use of Unfair Means (www.sheffield.ac.uk/ssid/unfair-means). This work has not previously been presented for an award at this, or any other, university.

I. Acknowledgements

I would like to thank my supervisors Dr. David Curtis and Dr. Graeme Manson for all their support and advice during my time at IDC Machining Science University of Sheffield while I pursued my EngD and eventually transitioned to an MPhil. I would also like to thank my family and my partner without whom this would not have been possible. Lastly and most importantly, I would like to thank The University of Sheffield AMRC for funding my studentship to give me an opportunity to pursue my thesis.

II. Nomenclature

Symbol	Description	Unit
In718	Inconel 718	
AE	Acoustic emission	
AMRC	Advanced Manufacturing Research Center	
a, a_e	Depth of Cut	**mm**
l_c	Contact length	**mm**
V_s	Grinding wheel surface speed	**m/s**
V_w	Workpiece feed rate	**mm/min**
d_s	Grinding wheel diameter	**mm**
Q	Material removal rate	**mm^3/min**
Q'	Specific material removal rate	**mm^3/s**
b_w	Grinding contact width	**mm**
e_c	Specific grinding energy	
P	Grinding power	**kW**
P_{NL}	No-load power	**kW**
P_f	Fluid drag power	**kW**
F_t	Tangential grinding force	**N**
F_n	Normal grinding force	**N**
F_v	Vertical grinding force	**N**
F_h	Horizontal grinding force	**N**
F_a	Axial grinding force	**N**
v_{ft}	Tangential feed speed	**mm/min**
v_{fn}	Normal feed speed	**mm/min**

Symbol	Description	Unit
θ	Normal force vector angle	
v_{fa}	Axial feed speed	**mm/min**
q_d	Roll speed ratio	
v_d	Dressing tool speed	**m/s**
v_s	Grinding wheel speed	**m/s**
CBN	Cubic Boron Nitride	
DTG	Difficult to grind	
G	Grinding ratio	
RMS	Root mean square	
CFAR	Constant false alarm rate	
ROP	Ratio of power	
MVD	Mean-value deviance	
EXWT	Energy of cross wavelet transform	
DWTC	Degree of wavelet coherence	
STFT	Short term fourier transform	
μ	Mean	
σ	Standard deviation	
s	Wavelet scaling	
CWT	Continuous wavelet transform	
DWT	Discrete wavelet transform	
SNR	Signal to Noise ratio	
CSD	Cross spectral density	
OWA	One Way Assembly	

1 Introduction

1.1 Motivation

Grinding of aerospace alloys stands as a pivotal facet in aviation manufacturing. As noted by Rowe [1], industries in the latter half of the twentieth century came to recognize grinding as the quintessential machining process defining part quality. Rowe [1] substantiates this claim by citing examples from industries such as aero-engines and missile guidance systems. Within the aviation industry, quality was critical to safety of design and advancement of technology in the industry. With intricate designs booming within the aviation industry to improve the capability of aero-engines and other aero parts, high accuracy was required to demand tight tolerances for size, shape and surface texture and grinding was the answer. To give an idea of the magnitude of tolerance limits and precision used within grinding, Rowe [1] mentions grinding was used for large parts where straightness is important and tolerance was considered in microns while grinding of small parts could tighten the tolerances into the nano range.

Grinding is considered an abrasive process within machining operations. Unlike conventional machining practise where it involves the use of tools with cutting edges using defined shapes, grinding implements an array of fixed abrasive particles which project out of a binding material surface and removes material as it meets softer material at high speed. This is a rather minimalistic definition for grinding and is only used in this script to set the scene for the project's motivation, a more venerate definition is given within the literature review.

Abrasive particles within grinding have complex shapes which means they have a complex geometry and when trying to understand the process, the kinematics to consider is also complex. Therefore Rowe [1] mentions that the knowledge required to advance the technology was limited in the second half of the twentieth century hence a great push to fill this gap within the industry was conceived by the industry naturally and still exists. Being one of the final steps within manufacturing there was great demand to conduct research within understanding grinding and being able to control the various outputs of grinding such that any costly mistakes towards the end of product manufacture is avoided. Adding to the complexity of grinding, the industry also pushed towards being able to use grinding as an opportunity of increased material removal rate and reaching final form with reduced number of operations. Therefore, it can be concluded that grinding is highly complex and dynamic, characterized by non-stationary behaviour. The grinding mechanism undergoes constant evolution during the process, transitioning through various stages of material removal, including rubbing, ploughing, and cutting. Rubbing occurs

when abrasive grains lightly contact the workpiece surface without penetrating it deeply, resulting in mild wear. Ploughing involves abrasive grains penetrating the surface and displacing material to form ridges without necessarily removing it entirely. Cutting, on the other hand, occurs when abrasive grains deeply penetrate the workpiece, carving out chips of material. These stages of material removal are not mutually exclusive; rather, grains may experience a combination of rubbing, ploughing, and cutting during the grinding process. The dynamic nature of grinding arises from the interplay of multiple input variables, such as grinding wheel properties, workpiece material characteristics, and process parameters, which influence the prevalence of each material removal mechanism over time. Additionally, the evolution of the grinding mechanism is influenced by the changing conditions within the grinding zone, including changes in abrasive wear, workpiece deformation, and heat generation. As a result, the grinding process exhibits non-stationary behaviour, with material removal rates and surface quality fluctuating throughout the operation. Understanding and controlling these dynamic aspects of grinding are crucial for achieving consistent and desired outcomes in precision machining applications. With such a complex process, monitoring it becomes imperative to detect faults, capture process parameter information, and optimize grinding systems accordingly.

Along with the advances in machining and grinding, another front which added to the intricacies of the technology was the changing materials that were present within the aerospace industry. The industry demanded superior properties from materials such that the industry could improve the capability of aero-structures and propulsion. This gave rose to superalloys which had high thermal properties, corrosion-resistance and superior mechanical strength. To give an example of the values, Wee et al [2] reviews mechanical thermal properties of superalloys and shows how conventional cast superalloys that have high thermal properties show a maximum ultimate tensile strength (UTS) of 550 MPa and maximum yield strength (YS) of 380 MPa at 1000°C and even higher strength of UTS: > 1000 MPa and YS:> 800 MPa at 800°C which are operating temperatures within gas turbines in jet engines. One of the main forms of superalloys which is widely used within the industry are nickel-based superalloys. Nickel based superalloys pushed the criteria limits for the operating temperatures of different aerospace components meanwhile maintaining the strength to provide safety and reliability. On the other hand, these superior properties of nickel-based superalloys made it difficult to grind material due to its high strength work hardening and low thermal conductivity. When grinding, the low thermal conductivity leads to significant heat generation and therefore if not controlled and monitored can affect the quality of the surface especially due to a heat affected zone that is created during grinding as described by Sinha et al [3]. Inconel 718 is one such superalloy which is widely used in the industry for production of gas turbine engine parts such

as compressor casings, discs and fan blades. This thesis has selected IN 718 as the primary material to be investigated due to its wide use in the industry such that it can advance process monitoring and stay relevant to the industry.

Various methods exist for monitoring the dynamic grinding process, including grinding force, spindle power, acoustic emission, and vibration. Research has advanced within these fronts to understand how grinding can be controlled and one of interest within this thesis is the use of acoustic emission (AE). AE sensors' capability allow for in-process detection of acoustic signals. Sensing technology has improved such that AE sensors with a large frequency range and high sensitivity has been packed into smaller dimensions. Therefore, AE sensors are more portable and can be easily integrated into a machine environment and can be rather considered a tool to deploy for dynamic sensing. Although AE sensors have been employed to detect contact between workpiece and tool, ongoing research aims to leverage AE for tasks such as grinding burn detection and wheel condition monitoring. However, a notable gap persists in establishing a clear link between AE data and grinding parameters—a gap this study seeks to address. The dynamic capabilities of AE sensors offer unprecedented opportunities for real-time monitoring and detection of faults during the grinding process. The insights gained from this research have the potential to not only advance the understanding of grinding processes but also pave the way for the industrialization and widespread adoption of AE-based monitoring systems. By providing actionable insights into the onset of faults during grinding, these systems have the potential to significantly reduce manufacturing defects, enhance product quality, and ultimately, reduce costs for aerospace manufacturers.

Advanced Manufacturing Research Centre (AMRC) are currently at a stage to improve the data acquisition capability during machining as part of Industry 4.0 advancements and have invested in DAQ systems which can incorporate acquisition of signal from various sensors at the same time and improve the data acquisition rate capability. Before the time of writing this thesis, AMRC was limited to 1 Mhz data sampling rates for AE sensors and did not have the capability of acquiring synchronised data from different sensors (signal sources at different sampling rates) such as force, power and AE. Previous work conducted at AMRC with AE sensors have always looked at AE signals limited to less than 500 kHz due to Nyquist criterion limitation and there was no protocol to understand if the AE sensors had degraded during testing. The only checks conducted was to ensure that the AE sensors were calibrated as when required. At AMRC, there has been works conducted with AE sensors to understand different machining process but none which have been able to test the reliability and repeatability of using AE sensors for monitoring grinding.

This context underscores the pressing need to bridge the knowledge gap and enhance the reliability of AE signal utilization at AMRC. By instilling a systematic process for data acquisition with AE sensors, this research endeavor aims to lay the groundwork for integrating AE technology into the grinding domain. Establishing this precedent not only facilitates advancements in process monitoring capabilities within AMRC but also creates avenues for broader industry applications. With enhanced process monitoring capabilities, AMRC can spearhead initiatives to fund projects aimed at leveraging acoustic emission for monitoring and optimizing manufacturing processes across diverse machining operations. Furthermore, the transferability of AE technology to other machining processes holds immense potential for driving efficiencies and improving product quality across the manufacturing spectrum. Thus, this study is poised to contribute significantly to the ongoing efforts at AMRC to harness cutting-edge technologies for enhancing manufacturing efficiency and competitiveness.

This study is centered on a comprehensive literature review aimed at delineating the intricacies of the grinding process, identifying key input-output relationships, and synthesizing existing research on AE sensor applications for process monitoring in the aerospace sector. Furthermore, it encompasses the design and execution of an experiment to systematically investigate the repeatability and reliability of AE signals recorded during the grinding of IN718—a widely used aerospace alloy. By integrating theoretical insights with empirical findings, this research endeavor seeks to advance our understanding of AE sensor applications in grinding processes, thereby paving the way for more efficient and reliable manufacturing practices in the aerospace industry.

1.2 Aim

This study aims to significantly enhance the Advanced Manufacturing Research Centre's (AMRC) process monitoring capabilities during the grinding of the aerospace alloy Inconel 718. The research will deploy a new and improved signal acquisition system to conduct a repeatability study, recording acoustic emission (AE) signals alongside force, power, and vibration signals under controlled and varied grinding parameters.

A key objective is to implement an optimized wavelet de-noising method tailored for AE signals from the grinding process, ensuring accurate analysis by removing background noise from the coolant and machine environment. The study will investigate how grinding wheel diameter progression affects AE signals across different grinding regimes, including finishing, semi-finishing, and roughing. By analysing signal coherence and frequency distribution, as well as repeatability of AE features such as RMS, MVD, and CFAR, this research aims to establish robust process monitoring techniques. The outcomes will enhance AMRC's capabilities and provide a foundation for future advancements in grinding process monitoring.

1.3 Objectives

1. To conduct a literature review on the understanding of grinding process and previous work conducted within process monitoring of grinding using acoustic emission signals. Therefore, address the knowledge gap that exists in this niche area of research.
2. To characterise a set of AE features and signal parameters which needs to be investigated for repeatability using the knowledge gap addressed within the literature review.
3. To design an experiment which is aimed at investigating the repeatability of recording AE signals with a varied set of grinding parameters and conclude on the reliability of using AE sensors for process monitoring during grinding at AMRC.
4. To develop the pre-process routine for the recorded AE signal which de-noises it and filters out the unwanted signal from the grinding process.
5. To deploy an upgraded signal acquisition system and thereby enhance the AMRC capability and its use of AE sensors for process monitoring in a machining environment.

1.4 Thesis structure

The thesis structure follows the format to introduce the concept of grinding and its basic understanding of the process before reviewing research conducted previously within process monitoring of grinding using acoustic emission and its signal processing techniques. Following this, the current capability of AMRC is explored and potential improvement to the system is identified. Having set the scene for the background of the project, the methodology for the experiment is defined and signal processing routine is detailed for the work. Finally, the results of the experiment is determined and discussed to evaluate the repeatability of AE signals during process monitoring of grinding IN718. The thesis concludes upon the lessons learnt from the experimental work and future work direction as an interpretation of the results. The detailed thesis structure is as follows:

Chapter 2: This gives an outline of the motivation for this thesis and justifies the various approaches taken towards investigating the repeatability of AE signals during process monitoring of grinding. The aims, objectives and scope have been defined and stated.

Chapter 3: This chapter entails the literature review conducted within this thesis. It introduces the grinding process and gives an overall review of the grinding mechanism and the key parameters which control the grinding process. Furthermore, the chapter dwells on the types of grinding wheels and how their dressing/topography affects the grinding process outputs. Another approach to the review is exploring

process monitoring by viewing the grinding process as a system and converging towards the use of AE signals within process monitoring of grinding. It concludes with the analysis of the AE signal pre-processing by detailing the study of wavelet denoising for this thesis.

Chapter 4: The current AMRC capability is examined within this chapter within aspects of grinding capability, force monitoring, power monitoring, acoustic emission monitoring and finally the data acquisition capability. This is an overview of the status of the capabilities before the work was conducted on the thesis and a realisation of the potential for improvement.

Chapter 5: Outlines the methodology adopted for experiment which defines repeatability of AE signals during process monitoring of grinding on IN718. The experimental set-up is detailed and a stepped approach to design the experiment to meet the objectives defined. AE sensor response reproducibility test that was developed to improve the AMRC capability for standardising AE signals and this also discussed within this chapter. The chapter concludes with the methodology to define AE signal de-noising using wavelet decomposition.

Chapter 6: Presents the results for the various objectives set out within the thesis. Initially, the chosen parameters for wavelet de-composition and de-noising are discussed thereby rendering the pre-processing required for AE signals before analysis. The pre and post AE sensor reproducibility test results are discussed to infer the reliability of the data captured through the sensors. Repeatability of the grinding parameters and output results are validated by analysing the grinding force and power results. Finally, the effect of grinding wheel diameter progression upon grinding force, power and AE response is explored while keeping the experiment controlled and hence repeatability discussed. Other aspects of repeatability is discussed from the perspective of power spectral analysis on the AE signals, spectral coherence and cross spectral density of AE response and the trends in AE features which were picked out from the literature review.

Chapter 7: Discussed the lessons that were learnt during the preparation of the experiment and also any learning which would be helpful for the future works within this field of research.

Chapter 8 : Brings in the conclusions to the objectives set out for the thesis and other findings which are relevant to the field of research.

Chapter 9: Entails how the conclusions from this thesis models the work for the future in this area of research. The next steps required towards progressing process monitoring during grinding with AE are discussed.

2 Literature review

2.1 Grinding

2.1.1 The grinding process

Grinding is defined as a machining process which makes use of hard abrasive particles as the cutting medium which are bonded onto a wheel to remove material off the machined workpiece. Grinding is an essential machining process due to its ability to produce fine surface finishes and accurate dimensions that are otherwise not easily achieved using conventional machining techniques such as turning or milling. The grinding wheel consists of two types, namely conventional and super abrasives [1]. Conventional grinding wheels usually have a hexagonal crystal structure, and the two main types are made from Aluminium oxide and silicon carbide which use vitrified, rubber or rubber reinforced bonds between grains. Super abrasive wheels have a cubic crystal structure, and the main types include diamond and cubic boron nitride which use vitrified, resin or metal bonds between grains. All wheels have a marking scheme which specify the properties such as the abrasive type used, abrasive grain size, grade, structure and bond type etc. In the grinding process, loading of the wheel with workpiece material or grains breaking off can cause two issues; i) sharpness of wheel lowers as the peak prominence of the grains reduce with the introduction of workpiece material loading onto the wheel ii) run-out of wheel increases when the workpiece material lodged onto wheel changes the macro-form of the wheel. These issues raise the need for dressing and truing which are key processes within grinding. Both these processes involve the removal of worn/unsharp grains and bond material off the wheel surface to reveal a fresh surface for which truing is done to maintain low run-out and good form while dressing helps regenerate and fresh sharp grinding wheel surface.

The process is mainly considered as a finishing process within the macro-scale process of machining a product. It gets this characteristic due to its capability of providing a fine finish on machined surfaces with lower material removal rates. But over the years, these trends seem to be changing, there is a drive towards the grinding process involving a high material removal rate and achieving final machined dimensions through grinding with higher dept of cut - a new method of grinding (creep grinding). This shows the need for different types of grinding processes to exist to provide various finishing on machined surfaces.

2.1.2 Grinding mechanisms

The cutting-tool geometry and its interaction with a workpiece during grinding is not easily defined and discrete. A grinding wheel has several cutting points which interact in an irregular pattern with the workpiece at random orientations and positions about the surface of the wheel. As a result, there is a great variation in the cutting geometry as the grinding process progresses. In the past, there has been several works to define the cutting mechanism and chip mechanism during grinding. The most favoured approach being looking at a single 'typical' or 'average' cutting point on a wheel and modelling the variability that can occur due to different amount of cutting points or even simulating the interaction between non-uniform surface and workpiece. The key parameters that can be picked out when analysing the kinematics involved would be the depth of cut (*a*), the contact length between grinding wheel and workpiece (*lc*), peripheral velocity of the grinding wheel (*Vs*) and workpiece feed rate (*Vw*). An example of the parameters described are shown in Figure 1 for straight plunge grinding, the same type used in this thesis experiment.

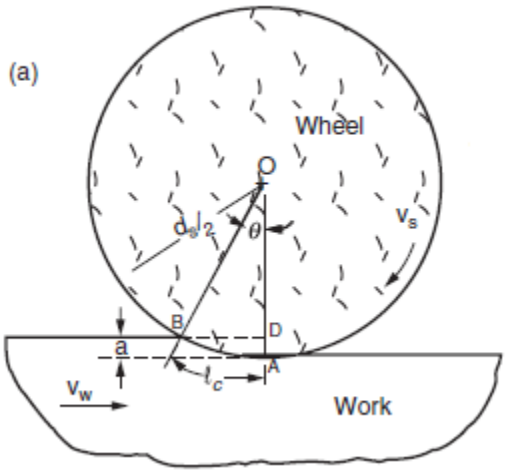

Figure 1 Illustration of straight surface plunge grinding operation [4]

In the diagram Figure 1 , the wheel velocity (*Vs*) and workpiece velocity /feed (*Vw*) is in the opposite directions and this is known as 'up-grinding' and if these velocities were in the same direction, this would be known as 'down grinding'. As the grinding wheel is in contact with the workpiece, there are normal and tangential forces generated between them which cause the grains to abrade the workpiece. An increasing depth of grain penetration determines the type of material removal experienced on the workpiece. A low depth of grain penetration initially causes rubbing on the workpiece, then with incremental depth of grain penetration, ploughing would result thereby creating ridges on the surface of

the material without removing the material. A high depth of penetration can develop the ploughing into a situation where the material is removed. Properties of the material is the strongest factor which determines the extent to which these grain cutting regimes affect the surface of a material. In down grinding, the grinding forces tend to be lower as the grains initially in contact can experience chip removal rather than rubbing initially as opposed to its counterpart and therefore benefit from better surface roughness and reduced wheel wear. There are also disadvantages to down grinding, one of the most important one being the control of colling fluid as it is difficult to carry the cooling fluid onto the grinding contact point as opposed to up-grinding. But over the years, coolant deployment technologies have caught up with this disadvantage to improve the cooling strategy during down-grinding. Therefore, in most situations, down-grinding is the most common type of grinding deployed.

Removal rate (Q) of material during grinding is directly related to the grinding forces, deflection and power consumption during grinding. The removal rate is given as the product of workpiece feed rate (v_w) in the direction of material removal and contact area. While specific material removal rate Q' is the removal rate per unit width of grinding contact [1]. In the equations below b_w is the grinding contact width and a_e the depth of cut.

$$Q = b_w . a_e . v_w \quad \text{removal rate}$$

Equation 1

$$Q' = a_e . V_w \quad \text{specific material removal rate}$$

Equation 2

From the equation above it is apparent that in order to increase material removal rate, the grinding contact area and the feed rate needs to be increased. These options have their own effects on the grinding mechanism. An increased grinding contact width would mean higher grinding energy, therefore requiring higher grinding power and grinding wheel's ability to withstand high deflection. Realistically, as grinding progresses, grinding wheel wears and the depth of cut at the periphery of the wheel can reduce. In a grinding wheel where the grains are not equally distributed this can bring other grains on the wheel surface to become active and the active contact area can change. Therefore, it is not realistic to imagine an ideal grinding wheel and grinding mechanism to be systematic throughout a grinding cut. Nevertheless, there are grain behaviours that can be studied and predicted from the process.

Grinding energy gives a measure of the ability for a grinding wheel to remove material and this depends on its sharpness and the grindability of the workpiece material. Grindability is a term mainly used to

describe how easy it is to grind a material with a given abrasive and grinding condition. There is a loose definition around the term grindability, and it is considered that material which require low specific grinding energy are more easily ground than those that require high specific energy. This specific grinding energy (e_c) is given as the grinding power divided by the removal rate Q.

$$e_c = \frac{P}{Q}$$

Equation 3

The griding energy can be identified by recording the grinding wheel spindle power during a grinding cycle. An example of a griding cycle is shown in Figure 2 where grinding power, noted as P, can be picked out by subtracting the no-load power (P_{NL}) and fluid drag power (P_f) after the power reading has stabilised within the grind.

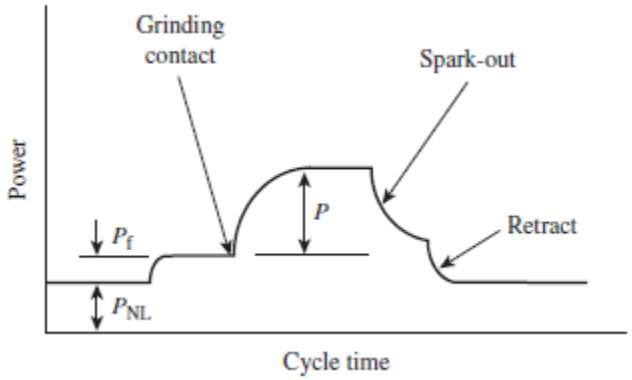

Figure 2 Graph showing representation of the grinding power P during a plunge cylindrical grinding [1].

Grinding power can also be calculated by resolving the grinding force and speed in which the direction of the force is acting. Grinding force can be resolved into three components (a) tangential force (F_t) (b) normal force (F_n) and (c) axial force (F_a). These force components within an experimental setup can be deduced using a dynamometer for which the components should be accurately defined. An illustration for these force components is shown in Figure 3.

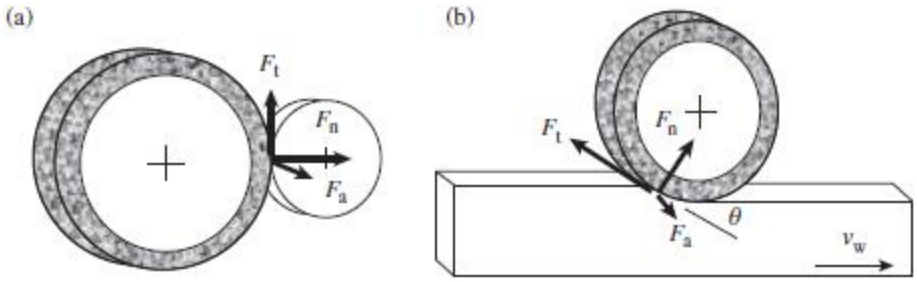

Figure 3 Three grinding force components shown (a) for small depth of cut during cylindrical grinding (b) large depth of cut for plunge surface grinding (exemplary to the type of grinding considered in this thesis)

$$P = F_t.(v_s \pm v_{ft}) + F_n.v_{fn} + F_a.v_{fa} \approx F_t v_s$$

Equation 4

$v_s - Wheel\ speed$

$v_{ft} - tangential\ feed\ speed$

$v_{fn} - normal\ feed\ speed$

$v_{fa} - axial\ feed\ speed$

The plus sign is applied when up-grinding and minus sign applied when down-grinding. The normal and axial feed speed is substantially smaller than the wheel speed therefore griding power can be closely resembled by the equation $P = F_t v_s$.

Within this project, a large depth of cut is considered and therefore the components of the horizontal and vertical force recorded using a dynamometer needs to be used to deduce the normal and tangential force. The equation relating these forces are given as :

$$F_n = F_v \cos(\theta) - F_h \sin(\theta)$$

Equation 5[5]

$$F_t = F_v \sin(\theta) + F_h \cos(\theta)$$

Equation 6 [5]

In order to evaluate the normal force vector angle, θ ;

$$\theta = \sqrt{\frac{Depth\ of\ cut}{Wheel\ diameter}}$$

Equation 7 [5]

Amongst these equations that have been used to define the grinding mechanism and its related grinding force, there has not been a simple way to define the concept of complicated and random process of grinding that helps the common shop floor technician. Badger [12 a] introduces this as a divide between the knowledge held in academia and the knowledge held on the shop floor. To close this gap, Badger [6] introduces the aggressive value that helps users easily evaluate their grinding parameters without the use of a complicated concept. Unlike turning, which can be easily represented in two dimensions using Merchant's chip formation model [7], the inherently three-dimensional nature of grinding makes it very challenging to calculate chip thickness. Machine operators, who are used to the clear "speeds & feeds" diagrams available in turning, often find it frustrating that no such straightforward relationship exists for grinding. One of the most common equation for maximum chip thickness [4] given in grinding, h_m, can be summarised as :

$$h_m = \left[\frac{6}{C \cdot r} \cdot \frac{v_w}{v_s}\sqrt{\frac{a_e}{d_e}}\right]^{1/2}$$

Equation 8

Where C is the cutting-point density (number of cutting points per unit area) , r is the shape factor , v_w is the workpiece velocity, v_s is the wheel velocity, a_e is the depth of cut, and d_e is the equivalent diameter. However, this complicated equation can be made simple to an equation that only takes into the account the machining parameters that can be varied i.e. – depth of cut, federate, wheel speed and wheel diameter and called aggressiveness[8]. Badger [12 a] further simplifies this equation and rewrites it as below:

$$Aggresiveness = 16.7 \times \frac{v_w\ (\frac{mm}{\min})}{v_{s(\frac{m}{s})}} \times \sqrt{\frac{a_e(mm)}{d_e(mm)}}$$

Equation 9

2.1.3 Grinding wheel dressing and topography

From reviewing the grinding mechanism, it is apparent how important the grinding wheel surface is for the output of the grinding task. Dressing is a task which prepares the grinding wheel surface and there are different stages to it. Firstly, truing to remove any deviations from the wheel's specified form or straightness. Dressing is conducted to achieve a fresh cutting surface which is uniform with a well-

balanced distribution of cutting edges and remove any workpiece material that would have loaded the wheel in previous grinds. Dressing also shares the responsibility of conditioning the wheel to an open wheel surface by removing the bond around abrasive grains (an important aspect to consider within resin bonded grinding wheels and vitrified super abrasive wheels)

Stationary and rotary dressing tools are the two basic types of dressing tools. Stationary dressing tools include single-point diamond and impregnated diamond dressing tools which are mainly used for dressing conventional abrasives.

The dressing process for a single-point dressing tool involves the dressing tool (normally diamond) in contact with the wheel and is traversed across the surface of the grinding wheel to create the required shape and cutting surface. Coolant also needs to be applied to keep the cutting tool cool during dressing. For single-point dressing tools, the dressing diamond can rapidly develop a flat with wear and this can affect the dressing forces. Therefore, these tools require it to be rotated 90^{o} about its axis at given intervals.

Vitrified CBN, resin-bonded CBN and diamond wheels are normally dressed using rotary dressing tools since this avoids rapid dressing tool wear. A rotary dressing tool takes the form of a narrow disk with a layer of diamonds set on the wheel peripherals or a cup form with a layer of diamonds around the edge . The rotary tool is used in a similar manner to the single point dressing tool by traversing across the wheel surface. A rotary dressing tool can also be wide to allow for form dressing the wheel and hence referred to as roll dressers. With a rotary dressing tool, the tool life is generally improved because of the increase in diamond contact points compared to single-point tool.

An important parameter for rotary dressing tool is the dressing-roll speed ratio. An appropriate roll speed ratio (q_d) is needed to output the required wheel surface.

$$q_d = \frac{v_d}{v_s}$$

Equation 10

$$v_d - dressing\ tool\ speed$$

$$v_s - grinding\ wheel\ speed$$

Roll speed can be either positive, grinding wheel and dressing roll run in the same direction, or negative i.e. vice versa. If the wheel speed is equal to the dresser roll, the speed ratio would be a +1 and this would

be a crushing action. The resultant output is a wheel of high surface roughness and high normal forces on the roll. To lower the surface roughness and lower dressing forces, the speed ration needs to be reduced and should be negative. For a precise grinding operation with conventional wheels for example, the roll speed ratio is adjusted within the range of -0.2 to -0.8 while a CBN would require a positive speed range to get an open wheel surface. It is recommended that dressing of the grinding wheel is run at normal operating speeds since this would reduce any run-out of the wheel due to unbalance. On the other hand, it can be necessary to reduce the wheel speed during dressing to avoid a vibration mode in the machine. With advances in machine technology, it is normal to have vibration sensors placed within the machine which can detect any vibrations for frequencies that can occur during dressing and check to ensure that it does not affect any dressing at a given speed.

Grinding force is heavily dependent on wheel grain sharpness. As grain becomes blunt the grinding forces increases, however, grains can sometimes fracture and pull-out, in which case forces reduce with tool wear. Dressing too fine or dressing too coarse can have adverse effects on the redress life of the grinding wheel. With dressing a wheel too fine, after initial wheel wear there will be a sharp drop in grinding power and then the surface of the wheel will stabilize followed by a period where the grinding force steadily increases as the wheel wears and blunts. For coarse dressing, whole grains break out of the wheel surface and number of active grains reduce but either way both fine/coarse dressing condition will eventually converge and stabilize towards the same value of grinding power. A redress is necessary when the workpiece parameters such as surface roughness, vibrations and size-holding are out of specification.

2.1.4 Types of Grinding wheels

Grinding wheels consist of abrasives grains held in a weaker bonding matrix. There are different forms of a grinding wheel with variation in grains, bond material, fillers and grinding aid materials. The performance and property of the different grinding wheels depend on these constituents of the wheel and the way it is manufactured. Type of abrasive grain material, size of the grain, the bond material, the property of abrasive and bond linkage and bond porosity are some of the parameters which define the grinding wheel.

‘Conventional’ wheels are mainly made from either aluminium oxide or silicon carbide abrasive with vitrified or resinoid bonds. To give further understanding of the bonds mentioned, vitrified bonds are made from a mixture of clay and ceramic material are baked at high temperatures of upto 1300 °C to create a strong bond. Resinoid bonds are made from synthetic resins that are cured under heat and pressure to create the bonds. ‘Superabrasive’ wheels are made from either diamond or cubic boron nitride

(CBN) abrasives with vitrified, resin and metal bonds. Conventional wheels is normally entirely composed of the abrasive grain and bond while superabrasive wheel is limited to a thin layer on the peripheral of a plastic or metal hub. The different requirements of wheel shapes and sizes to fit all the diverse grinding machines and jobs means grinding wheel can be manufactured in a diverse range.

The focus of this literature review will be on vitrified Aluminium oxide which is used in this experiment to grind IN718. Aluminium oxide or otherwise known as corundum is used for grinding mainly ferrous materials. Depending on the purity or preparation of the grains, they can be blocky or sharp. Blocky grains have high impact resistance and are best for heavy material removal operations while grains that micro-fracture are more durable and are kept sharp while minimizing force on the grains. There are other types of alumina such as zirconia alumina which are very tough grains, addition of chromium oxide in Pink/Ruby alumina increases friability. Brown alumina is a general purpose abrasive used for rough grinding.

A vitrified wheel is a structure of grains, bond material and pores. The bonds are harder than organic bonds (e.g. resinoid bonds) but softer than metal bonds. An advantage of vitrified wheel is that it is flexible due to its structure allowing for different forms for different grinding profiles by truing the wheel. These bonds are made from vitreous materials which have a low melting point, these are glasses formed when glass frits, clays are mixed with mineral fluxes e.g. feldspars and chemical fluxes e.g. borax. These bonds materials are mixed with water, binder, abrasive grains and compacted into a mould. The wheel is thereafter heated and cooled in a controlled cycle using an oven. The temperature can reach upto 1300^{o}C and the temperature needs to be controlled to ensure that the bond becomes glassy and can flow just sufficiently in that state.

The grinding wheels have a nomenclature to define wheel specification using a marking system. The marking system for the wheels are shown in Figure 4.

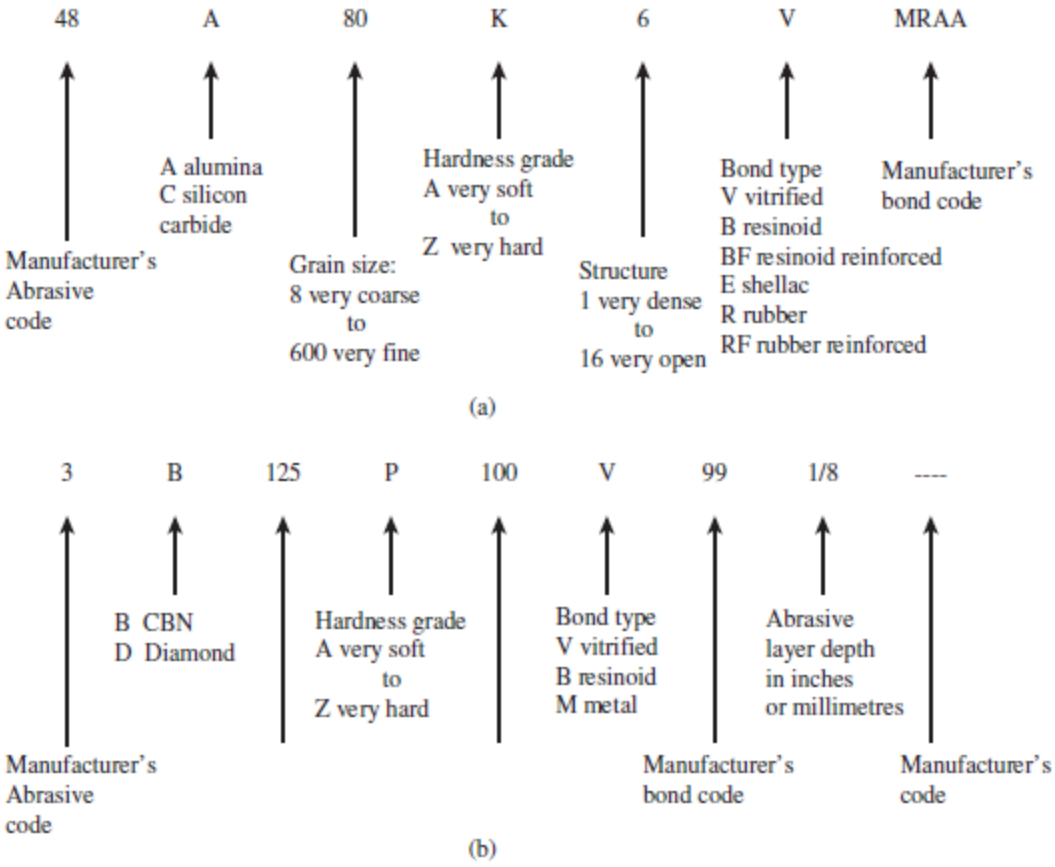

Figure 4 (a) Grinding wheel nomenclature for conventional abrasive grinding wheels. (b) Nomenclature for super abrasive grinding wheels. Figures adopted from Rowe [1].

For heavy stock material a coarse grit is used while a fine grit is used for low surface roughness material removal during grinding. The wheel grade gives an indication of the way in which a wheel wears. A softer wheel would wear much quicker than a hard wheel and the grade is directly linked to the volume of bond used within a wheel i.e. a larger portion of bond makes a wheel harder and vice versa. These characteristics of the wheel can also be influenced by the dressing procedure deployed. Coarse dressing would essentially make a more open surface on the grinding wheel and as a result making the wheel softer. Wheel structure refers to how densely packed the grains are in a grinding wheel. A lower numbered structure on the wheel indicates the grains are densely packed while a higher numbered structure indicates the grains are widely spaced. An open structure essentially allows for better swarf removal and also allows for better access for grinding fluids. Porosity and structure of wheel are parameters which are closely related, porosity is also defined by the proportion of bond in the mix. For example, a highly porous wheel can have an open structure and lower proportion of bond than a wheel of the same structure but lower porosity. Wheel with higher porosity will act soft while wheel with low porosity will tend to act hard.

2.1.5 Grinding IN718 and its application in the industry

Inconel 718 is a precipitation strengthened Ni based super alloy which is widely used in the aerospace industry. The metallurgy of the superalloy provides unique properties which helps with its application in the industry. One of its main benefits being able to operate at high strengths in extreme temperatures while exhibiting high yield, tensile and creep-rupture strength. The alloy has additions up of Nickel, Cobalt and Chromium which adds to its corrosion-resistance and resistance to oxidation. Different element additions supplements to the properties IN 718 possess as shown by Table 1.

Table 1 Shows the relevant metallurgical properties attained due to element additions in IN 718

Element addition	**IN718 metallurgical property**
Al, Ti, Nb	Hardening precipitates and/or intermetallic
Al, Cr, Y, La, Ce	Oxidation resistance
La, Th	Improve hot corrosion resistance
Cr	Sulfidation resistance
B	Improves creep properties
B(if present in large amounts, borides are formed)	Increase rupture strength

With its properties, it finds its application in turbines of jet engines including parts such as shafts, sheets, blades and discs. One of the less common applications within the industry is its use in tanks, containers, rings and pressure vessels in rocket engines. At these extreme operating conditions, the properties defined for this material is dependent on the surface quality. Grinding is therefore one of the key machining processes used which influence the surface quality for these parts and hence demand attention to understand its grindability. IN718 possess low thermal conductivity and has high strain hardening which renders the material as a difficult-to-grind (DTG) material. Supplementary to this property, high chemical affinity towards conventional abrasives means that grinding chips stick onto grinding wheels easily, also resulting in re-deposition over the ground workpiece [9]. This phenomenon increases wheel wear and also affect end-surface quality of the ground product. Although conventional wheels show this behaviour, they are still the most preferred choice in the industry mainly due to lower abrasive cost and ease of use compared to super abrasive wheels.

Surface burn is a serious issue within grinding of IN718 because of its low thermal conductivity. Surface burns are based on the heat partition ratio; the ratio of heat absorbed by the workpiece against the total heat generated during grinding. Since IN718 has low thermal conductivity, there is accumulation of heat over the ground surface which creates the heat affected zone. During grinding of IN718, the heat partition ratio is 75 – 85 % [10] and as a result there is a high temperature accumulated over the surface of the workpiece. On the other hand, sub-surface temperature of the workpiece would be relatively lower, and this unequal distribution of temperature can cause the development of tensile stresses on the surface. This steep temperature gradient normally instils tensile residual stress which is opposing to the beneficial residual compressive stress that arise from crushing effect of abrasive grain and workpiece. Greater tensile residual stress can result in decreased fatigue strength of the workpiece. Therefore, it is vital to control grinding conditions/parameters to increase residual compressive stresses and decrease residual tensile stress. A high grinding zone temperature can also result in metallurgical phase changes that affect the mechanical strength properties of IN718.

Tso [11] had studied IN718 grinding with different wheels and concluded that CBN wheels were the most suitable wheel for grinding of IN718 compared to silicon carbide and white aluminium oxide wheels. Tso [11] study was based on understanding the effect of various process parameters (including wheel speed, table speed and down feed) on the surface roughness, grinding forces and dimensional accuracy. It concluded that silicon carbide wheels had issues with rapid dulling during wet grinding and during dry grinding workpiece burns and re-deposition on the workpiece surface was identified. This paper definitely shown the superiority of CBN when grinding IN718 but as discussed previously current industry practise has been favouring the conventional wheels due to cost and ease of use. For the benefit of this project, this paper did provide a initial point of reference for the parameters that were used when grinding IN718. Looking closely towards the use of alumina wheels for IN718, Zhong et al. [12] had conducted work on surface grinding of IN718 and Hastelloy with alumina wheels. The conclusions from the study reported that a high wheel speed (upto 160 m/s) resulted in smaller cutting depth (400 µm) and smaller undeformed chip thickness. As a result, grinding force can be reduced and surface quality improved with reduced residual stress. Pioneering work which clearly defined the comparison between Alumina wheels and CBN wheels was paper by Liu et al. [13] which declared that even though the grinding ratio (G) with CBN wheel was much higher than the alumina wheel the cost aspect tipped the scales in favour of the alumina wheel. Lie et al. [13] showed that cost-performance model based evaluation means that the material removal volumes of a CBN wheel must be 14 times as large as that of a 60E aluminium oxide wheel and in practise it is not an easy task to reach this performance level due to severe loading. Huddedar

et al. [14] showed with their work that with alumina wheel the grit size of the wheel had the dominant effect on the surface roughness during the surface girnding of IN718. Within this study, workpiece speed, infeed, grit size and type of lubricant were the control parameters. Therefore, it was a significant factor to consider within the experiment design for this project. Ways in which the grit size can be controlled is to ensure new wheels are used and the constant grit size wheel type is used for all grinding regimes that are investigated in this project. Comparison of vitrified bonded single alumina (SA) and resin bonded CBN wheels for surface grinding of IN718 that was conducted by Yao et al. [15] showed that better surface integrity was obtained with SA wheel for the same grinding parameters. For the perspective of this thesis, it is important to control the grinding end result as the acoustic emission signals are analysed from repeatable grinding regimes and therefore paper by Yao et al. [15] gives confidence in the use of alumina wheels for this experiment. Sinha et al. [16] which studied surface burn during grinding of IN718 also showed comparison of alumina and Silicon carbide wheels and concluded that Alumina wheels ground IN718 more effectively. Surface burn is a phenomenon to avoid within the experiment for this thesis as this study focuses on being able to realise the repeatable features with the use of acoustic emission signals and therefore improve the confidence on using acoustic emission for process monitoring during grinding on IN718. Having conducted a review on papers that have been written with respect to grinding of IN718, it evident there is not a single paper that targets the acoustic emission signal acquisition during grinding of IN718. This review rather helps evaluate a starting point for understanding the grinding regimes which are relevant to investigate when acquiring the acoustic emission signals.

From the review of literature, it is evident that researchers can agree CBN wheels are the most effective wheel to use for grinding of IN718 but the cost aspect and ease of use nudges the industry to stick to using alumina wheels. There has been work done with varying parameters as control to understand the mechanism of grinding for IN718. Understanding the grinding parameters has concluded key parameters which influence the output of grinding as: depth of cut (a), the contact length between grinding wheel and workpiece (lc), peripheral velocity of the grinding wheel (Vs), workpiece feed rate and choice of grinding wheel.

2.2 Process monitoring in grinding

In this literature review, the term ‘process’ is considered as steps involved in successfully carrying out a grinding task/job in an industrial environment. Therefore, process monitoring involves the assessment of its output quantities to make a judgement regarding the state of the process at a given instance. Figure 5 shows a systematic approach of the grinding task, adapted from Tönshoff et al. [17], highlighting how the

different output quantities form part of the system hence opening the opportunity for the process to be monitored. System behaviours and system parameters have already been discussed within section 2.1 and it is clear how these parameters influence the grinding mechanism and hence form as inputs to the grinding system. As a result, the outputs are the quantities which can be quantified or measured to understand the result of the grinding process. Methods of evaluating these quantities from the process are highlighted in section 2.4.

From reviewing the grinding process, it is relevant how the workpiece material influences the output of the grinding process. The grindability of a material defines with how ease a material can be ground without resulting in grinding burn or even high grinding forces which are not efficient for the process. Coolant/lubricant helps regulate the grinding zone temperature which directly affects the chip formation during grinding and also helps with the progression of wheel wear. The stability the grinding machine provides during a grinding cut can reduce vibrations or other dynamics during the process which directly influences surface quality on workpiece. Grinding wheel properties have already been review within section 2.1.42.1.4 and its dressing/truing in section 2.1.3 which shows how the choice of grinding wheel can influence the grinding parameters chosen and the ouput. It is evident that, these inputs (grinding parameters and grinding wheel choice) into the system directly influence the outputs when working together within the process. Therefore, monitoring the outputs of the grinding process is a great way of defining the status of the process. Furthermore, the state of the process can be used to make a change in the process input parameters and system behaviour in a closed-loop or open loop feedback system to get desired process state which in turn gives desired output from the grinding system. The feedback system allowing for such control within grinding is beyond the scope of this literature review but can be read further within the review by Tönshoff et al. [17].

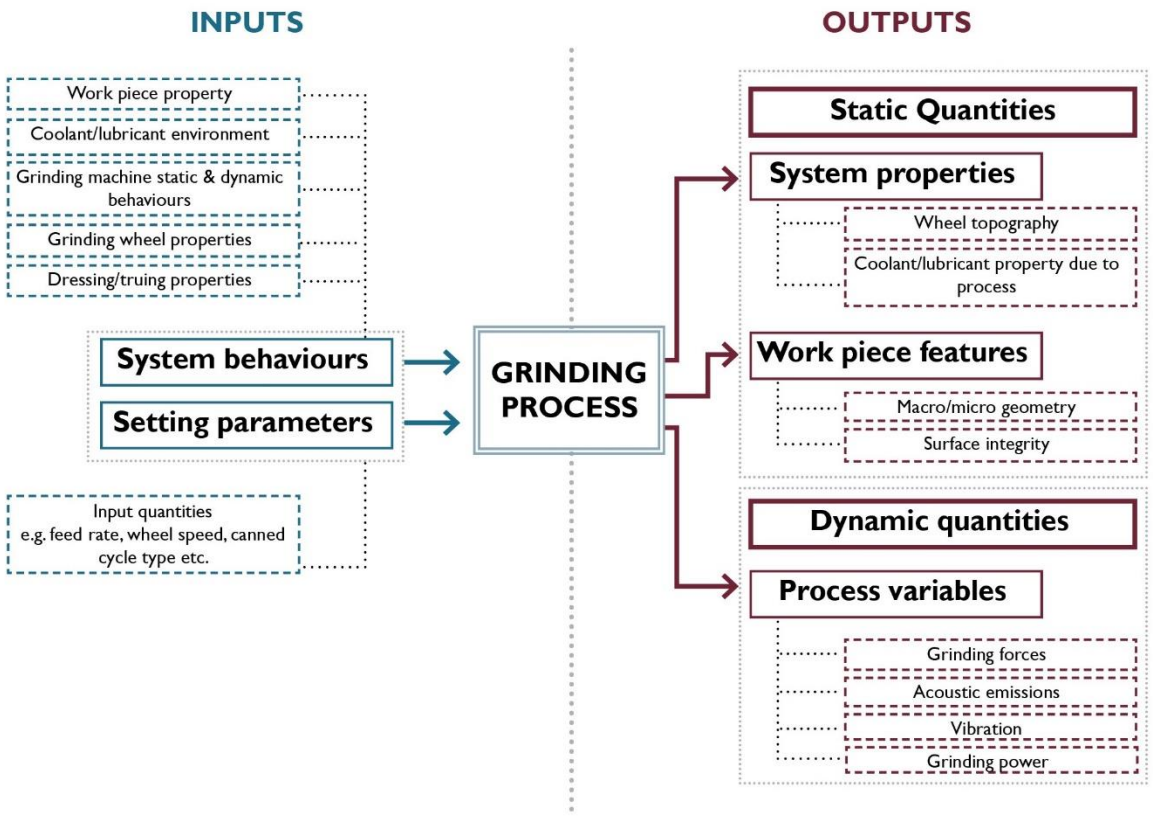

Figure 5 Systematic breakdown of the grinding process adapted from Tönshoff et al. [17] *to show quantities which can be evaluated for process monitoring.*

2.3 Quantities evaluated through process monitoring

Grinding force, power, acceleration, acoustic emissions and temperature are some of the process quantities which can be assessed either through peripheral sensors which are connected to a grinding machine or through the in-house sensors of controllers within the machine. On the other hand, output quantities such as the workpiece macro/micro geometry, workpiece surface integrity or the abrasive tool macro/micro geometry could be assessed to evaluate the process status. Figure 6 gives an overview of evaluation methods for these quantities which has been gathered and summarised from the literature by Tönshoff et al. [17].

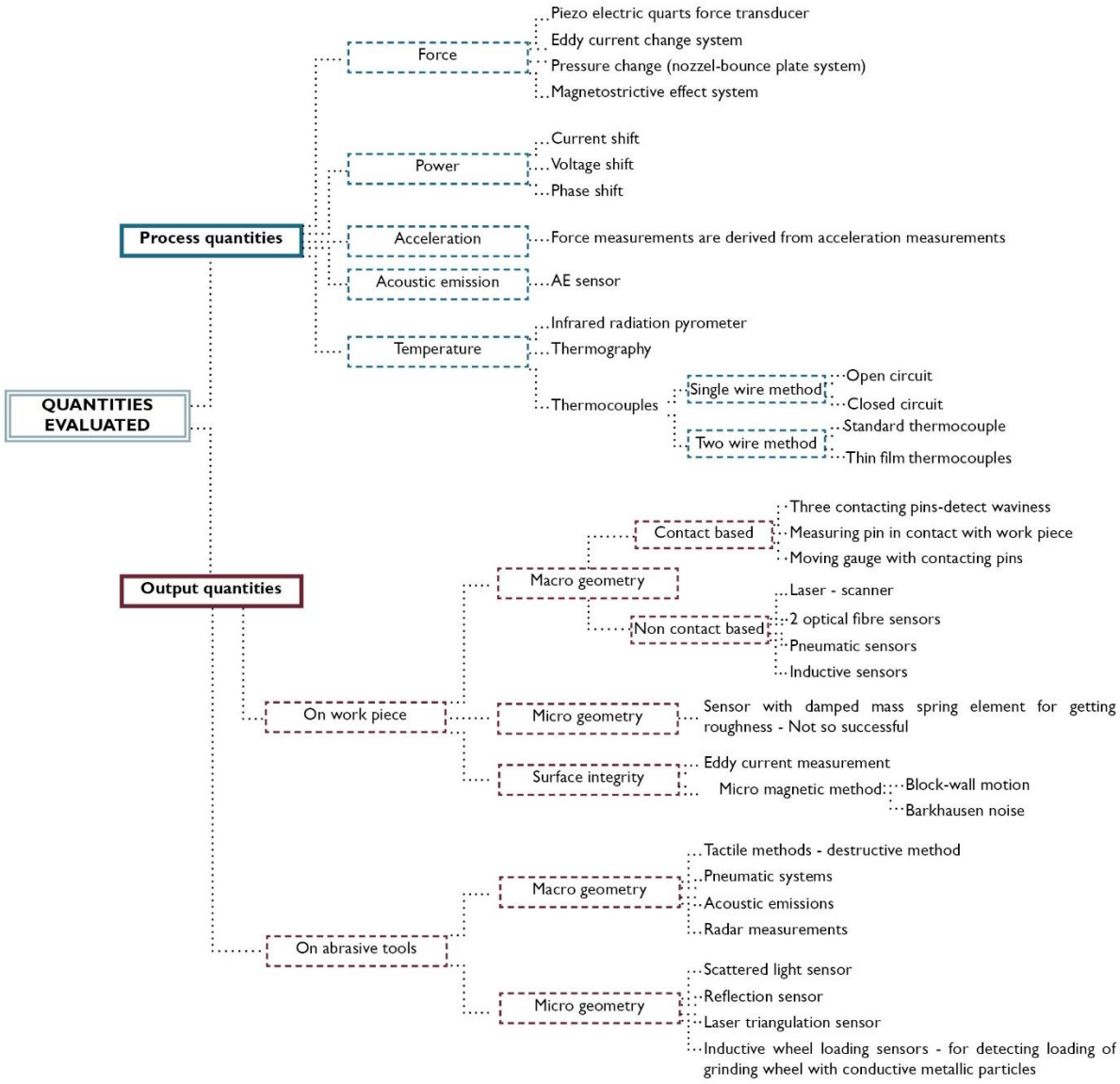

Figure 6 Overview of measurement devices/techniques used to evaluate quantities within the grinding process.

2.4 Process quantities

2.4.1 Process quantity and state of art sensing: Force

Force measurement was directly linked with the measurement of displacement for a material which has been subjected to a force and displacement could be measured by different sensors. The stiffness of a system plays a crucial part in defining displacement and in the past strain gauges struggled to accurately define displacement during grinding as system components which needed to be in direct contact with the strain gauge needed to be weak to record enough strain. Piezo electric quartz force transducers fit the

requirements to overcome this issue with strain gauges. Piezo electric force transducers' directional measurement capability also meant they could be stacked in a housing to form a three-component force measurement device, forming the dynamometer, which could be used during measurement of cutting force in grinding. These force measuring devices can be formed of different types and sizes with required protection for it to be deployed in industrial application. Along with the piezo system, a charge amplifier would be required to amplify the signal from the transducers to voltage signals which can be deciphered as cutting forces during grinding.

Other sensors for measuring force can use eddy current changes or pressure changes between a nozzle-bounce plate system between components of a system. Compared to piezo electric transducers these sensors cannot reach the same sensitivity. Use of Magnetostrictive effect for sensing force or torque is the other type of sensors available. This can only be applied to ferromagnetic materials which change permeability under mechanical load.

2.4.2 Process quantity and state of art sensing: Power

Power measurement was rather simple and depending on the type of system used to provide power to a spindle system, the current, voltage and phase shift can be detected. It is possible to deduce this information from the system without any sensor and affecting the machine environment as a result. The only concern with power measurement is the sensitivity of the measured quantity. Power required for grinding was only a proportion of the total power consumption for a spindle and therefore information gathered from power system would also require information from force measurement to infer any changes in power measurement.

2.4.3 Process quantity and state of art sensing: Acoustic emission

Acoustic emission is defined as the stress or pressure waves generated during the dynamic process in materials[18]. Irreversible changes in materials such as crack propagation, metallurgical phase changes and dislocation movements causing plastic deformation are prime sources of acoustic emission in metals [19]. These acoustic emissions had a high-frequency range which allows it to be critical in being easy to monitor [20] during operations such as grinding as it is discrete from environmental noise or machine vibration, typically between 50 kHz and 20 MHz today [21]. These advantages give reasons for studies to be developed towards using acoustic emission technology within process monitoring in machining.

Use of AE for process monitoring during grinding has predominantly been used in the industry for detection of grinding burn. This is an area of fault diagnosis during grinding which has witnessed most

development and promise such that it shows potential to be used in industry. Therefore, within the pursuit to understand the AE features that could be used for process monitoring this review will heavily focus on work that has been related to grinding burn detection.

One of the first works in using AE for detection burn [22] was conducted in order to study surface grinding burn occurring within the camshaft production line for constant grinding wheel/workpiece speed (not transient conditions). In the study, instrumentation setup within the production line flagged suspected grinding burn by monitoring the AE amplitude against a threshold. This work was part of the most primitive forms of work using AE. This study was not specific to a certain material but was rather focused on camshafts for V6 and V8. The paper did not thoroughly examine how different grinding parameters such as wheel speed, feed rate and coolant application affected AE signals. The study primarily relied on the flank energy ratio derived from AE signals to detect grinding burn on the shop floor but this is only one of the features that can be derived from the AE signal. The idea within the paper for detecting grinding burn showed promise but still acknowledged the occurrence of false positives thereby showing the technology or concept of monitoring the acoustic emission signals was still in its infancy. For practical industrial application, it is critical to ensure repeatability of AE-based monitoring systems and this is the level of work and knowledge gap that needs to be addressed within this thesis.

Wang et al. [23] made a detailed statistical inspection of the raw AE signals as input features vectors for neural networks for grinding burn detection. The study found that traditional statistical such as zero-crossing rate, ratio of power and amplitude histogram, were ineffective in detecting grinding burn reliably due to their sensitivity to noise and variations in the grinding process. However, more advanced methods like Constant False Alarm Rate (CFAR) power law and Mean-Value Deviance (MVD) showed promise in detecting transients indicative of burn. The neural networks proved to be promising at detecting burn and the two feature vectors used included statistical features of the AE signal comprising of band power, kurtosis and skew and autoregressive coefficients which capture the spectral characteristics of the AE signals. The study focuses on 52100 bearing steel which will have different characteristics to IN718 and therefore learnings from the paper would be inspiration to the methods used for detecting grinding burn but the difference in mechanical properties will have an effect on the AE signal characteristics and results cannot be considered comparable. The study mainly varies the depth of cut to induce burn and does not look at how other grinding parameters may impact burn occurrence and even the AE signal characteristics and its effect on the neural network performance.

In 2004, Aguiar et al. [24] also looked at using AE statistics such as Root mean square (RMS), Constant false rate (CFAR), Ratio of power (ROP) and mean-value deviance (MVD). These AE statistics related terms and AE features are shortly explained within section 2.4.3.1 to 2.4.3.5. From this study, ROP was shown to be a good indicator for burn since it clearly showed the beginning and end of wheel-workpiece contact and a distinction between burn/no-burn conditions. While the study demonstrates the effectiveness of statistical tools in detecting grinding burns, it does not thoroughly address the repeatability of these statistical tools across the 15 experimental runs. There is still variability witnessed within these experimental runs suggesting the need for more extensive testing to consistently detect burns across different batches and operating settings. The study does not discuss the long-term stability and calibration of the AE sensors and the data acquisition system. For a repeatable process monitoring solution, the AE sensors and signal processing algorithms must maintain their accuracy and reliability over time, even with regular wear and tear of grinding equipment. The study concluded that while RMS, CFAR, ROP and MVD were useful for burn detection on ABNT 1045 steel with an aluminium oxide grinding wheel, skew and kurtosis required further investigation to determine their potential utility. The statistical features of AE signal used in this paper showed confidence in the ability to use AE data and can be used as the study base to develop AE features for process monitoring during grinding. Although, in this context these features are used for grinding burn, these are statistical features of the AE signal that may pick up other changes within the material during grinding and hence support process monitoring.

Wavelet packet transforms have also been used with AE signals in order to extract features for AE signals, Liu et al [25]. used fuzzy pattern recognition to detect burn with this method and was successful in creating a well-performing algorithm. The study leverages wavelet packet transforms to extract features from AE signals and employs fuzzy clustering to optimize these features for accurate grinding status identification. The experimental setup involved grinding IN718 using a Makino A55 CNC machining center. The study found that wavelet packet transforms captured the intrinsic properties of AE signals, allowing for detailed analysis in both time and frequency domains. The fuzzy clustering successfully optimised the extracted features, reducing information redundancy and improving classification accuracy. The experimental results demonstrated a high recognition rate for grinding burn detection, with over 92 % accuracy.

Following on, Aguiar et al. [26] later used grinding power, AE RMS and AE mean value deviance with fuzzy logic models developed to interpret the AE signals and predict the occurrence of grinding burns. Fuzzy clustering method were used to handle the imprecision and variability in data; an aspect which was considered a shortfall in the previous paper that focused on the same statistical AE features. Similar to

the previous study, varied grinding parameters such as depth of cut, wheel speed and feed rate was used to induce different grinding conditions on AISI 1045 steel using aluminium oxide grinding wheel. RMS, CFAR, ROP and MVD were effective in detecting grinding burns. RMS provided a stable level for non-burn workpieces and significant variation for burnt workpieces. For instance, RMS values for non-burn conditions were consistently around 0.5 V, while severe burns showed RMS values exceeding 1.5 V. CFAR showed high sensitivity to burn detection, maintaining a high detection rate without significant signal decrease. CFAR values for burn conditions were approximately 1.2 times higher than for non-burn conditions. ROP was found to be a good indicator for burns, with low levels for non-burn parts and high levels for burnt parts. Non-burn ROP values were around 0.3, whereas burn conditions had ROP values close to 0.8. MVD presented behavior similar to RMS but was less effective in some tests. MVD values varied from 0.4 for non-burn to 1.3 for burn conditions. Kurtosis and Skewness displayed variations during burn events but were inconsistent and less reliable indicators. For example, kurtosis values fluctuated between 2 and 4, while skewness ranged from -1 to 1. The fuzzy models demonstrated high accureacy in predicting grinding burns, with over 92 % accuracy. Specifically, the model using RMS and grinding power inputs achieved an accuracy of 94%, while the model incorporating MVD reached 92%. As previously mentioned, the study focused on AISI 1045 steel and not IN718 which have properties that can affect the AE signal characteristics. This paper is still at a stage of demonstrating offline analysis of AE signals. Implementing real-time burn detection would require ensuring that signal processing and fuzzy logic analysis can be performed in a quick manner with enough computing capacity to support intervention during the grinding process. This paper does form the foundation of understanding AE statistical features from a point of view for detecting grinding burn and can be a starting point when evaluating the rightful statistical features that would be of help within process monitoring during grinding. There is not another paper in the field that explicitly analysis acoustic emission signals during grinding.

Some of the latest studies includes the use of AE to detect grinding burn successfully using the energy of cross wavelet transform (EXWT) and degree of wavelet coherence (DWTC) at specific frequency bandwidth [27]. Gao et al. [27] conducted two sets of experiment: laser-induced metal burns to produce pure burn signals and actual grinding experiments to generate grinding burn signals. This approach is also considered based on understanding the degradation of surface integrity of workpiece caused by excessive heat during the grinding process. For the former experiment, Laser heating was used to create pure metal burn signals on 1045 steel. The AE signals were captured using a PAC-II system with a sampling rate of 2 MHz and an amplification factor of 40 dB. For the latter experiment, grinding burns were produced by varying the sharpness of the grinding wheel and conducting the grinding process without coolant. The

same AE acquisition system was used to capture the signals for both experiments. The AE signals were analyzed using XWT and DWTC to identify the coherence between the pure metal burn signals and the grinding burn signals, thereby distinguishing burn signals from other AE sources. The study found that from the laser burn experiment, the AE signals for no-burn and burn conditions showed distinct differences in their frequency content. Burn signals had higher amplitudes and were concentrated in the 250-400 kHz range. Similar to the laser burn signals, the grinding burn signals exhibited distinct frequency components, particularly in the 250-400 kHz range, although the grinding process introduced more noise. XWT analysis revealed common areas with high power in the frequency band around 310 kHz, indicating the presence of grinding burns. WTC analysis showed high coherence between the laser burn signals and the grinding burn signals in the 200-530 kHz range, with the highest coherence observed between 600-650 kHz, providing a reliable indicator of grinding burns. The novel parameters derived from XWT and WTC (EXWT and DWTC) achieved a 100% detection accuracy in distinguishing between normal and burn conditions in the grinding signals. As with most of the work in grinding burn literature, this work was also conducted using AISI 1045 steel which further elevates the gap in literature regarding use of similar acoustic emission signals and processing techniques within grinding of IN718. The control in this paper for creating different grinding regimes was through varying sharpness of grinding wheel. The technique of varying wheel sharpness through wear or dressing can introduce variability that is difficult to quantify accurately leading to inconsistent experimental conditions. This lack of precision can affect the repeatability and reliability of the process. Ther is risk that grinding wheel wear is not uniform and different sections of wheel may experience varying degrees of wear. This inconsistency can result in uneven grinding conditions, making it challenging to draw definitive conclusions about the relationship between wheel sharpness and grinding burns. From previous review on the grinding mechanisms suggests that the sharpness of the grinding wheel influences the heat generation during the grinding process. However, this technique does not allow for precise control over the exact amount of heat generated. Other factors, such as feed rate, wheel speed, and coolant application, also significantly impact heat generation and need to be controlled rigorously but is not discussed within the paper. In industrial settings, the sharpness of grinding wheels is typically maintained within specific tolerances to ensure consistent performance. The experimental variation of sharpness may not accurately reflect real-world grinding conditions, limiting the applicability of the findings to practical scenarios.

While there have been studies conducted towards using AE for detecting grinding burn there have also been studies going into understanding the behaviour of AE signals with high temperature condition to simulate grinding burn conditions. In the past, Liu et al. [28] has shown that energy distribution of AE signals of thermal expansion under high-temperature (simulative of grinding conditions) is concentrated in the higher frequency bands and proposed that this would give direction towards burn detection. The study employed wavelet packet transforms (WPT) to extract AE signal features that indicate grinding burn, aiming to improve real-time monitoring and quality control in grinding processes. The experimental setup consisted of simulating grinding thermal behavior using laser irradiation to produce thermal expansion AE signals. This approach helped in isolating the AE signals related to thermal effects from other mechanical interferences. Experimental setup was similar to the work by Goa et al. [27] but distinction being on the signal processing technique , WPT. The laser experiment was conducted using AISI 1045 steel, laser irradiation was used to induce thermal expansion. AE signals were captured using a PAC-II system with a 2 MHz sampling rate and a 40 dB amplification factor. The objective being to obtain pure thermal AE signals for feature extraction. The grinding experiment was conducted on CMSX4 nickel-based alloy, Grinding was performed under conditions that varied the grinding wheel's sharpness and coolant application to induce burns. AE signals were captured under these conditions. The objective being to compare AE features from real grinding burns with those obtained from laser-induced thermal expansion. WPT was used to decompose AE signals into time-frequency representations. The energy of wavelet packets was calculated to identify features indicative of grinding burns. AE signals from laser irradiation showed distinct features at high temperatures, with energy concentrated in high-frequency bands (250-400 kHz). High coherence was recorded between laser-induced AE signals and grinding burn AE signals at specific frequency bands (200-530 kHz). AE signals from grinding without coolant exhibited higher amplitude and energy concentration in the 750-880 kHz range, indicating grinding burn. Features extracted using WPT showed clear distinctions between normal and burn conditions, with significant peaks in high-frequency bands for burn conditions.

Chen et al. [29] uses 3 levels of temperature detection levels from laser irradiation test and classifies the temperature rise as those seen in grinding burn conditions. Chen et al. [29] uses artificial neural networks to make these classifications with short-time Fourier transforms (STFT) of AE as inputs. The papers divides its experiment into 3 sections including laser irradiation tests, grinding experiments and signal processing. The idea behind the work was to use AE features from laser irradiation as a basis for developing artificial neural networks (ANNs) to monitor grinding thermal performance. IN718 and MARM002 workpiece was used during the laser irradiation tests using a Lumonics JK704 Nd laser machine. AE signals were captured

using a physical acoustic WD sensor with a frequency range of 100 kHz to 1 MHz, and thermocouples were used to measure temperature. Three off-focal distances (34 mm, 40 mm, and 46 mm) were used to vary the laser power density used during tests. IN718 was used to conduct grinding trials performed on a Makino A55 machine center with different depths of cut (0.02 mm and 0.2 mm) and no coolant. AE signals, force, power, and vibration were monitored. This grinding trial data would be used to fair the application of ANN in classifying grinding temperatures (high, medium & low) and detect burn. AE signals from laser irradiation showed higher amplitude and frequency components at higher temperatures. For IN 718, signals at 34 mm off-focal distance had higher amplitudes in the higher frequency range compared to those at 46 mm. Grinding at larger depths of cut produced higher amplitude AE signals with significant high-frequency components, similar to those observed in laser irradiation tests. The ANN, trained with laser-induced AE data, effectively classified AE signals from grinding trials. For instance, at a 0.02 mm depth of cut, the ANN classified 60.66% of AE data as medium temperature and 30% as low temperature in the first cut, with minimal high-temperature features. This distribution changed in subsequent cuts, reflecting the wheel's wear and thermal performance. Although the study showed that grinding burn is not only detected by temperature rise and there are other factors that promote burn, Chen et al. [29] has been successful in showing a concept that could save grinding experiments to build datasets for grinding burn.

The paper by Adibi et al. [30]presented a study on the efficiency of acoustic emission (AE) signals to monitor the grinding performance of IN738. The research investigated the grinding process using cubic boron nitride (CBN) wheels and examines the relationship between AE parameters, such as the root mean square (AERMS) and amplitude, with grinding performance indicators. The paper showed that increasing the depth of wheel engagement generally resulted in higher specific grinding energy and AE amplitude. This was attributed to the increased material removal rate and greater interaction between the grinding wheel and the workpiece. Higher depths of engagement also led to increased surface roughness, indicating a rougher finish due to more aggressive grinding conditions. An increase in work feed speed resulted in a reduction of specific grinding energy. This was due to fewer contacts per grinding pass, leading to less wheel loading. The AE amplitude increased with work feed speed, indicating higher forces per grain but reduced overall contact frequency. Surface roughness increased with work feed speed, which was consistent with the higher forces per grain leading to a rougher surface finish. Higher wheel speeds reduced the cutting force but increased the number of contacts per pass, resulting in higher specific grinding energy. AE amplitude decreased with increasing wheel speed due to lower cutting forces. Surface roughness showed a decreasing trend with increasing wheel speed, demonstrating that higher

wheel speeds contributed to finer finishes. The AERMS values mirrored the trends observed in surface roughness, confirming its effectiveness as a monitoring tool. This paper works as a cornerstone for comparing the results that will be analysed with the thesis in question since the material used is close to the IN718 with variation being experimental setup and grinding machine.

Since the grinding trials were completed in 2019 & 2020, further papers were also reviewed to evaluate the current gap in the field to remain relevant in the field of research. Some of the papers reviewed during this time period include :

Yesiluirt et al. [31] presents a paper that explores the use of scalogram-based instantaneous features of acoustic emission (AE) signals for detecting grinding burn. The authors have focused on two primary features: instantaneous energy and signal phase. The instantaneous energy (IE) values for burnt conditions were consistently lower than those for non-burnt conditions. For example, in regular grinding, the IE was observed to be approximately 0.074 for intact conditions and dropped to about 0.040 for burnt conditions. This significant reduction indicates the reliability of IE as an indicator of thermal damage. The phase deviation also exhibited noticeable differences. For instance, in the high cutting speed condition, the phase deviation for intact conditions was around 62684 radians, whereas it dropped to 37580 radians under burnt conditions, highlighting the sensitivity of the phase deviation to grinding burns. Experiments were conducted under various grinding conditions including normal grinding, higher cutting speed, larger infeed rate, and smaller dressing depth of cut. The results consistently showed that the proposed scalogram-based features could detect grinding burns with higher precision than traditional methods building on the confidence on these features. As with other previous studies, the work was focused on using the outer ring of the 6806 ball bearing made of DIN 100Cr6 steel and case hardened to a depth of 0.15mm at 60HRc therefore different from IN718 which would showcase different properties during grinding. Conducting a detailed study on the repeatability and reliability of AE features across multiple grinding cycles would have helped address one of the critical gaps in the current research. Ensuring that the AE features can consistently detect grinding burns will enhance the trustworthiness of this monitoring technique in industrial applications. Although the paper suggests positive conclusions from the capability of the process monitoring technique , the paper acknowledges limitations such as the need for real-time implementation and the challenge of handling large data volumes. For instance, the high calculation load due to the octave band-based fast calculation procedure was noted. Future work will focus on developing algorithms for real-time processing and further validating the features across different materials and grinding conditions. This is another aspect to consider when looking at features that are picked up from

acoustic emission signals and its viability of implementation in the industry as an in-process monitoring technique. In conclusion, the study makes a significant contribution to the field of grinding process monitoring. The proposed scalogram-based features show great promise for enhancing the detection of grinding burns, though further research is necessary to address the identified gaps and fully realize the method's potential in industrial settings.

Yin et al. [32] investigated the relationship between grinding and AE signal characteristics, and develops a prediction model for grinding surface roughness using a BP neural network optimized by a genetic algorithm. The study focused on GH4169 superalloy, TC4 titanium alloy, and SiCp/Al composite materials for conducting its experiments. The paper evaluated the effect of grinding parameters on AE signal which was good to understand the effect of different materials being tested with controlled grinding conditions. The RMS value of AE signals increased with the increase of grinding depth for GH4169, TC4, and SiCp/Al, indicating higher energy release and interaction between the grinding wheel and workpiece. For instance, the RMS value for GH4169 increased from approximately 0.074 to 0.040 with increased depth. The RMS value of AE signals decreased with the increase of grinding wheel velocity (vs) due to reduced strain rate and plastic deflection of the material. The RMS value of AE signals increased with the increase of feed velocity (vw), corresponding to higher material removal rates and energy release. When evaluating the spectral distribution of the AE signals it was noted that spectral amplitude between 90 and 140 kHz increased as the grinding depth increased. This trend was consistent with the AE signal RMS values, which also increased with greater grinding depth due to higher energy release during the grinding process. The spectral amplitude of the primary energy concentration band (90-140 kHz) decreased with increasing grinding wheel linear velocity. This reduction in spectral amplitude correlated with a decrease in strain rate and plastic deflection of the material, resulting in lower energy release. This observation aligned with the decrease in the AE signal RMS value as the grinding wheel linear velocity increases. Higher feed velocities lead to increased material removal rates and strain rates, thus releasing more energy and increasing the spectral amplitude between the band of 90 – 140 kHz. This finding is consistent with the trend observed in the AE signal RMS value, which also increased with higher feed velocities. There was a positive correlation between the AE signal RMS value and surface roughness. As the RMS value increases, the surface roughness also increased. This indicated that higher energy release, as captured by the RMS value, corresponded to rougher surfaces. Similarly, the ringing count of the AE signal showed a positive correlation with surface roughness. An increase in the ringing count value corresponded to higher surface roughness. The FFT peak value of the AE signal also correlates positively with surface roughness. Higher FFT peaks indicate greater surface roughness. It is evident from this study how significant the output

surface roughness needs to be monitored from samples if repeatability is validated during process monitoring of grinding. As with most research literature in this field, the focus on GH4169, TC4, and SiCp/Al composites means it does not address IN718, a material critical to aerospace applications. Investigating AE response features specific to IN718 will provide valuable insights for industries relying on this material.

Another aspect that has made progress within process monitoring using AE has been work done towards understanding wheel condition. González et al.[33] recently released a novel approach for monitoring the wear of grinding wheels using AE signals and deep learning techniques. Their experimental methodology involved conducting surface grinding tests under different conditions and collecting AE signals, which were then processed using Fast Fourier Transform (FFT) to extract frequency domain features. These features were analyzed using pre-trained Convolutional Neural Networks (CNNs) to automatically extract relevant information, followed by clustering using Principal Component Analysis (PCA) and t-Distributed Stochastic Neighbor Embedding (t-SNE). The pre-trained CNN effectively extracted features from the FFT plots of AE signals, eliminating the need for manual feature extraction, this is a novel method in comparison to the thresholding concepts adopted within this thesis. Both PCA and t-SNE showed good clustering performance in identifying the initial stage of the grinding wheel i.e. the dressing influence on the AE signal but found it difficult to categorise mid-life and end of life for wheel wear. The experiments were conducted using ASTM A681 tool steel but the generalization of this approach to other materials, such as IN718 used in aerospace applications, remains unexplored. The paper does not go into detail of its shortfalls on its ability to categorise the wheel wear to its different stages but promises better clustering with further research on other clustering techniques such as 3D clustering which help classify stages accurately.

Bi et al. [34] focused on the condition monitoring of diamond grinding wheels using AE signals during the grinding of brittle materials – fused silica glasses. It is important to note that the material ground in Bi et al.'s paper is not representative of the superalloys discussed within this paper but highlights a different method for examination of the AE signals. The study highlighted the complexity of AE signals in such processes, characterized by a mixture of continuous-type AE (c-AE) and burst-type AE (b-AE). The researchers used CNN and Long Short-Term Memory (LSTM) networks for feature extraction and classification of the wheel state. They found that the AE frequency spectrum provided a more distinct representation of the grinding process compared to the time waveform, due to the separation of different crack mechanisms in the frequency domain. The LSTM model showed high prediction accuracy for the

wheel's state, further demonstrating the efficacy of deep learning in AE-based monitoring. The research utilized CNNs to classify the state of the grinding wheel based on original AE time waveforms, achieving over 90% accuracy in multi-class classification. Additionally, LSTM model was employed for regression analysis of wheel state using AE spectrums. The model demonstrated high prediction accuracy, with the Mean Absolute Error (MAE) and Mean Squared Error (MSE) significantly lower compared to traditional Back Propagation Neural Networks (BPNN). The LSTM model reduced the MSE by 78.1% and the MAE by 50.9% compared to the BPNN model.

Yang and Yu [35] presented a novel system for monitoring grinding wheel wear using discrete wavelet decomposition and support vector machine (SVM) classification. The acoustic emission (AE) sensor collected grinding signals, which were then preprocessed to identify the grinding period signals. The feature vectors were created using the root mean square (RMS) and variance of the wavelet decomposition coefficients, which are used to classify wheel wear conditions. The results showed high classification accuracy, suggesting the system's efficacy in monitoring wheel wear. The classification accuracy of the system was tested under two different cut depths (10 µm and 20 µm) with 99.39 % achieved for the former and 100% for the latter. The extracted features(RMS and variance) were processed using a five-level coif2 wavelet decomposition. novel preprocessing method was employed to extract grinding period signals and eliminate noise. The preprocessing included high-pass filtering with a cut-off frequency of 90 kHz, which significantly improved the classification accuracy compared to a 30 kHz cut-off frequency which the authors suggest is due to its ability to retain useful information about wheel wear, which was otherwise submerged by lower frequency noises. The study noted that while 90 kHz was optimal for their conditions, different grinding setups might require different cut-off frequencies. This paper conducted a thorough investigation into the performance of signal processing techniques deployed to ensure the process was optimised. Study showed that Investigating the high pass filter at 90kHz performed better in classification compared to those filtered at 30 Hz. Various wavelet bases were tested (e.g., db1, db2, coif1, coif2, sym2, etc.), and the results indicated that while the choice of wavelet base affected classification accuracy, the coif2 wavelet at level 5 performed consistently superior. Although the paper discusses the selection of the wavelet base, it does not provide a comprehensive analysis of how different wavelet bases might perform under varying conditions or with different types of AE signals. This indicates a gap in understanding the optimal wavelet base for different grinding scenarios. The SVM classifier showed superior performance compared to the Backpropagation (BP) neural network, particularly under the 10 µm cut depth condition where the BP neural network's accuracy dropped to 90.91%. The study suggested that the high classification accuracy obtained demonstrated the potential of

the proposed method for industrial applications, though it acknowledged the need for further testing under more complex and varied conditions.

Literature review have shown that AE can be successfully used for the detection of burn and there has been a lot of work done towards understanding AE signals. Acoustic emission features that were chosen for this study were a collection of promising AE features that has shown to be useful in studies for detection and prediction of various faults or condition during grinding. Aguiar et al. [36] showed that AE root mean square (RMS), Constant false alarm rate (CFAR), Ratio of Power (ROP) and Mean value dispersion (MVD) were some of the statistics that helped detect burn while skew and kurtosis showed interesting behaviours in the signal. Therefore these AE features are further evaluated below:

2.4.3.1 AE RMS

This statistic gives the average sense of magnitude of signal in the block of AE data which is evaluated therefore considered an effective way of quantifying a varying signal. The RMS value of a signal gives a measure of the power content of the signal. See Figure 7 which shows a graphical representation of a signal. The equation to calculate AE RMS from signal data can be given as :

$$AE_{RMS} = \sqrt{\frac{1}{N}\sum_{i=1}^{N} AE^2(i)}$$

Equation 11

N is the number of discrete data points in a block of AE dataset during a grinding pass.

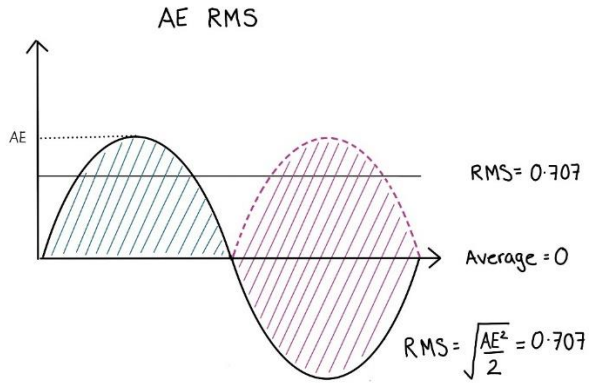

Figure 7 Graphical illustration of the calculation and reference of RMS for a sinusoidal signal.

2.4.3.2 CFAR

CFAR is used for detection of events within the signal. For this statistic, the fast fourier transform of the signal needs to be derived initially. X_K represents the k[th] magnitude-squared Fast Fourier Transform (FFT) bin and v is a changeable exponent while $2M$ is the total number of FFT bins. See Figure 8 which illustrates the FFT bins and illustration that are relevant to substitute into the equation for calculating CFAR. In this study, v = 2 is used as a suitable exponent for this investigation as it works as a good energy detector when evaluated against the whole signal. This statistic makes use of pre-normalised data.

$$CFAR = \sum_{K=0}^{M-1} X_k^v$$

Equation 12

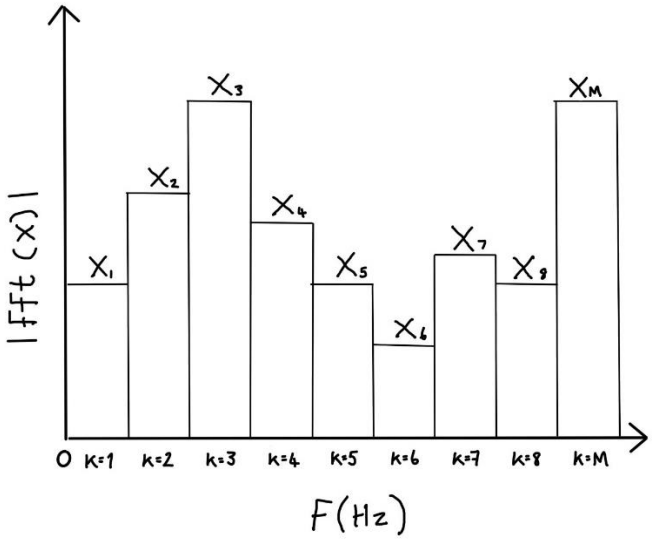

Figure 8 Graphical illustration of Fast Fourier Transform bins calculated from the AE signal (X) showing the bins and magnitude of each bin.

2.4.3.3 MVD

MVD quantifies the average deviation of the AE signal from its mean value in a given block of data. A large value would indicate that the deviation is too great to be explained using a simple exponential distribution model. Similar to CFAR, X_K represents the k[th] magnitude-squared Fast Fourier Transform (FFT) bin, $2M$ is the total number of FFT bins and $\bar{X}$ represents the mean of magnitude-squared FFT.

$$MVD = \frac{1}{M} \sum_{k=0}^{M-1} log \left[\frac{\bar{X}}{X_k} \right]$$

Equation 13

2.4.3.4 Kurtosis and Skew

Skew is a statistic which shows if the distribution tail is longer than the other while Kurtosis expresses the tail size. They both can be used to indicate the variations in the AE signal. See Figure 9, Figure 10, Figure 11 where graphical illustrations show how sample data is shaped with different values of kurtosis and skew. Any abrupt changes in AE signal will show up as spikes using this statistic. In Equation 14 and Equation 15, x is the value of the acoustic emission while μ represent the mean of the block signal. N is the number of samples recorded in a block of signal while σ is the standard deviation of the signal.

$$Kurtosis = \sum \frac{(x-\mu)^4}{N\sigma^4} - 3$$

Equation 14

$$Skew = \sum \frac{(x-\mu)^3}{N\sigma^3}$$

Equation 15

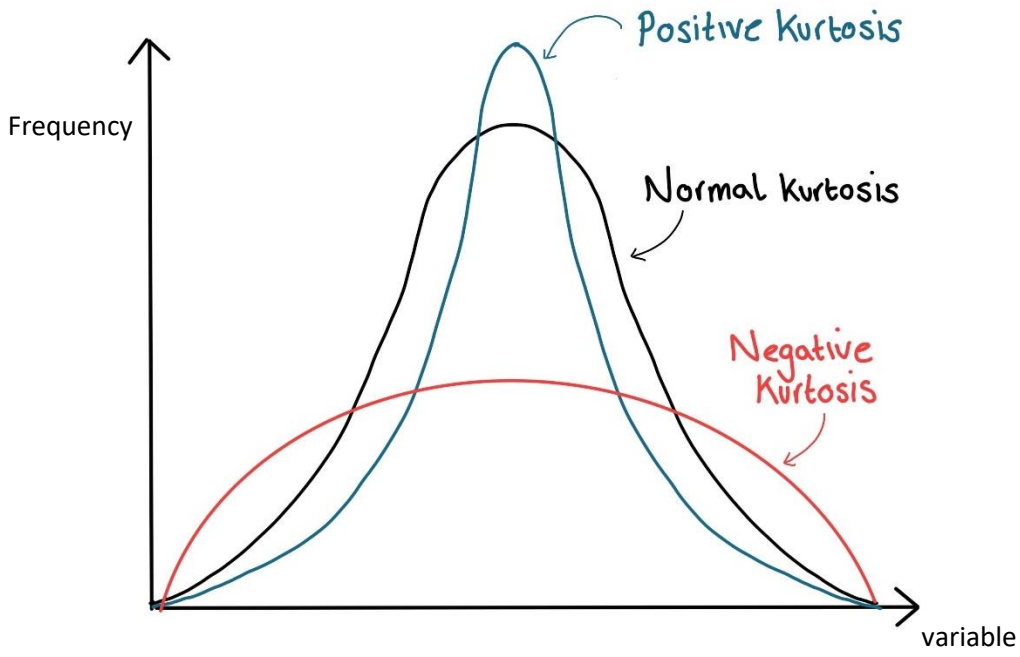

Figure 9 Graphical illustration of positive, negative and normal kurotsis for a sample variable.

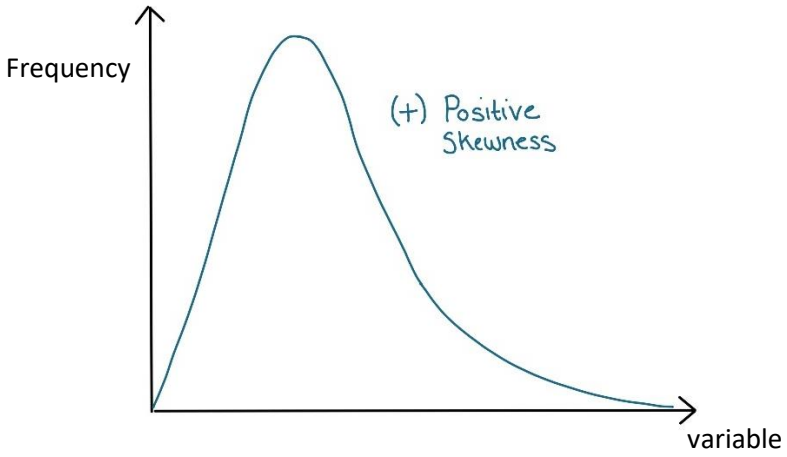

Figure 10 Graphical illustration of a sample of data with positive skewness

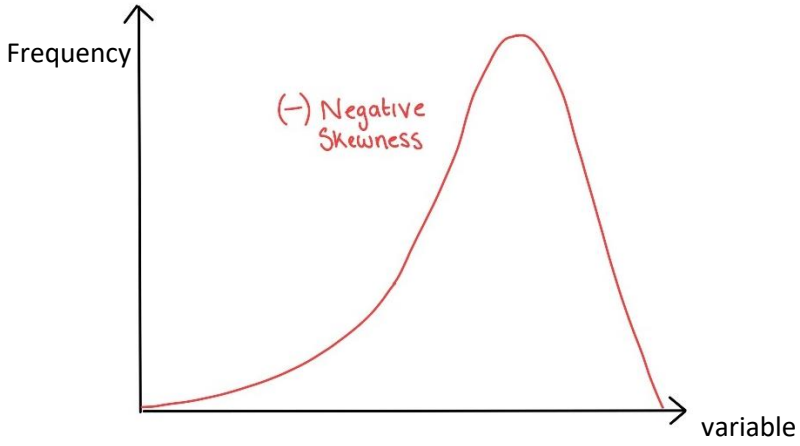

Figure 11 Graphical illustration of a sample of data with negative skewness

2.4.3.5 Ratio of Power

This statistics helps observe different parts of the frequency spectrum of the AE signal . Each block of AE data is investigated in a given frequency range just as frequency bands. The denominator eliminates the local effect of the power in equation. For the ratio of power, n represents the frequency band which has been selected to evaluate the ratio of power. X_K represents the k[th] magnitude-squared Fast Fourier Transform (FFT) bin and $2M$ is the is the total number of FFT bins in the frequency band selected to calculate the ratio of power.

$$ROP = \sum_{k=n_1}^{n_2} \frac{|X_k|^2}{\sum_{k=0}^{M-1}|X_k|^2}$$

Equation 16

2.5 Wavelet de-noising of AE signal

Acoustic emission signals recorded have both wanted and unwanted signal from a machining environment and these need to be separated effectively to ensure useful data analysis. Moreover, any noise/unwanted AE signal can affect the diagnosis of fault during process monitoring which is one of the main challenges within process monitoring. Noise can be present in the signals as electric noise, electromagnetic interference, background acoustic noise, rubbing noise and other sources during measurement[37]. To improve the noise immunity of these signals, data filtering algorithms needs to be considered and these have been widely discussed in the AE community.

Noise in AE signals can be divided into three groups and these groups show the difference in difficulty dealing with these types of noise.

Table 2 Types of noise signal, filtering methods and their difficulty.[26]

	Type of noise signal	Cause of appearance	Filtering methods	Filtering complexity
1	Spikes (short impulses), harmonic noise, high-frequency and low-frequency noise	Electric and electromagnetic noise	FIR filters, IIR filters, median filter	low
2	White stationary noise	AES noise, noise of electronic components	Wavelet-filtering	average
3	Impulse, non-stationary noise	Rubbing noise, hydro-dynamic disturbances and cavitation	Analysis of long realisations of AE signals	high

The noise of interest within this project is the white stationary noise which can also be a form of noise due to the coolant supply for which the wavelet transforms de-noising is utilised. The AE signal recorded from the grinding cuts has short impulses which can refer to the instantaneous impulses where the tool comes in contact with the workpiece, and this cannot be considered as noise nor removed from the overall signal. Any noise which is characteristic as high-frequency noise or low-frequency noise can be easily removed from the signal using band-pass filter with relevant knowledge of the non-essential frequency bands during a grinding cut.

At this point, it is worth noting that the writing used for understanding the wavelet transforms and its relative de-noising concept has been compiled within this report as a descriptive approach to comprehend the technique and with less prominence on the mathematical approach. Further readings outside the remits of this thesis is needed to fully grasp the mathematics behind the concepts and is not relevant for its application within this project. Burrus and Gopinath has the book “Introduction to wavelet and wavelet transforms” [38] which is maybe of use to the mathematical minded audience while a much more concise version of the content can be found in “A mathematical introduction to wavelets” by Wojtaszczyk [39] . The algorithm used for wavelet-filtering is based upon using discrete wavelet transformations. The AE signal is broken down into wavelet decompositions given as detailed and approximation coefficients. In order to grasp this concept, it is essential to understand that a wavelet is a localised waveform of effectively limited duration that has an average value of zero. Contrary to Fourier transforms, the information of the timeframe for a signal in the frequency domain is kept. The method used to understand a signal’s timeframe within Fourier transforms is to use windowing, i.e. splitting the signal into separate blocks of signal and evaluating the Fourier transforms for each block and investigating i.e. known as short-time Fourier transforms. This method would result in a narrow window giving good time resolution and poor frequency resolution to the evaluation. On the other hand, a wider window can provide good frequency resolution but poor time resolution. Moreover, general trends within acoustic signals has shown that a lower frequency components often last a longer period of time i.e. a high frequency resolution is required. Also, the high frequency signal components often appear as short bursts, therefore a higher time resolution is needed. This renders wavelet transforms technique to have a key advantage of extracting local spectral and temporal information simultaneously[40].

Therefore, wavelet transforms are used to create a non-linear method where these windowed spectra overlaps. The wavelet transform performs a correlation analysis against a mother wavelet and therefore the output is expected to be maximal when the input signal most resembles the mother wavelet. This mother wavelet that the signal is compared against can have different scales (scaling) and be shifted along the timeline (translation) when conducting the correlation analysis. Scaling (given as value, *j*, in Figure 12) changes the width of the mother wavelet and its central frequency as a result. Smaller values of *j* is an expanded mother wavelet which is better at resolving low frequency components of signal with bad time resolution hence overcoming the short fall of Fourier transforms discussed earlier. A higher value of *j* shrinks the mother wavelet and makes it better at resolving higher frequency component of the signal with good time resolution, just as needed.

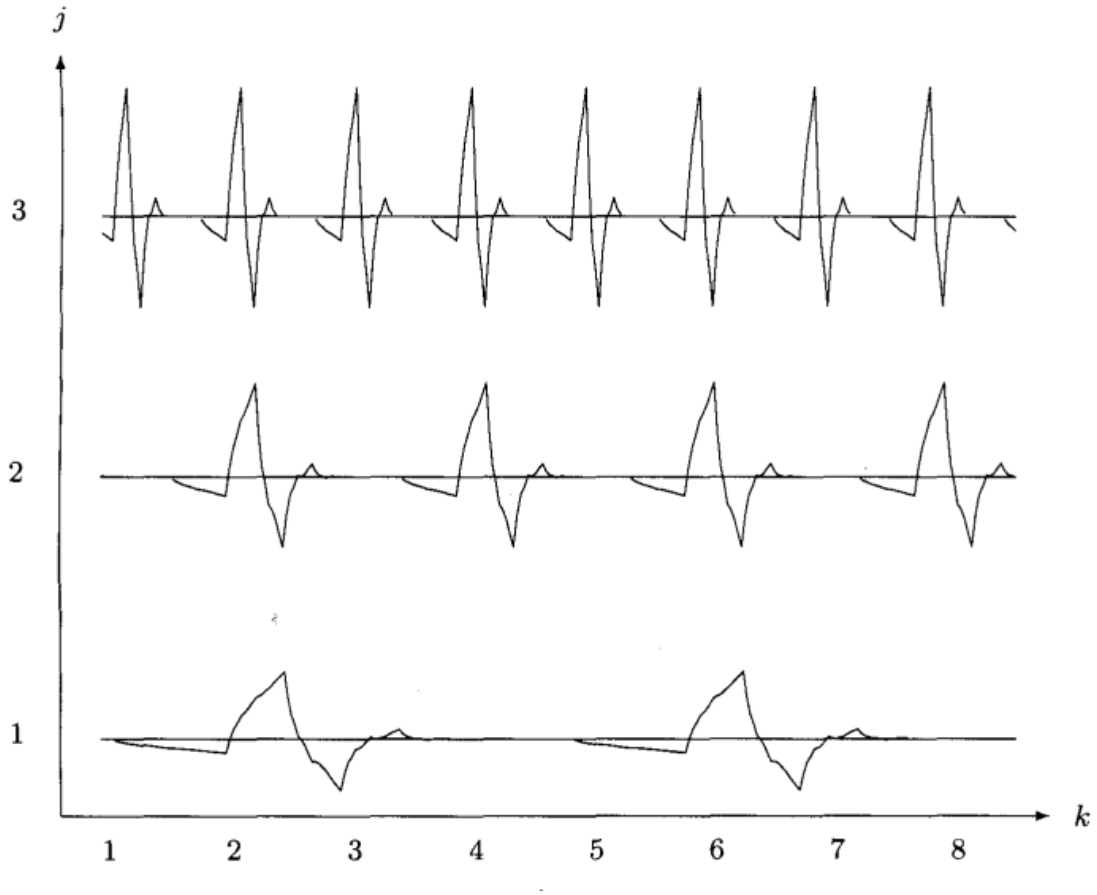

Figure 12 A pictorial representation of translation of wavelet (every fourth k) and scaling (j) of a Daubechies (D4) wavelet [38].

Another aspect which can also give flexibility to the wavelet analysis is the shape of the wavelet itself, therefore there are different wavelet functions (different shape) available within wavelet transforms. This aspect will be further discussed within section 2.5.1

2.5.1 Wavelet Bases

There is a range of wavelets available in literature which find its application in different signal processing techniques based on their shape and function. One of the simplistic and primitive model is the Haar wavelet and there are also complex wavelets functions available too. These wavelets can be divided into two, wavelet with filters and wavelet without filters. Wavelet with filters can be used with filter bank theory while the other group of wavelets cannot be used to realise the decomposition of the signal. Within this group of wavelet with filters, there is a distinction between some with compact support and other non-compact supported. Compact supported wavelet are ones which are finite and are only non-zero within a given interval while non-compact are not just defined for a given interval. Within signal processing, wavelets with compact support have been identified as the most suitable and these are

further divided into orthogonal and Biorthogonal. Orthogonal wavelet filter banks generate a single scaling function and wavelet while Bi-orthogonal creates a pair of wavelets which can be used separately for decomposition and reconstruction [41]. Bi-orthogonal wavelets has linear phase filters which are highly desirable in reconstruction of signals. The grouping and division of wavelets available are shown in Table 3**Error! Reference source not found.** below:

Table 3 Types of wavelet bases and abbreviations used.

Wavelets	Abbreviations
Haar Wavelet	Haar
Daubechies wavelet	Db
Symlets	Sym
Coiflets	Coif
Bi-orthogonal wavelets	Bior
Meyer wavelet	Meyr
Discrete meyer wavelet	Dmey
Battle and lemarie wavelet	Btlm
Gaussian wavelet	Gaus
Mexican hat wavelets	Mexh
Morlet wavelet	Morl
Complex gaussian wavelets	Cgau
Complex shannon wavelets	Shan
Copmlex B-spline frequency wavelets	Fbsp
Complex Morlet wavelets	Cmor

Table 4 Grouping of wavelet functions shown in Table 3 [31]

Wavelets with filters			Wavelets without filters	
With compact support		With non-compact support	Real	Complex
Orthogonal	Biorthogonal	Orthogonal	Gaus, mexh, morl	Cgau, shan, fbsp, cmor
Db, haar,sym, coif	bior	Meyr,dmey,btlm		

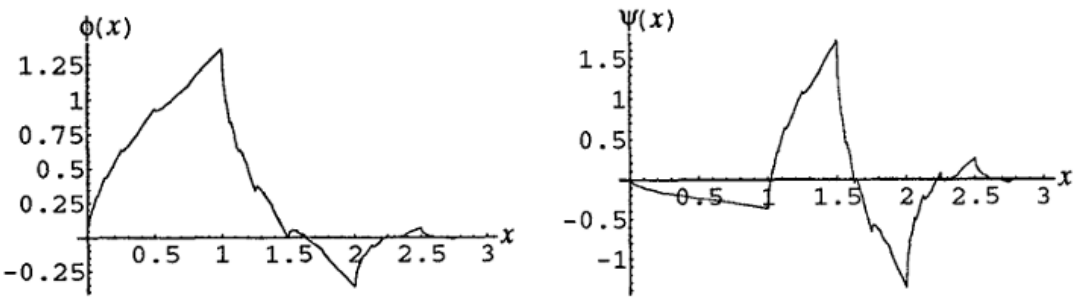

Figure 13 Example of fourth-order Daubechies (D4) scaling function $\phi(x)$ and its fourth-order mother wavelet $\psi(x)$ [42]

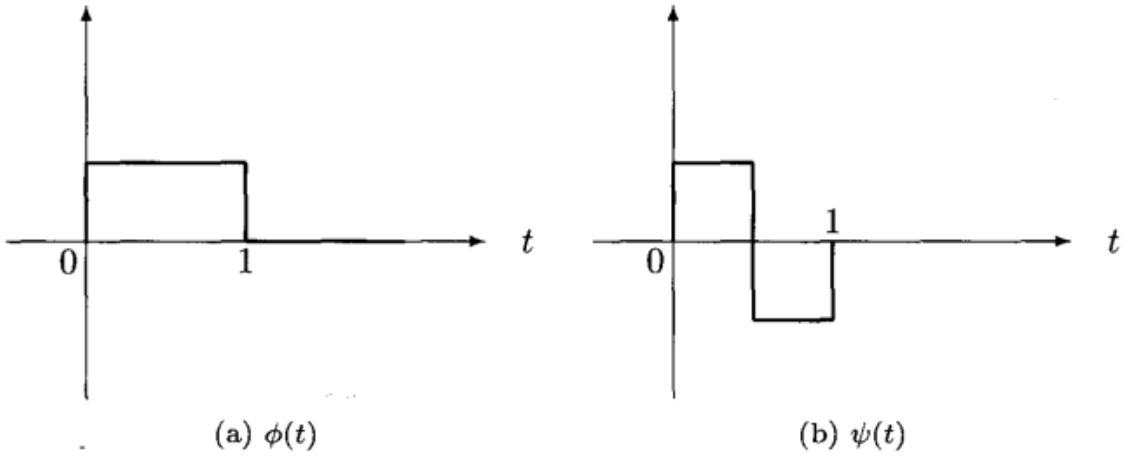

Figure 14 Example of Haar scaling function (a) and wavelet (b) [38]

Since there are various wavelet base functions available, the choice of the correct wavelet base function for de-noising needs to be matched up with the type of signal that is to be analysed during wavelet decomposition. They all have different properties such as order of approximation, vanishing moments, orthogonality and compact support [43]. Orthogonal wavelets could reduce the redundant information within the signal and improve the calculation speed. Compactly supported wavelet could reduce computation complexity and have better time resolution. The shape of the wavelet should reflect the type of features present within the signal being analysed and therefore can be accurately extracted through wavelet decomposition. One of the key aspects which affects the shape of the wavelet is the filter length and in this study, the filter length for the different type of wavelets are studied for analysis. Some of these wavelet types which are equipped with these properties are evaluated in this study which include Daubechies, Symlet and Coiflets.

The concept of wavelet coefficients (i.e. the output of the correlation analysis discussed above) is merely the idea of receiving a high output when the frequency of the mother wavelet matches part of the signal with very similar frequency and vice versa, as it is compared against each other and shifted along the

timeframe during the correlation analysis. Mathematically, this correlation is carried out by the convolution of the input signal against the scaled and translated version of the mother wavelet.

A continuous wavelet transform (CWT) does not limit the level of scaled and translated versions of the mother wavelet that it is used for the correlation analysis. This would means CWT works with a huge amount of data. In order to simplify this method, the discrete wavelet transforms uses a multi resolution analysis (MRA) and uses scaling and the translation factor on power of 2 (dyadic) which makes the analysis much more efficient and accurate. Using this discrete sampling approach, down sampling is also used with discrete wavelet transforms (DWT) to reduce the amount of data used by passing it through a series of filters according to the filter bank theory. The signal of interest is generally decomposed to different levels. Matlab provides one of the most efficient tools for the multi-level decompositions of signal using DWT and resources available from their websites gives a simpler explanation of the process. Within this section, the graphical representation from Matlab have been used to support the description of wavelet decomposition using DWT. As an example, take into consideration the one-dimensional signal Figure 15.

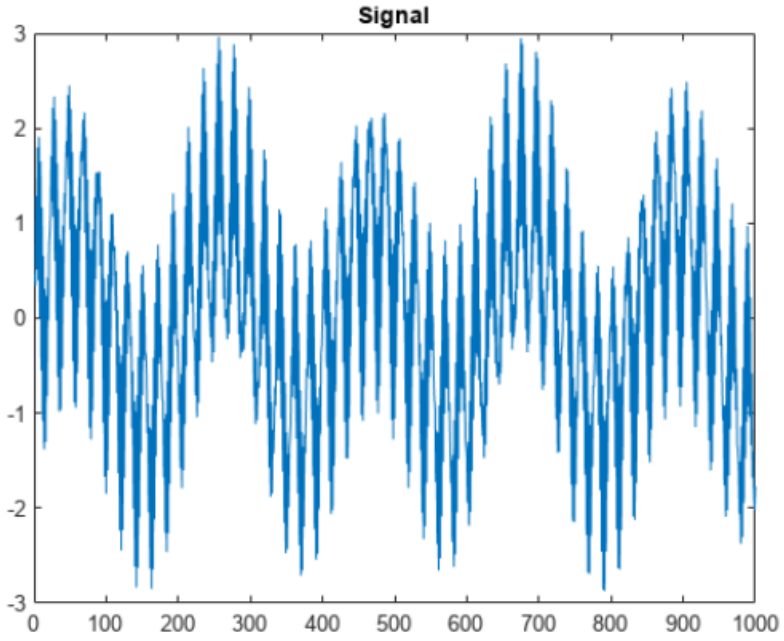

Figure 15 Example of signal used for wavelet decomposition.[44]

In one level of decomposition, the signal is passed through a high pass finite impulse response (FIR) filter and a low pass FIR filter and down sampled such that the number of data points is halved and wavelet coefficients received (see (a) in Figure 16 Figure 16). The output through the high pass filter gives high frequency wavelet coefficients which are known as the detailed coefficients (shown in Figure 16). The output through the low pass filter gives low frequency wavelet coefficients which are known as the approximation coefficients (shown in Figure 16). In multi-level decompositions, the approximation coefficients are further decomposed using the same technique to down sample and gain another set of detail and approximation coefficients at that level (see Figure 17 which shows 3 levels of decomposition on signal s). Applying the technique to an example signal such as the one shown in Figure 15 gives the output of the 3 levels decompositions in Figure 18). The maximum number of decomposition levels that can be attained with a signal is given as $log_2 N$, where N is the length of the signal of interest. This multilevel decomposition can also be reversed to reconstruct the signal using up-sampling, direct opposite of the decomposition method. It is at this point between decomposition and re-construction where de-noising can be carried out. After multi-level decomposition, different thresholding algorithms can be applied to the detail coefficients (high frequency components) in order for it to be removed from the signal and re-constructed. During this thresholding method, it is vital to understand what is representative as the noisy component within the detail coefficients and hence use an appropriate threshold to remove this from the decomposed signal.

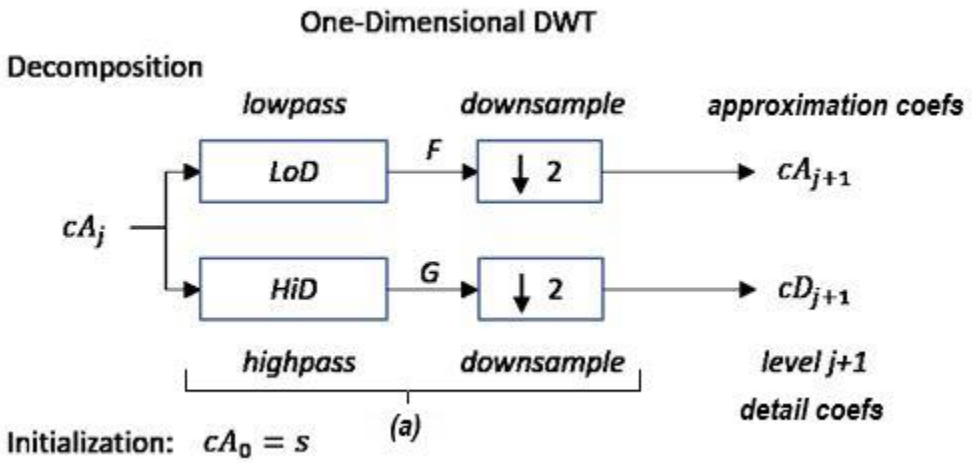

Figure 16 Illustration of one-dimensional DWT for wavelet decomposition of a signal (S).

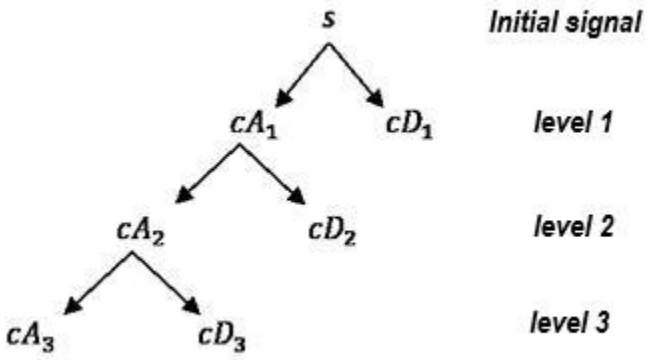

Figure 17 illustration showing the level of decomposition of signal using DWT. [45]

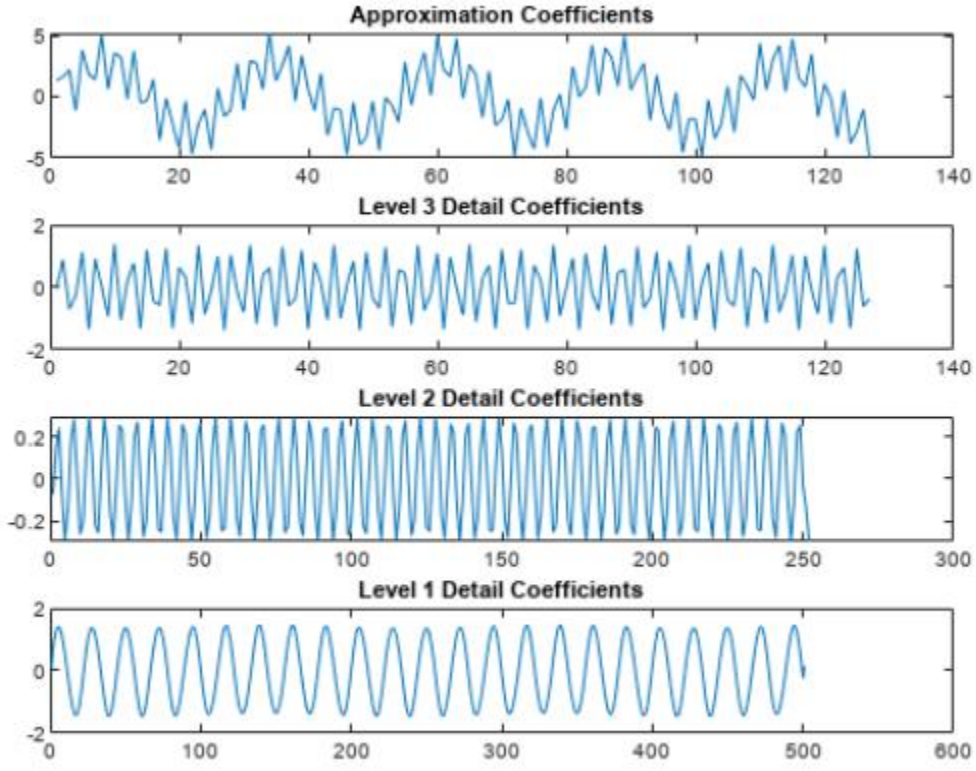

Figure 18 A 3 level wavelet decomposition of the signal in Figure 15 using order 2 Daubechies wavelet.

2.5.2 Wavelet de-noising thresholding methods

There have been various thresholding methods identified within various studies conducted with wavelet de-noising and these offer best performance on the basis of its application. MATLAB wavelet toolbox support certain thresholding methods which are most commonly used in signal processing and these are going to be studied within this review.

2.5.2.1 'Rigrsure'

This is a thresholding method based off the Stein's unbiased risk estimation (a quadratic loss function) criteria [46]:

$$\text{Threshold value} = \sigma\sqrt{2\log(\text{N}\log_2\text{N})}$$

Equation 17

Where N represents the length of the signal and σ the standard deviation of the noise. The noise is estimated from the first level of signal decomposition:

$$\sigma = |\text{median}(\text{Detail coef.})|/0.674$$

Equation 18

2.5.2.2 'sqtwolog'

A fixed-form (universal) threshold yielding minimax performance multiplied by a small factor proportional to log(length(X)) [47]. Thereby given as:

$$Threshold\ value = \sigma\sqrt{2log_e(N)}$$

Equation 19

2.5.2.3 'heursure'

A thresholding method which is a mixture between 'rigrsure' and 'sqtwolog'. It rather allows for a heuristic approach to the estimation of the thresholding value using both techniques.

2.5.2.4 'Minimax'

This gives a fixed threshold which makes use of the minimax principle. Therefore a fixed threshold is selected in order to get the minimum of the maximum mean square error, obtained for the worst function in a given set.

2.5.3 Hard/Soft thresholding

The thresholding applied on the detail coefficients restrict the components of the signal and therefore will be discarded when reconstructing the signal. Thresholding methods can be applied through soft thresholding and hard thresholding. Hard thresholding has a linear approach where it discards the wavelet coefficients above selected threshold ands sets it to 0 whereas a soft threshold is a much more non-linear function and it shrinks the large magnitude wavelet coefficients above the threshold [48] as illustrated in Equation 21. In Equation 20 and Equation 21, $w_{j,k}$ is a representation of the wavelet coefficients at decomposition level *j* and index *k* while γ is the representation of the threshold value applied. In Equation 21, sgn is the symbolic piecewise function of the signal.

Hard thresholding [49] given as:

$$w_{j,k} = \begin{cases} w_{j,k}, & |w_{j,k}| \geq \gamma \\ 0, & |w_{j,k}| < \gamma \end{cases}$$

Equation 20

Soft thresholding [50] given as:

$$w_{j,k} = \begin{cases} sgn(\, w_{j,k})\, (|w_{j,k}| - \gamma), & |w_{j,k}| \geq \gamma \\ 0, & |w_{j,k}| < \gamma \end{cases}$$

Equation 21

Once the apt thresholding method is applied to the decomposed signals, the signal can be reconstructed to attain the de-noised signal.

The comprehensive literature review on the use of Acoustic Emission (AE) for process monitoring during grinding underscores the evolving application of AE technology in industrial machining. From literature review, it can be summarised that the state of the art within process monitoring during grinding includes work towards grinding burn detection, grinding wheel monitoring and wheel contact detection technology. Previous works have focused on AE signals in isolation, without integrating them with other sensor data (e.g., force, power, vibration) to provide a comprehensive process monitoring solution. Synchronizing data from multiple sensors could offer more robust insights into the grinding process. This integration is essential for understanding the complete picture of the grinding mechanism and optimizing process parameters effectively and this is one of the objectives that this thesis focuses on.

Early studies highlighted the potential of AE for detecting grinding burn, laying the groundwork for further exploration and refinement. For instance, initial works focused on AE amplitude thresholds to flag grinding burn, but these approaches often resulted in false positives due to their rudimentary nature. Advancements in statistical analysis of AE signals, as explored by Wang et al. [23], introduced more robust detection methods, such as the use of neural networks with statistical features like band power, kurtosis, and skewness. These studies demonstrated significant improvements in detecting grinding burn but were limited by material-specific characteristics and the variability of grinding parameters.

Further refinement of AE process monitoring was achieved through the incorporation of advanced signal processing techniques like wavelet packet transforms and fuzzy logic models, as seen in the works of Liu et al. [13] and Aguiar et al. [26] [24]. These methodologies improved the accuracy and reliability of AE-based monitoring by leveraging detailed time-frequency analysis and handling data variability with fuzzy clustering. However, challenges remained in terms of the repeatability and long-term stability of these systems in industrial settings. Previous studies have shown AE's potential in detecting grinding burns but often result in false positives and do not extensively explore different grinding parameters. The variability in AE features such as Root Mean Square (RMS), Mean-Value Deviance (MVD), and Constant False Alarm Rate (CFAR) under different conditions has not been thoroughly investigated. For instance, Wang et al [23] and Aguiar et al. [24],[26] demonstrated the use of AE for burn detection but did not address long-term stability and calibration of AE sensors, which are critical for industrial applications. Therefore this thesis takes into consideration the need to take the characterised set of AE features, signal parameters and applying a repeatability study to cement the confidence in these features under different grinding regimes and improving the reliability of acoustic emission signal monitoring in the process.

Recent studies have pushed the boundaries further by integrating deep learning techniques. González et al. [33] and Bi et al. [34]utilised Convolutional Neural Networks (CNNs) and Long Short-Term Memory (LSTM) networks to automate feature extraction and enhance the classification accuracy of wheel wear states and grinding burns. These studies achieved high prediction accuracies but often fell short of addressing real-time applicability and generalization across different materials.

The literature review also brings into prominence the requirement for clean signal and data which allows for accurate analysis. Some of the literature share the different techniques that have been employed to de-noise the acoustic emission signal but there is inadequate exploration into wavelet de-noising. While wavelet packet transforms (WPT) and other signal processing techniques have been utilized, there is a lack of optimized wavelet de-noising methods tailored for AE signals in grinding. Effective de-noising is

crucial for accurate signal analysis, particularly in noisy environments like grinding. For example, Liu et al. [28] and Gao et al. [27]used WPT and cross wavelet transforms (XWT) but did not optimize de-noising specifically for AE signals from grinding. Wavelet de-noising showed great potential in cleaning acoustic emission signals within the machine environment during grinding. There is a need to optimise parameters for wavelet denoising which will allow for successful de-noising and opportunity to filter out the unwanted signal from the grinding process. This thesis will aim to develop this pre-process routine for the acoustic emission signal acquisition using wavelet de-noising.

Despite the significant progress, gaps remain in the literature, particularly concerning the application of AE monitoring in the grinding of high-value aerospace material, IN718. Most studies have focused on materials such as AISI 1045 steel which exhibit different AE signal characteristics compared to IN718. Additionally, the feasibility of implementing these advanced monitoring systems in real-time industrial environments remains largely unexplored. This thesis aims to address these gaps by focusing on the feasibility of using AE signals for process monitoring during the grinding of IN718 at the Advanced Manufacturing Research Centre (AMRC). By enhancing the existing monitoring system with advanced signal processing techniques like wavelet de-noising and conducting a repeatability study with improved signal acquisition systems, this research seeks to provide a robust and reliable process monitoring solution. The experimental work will not only validate the effectiveness of AE features but also assess the system's repeatability and reliability across multiple grinding trials, thereby contributing valuable insights for practical industrial applications in the future.

3 Experimental method

3.1 Grinding machine : Makino G7

The Makino G7 is a 5-axis horizontal spindle machining centre (shown in Figure 19)which is capable of grinding, milling, drilling and tapping which features a Makino Professional 5 control system. The machine is capable of processing all main aerospace alloys and most importantly the nickel-based alloy (Inconel) which is used within this thesis. The machine is equipped with 24kW spindle with a 12,000 rpm limit which uses an ISO 40/BT40/BBT 40 (Big Daishowa Seiki Big Plus) interfaces. Machine has a working volume of 690 (X-axis) x 650 (Y- axis) x 730 mm (Z-axis) with infinite C-axis rotation and 270-degree B-axis rotation, with maximum workpiece weight limit of 120 kg. The accuracy attainable on this machine is a positional capability of 0.0025 mm, and repeatability 0.0015 mm, in all axis directions. This precision is important to ensure the grinding contact point and movement is repeatable during the experiment. The smallest depth of cut investigated in this thesis is 0.1 mm and in comparison to the 2.5 % positional accuracy and 1.5 % repeatability is close to negligible for this kind of experiment.

The grinding machine makes use of an intermittent dressing system which allows for single point, CNC disc or crush dressing capabilities. For this experiment, the crush option was used. The crush option means that the surface roughness of the wheel after dressing will be high as required for the grinding of IN718 within this project. IN718 generates significant heat during grinding due to its high strength and low conductivity. A grinding wheel with high surface roughness would allow for better heat dissipation and better coolant flow due to the spacing between the abrasive grains. Larger surface roughness on the grinding wheel would mean larger abrasive grains or a more open structure which allows the wheel to cut deeply into a material like IN718 thereby enhancing the rate of material removal. A higher surface roughness also encourages the creation of larger chip formation preventing the build-up of material on the wheel surface. This would ensure consistency in the grinding performance during the experiment. This thesis is focused on the repeatability of acoustic emission signals during grinding and therefore the higher surface roughness helps maintain the consistency and control but the dressing technique and planning of experimental method is crucial to ensure this is kept true.

The dresser unit used was a hybrid vane dresser roll mounted onto the C-axis (shown in Figure 20). This dresser unit was chosen due to its ease of instalment on the machine and it was readily available to support the testing. The dressing method for all wheels within this machining trial was kept constant and

was control for the experiment. Measurement of the grinding wheel diameter pre and post dressing was measured using the Renishaw laser measurement system to ensure consistency and control.

Figure 19 Makino G7 igrinder

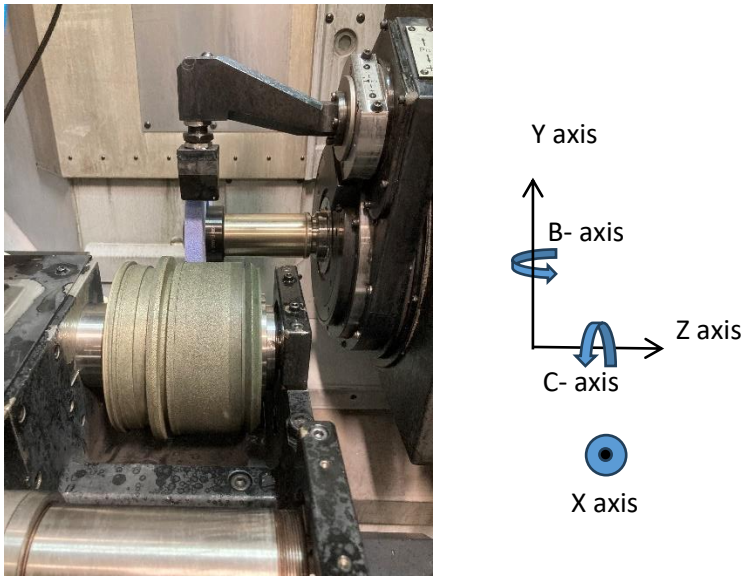

Figure 20 Hybrid vane dresser roll unit used for dressing of wheels. Sketch shows the coordinate system used to represent the motion while grinding with respect to the machine. Note the X-axis is represented as coming out of the paper.

The coolant system allows for coolant to be delivered at pump pressures ranging from 30 bar to 70 bar. A 360^0 programmable nozzle is used to maintain positioning throughout the grinding process and maintains the coolant temperature between 18 and 22 $^{\circ}$C . For this experiment, Trim C272 Coolant was used which

was delivered via RBM system two stage IFDR type (hydro-cyclonic) filtration system. Trim C272 is a semi-synthetic coolant specifically formulated for a broad range of machining and grinding applications [51]. It offered a unique combination of advantages found in both synthetic and soluble oil coolants, hence delivering superior cooling and lubrication properties. The coolant maintains low foam levels, even under high pressure conditions which is also handy when it come to reduction of acoustic noise since foam formation also results in noise which can be propagated as it increases the turbulence of coolant flow. The RBM two-stage IFDR (hydro-cyclonic) system represents a cutting-edge filtration technology designed for use with machine tools which can separate and capture particles larger than 5 µm. This will allow for improved precision during the grinding process and consistency in the flow entering the machining environment which also contributes to the machine noise.

Figure 21 shows the setup of the machine when conducting the grinding trials with the workpiece clamped on the workpiece fixture covered with protection from the high coolant flow. The G7 uses the EROWA pallet type chuck system, the PowerChuck P ITS system [52]. Therefore, the complete range of compatible EROWA pallets are available for installation on the G7, with pallet loading repeatability within 5µm. For this experiment, where small blocks of Inconel were used as coupons, EROWA pallet ER-008517 with a small pallet interface was found to be most compatible and used to attach to a dynamometer. The dynamometer had the workpiece fixtured attached to it to take recordings of grinding forces. The design and build of the workpiece fixture is described in section 3.3.

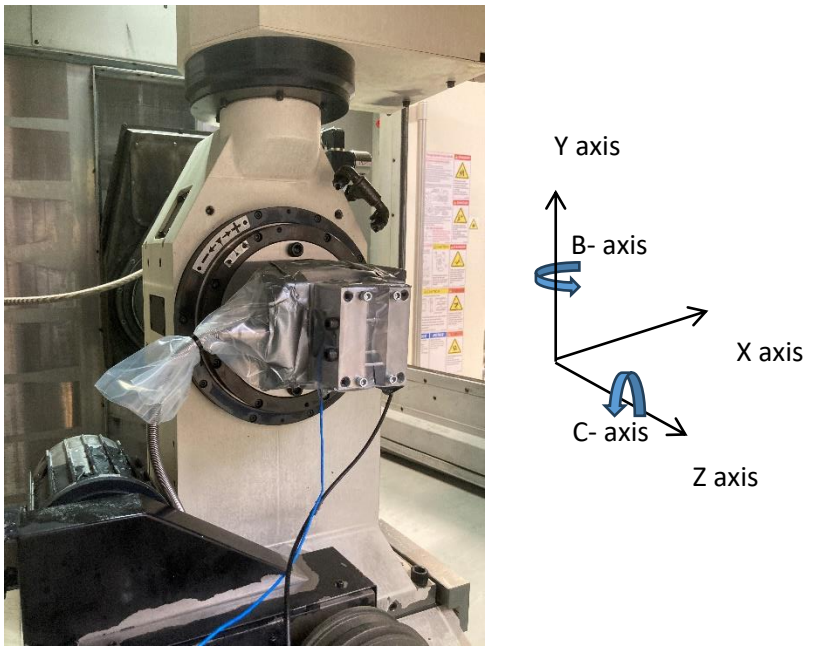

Figure 21 Setup of workpiece fixture onto dynamometer attached to pallet held on machine. Sketch shows the coordinate system used to represent the motion while grinding with respect to the machine.

3.2 Workpiece preparation – IN718

IN 718 workpieces were cut into the required coupons measuring 49 mm (L) x 20 mm (W) x 24 mm (H) using wire EDM (electric discharge machining). The IN718 stock was cut from solution annealed flat blank (at 1032 °C) for 1.08 hours, water quenched, aged at 800 °C for 7 hours and air cooled. The mechanical properties of the stock was given as 837 MPa 0.2% Proof stress (PS) at 20 °C and 1175 MPa Ultimate tensile strength (UTS) in the longitudinal axis. The certificate of conformity on the stock confirmed that the material recorded Rockwell C hardness test results of 32,36 and 38 HRC on its surface (ASTM E18).

Table 5 Chemical analysis of the stock as provided by the certificate of conformity

Chemical composition					
Ni %	54.3	Si %	0.05	Si %	< 0.001
Cr %	18.5	Co %	0.04	Ca %	0.001
Fe %	17.49	Cu %	0.03	Mg %	0.001
Nb Ta %	5	Mn %	0.02	Se %	< 0.0003
Nb %	4.99	C %	0.012	Pb %	0.0002
Mo %	3.05	Ta %	< 0.01	Bi %	0.00003
Ti %	0.95	P %	0.004		
Al %	0.5	B %	0.004		

3.3 Work piece fixture

The workpiece fixture was designed to cater for several functions. With the requirement to record grinding force, the dynamometer needed to be integrated into the machine bed allowing for the grinding forces from contact point to be transferred onto the dynamometer pallet. The fixture needed to also integrate the AE sensors and accelerometers into the environment closest to the grinding contact point. Moreover, these sensors needed to be protected from coolant/lubricants, especially since the Ingress Protection (IP) rating was not sufficient to handle the flooding of coolant in the machine environment. The fixture ensured repeatability in workpiece positioning and clamping since during the trials there was several changeovers of workpiece. Finally, the most important requirement for the design of fixture is to ensure that its designed for ease of machining programme.

The programme featured straight grinding cuts on coupons and this took out the complexity involved with differential cuts and positioning change of tool path. The fixture had a cavity of 25 mm run through the middle of the fixture allowing for the workpiece to be held in place by locators and a clamp system. Figure 22 shows the machined workpiece fixture while Figure 23 shows the drawing of the workpiece fixture focused on the cavity for workpiece to be clamped in place. The three locator dowels shown in Figure 25 restricted the degree of free rotation of the workpiece within this cavity, worked as a reference for the placement of workpiece and “fool proofed” the placement of workpiece by preventing improper loading. The clamping was provided by two 8 mm bolt pushing against a clamp plate (3 mm (H) x 12 mm (W) x 30 mm (L)) which transferred the force to hold the workpiece against the locators. Calculations were considered to evaluate the suitability of the clamping provided by the M8 bolt on clamp plate and then compared against grinding force data that have been recorded in previous literature closest to the grinding setup explored in this thesis.

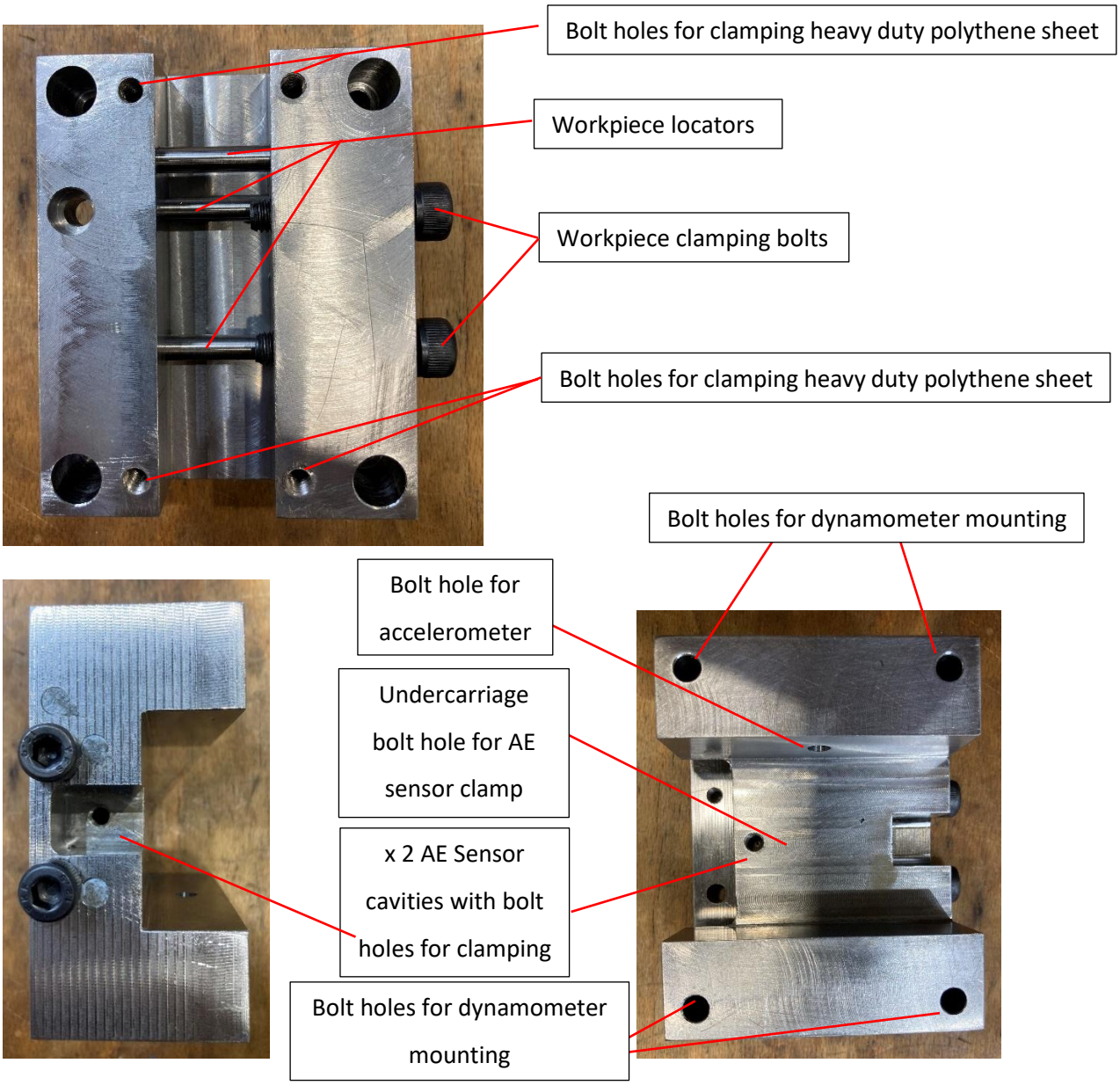

Figure 22 Workpiece fixture design

The relation between applied torque and axial force - or load - in a bolt can be calculated in this general equation as:

$$T = K\ x\ F\ x\ d$$

Equation 22 [53]

Where,

T = wrench torque (Nm, lbf ft)

K = constant that depends on the bolt material and size

d = nominal bolt diameter (m, ft)

F = axial bolt force (N, lbf)

l = lubrication factor (%)

The typical value K for a normal dry application within the application of this thesis is 0.2 considering a normal dry condition for this evaluation. Therefore, considering Equation 22, the axial bolt force for an M8 considering worst case tightening torque of 9.87 Nm (inclusive of lubrication factor) gives an approximation of 6200 N. This is for a 1 bolt configuration but for the application in this workpiece fixture 2 bolts are transferring the axial force onto the clamp plate of 360 mm^2, evenly distributing the force load. For comparison against grinding forces that would be experienced during the experiment, previous literature by Ruzzi et al [54]looked at the influence of grinding parameters on IN 625 (another nickel superalloy with mechanical properties close to the IN718) during surface grinding using silicon carbide wheel. The magnitude of grinding forces experienced with varying grinding parameters is in the magnitude of 0 – 200 N and hence suggesting how the safety factor considered using the clamping force of bolts is in the region of x10 magnitude giving confidence in the setup used. Furthermore, grinding force recorded from the dynamometer in thesis under section 4.4.1 also proved the safety factor to be in the same region giving confidence in the workpiece fixture clamping design. Grinding force measured in this thesis was in the region of maximum 70 N for tangential grinding force and normal force in the region of 192 N as shown in Figure 52 which ensures a safety factor in order of magnitude of 10.

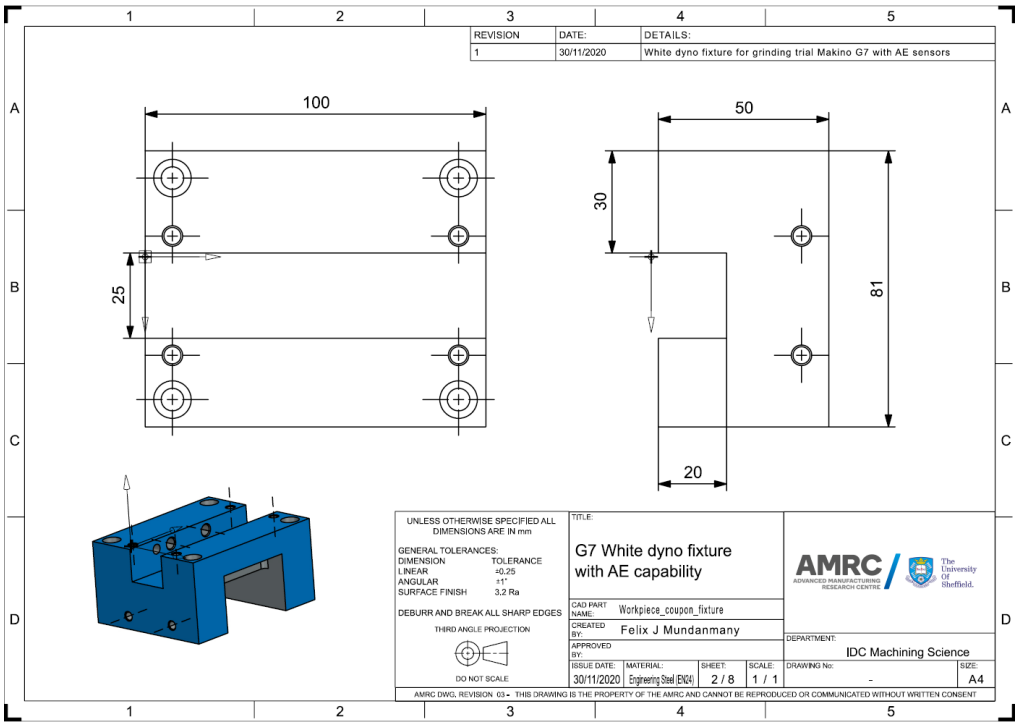

Figure 23 Drawing illustrating the cavity for coupons to be held within the workpiece fixture with general dimensions of the fixture stock for illustrative purposes.

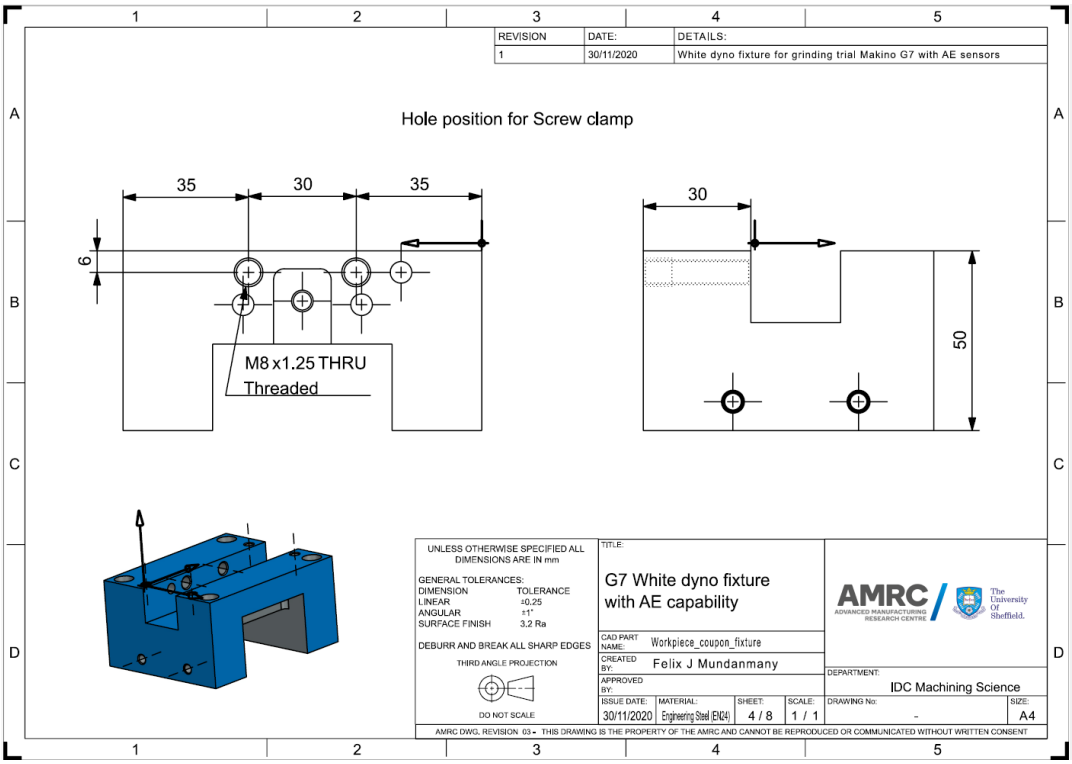

Figure 24 Drawings showing the holes for the screw clamp devised to hold the workpiece in place. A 3 mm clamp plate was also machined to provide enough shim for clamp plate to hold coupon in place once M8 bolts were placed to transfer the clamping force when tightened.

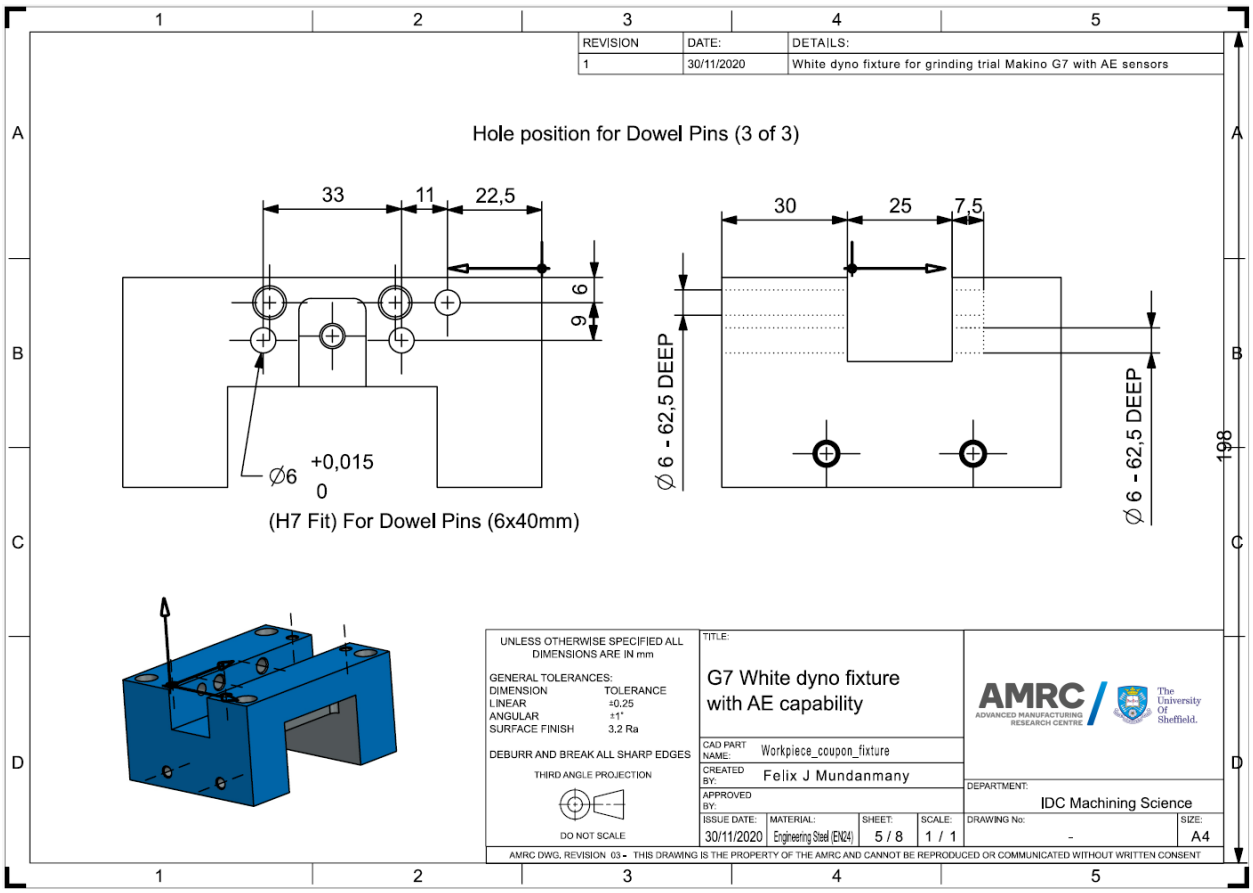

Figure 25 Drawing showing the position of holes for dowel pin that act as locators for the workpiece coupon.

4 counterbore M6 holes were machined 20 mm deep to allow for bolts to clamp down the workpiece fixture directly onto the mounting plate on the dynamometer. This was designed based on the best way to interact with the mounting plate covering most of the surface and it was critical to ensure the holes were machined with positional accuracy to allow for good alignment with the bolt holes on the mounting plate. Figure 26 shows the drawing highlighting these 4 holes. Once the fixture was fitted to the dynamometer mounting plate there is no requirement to remove or make any changes to the fixture position during the experiment. This alongside the clamping and locators ensured repeatability in the workpiece position and sensor positions during all the experiments/trials.

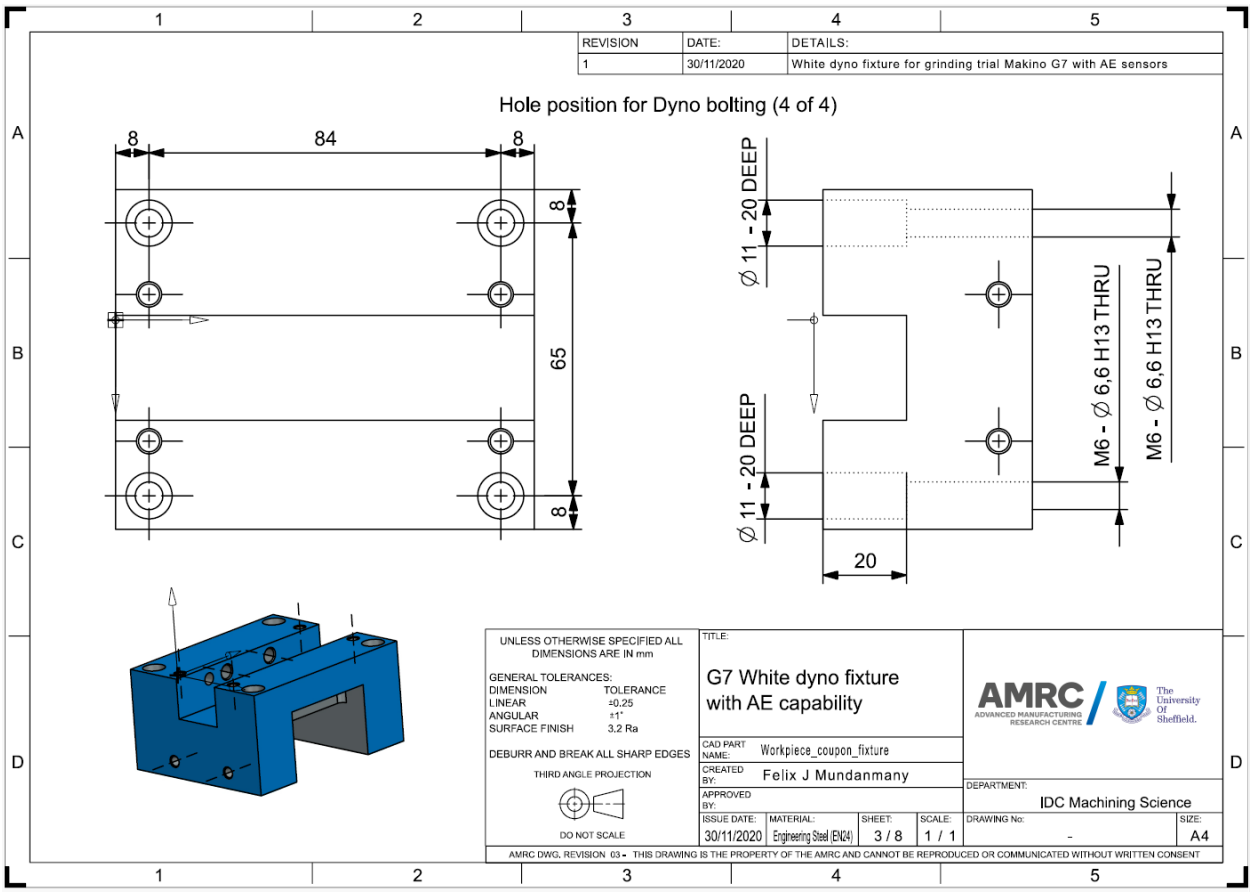

Figure 26 Drawing showing the 4 counter bore M6 holes which allows for the workpiece to be fastened to the mounting plate of the dynamometer.

The other design aspect to consider was to accommodate the AE sensors and accelerometers with closest proximity to the grinding contact point to get quality data. Moreover, these sensors needed to be protected from coolant/lubricants, especially since the Ingress Protection (IP) rating was not sufficient to handle the flooding of coolant in the machine environment. 8 threaded M6 holes were machined (shown in Figure 29 strategically designed to allow for a heavy duty polythene sheet covering to be held around the workpiece fixture providing cover for the sensors from the jets of lubricant that floods the machining environment.

Cavities were designed for the Kistler type 8152001 sensor, Mistras WSa sensor and the 3 axis accelerometer allowing for the wires to be routed safely within the workpiece fixture and in the direction of exit within the machine. There were 2 suitable cavities created for the Kistler AE sensor initially, (i) with the sensor seated vertical in line with the Z-axis of the machine (shown in Figure 27) and (ii) the sensor seated horizontal in line with the Y axis (shown in Figure 28). Due to the wire routing being difficult with increased risk of fretting against workpiece fixture when routed in position (i), it was decided that position

(ii) would be the most suitable for this investigation. For future experiment, this design also lends the opportunity to allow for an investigation into how the AE signal maybe affected from different orientation of AE sensors during the grinding trials. Figure 28 shows M6 threaded holes machined into the fixture in the undercarriage which allows for placing the Mistras AE sensor and accelerometer in position using a jig. The jig was an arbitrary design created to allow for the Mistras AE WSa sensor to be clamped and help in place while guiding the accelerometer in position when bolted onto the workpiece fixture. Figure 30 shows the drawing which illustrates the through hole designed to allow for a threaded bolt to fasten onto the accelerometer against the fixture stock using the inbuilt female threaded hole on the sensor. Figure 33 shows a complete arrangement of the sensors in their situ during the experimental trials giving an understanding of the setup.

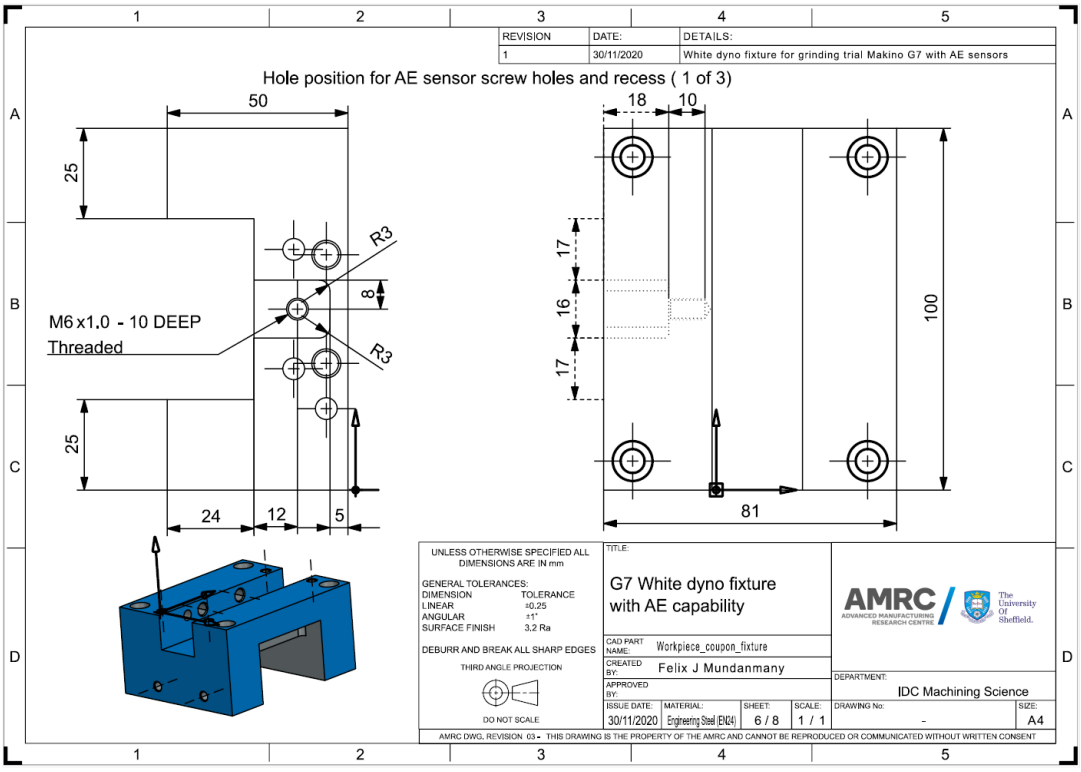

Figure 27 Drawing showing postion (i) described for the Kistler type 8152001 AE sensor seated vertically in the machine Z-axis.

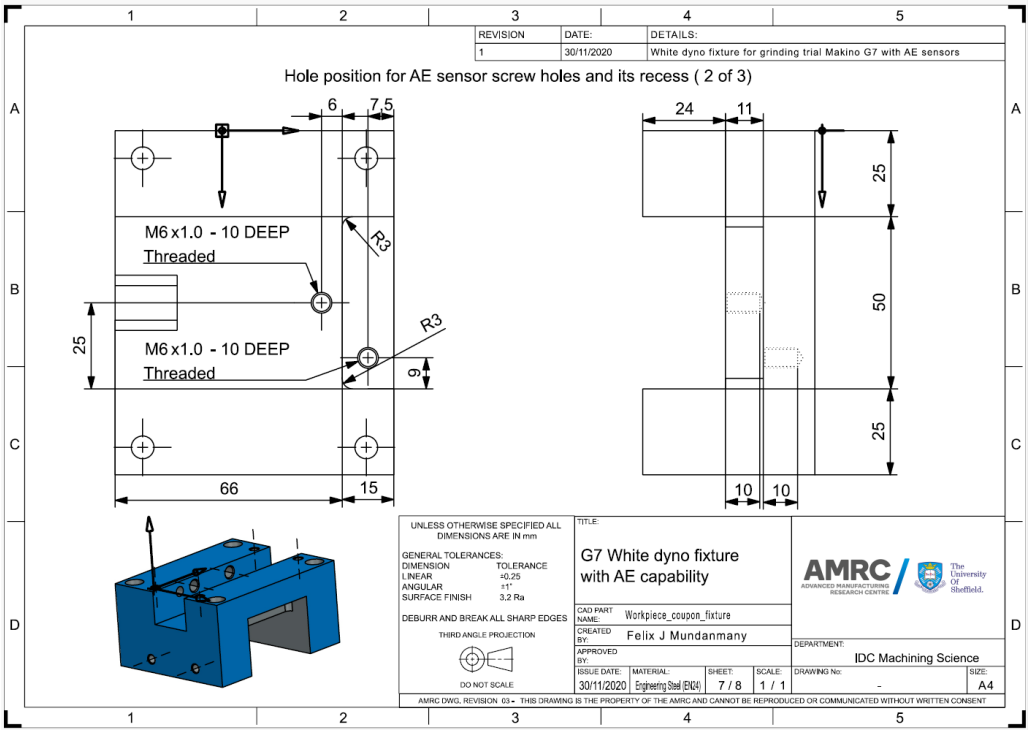

Figure 28 Drawing showing position (ii) for Kistler Type 8152001 sensor and M6 threaded hole to accomodate jig that clamps Mistras AE sensor and holds accelerometer in place.

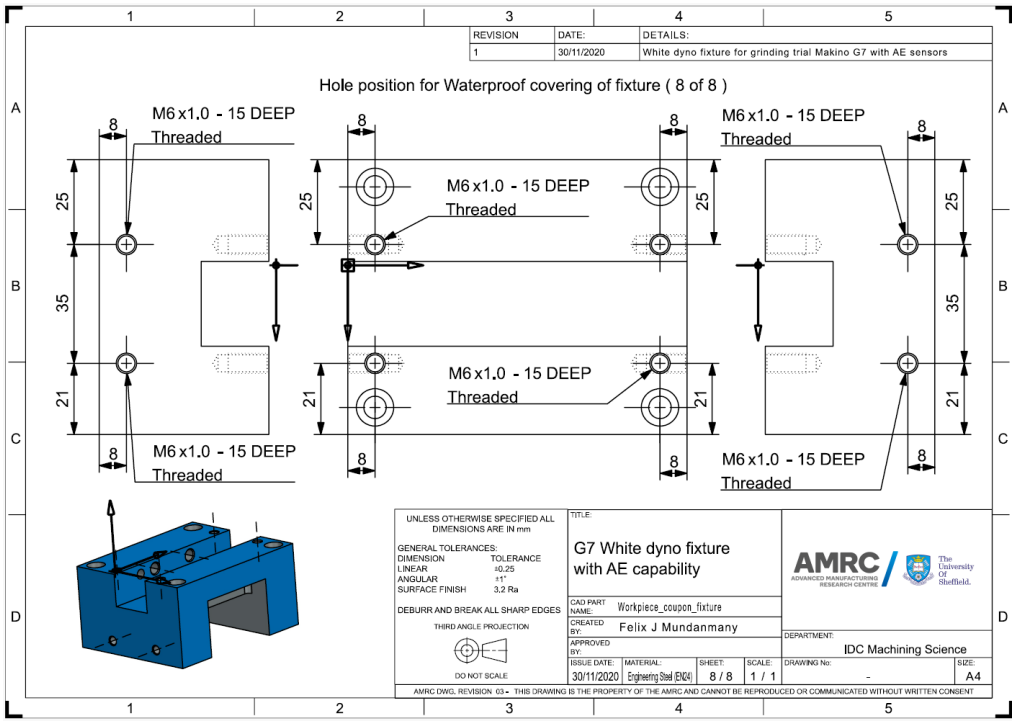

Figure 29 Drawing showing the 8 off holes that help to clamp down the plastic covering for the workpiece fixture protecting the sensors.

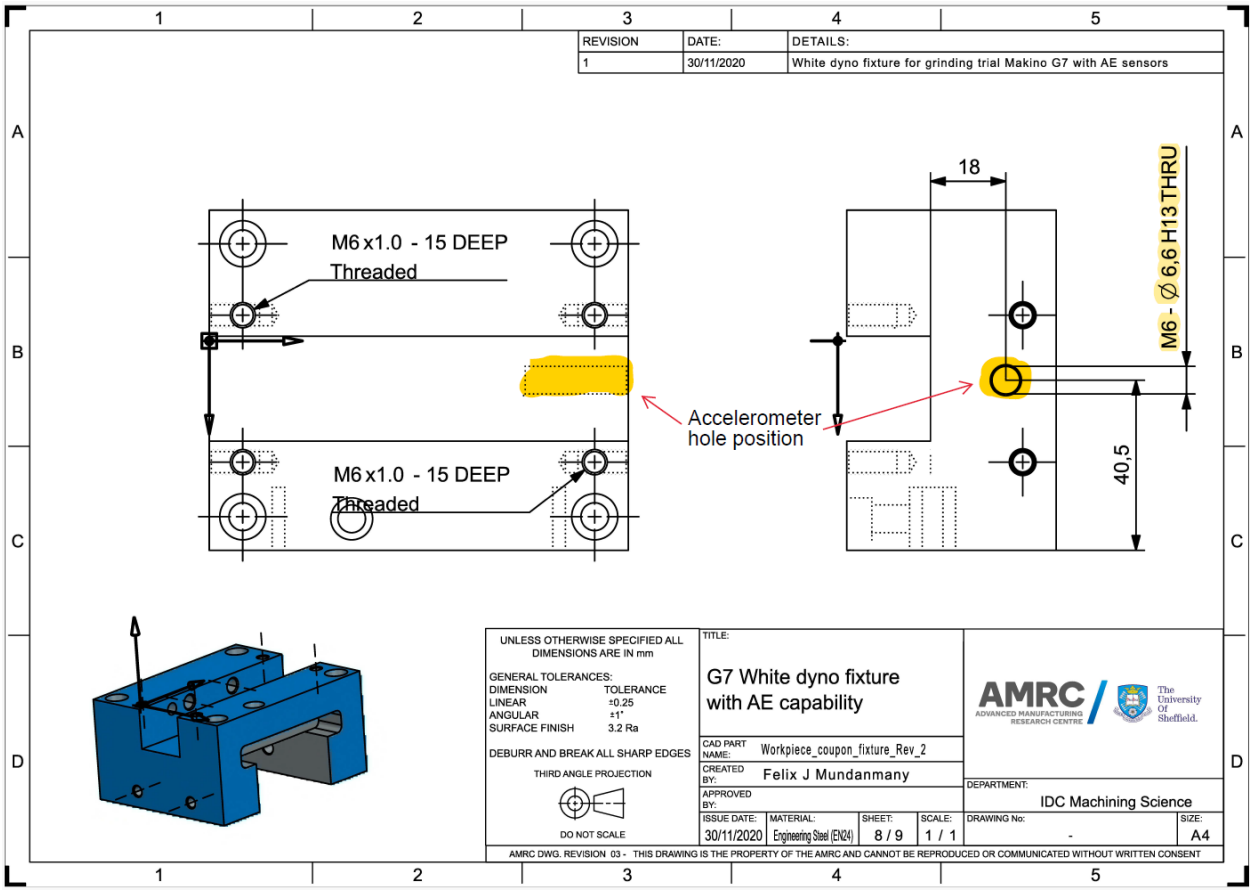

Figure 30 Drawing showing hole position for accelerometer clamping. M6 through hole was machined into the workpiece fixture allowing for a threaded bolt to fasten the accelerometer in position against the fixture stock.

All the sensors had different mounting techniques, and this needed to be accounted for within the fixture design. Threaded holes were used for sensors that were bolted onto fixture and 3D printed parts designed to hold sensors in a set position/orientation. The sensors were mounted in the undercarriage, under the cavity provided for the workpiece clamp such that the wiring and sensors were protected from direct coolant delivery. The Kistler and Mistras sensor were also placed in different orientations within 90° to each other. The AE sensors were place in these different orientations to understand how this affected the AE signal received from grinding contact point. The workpiece fixture was made by machining a block of Engineering steel (EN24).

3.4 Signal acquisition system

3.4.1 Force monitoring

Kistler Multicomponent dynamometer type 9129AA was used to record the cutting forces during grinding for this experiment. The 9129AA is a precision instrument designed for the measurement of forces and moments in 3 orthogonal directions which is pre-dominantly used during force measurement in machining operations. It is built with stainless steel and high-strength aluminium alloy which has a measurement range of +/- 5 kN within the lateral forces (Fx and Fy) and +/- 10 kN within the vertical forces (Fz) while the moments range for Mx, My is +/- 200 Nm and +/- 100 Nm for Mz. The sensitivity is a crucial factor that makes the Kistler 9129 AA suitable for application within grinding giving Fx, Fy lateral forces ≈ -7.5 pC/N and Fz ≈ -3.7 pC/N. Another aspect to consider is the thermal sensitivity shift of the dynamometer and how this may affect the experimental results, given that all experimental trials were conducted on the same day there is minimal shift in ambient shop floor temperatures. Adding this information to the low thermal sensitivity shift, ≤±0.02% per °C on the Fx, Fy and ≤±0.02% on the Fz, gives confidence in using the dynamometer for this experimental setup. The mounting plate (90 x 105 mm) was attached to the pallet interface which allowed for the custom built machine fixture to be attached directly to the mounting plate. All components that are within the machine environment were covered with heavy duty polythene sheet to protect them from coolant spray as shown in Figure 31 and Figure 32. The dyno uses an 8-channel measurement of the force, 4 channels on the x-axis, 2 axis on the y-axis and 2 on the z- axis. Within this experiment, the standard Kistler charge-amp has been omitted in order for the signal from the dynamometer to be directly fitted to an NI (National instruments) system. The 8 channel signal is directly fed into NI9201 module using a D-SUB cable. This module has been fitted to a compact chassis cDAQ-9178 which allows for the force signals to be captured in tandem with other signals synchronously. NI9201 has the capability of capturing signal at maximum frequency of 62.5 kHz. This NI system is an improvement from the old system where the signals from force, AE or power would have been captured using separate DAQs asynchronously making data analysis difficult. For this experiment, the force measurement was captured at 51.2 kHz as this is one of the capturing frequencies out of the 3 different sampling rates which can be applied using the NI Flex logger software used for data capture.

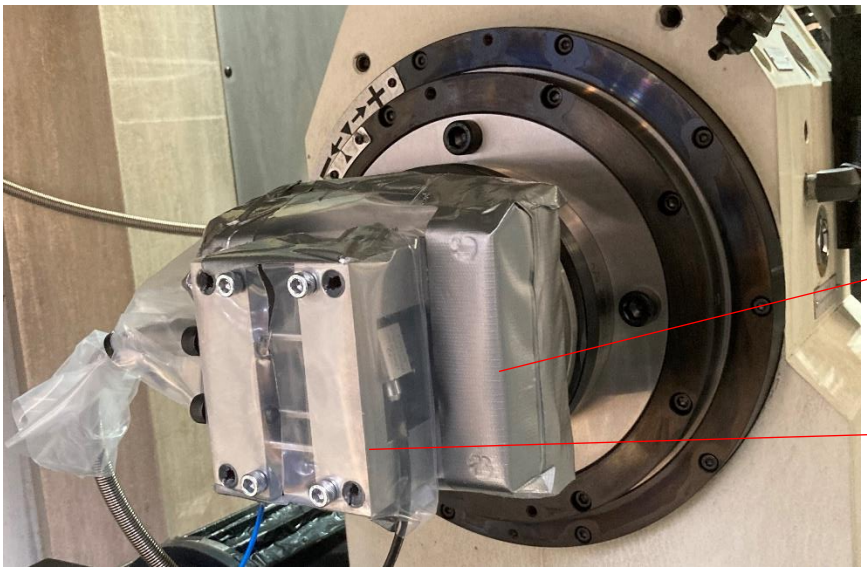

Figure 31 Setup of dynamometer in Makino G7 machine environment

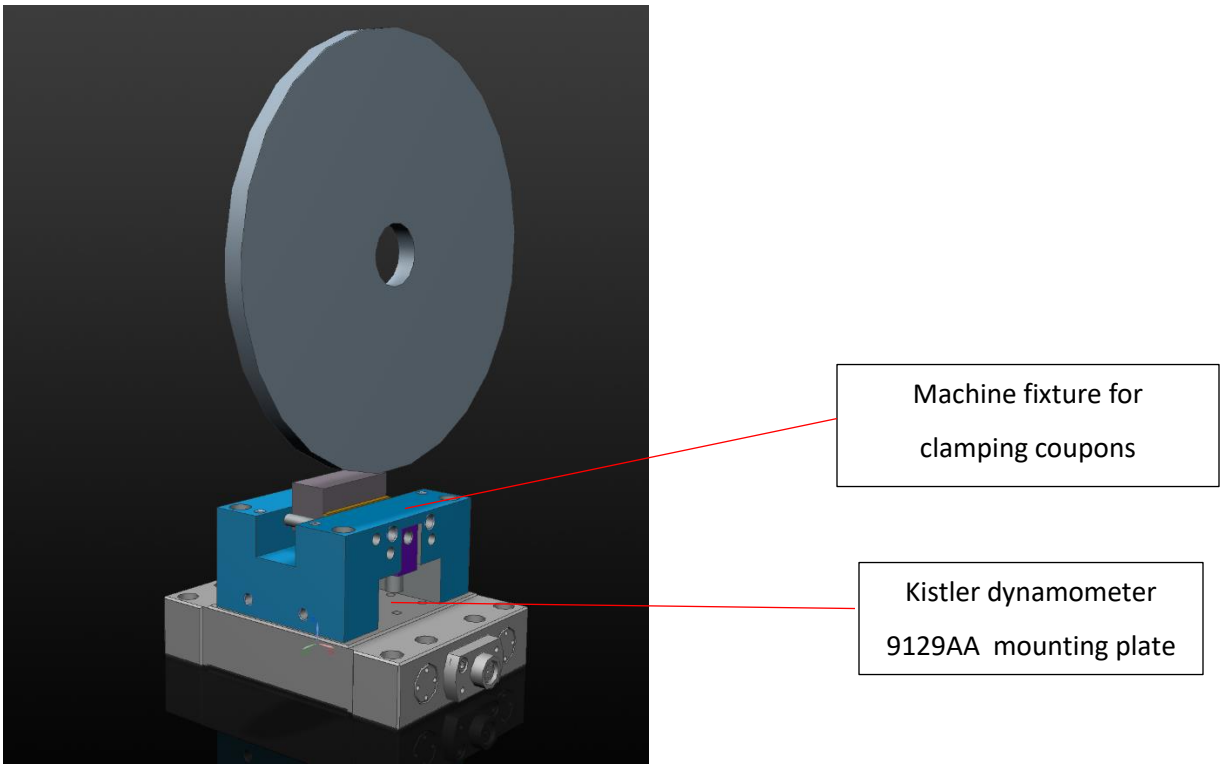

Figure 32 graphical illustration of the machining setup without coolant protection covering.

The Kitler 9129AA is calibrated annually under controlled conditions to ensure accurate force measurement, before the grinding trial it was checked to have a valid calibration report before proceeding. While considering the grinding force measurement, it is also important to consider the external factors that can affect the accuracy of grinding force measurement. Rotational accuracy of the

grinding wheel is a critical factor when used on the grinding machine. Poor rotational accuracy which is often manifested as spindle runout and vibration can introduce significant error in force measurements. Runout causes the grinding wheel to move eccentrically, leading to inconsistent contact between the wheel and the workpiece. This inconsistency generates fluctuating forces that are not representative of the true grinding forces that are not representative of the true grinding forces. These rotational accuracies can cause variations in the grinding depth of cut, leading to an uneven surface finish on the workpiece and even unexpected acoustic emissions being generated which deems this experimental data irrelevant. The Makino G7 has spindle with a runout within 2 microns ensuring minimal eccentricity and vibration to give confidence in the results obtained in this experiment. Moreover, the Makino G7 system adjusts coolant flow dynamically to accommodate the changes in wheel diameter improving the cooling efficiency and precision. The Makino G7 also has a robust build with damping capability that minimizes vibrations and enhances the overall stability during grinding operations. Section 3.6.1 discusses further the dressing parameter used to control and monitor the grinding wheel wear to ensure that rotational accuracy affected by wear does not influence the data collected from force measurement, acoustic emission measurement and spindle power data. Section 3.7.3 discusses further on the signal processing conducted on the force measurement signal that was collected during the experiment which gives further confidence on the quality of data.

3.4.2 Power monitoring

The spindle power was measured using a BNC connection going directly from the spindle to the NI9215 module on the cDAQ-9178. This module has the capability of capturing a maximum frequency of 100 kHz with a +/- 10 V input range suitable for this application and provides a 60 VDC isolation for safety and noise reduction. For this experiment, the spindle power was recorded at 51.2 kHz on the same sampling rate band limited to the force signal on flex logger software package.

3.4.3 Acceleration monitoring

A 3-axis accelerometer was used for this experiment which was placed attached to the workpiece fixture to pick up the vibration from the grinding trials. This data is not further used for analysis within this experiment but showcases the ability to capture synchronous data using the new NI data capture system. The accelerometer was directly fitted to the NI9234 module fitted onto the cDAQ-9178 capturing the accelerometer signal at 51.2 kHz.

3.4.4 Acoustic emission monitoring

2 different AE sensors were used for this experiment. Kistler Type 8152C01 AE sensor which has an operating frequency range of 50 – 400 kHz and the Mistras WSa sensor which has an operating frequency range between 100 – 1000 kHz. The Kistler AE sensor was attached to the AE-piezotron coupler type 5125C charge amp which is then attached to the NI9775 module. The AE sensor outputs a very small charge signal, which needs amplification to be accurately measured. The charge amplifier converts this small charge into a proportional voltage signal. The charge amplifier also matches the high impedance of the AE sensor to the lower impedance required by the data acquisition system ensuring the signal integrity. Similar amplification is required for the Mistras WSa sensor. The Mistras WSa sensor was attached to the 2/4/6c pre-amplifier from which a BNC cable attaches to the NI9775 module. The pre-amplifier helps reduce noise improving the signal-to-noise ratio and conditions the signals to be within the acceptable range for the NI9775, facilitating accurate measurement and analysis. The NI9775 module has got a maximum frequency capture of 20 MHz on all channels when the module is on trigger mode on flexlogger. In triggered mode, data acquisition starts based on predefined conditions or triggers, such as a specific signal threshold or an external event. This mode is useful for capturing data during specific events or intervals rather than continuously. For this experiment, for continuous capture of the AE signal during the experiment, the module is limited to a frequency capture of 4MHz across all channels by flexlogger. Therefore, this limitation is split amongst the 2 AE sensors such that 2MHz sampling rate is used for each sensor. The cDAQ-9178 allows for the 2 MHz sampling rate using the NI flex logger to capture the data synchronously with the other signals. The two AE sensors have been placed in different orientations and positions on the workpiece fixture as shown in Figure 33.The AE sensors were positioned to be equidistant from the point of contact between the grinding wheel and the workpiece such that AE signals can be compared to understand in the future how orientation of signal could also affect the AE signal recorded.

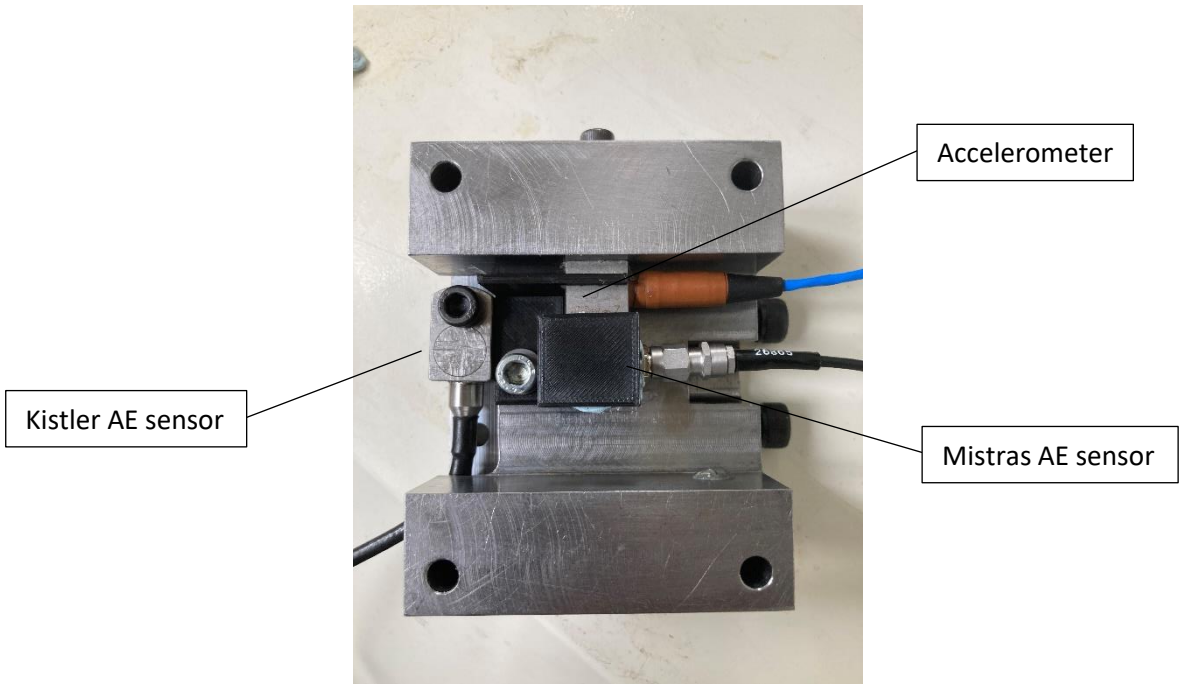

Figure 33 Shows the arrangement of AE sensors and accelerometer in the undercarriage of the workpiece fixture.

3.5 Data acquisition system

Prior to this project, AMRC capability involved acquisition of force data from the dynamometer separately using a sole DAQ provided by the Dyno supplier in tandem with any other signal (i.e. accelerometer, acoustic emission or spindle power monitoring) that needed to be investigated acquired using another suitable DAQ. The signals from these separate DAQs would then be stored onto a PC and captured with separate time stamps. This process limited the capability of having synced data for the different streams of signals with a single time stamp such that relations between signals could be drawn clearly. Moreover, the old methods of data acquisition from the separate DAQs were heavy files for which any attempt to synchronise using approximations or thresholding would require high cost of computation. Therefore, a new type of data was required for acquisition and storage of synced signals.

This project introduced the use of a NI cDAQ-9178 and respective modules, described in section 3.4.1 - 3.4.4, which could sync data from the different streams of signals at different sampling frequencies on the same time stamp. Although, this introduction was a step forward for data acquisition, there were limitations to the data acquisitions. Using NI Flexlogger, an easy-to-build data logging system software used in this project, there were three analog data rate levels (slow, medium and fast) at which sampling frequencies could be applied for data acquisition. The medium data rate level configuration was used for force, accelerometer, and spindle power signals at 51.2 KHz, slow rate of 10Hz was used for the ambient

shop floor temp from the thermocouple and the fast data rate level was used for Acoustic emission at 2 MHz. The data acquired using flexlogger gets saved as a tdms format which is well structured and gives great performance being in binary format compared to the usual csv format used. The NI Flexlogger also gives the capability to monitor the signal while running the test in time domain and frequency domain to ensure the signal being captured is as expected. With introduction of the NI data acquisition system there is time saved with setup and post processing of data results is much quicker with all channels synced on the same time stamp. Figure 34 gives an overview of the full data acquisition system deployed during the grinding trials.

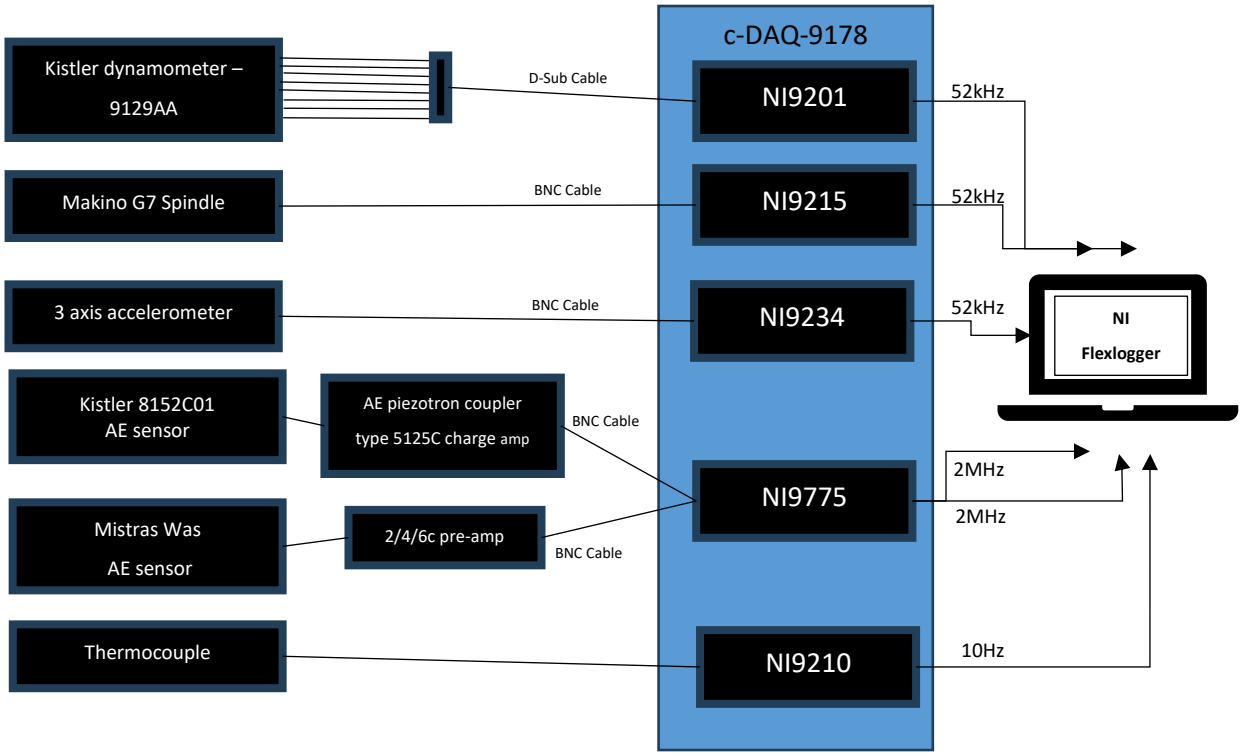

Figure 34 Schematic showing the data acquisition system deployed for the grinding trails on the Makino G7.

3.6 Experimental set-up

3.6.1 Design of experiment and chosen grinding parameters

3 different wheel are used for the three different grinding cycles deployed within this experiment including a clean up cycle, base grinding wheel and parameter grinding wheel. The wheels used for clean-up, surface prep and parameter grind has been recorded in Table 6.

Table 6 Grinding wheel specification used for the various wheels.

	Wheel Description	Wheel Spec	Wheel dimensions (mm)
1	Clean Up wheel	VU33 A80 2HH 10VB1	220x30x32
2	Base grinding wheel (BGW)	VU33 A60 2HH 10VB1	220x30x32
3	Parameter grind wheel (PGW)	VU33 A60 2HH 10VB1	220x10x32

Literature review discussed how aluminium oxide wheels and CBN wheels are common contenders for being used to grind IN718. CBN wheels are highly recommended because of their hardness and ability to maintain sharpness. They provide efficient material removal and good surface finish, although they are expensive and require precise dressing. While not as effective as CBN, aluminium oxide wheels can be used, particularly with a more open structure to help with heat dissipation. They are more affordable and easier to dress but may require frequent dressing and coolant use to prevent overheating. Given the industrial wide use of aluminium oxide wheel for grinding IN718 and the availability of wheels within AMRC, aluminium oxide wheels were chosen for this grinding experiment. The emphasis in this study is to understand the acoustic emission signal during grinding and therefore there is less significance in creating a superior surface finish but a consistent surface finish on IN718 workpieces. Given the availability of aluminium oxide wheels at disposal for the experiment, a clean up wheel with a 30 mm width was chosen to ensure the clean up of workpiece and essentially create a set “zero” surface on all workpieces. The width of the workpiece is 20mm and this clean up wheel has overhang that allows for full clean up on the surface of the workpiece. A coarse grain size of 80 was chosen for the clean up cycle and an open structure was used to help keep coolant supply and managing chip load during the grinding process thereby avoiding any thermal damage to the workpiece surface.

The base grind wheel and parameter grind wheel had the same specification except for the width of the grinding wheel. Similar to the clean up wheel, the purpose of the base grind wheel was to ensure a known controlled starting surface was established before parameter grind was recorded. The parameter grinds were carried out within 3 different grinding regimes of changing aggression values calculated using Equation 9. As previously discussed within the literature review, aggression values indicate a difference in the chip creation and complex process of grinding which is a combination of the process parameters including feed rate, depth of cut and wheel speed which collectively defines the intensity of the grinding process. By varying these parameters, the aim is to simulate different grinding conditions from a light finishing pass to an aggressive high material removal rate scenarios. With the context of the objectives defined within this thesis, the different grinding helps understand how the acoustic emission signals and features may be affected by changes in the grinding regime. This investigation helps to investigate if the signals are repeatable to help validate findings about the AE features that have been gathered in previous literature under different grinding regimes. The three different grinding regimes were chosen to understand how change in grinding regimes can affect the repeatability in the AE response gathered and these grinding parameters used have been recorded in Table 7. These grinding regime cuts were repeated 5 times using the same workpiece after each clean up and base grind such that most variables in the grinding environment could be kept constant. This left the experiment to have one variable which changed during the 5 repeats of the grinding cuts, i.e. the parameter grind wheel diameter.

Table 7 Grinding parameters for the three different grinding regimes selected for repeatability study

	Grinding regime	Width of grinding cut - Ap (mm)	Depth of grinding cut - Ae (mm)	Wheel surface speed – Vc (m/s)	Feed rate- Vw (mm/min)	Q' (mm^2/s)	Aggression value
1	Finishing	10	0.1	30	1000	1.67	11.87
2	Semi-Finishing	10	0.25	30	1000	4.17	18.77
3	Roughing	10	1	30	1000	16.67	37.53

For the grinding wheel diameter to be varied within the repeats systematically and have this monitored, the wheel was dressed with a decremental approach. Before each parameter grind, the PGW radius was

measured before and after dressing using the Renishaw laser measurement kit. The laser measurement kit used laser interferometry to measure the diameter of the grinding wheel upto 1 nanometre resolution to ensure that the dressing conducted was consistent with the dressing parameter set. Each dressing applied demanded the machine to dress off 1mm radius from the PGW. This controlled the PGW radius to reduce by 1mm every repeat cut and understand how this would affect the repeatability in using AE for process monitoring during grinding. The diameter of the grinding wheel significantly influences the grinding mechanism, affecting various aspects of the grinding process. The fundamental principle is that a larger wheel diameter increases the contact length between the wheel and the workpiece. This larger contact area distributes the grinding forces over a wider surface, potentially reducing the specific grinding energy required. Consequently, this can lead to lower temperatures and reduced risk of thermal damage to the workpiece. Another perspective to consider is that a larger diameter wheel tends to have a higher rotational inertia, which can stabilize the grinding process by reducing vibrations and improving surface finish. However, the increased mass and inertia also demand higher spindle power to maintain operational speed. This effect of rotational intertia and mass may not be as drastic with change of grinding wheel as far as 1mm redius reduction but may have a cumulative effect once several dressing and grinding passes have been completed during the grinding process. Additionally, a larger diameter wheel typically exhibits slower wear rates, contributing to more consistent grinding performance over time. Conversely, smaller diameter wheels concentrate the forces on a smaller contact area, increasing the grinding force per unit area, which can enhance material removal rates but also raise the risk of localized overheating and potential surface damage. Therefore, selecting the appropriate grinding wheel diameter is crucial for optimizing grinding efficiency, surface quality, and overall process stability

3.6.2 Grinding machine programming & tool path

The NC programme was written on Easygrind, in such a way that a simple tool path was programmed, and parameters of the cut varied such that the programme could be duplicated to change any parameters and make different grinding cuts to ensure efficiency in the design of experiments. The workpiece and its fixture was designed in such a way that a straight grind cut can be made across the workpiece, down grinding the workpiece, moving upwards on the sample edge as shown in Figure 35 and Figure 36.

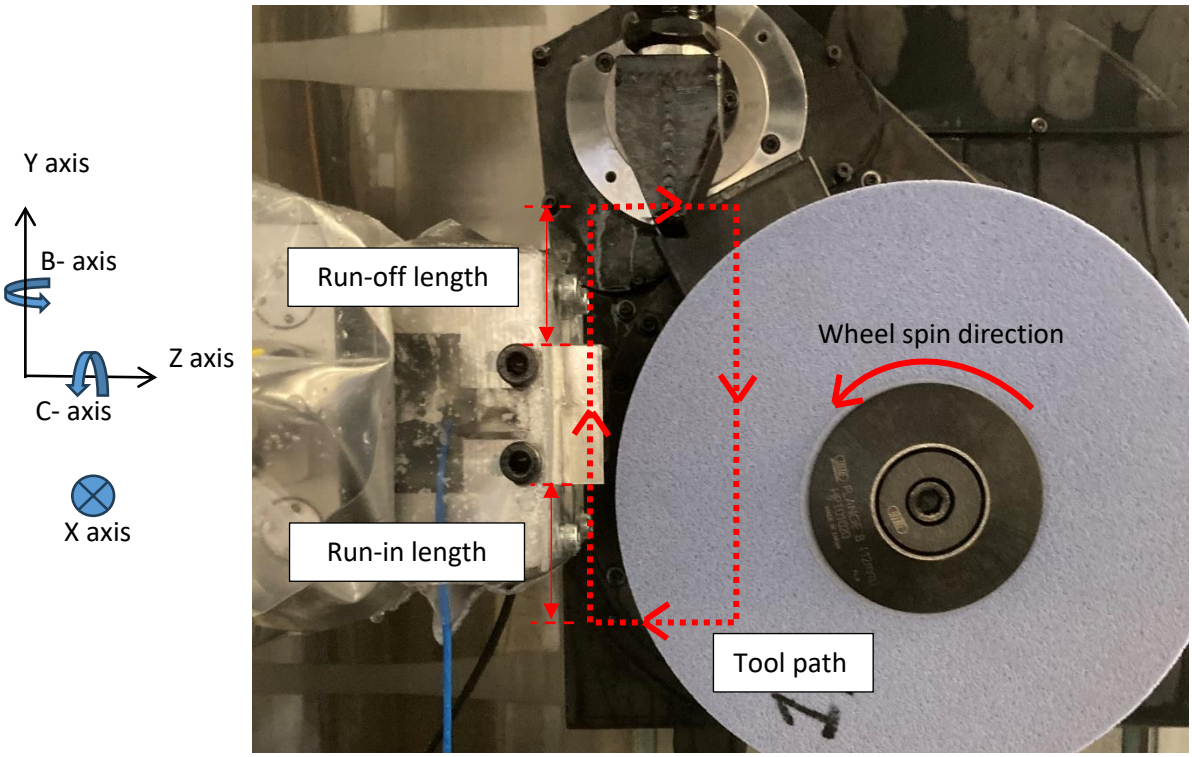

Figure 35 Illustration of the tool path used within a grinding cycle. Sketch shows the coordinate system used to represent the motion while grinding with respect to the machine. Note the X-axis is represented as directed into the paper.

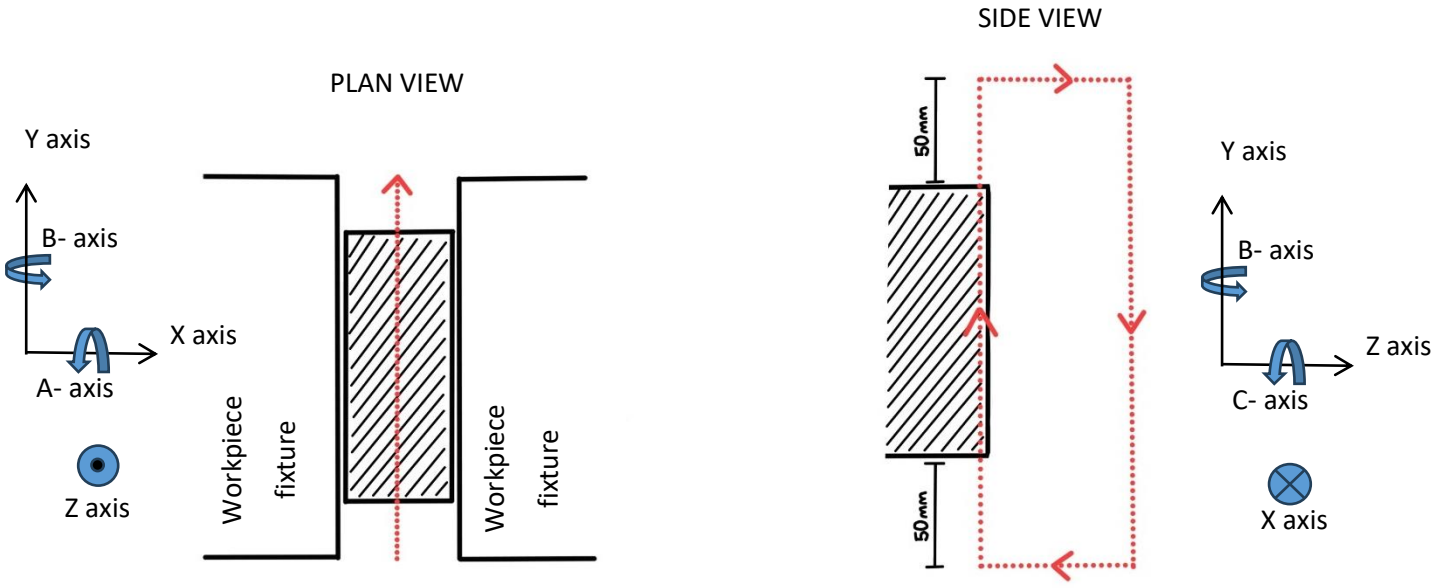

Figure 36 Drawing illustrating the plan view and side view of the workpiece coupon as it is subjected to the down grind tool path during the grinding cycles. Sketch shows the coordinate system used to represent the motion while grinding with respect to the machine

Each grinding cycle is a straight movement including a run-in length of 50mm of the grinding cut before the grinding wheel gets in contact with the workpiece edge and 50mm after the contact with sample edge.

The first grinding cycle administered on a sample workpiece involves a clean-up process. This cycle uses a 0.5 mm depth of cut, removing a total of 1 mm of material from the workpiece, starting 0.5 mm above the designated height of the workpiece. The clean-up cycle (shown in Figure 37) employs a wide grinding wheel to ensure the entire surface of the workpiece is free from tapers and to account for any slight fixture errors.

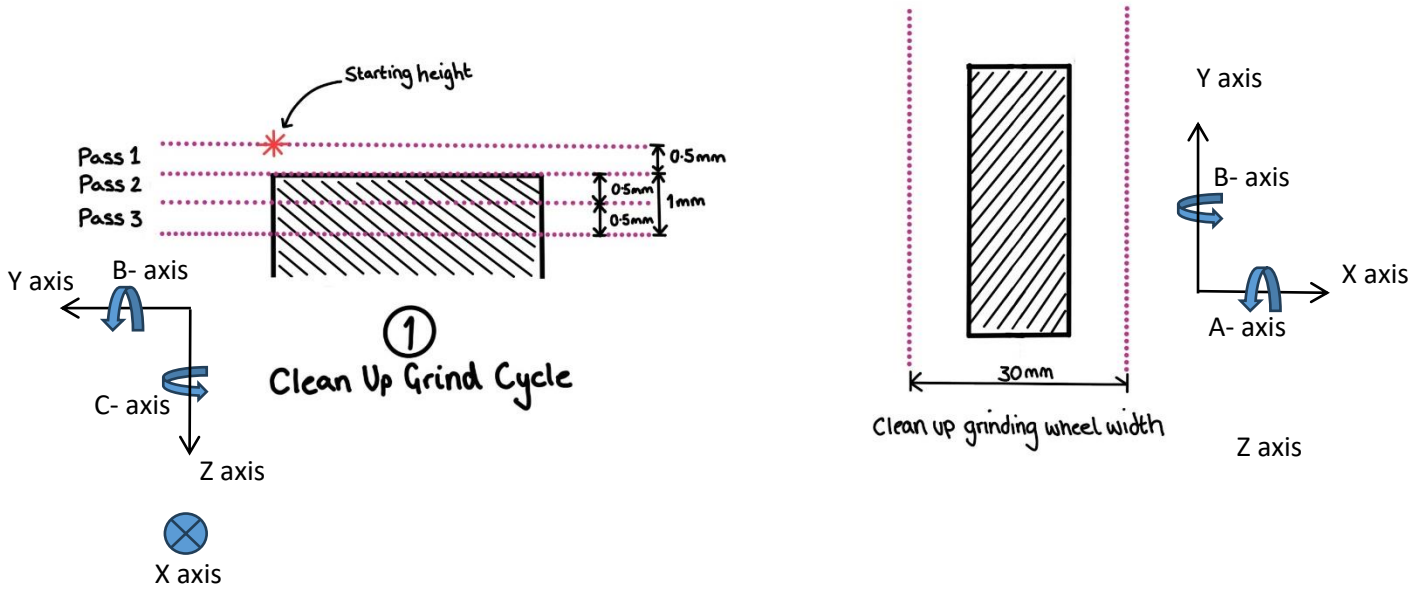

Figure 37 Clean up grinding cycle used within the grinding trial to prepare all sample workpiece coupons before they are subjected to grinding trials. Sketch shows the coordinate system used to represent the motion while grinding with respect to the machine.

Following the clean-up cycle is the surface preparation cycle, where a base grinding wheel is used. Before this cycle, the wheel is dressed, and actual pre-grind measurements are taken using a Renishaw laser measurement system. The surface preparation cycle also utilizes a wide grinding wheel, which grinds the full surface of the sample edge with two grinding cuts at a 0.25 mm depth of cut each, removing a total of 0.5 mm of material from the sample edge (Figure 38). This creates an even surface for the actual parameter grind, which is to be monitored.

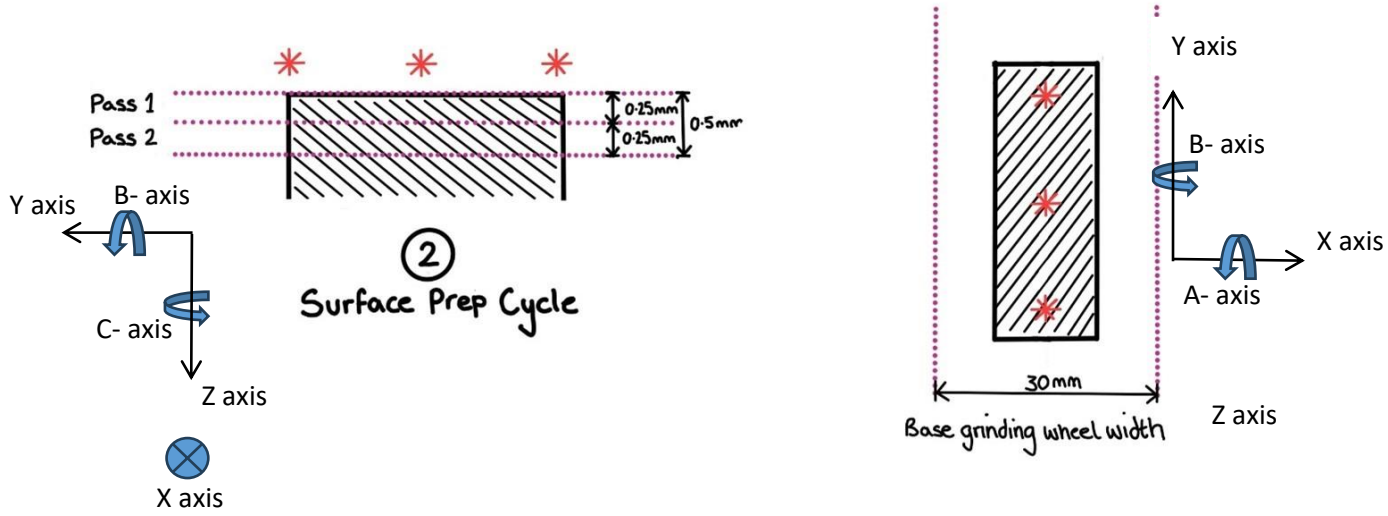

Figure 38 Surface prep cycle used within the grinding trial to "zero" and even workpiece coupon before they are subjected to grinding trials. Sketch shows the coordinate system used to represent the motion while grinding with respect to the machine.

The thesis/project previously involved in its scope, analysing the surface after a grinding cut compared to the initial surface, the parameter grind is conducted with a narrow wheel covering half of the sample edge (Figure 39). This allows the initial surface on the sample edge to remain available before and after the parameter grind. Following the parameter grinding cycle, an air pass cycle is included within the program, which is a repeat of the parameter grind cycle with a 0.1 mm offset from the tool path.

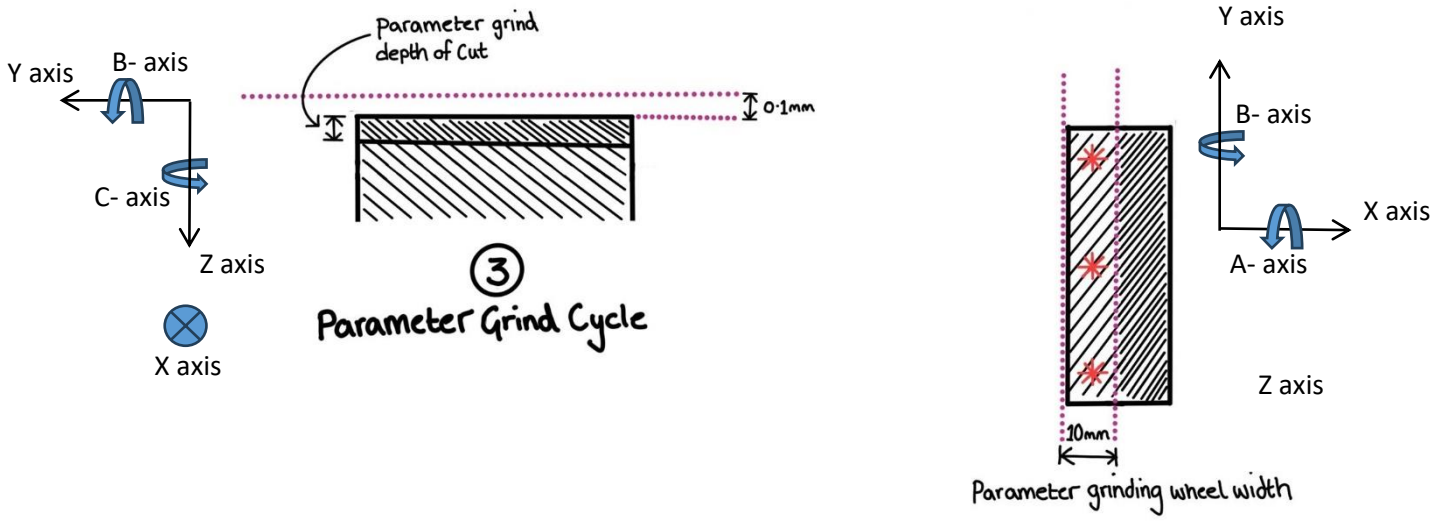

Figure 39 Parameter grind cycle used within the grinding trial to "zero" and even workpiece coupon before they are subjected to grinding trials. Sketch shows the coordinate system used to represent the motion while grinding with respect to the machine.

After both the surface preparation and parameter grinding cycles, the workpiece surface is probed to determine the actual height of the workpiece after the grinding cuts. This probing is done using a three-

point plane, with points equidistant within the 20 mm sample area of the clean-up/surface preparation grinding cut and the 10 mm width sample area of the grinding cut from the face of the fixture. The probing is carried out to ensure consistency in achieving the commanded depth of cut and an average of the three-point measurements is used to finalize the measurement. Similarly, the diameter of the base grinding wheel used for surface preparation and parameter grinding is measured before and after the grinding pass using the Renishaw laser measurement kit.As discussed, this machining programme and tool path was designed to cater for a larger design of experiment which looked at surface analysis of the workpiece before and after grinding cuts by subjecting the workpiece to destructive analysis. As scope of this thesis changed, the same machine programme and tool path has been used in order to conduct repeatability study on the grinding machine.

3.6.3 Control for repeatability test

From literature review, it is apparent how different variables affects the grinding process and can directly influence the AE signals that are recorded along with the grinding force and spindle power. In this thesis, the objective is to control these parameters to understand how repeatable the AE signals are for the grinding process. A mind map was devised to understand what are these variables that can influence the repeatability and how can this be controlled for this thesis as shown in Figure 40.

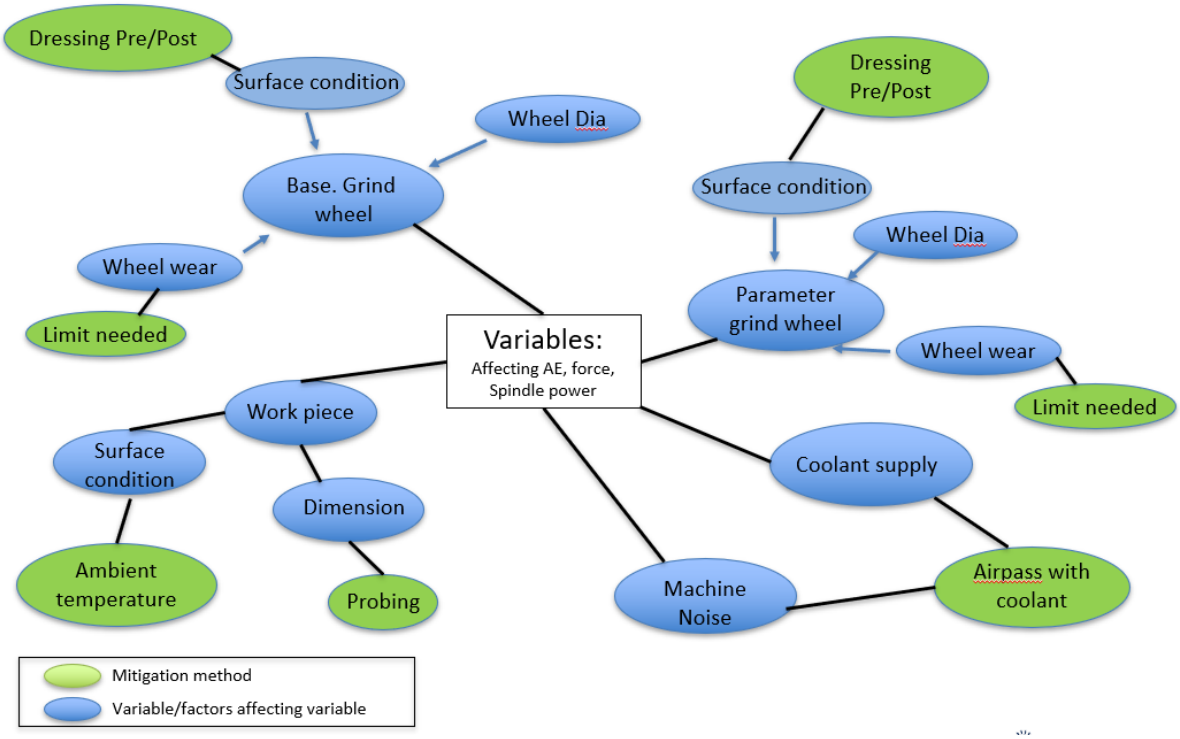

Figure 40 Mind map showing the relationships between variables of the grinding process and mitigation methods to control any variation in studying the repeatability of AE signals.

Starting from the base grind wheel, the wheel surface condition is directly linked to the workpiece quality that can be achieved as a function of the grinding mechanism deployed due to the surface condition. Finer grains produce a smoother finish, while coarser grains leads to a rougher finish on the workpiece. For this experiment, the grinding wheel have a grain size of 60 which is rather course and a rougher finish can be expected but what is important is the grain distribution. The uniformity of grain distribution affect the consistency of the surface finish. As the wheel wears, the effective cutting edges decrease and the wheel may develop an uneven surface which results in inconsistent surface finishes on the workpiece. Sharp grains cut more effectively, leading to higher material removal rates. As the grains become dull, the cutting efficiency decreases, requiring more force to remove material and reducing the material removal rate. Accumulation of material on the wheel surface (loading) increases friction and grinding forces. The base grinding wheel has an open structure which should facilitate reduction in wheel loading. An open structure wheel has more voids or spaces allowing for a better chip clearance during grinding. The larger space between grains also enables better coolant flow through the wheel which means lowered heat generation during grinding and reducing the chance of chip material adhering to the wheel. Dressing the base grind wheel before and after a grinding pass to a set amount of wheel diameter change using the same dressing parameters can control this variable during grinding.

On the other hand, changes in the wheel wear mechanism means the grinding mechanism can change and this directly influences the grinding force which can show in the AE signals. To elaborate further into this concept, the grinding mechanism that were discussed in the literature review can be revisited; rubbing, ploughing and material removal were mechanism in which the grains of the grinding wheel would interact with the workpiece material. This different mechanism can instigate different levels of acoustic emissions with the micro-cracks and shear planes that arise during grinding. The level at which each mechanism takes prominence during the grinding process can effect the acoustic emission recording from the sensors. Therefore it is important to ensure consistent condition of the grinding wheel to avoid influence of the grinding wheel condition to affect the acoustic emission data that is gathered during this grinding trial. Controlling the wheel wear would be to ensure that the wheel is dressed, and a fresh surface generated for each grind pass and therefore wheel condition or progression of wheel wear is alike and repeatable for each grinding pass.

The grinding wheel diameter typically increases the contact area between the wheel and workpiece, distributing the grinding force over a large area and potentially reducing the specific grinding force (force per unit area). The larger contact area leads to a more distributed load, which can lower the grinding force per unit area but may require a higher total grinding force due to the increased material removal rate. A smaller wheel diameter results in a smaller contact area, concentrating the grinding force on the smaller force on a smaller surface. This concentration of force increases the grinding force per unit area, potentially enhancing material removal rates but also increasing the risk of higher stress and thermal damage on the workpiece. In terms of the effect on spindle power, it is important to note that a larger wheel requires more spindle power to maintain the same rotational speed due to the higher mass and inertia. Wheel diameter is a parameter that will change with every dressing and the only way to control this variable would be to use a new grinding wheel for each grinding pass. Such an initiative would have a lot of material waste, not a sustainable practise and farfetched from a realistic grinding scenario in industry. Therefore, within this thesis, repeatability study will look at AE signals as the grinding wheel diameter progresses (reduces) as it is dressed every grinding pass.

The parameter grinding wheel have variables connected to it just as the base grinding wheel. As a result controlled dressing of the wheel is conducted before and after grinding pass and the wheel wear limited using a fresh wheel surface. The wheel diameter progression is also controlled using a set amount of wheel diameter change during dressing of the wheel and this is monitored using the laser measurement kit installed on the machine.

Machine noise and coolant supply could directly affect the AE signals recorded during the machining trial. The best way to take this variable out of the experiment and control it was by separating the noise signature from the recorded AE signal and using signal processing techniques to remove the corresponding noise signals from the overall grinding pass signal. This can be done by implementing an air pass , discussed in section 3.7.2 to 3.7.4 and recording the AE signal to be further analysed. The coolant supply can influence the grinding force especially if the coolant direction is towards the workpiece during the movement of grinding wheel and coolant supply nozzle system. The grinding programme needs to take this into account and have the nozzle positioned for the coolant to be fed into a point on the wheel before it contacts the workpiece. This allows for the coolant to regulate the temperature at the contact point, which is its primary function and as a secondary benefit the porous/vitrified wheel can carry the coolant into the grinding cut. Similar to handling the AE signals from the airpass, the grinding force signals can be recorded during the airpass to process the overall grinding pass signal and remove the grinding force that may be attributed due to the coolant contacting the workpiece/workpiece holder.

The final set of variables that can affect the grinding process would be the state of the workpiece. The workpiece surface condition needs to be constant before any repeat grinding pass to ensure that repeatability comparison is done correctly. Firstly, the stock block of IN718 material from which the workpiece has been machined has been tested with a certificate of conformity to adhere to the API6A 718 standard to ensure that the surface hardness, material microstructure, residual stress, heat treatment method are monitored. Since all the workpiece generated for this experiment is from the same block, it can be assumed that this is constant. To meet the API6A 718 standards, the IN718 flat blank from which the workpieces have been generated from has gone through micrograph imaging checks on grain size, defects, duplex grains, deleterious phases, delta and laves phases and an ultrasonic examination to the ASTM A388 standard [55]. IN718 is material which has a high hardness and harder workpiece surfaces results in higher grinding force to achieve material removal and the abrasive grains will need to exert more force to penetrate and shear off the material. Variation in microstructure closer to the surface can depend on its heat treatments. Variations in microstructure can cause uneven wear on the grinding wheel and fluctuating grinding forces due to differences in the material hardness and toughness at the microstructural level. Residual stress within the workpiece can also influence the grinding process which can affect the grinding force and even the acoustic emissions that result during grinding. Residual stress can lead to localised deformation and micro-cracking during grinding which can affect the acoustic emission signals that arise during grinding. The workpiece in this experiment has been through heat treatment under a controlled and monitored method that allows it to bear the certificate of conformity.

These interactions of factors show the significance of control within the workpiece condition. Alongside the confidence in creating workpiece from the same stock of IN718 it is also important to create a uniform defect-free and residual stress surface before conducting the grinding trials. For this, a base grind has been incorporated into the grinding cycle of the experiment such that each time a parameter grind is conducted, it is ensured that the surface of the workpiece has been returned to its controlled initial state with repeatable surface roughness and surface quality. Another aspect that is closely related would be the dimensions of the workpiece before and after the base grind pass. After every base grind, there needs to be assurance that the material taken off and grinding parameters used have been successful to repeat a fresh workpiece surface as it was done before a previous parameters grind. For this purpose, the workpiece is probed to ensure that the material taken off during the base grind and parameter grind is consistent for each repeat.

3.7 Handling signal acquisition and pre-processing signals

3.7.1 Pre- Grinding trials:AE sensor response reproducibility test

At AMRC, the only measures taken to ensure AE sensors performed accurately within a test was to ensure that the AE sensors were updated with their latest calibration. There was no indication to ensure that the AE sensors go through degradation before/after use in test. Therefore, this project also incorporated the ASTM E976 standard method of determining the reproducibility of acoustic emission sensor response. From the standard guide, the acrylic rod method was used to test the sensor reproducibility. An acrylic rod was sourced similar to the dimensions provided by ASTM E2075 [56]. The standard followed the US metrics and therefore had the diameter for the rod set as the dimensions available in the US. In order to source the correct dimensions in the UK, the acrylic rod diameter had to be changed from 3.8 cm to 4.0 cm as this was the standard acrylic rod diameter available in the UK, any machining of 4.0 cm rod to make it 3.8 cm was beyond the time scope of this project. All other dimensions were kept as accurate to ASTM E2075, as shown in Figure 41.

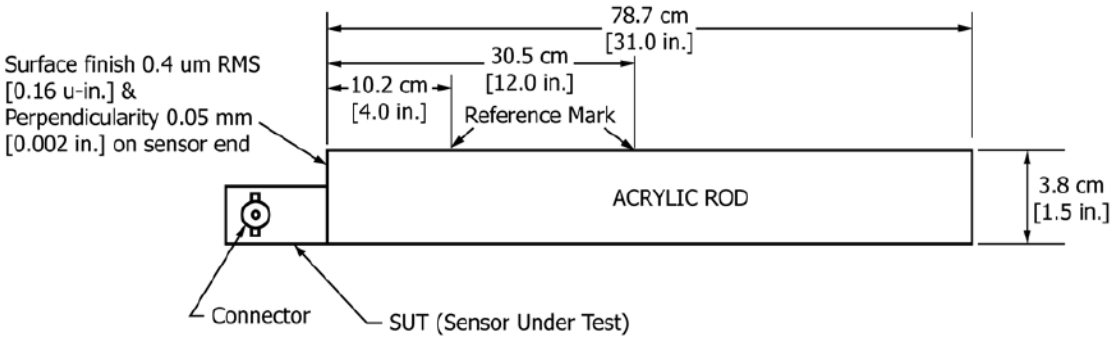

Figure 41 Acrylic rod description under ASTM E2075 standard. [56]

For the reproducibility test, the AE sensor was attached to the end of the Rod which was closest to the reference point marked as pencil break regions. Silicone grease is applied to the AE sensor surface in contact with the end of the road and the tape used to hold the sensor firmly against the surface. The acrylic rod is place flat on a bench and held in position by two weights preventing the rod from rolling. The sensor is connected to the data acquisition system and set to record data at the standard sampling rate of 2Mhz for the AE sensors. The recording is taken for the time frame in which a pencil lead is broken using a special crafted shoe fitted to the end of the lead pencil to ensure the lead is broken in a repeatable manner on the reference mark. Two reference marks can be set and used depending on the type of lead used. The 10.2 cm reference mark from the end with the AE sensor is used for 0.3 mm pencil lead and the 30.5 cm reference mark is used for the 0.5 mm pencil lead.

For this project, the pencil lead break was repeated 5 times to ensure an average response of the lead pencil break can be used to compare before and after the test. For the AE response gathered, it is ensured that a clean ping is recorded in the data acquisition system as a peak in signal when the pencil lead breaks. For comparison of AE reproducibility, the AE frequency response is compared to ensure similar signals were recorded for pre and post reproducibility test. To ensure quantitative analysis, the AE response on the time domain is converted to dB and peak signal compared for before and after a test. Any variation in sensor response to the pencil break greater than 4 dB indicates that there is damage or degradation that has occurred to the AE sensors and any variation more than 6 dB can be considered as criteria unfit for further service.

3.7.2 Signal wavelet De-noising

Wavelet decomposition and de-noising is a new method which has not been dominantly used in machining science. From literature review, wavelet packet transforms and related methods have been applied to acoustic emission (AE) signals for feature extraction in grinding processes. Liu et al. [25] successfully used wavelet packet transforms combined with fuzzy pattern recognition to detect grinding burns in IN718, achieving high classification accuracy by optimizing AE signal features. Similarly, Gao et al. [27] employed the energy of cross wavelet transform (EXWT) and degree of wavelet coherence (DWTC) to distinguish grinding burns, demonstrating a 100% detection rate. These studies primarily focus on specific materials like AISI 1045 steel and employ various signal processing techniques, but they do not explore wavelet denoising methods. This indicates a gap in the application of wavelet denoising within machining science for real-time monitoring and quality control, particularly for complex materials like IN718.

Wavelet de-noising can be a highly effective method for removing noise from Acoustic Emission (AE) signals during grinding due to its ability to analyse and process signals in both time and frequency domains simultaneously. AE signals in grinding are typically high-frequency and can be contaminated by noise from various sources such as machine vibrations, ambient environmental sounds, and electrical interference. Traditional filtering methods might not effectively distinguish between noise and the valuable signal features. However, wavelet de-noising leverages the multi-resolution analysis capability of wavelets to decompose AE signals into different frequency components. This allows for precise identification and separation of noise from the actual AE signal generated by grinding phenomena. The wavelet transform's ability to retain important signal characteristics while removing unwanted noise results in clearer, more accurate signal representation. By improving the signal-to-noise ratio, wavelet de-noising facilitates more reliable and efficient grinding process monitoring, ultimately leading to better control over machining parameters and improved workpiece quality.

This project explores the opportunity to devise this method to de-noise the acoustic emission signal which has been recorded for each grinding cut using the air-pass data gathered. Within the results and discussion section, the best set of parameters to use for wavelet de-noising within this application is discussed. For this project, the air-pass data has been collected to help with the parameter selection. The air pass data is full of noisy signal information which is unwanted AE noise signal during the grinding cut as it is not representative of the AE signal that occurs due to the interaction of the grinding wheel and the workpiece.

The use of air-pass has therefore become an ultimate tool to set the thresholds for the detailed coefficient for wavelet decomposition and thereby vary the parameters applied for wavelet denoising and compare.

The method used within this thesis is to decompose the airpass signal to different levels and manually investigate the air pass to infer the threshold values at which the airpass data peaks for the different decomposition levels. Once this threshold values are inferred from the decomposition levels, this threshold value can be applied on the original signal with the optimised wavelet de-noising parameters finalised within this thesis. Figure 42 shows the final output of an example signal that has been wavelet denoised using the thresholding of air pass data, most importantly, the decomposition of coefficients before and after de-noising shown in Figure 43 show the significant improvement in removal of coefficient from the signal without the loss of the important signal through a grinding trial. Manual thresholding completely eliminates signal coefficients outside the contact period between wheel and workpiece which gives confidence that the unwanted signals are removed while important signals are kept through wavelet de-noising.

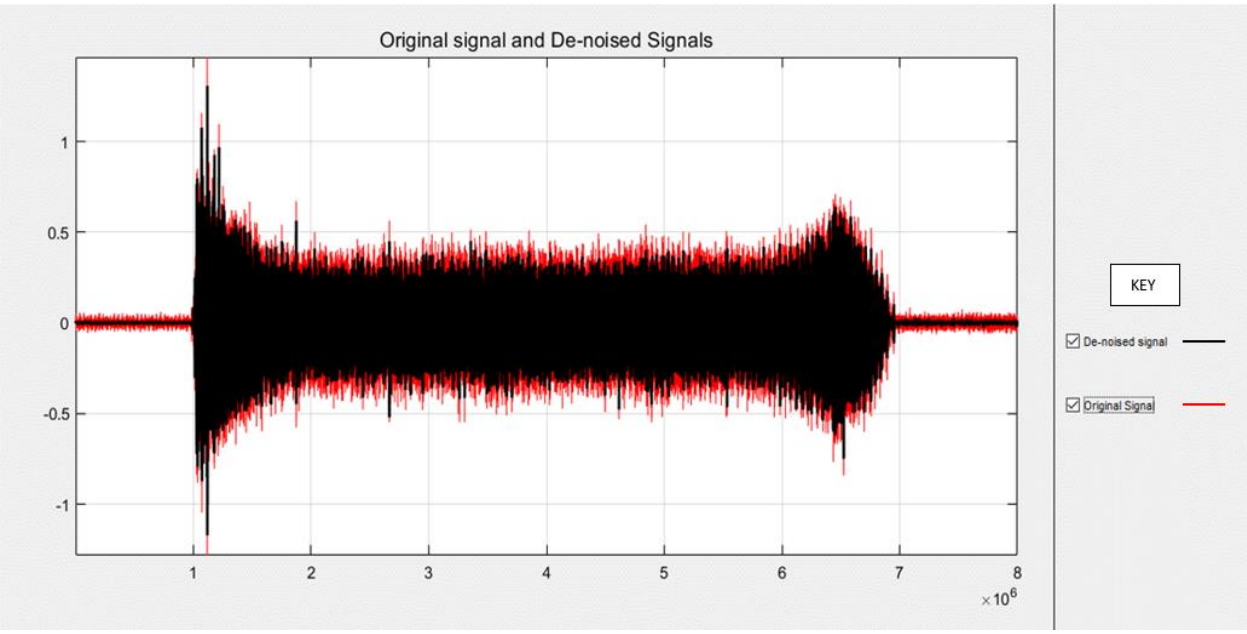

Figure 42 Graph showing the output of wavelet de-noising where manual thresholding has been applied using the airpass data. The signal in black is the de-noised signal while the original signal is in red.

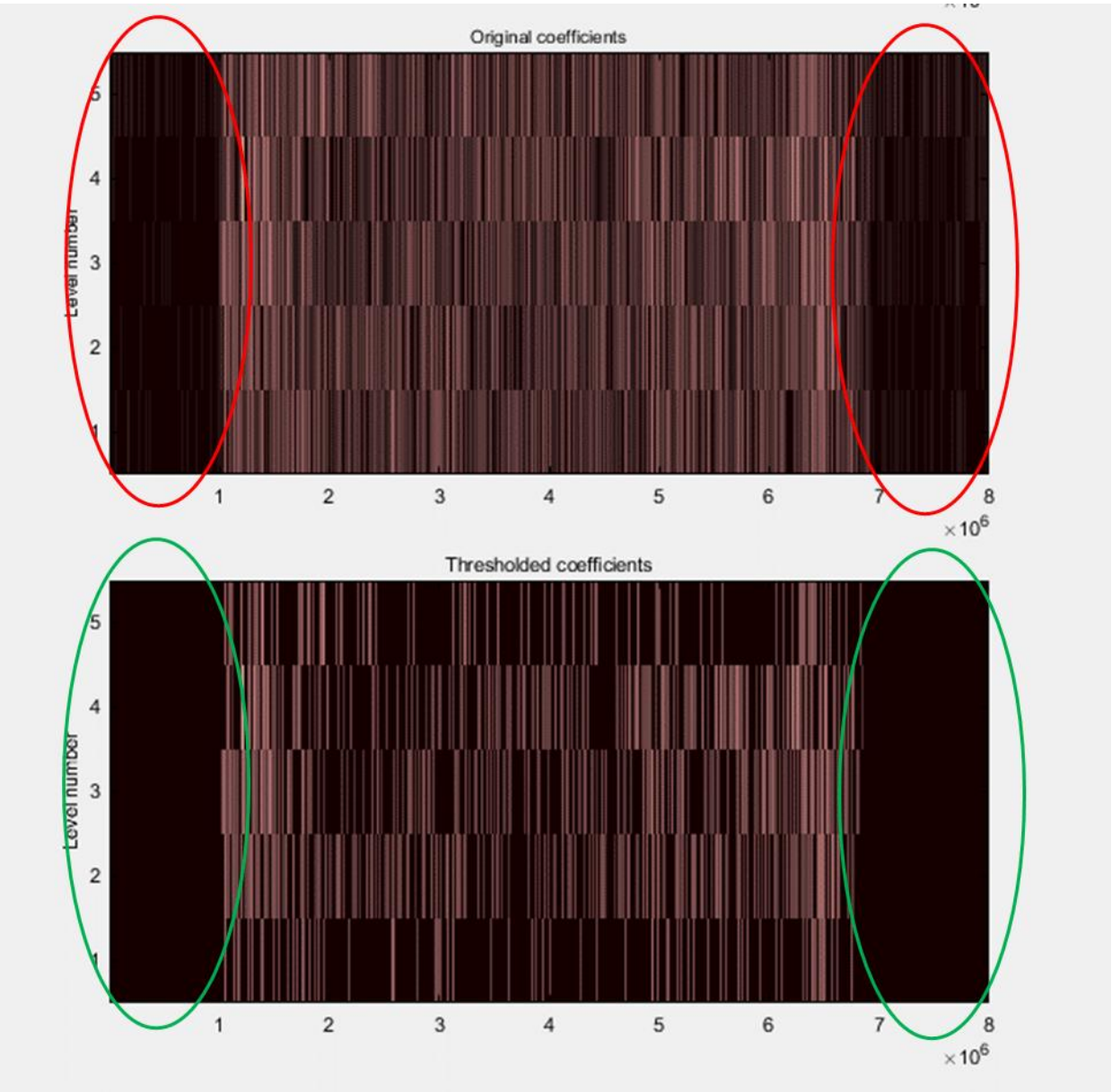

Figure 43 Spectogram showing the difference between the original coefficients from wavelet decomposition of original signal upto 5 levels and after de-noisning using air-pass data thresholding.

From this study, it can be gathered that the technique of wavelet de-noising has variable parameters which can affect the de-noising performance. Therefore, there needs to be a set way to analyse the performance of a signal that has been de-noised and a set design of experiment to evaluate all the possible parameter's effect. The signal evaluated in this project is acoustic emission signals from grinding cuts and therefore prior knowledge that what is representative of noise in the signal is fully represented by the air pass dataset that is gathered alongside the grinding trials. This makes us reach a conclusion that the performance of de-noising technique can be compared using the parameter signal-to-noise ratio (SNR)

for the de-noised signal against the original signal after thresholding picked from air-pass is applied with different wavelet de-noising variables. Two approached that can be used to evaluate signal to noise ratio equations can be given as:

$$SNR3 = \frac{mean(Denoised\ RMS\ signal)}{standard\ deviation\ (denoised\ RMS\ signal)}$$

Equation 23 adapted from[57]

$$SNR2 = 10log_{10}\left(\frac{\sum_n I}{\sum_n (I_n - I'_n)}\right)$$

Equation 24 adapted from[58]

In Equation 24 (SNR 2), I is the denoised signal while I' is the original signal and n is the length of the signal. In some application of this SNR formula, usually the power of the signal is considered but in this equation, we are simply investigating the amplitude of the signal itself. Equation 24 requires the noise of the signal to be clearly defined otherwise the equation would merely be a calculation of the amount of de-noised signal removed from the original signal. This would have been proved to be a challenge within this trial scenario if it wasn't for the introduction of airpass. The collection of airpass data within the grinding trials helps differentiate the distinct noise signal (machine noise, coolant supply noise, ambient noise, tool movement noise) against the original signal itself thereby calculation of the denominator in this equation is straight forward. In the equation, air pass data would be classed holistically as the $\sum_n (I_n - I'_n)$ without requiring it to be subtracted from the original signal.

In this thesis, Equation 23 (SNR 3) was investigated because the noise was not initially defined clearly from the full signal until the air pass data was analysed. A larger SNR for Equation 23 (SNR 3) indicates better performance of the de-noising algorithm, as it implies a higher mean of the de-noised signal (indicating reduced signal amplitude loss) and a lower standard deviation (indicating less signal spread and less noise interference). However, SNR 3 was not used further for parameter optimization because the signal amplification for the AE sensor varied drastically during the initial contact between the workpiece and the grinding wheel, significantly affecting the mean and standard deviation of the AE signal. This variation meant that the SNR 3 calculated by the equation was not representative of the full signal but was instead heavily influenced by its temporal nature, failing to provide a reliable indication of the signal-to-noise ratio. SNR 3 might be useful in other applications with constant signal acquisition rather than those involving transient response signals.

The literature review indicates that the key parameters for wavelet de-noising include the choice of wavelet, wavelet filter length, wavelet decomposition level, threshold algorithm, and type of thresholding. Specifically, the wavelet choices that closely resemble acoustic emission signals are symlets, Coiflets, and Daubechies. Figure 44 gives a graphical representation of the 3 types of mother wavelets discussed in comparison to the simple Haar wavelet. One aspect initially studied was how these three different wavelet bases affect the SNR across four different datasets. To define the optimal parameters for wavelet de-noising, a step-by-step elimination of parameter options was employed to systematically control and refine these parameters.

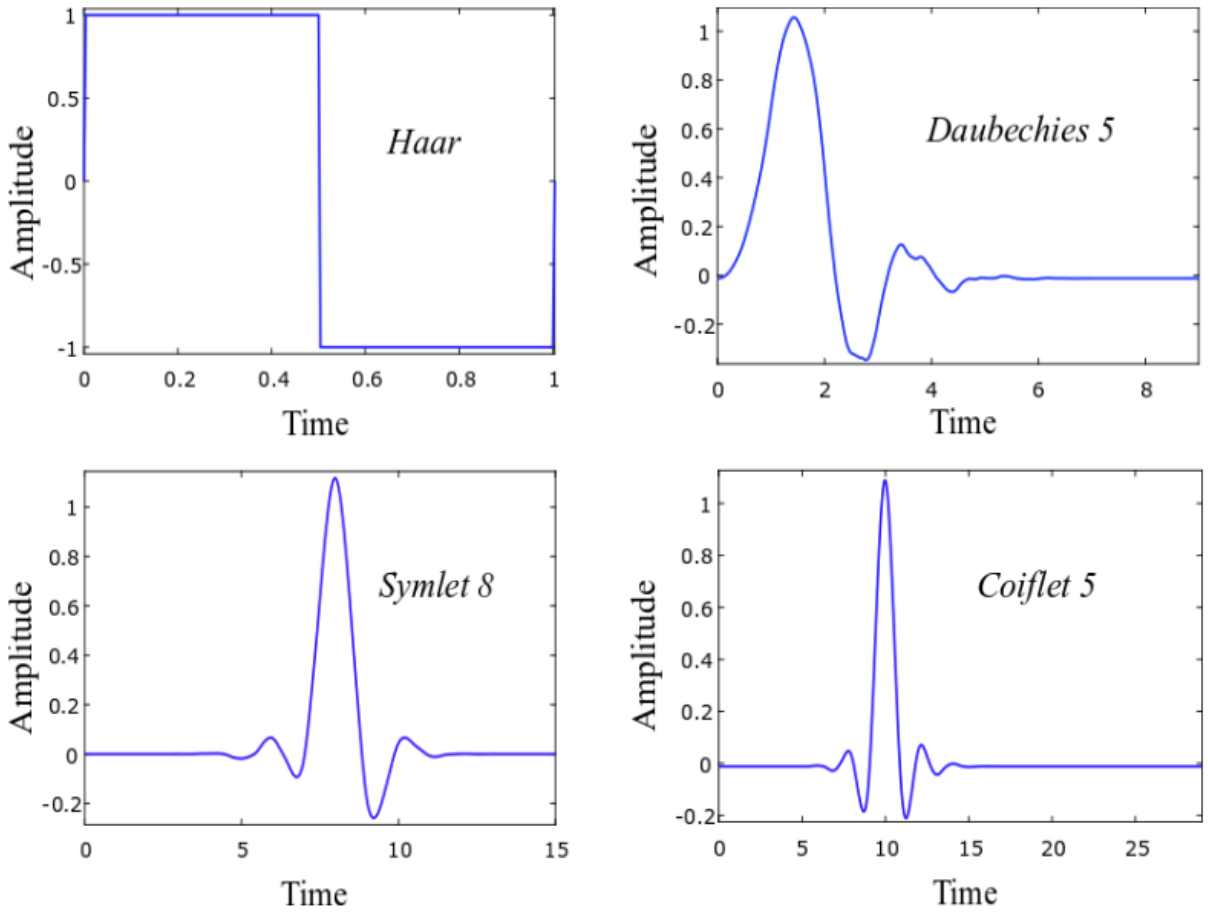

Figure 44 Figure shows examples of Haar, daubechies-5, symlet-8 and coiflet-5 mother wavelets. These are some of the common wavelets used to characterice acoustic emission signals within machining science. [59]

The first step involved identifying the optimal filter length for the three wavelet types while maintaining a constant wavelet decomposition level of five for a sample grinding cut signal. During this phase, the 'rigrsure' thresholding method and soft thresholding were consistently applied across all trials. Subsequently, to determine the optimal wavelet decomposition level, the previously identified optimal

wavelet filter length was kept constant while the decomposition level was varied from 1 to 8 for the three wavelet bases on the sample signal.

The final choice of decomposition levels is a trade-off between a few factors including performance and computational costs. Theoretically, the maximum decomposition level (M) can be calculated as:

$$M = log_2(N)$$

Equation 25

Where N is the length of the signal. Therefore, the most suitable level of decomposition has to be determined by analysing the performance of de-noising algorithm such that quality de-noising performance can be achieved without decreasing computing efficiency and being lower than the maximum limit. Another aspect to consider, wavelet decomposition at different levels means that this is breaking down the signal coefficients into bands of frequencies (halved at each level) therefore, more the number of levels, more the resolution of frequencies when the signals are reconstructed from the wavelet coefficients. All matlab code that was used for data processing within this thesis has been included within the appendix in section 9.2 for reference.

3.7.3 Analysing the grinding force signal

Grinding force was measured from the 8-channel dynamometer and within the results section, the horizontal and vertical grinding force is collected from the dynamometer. These two forces have been observed for the changing grinding wheel diameter for the 5 repeat grinding cuts for the three grinding regimes. The grinding force recorded has been post processed to ensure that (1) air pass data is used to remove grinding force components which are a resultant of coolant supply (2) drift in the dynamometer is monitored and compensated for in the grinding signal by evaluating the drift curve for each grinding pass and removing the offset using a linear curve fitting (3) grinding force data is trimmed to remove the lead-in and lead-out section of the grinding cut, this is done to remove the section of the grinding cut where the depth of cut is variable and as a result leaving the stable region of the grinding cut. In order to pick up the stable region of the grinding cut, a threshold was applied to the AE signal such that the data selected is post the peak of the AE signal (section where the most variable depth of cut is noticed during lead-in of cut) and in a region where grinding force would be stable. Time stamps picked up using the AE signal thresholding is used to determine this start point for the grinding force signal. Hereafter, a grinding force dataset of length of 1 sec is extracted from each grinding cut. This AE signal threshold technique ensured that the grinding force section picked up from a grinding cut was a consistent, fair selection and

an easily automated process. Once the griding force signal was trimmed down, the signals collected were also inspected case-by-case to ensure that there were no anomalies in the data set. Equation 5[5] , Equation 6 and Equation 7 were used to evaluate the normal grinding force and instantaneous tangential grinding force by solving with horizontal and vertical grinding force measured. In order to evaluate θ, the actual depth of cut was calculated from the difference in measured height of the coupon pre and post grinding cut. Section 9.3 in appendix shows matlab code used for all data processing from the grinding results. The actual wheel diameter measured from the Renishaw laser measurement system was used as average of wheel radii pre and post grinding cut.

3.7.4 Analysing the grinding power signal

For the analysis of grinding power, the data technique used for the trimming and sectioning was the same as grinding force where AE data thresholding was used to time stamp the dataset and extract the data for the stable section of a grinding cut. Power data from each airpass was used to evaluate and subtract no-load power (P_{NL}) and fluid drag power (P_f) from the each grinding cut. Section 9.4 in appendix shows matlab code used for all data processing from the power data signal.

4 Results & Discussion

4.1 Parameters for wavelet denoising

The parameter study conducted have been reported for a sample grinding cut from both AE sensors with the approach identified under section 3.7.2. Although SNR 2 (Equation 24)comparison does not show drastic differences between the wavelet filter length and type of wavelet used, Figure 45 & Figure 46 shows that Coiflet of filter length 5 gives the best SNR across all grinding regimes and both AE sensors. The SNR values from both AE sensors are very different and this can be owed to the different operation of both sensors but what stands out is that the behaviour of wavelet filter type and length is consistent within the two AE sensors.

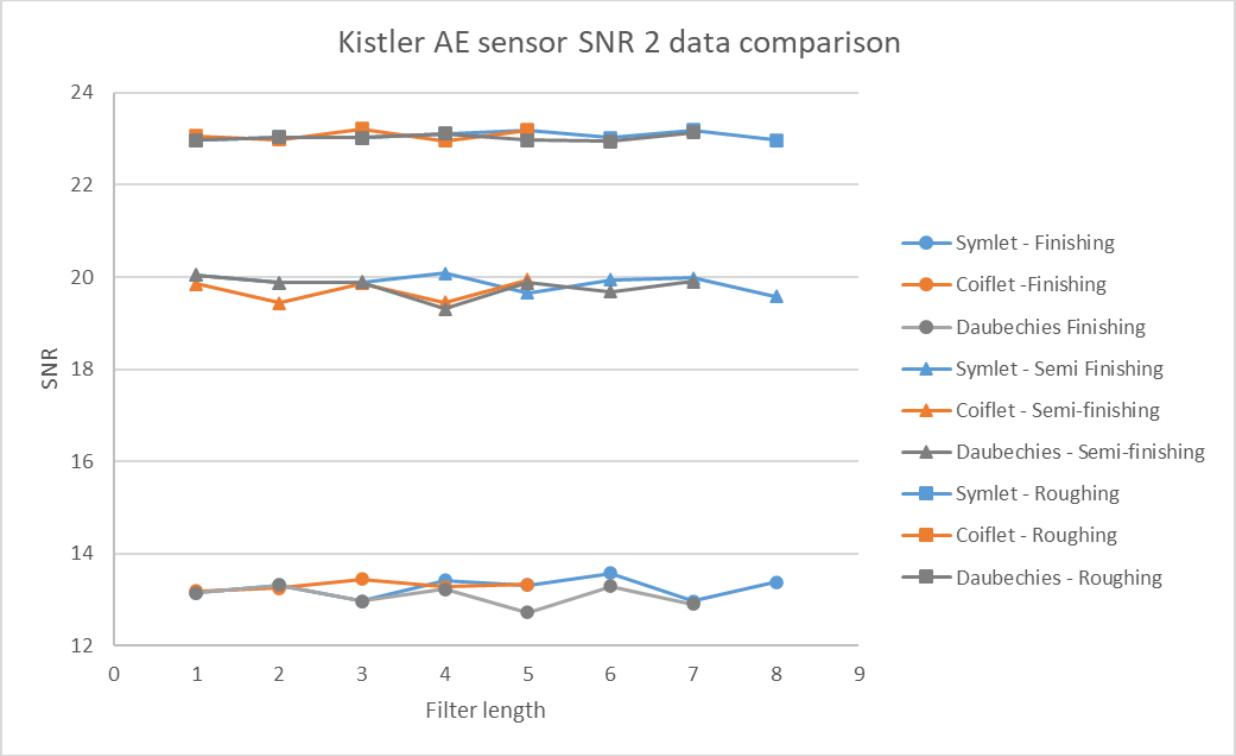

Figure 45 Graph showing the comparison of SNR 2 for Kistler AE sensor data from the first trial sample of each grinding regime.

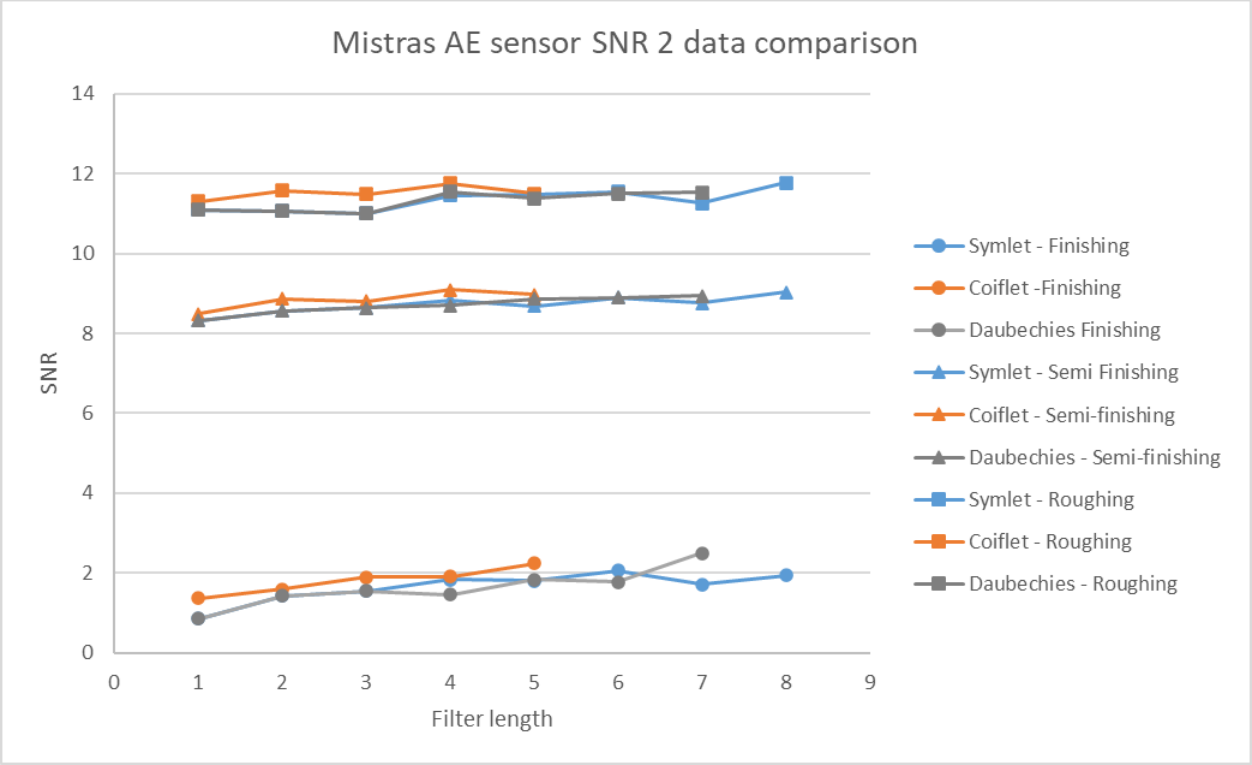

Figure 46 Graph showing the comparison of SNR for Mistras AE data from first trial sample for each grinding regime.

For the Kistler AE sensor (as shown in Figure 45) , the roughing operations displayed consistently high SNR values around 22-24 across all wavelet bases and filter lengths, with minimal variation. Semi-finishing operations yielded SNR values around 19-20, while roughing operations reported SNR values between 12-14. Among these, Coiflet demonstrated slightly better performance across all operations, maintaining higher SNR levels with increased filter length stability which is optimised at filter length 5.

Similarly, for the Mistras AE sensor (as shown in Figure 46), roughing operations reported SNR values around 10-12, semi-finishing around 8-9, and roughing operations yielded lower SNR values in the range of 1-4. Again, Coiflet exhibited superior performance, particularly noticeable in the finishing operations where SNR was slightly higher and more consistent compared to Symlet and Daubechies.

The general trend noticed within the SNR values is an increase with the grinding regime being rougher and this can be lend to the increased contact length of grinding wheel accompanied by increased material removal rate, leading to higher amplitude of acoustic emissions which does not increase proportionally with the noise within the environment. The other perspective to consider is that with increased acoustic emission activity during grinding, the wavelet de-noising technique might perform better under

conditions since the matching of the mother wavelet basis against the noise signal would be much easier and efficient. The stronger acoustic emission signal will be distinct from the noise signal which is being effectively filtered out from the signal.

Based on this comprehensive analysis, Coiflet-5 was selected as the preferred wavelet base due to its consistent and relatively higher SNR performance across all grinding regimes and filter lengths. This choice ensures optimal de-noising efficiency, crucial for accurate signal interpretation in grinding operations.

To optimize the decomposition level for wavelet de-noising, the change in SNR is compared for different grinding regimes in both AE sensor data samples for the first set of grinding trial data. From Figure 47, it is evident that the SNR plateaus after a decomposition level of 5. Specifically, the Kistler sensor shows a sharp initial decline in SNR across all regimes (finishing, semi-finishing, and roughing) until reaching a more stable trend around level 5. Similarly, the Mistras sensor exhibits a comparable pattern where SNR decreases with increasing decomposition levels but stabilizes beyond level 5.

For the Kistler sensor, roughing operations start with the highest SNR, maintaining superior performance even after the plateau, which suggests effective signal retention despite increased decomposition. Semi-finishing and finishing operations show a more significant drop initially but also stabilize around level 5, indicating an optimal balance of noise reduction and signal preservation at this level. The Mistras sensor, although demonstrating lower overall SNR values compared to Kistler, follows the same trend of initial decline and subsequent stabilisation around level 5 across all regimes.

This observed plateau at decomposition level 5 aligns with the discussion in section 3.7.2, highlighting it as the compromise point between computational cost and performance. Higher decomposition levels may lead to diminishing returns in SNR improvement, while lower levels may not sufficiently reduce noise. Thus, selecting level 5 ensures an optimal balance, providing adequate de-noising without incurring unnecessary computational complexity. Therefore, the final optimum level of decomposition required for

wavelet de-noising is conclusively determined to be level 5, ensuring both efficiency and performance in signal processing for both Kistler and Mistras AE sensors.

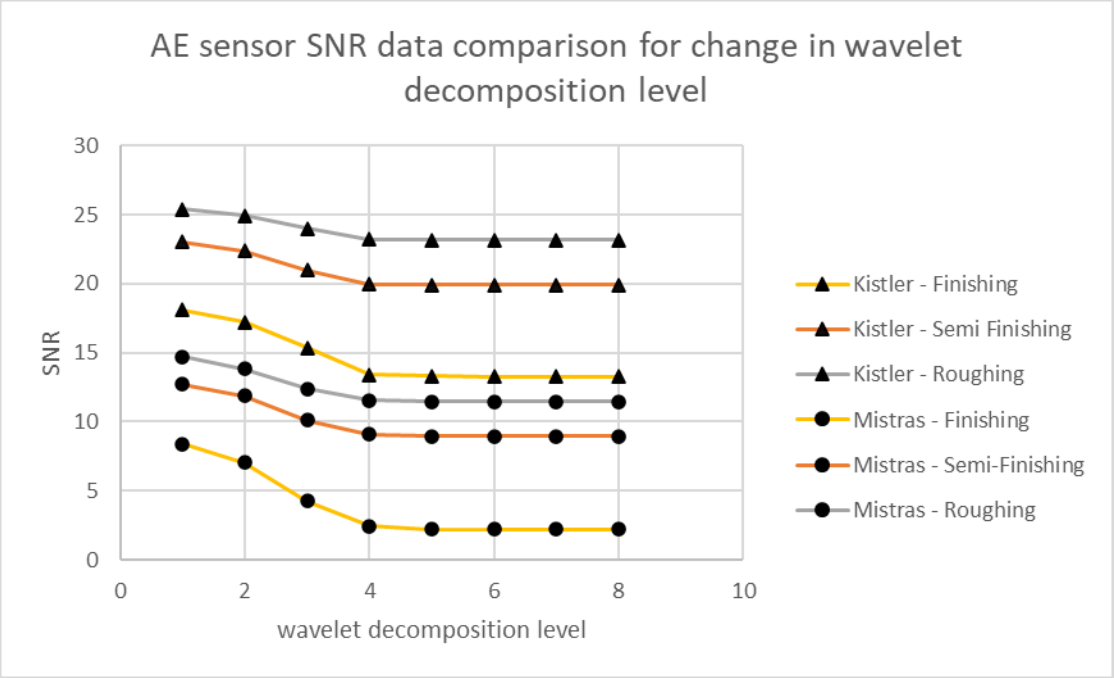

Figure 47 graph showing comparison of the change in SNR as AE sensors SNR change with wavelet decomposition level for the different grinding regimes.

To finalise on the parameters used for wavelet denoising within this thesis, for each parameter grind signal, threshold values are determined from the air pass data for each parameter grind (as discussed in section 3.7.2) and the signal decomposed using wavelet 'Coiflet 5' and decomposed to level 5 using soft thresholding.

4.2 Pre and post AE sensor response reproducibility

The two AE sensors, Kistler and Mistras, were run through the ASTM E976 reproducibility test before and after the grinding trial experiment was conducted. Each reproducibility test was repeated 5 times and the results averaged to compare the time domain signal response in dB to understand any changes. A MATLAB app had been coded to compare the average of these repeat runs automatically and ensure the standard AE signal produced by the pencil break was reproducible within the given limits of degradation. Both AE sensors showed good reproducibility and built confidence in ensuring the signal recorded are accurate without being exposed to degradation. The Mistras sensor showed higher amplification when compared to the Kistler which can be routed to the difference in the pre-amplifier systems used but the reproducible signals were within the tolerances of ASTM E976.

4.3 Grinding trial results

Table 8 Shows actual measurements taken for the different trials in relationship with the targets given in Table 5

Trial	Type	Target Depth of grinding cut Ae(mm)	Actual Pre-grind Wheel radius measurement (mm)	Actual Post-grind Wheel radius measurement (mm)	Actual depth of cut (mm)	Actual wheel diameter (mm)
010	Finishing	0.1	108.4	108.4	0.10	216.9
020	Finishing	0.1	107.4	107.4	0.09	214.8
030	Finishing	0.1	106.4	106.4	0.09	212.8
040	Finishing	0.1	105.3	105.3	0.09	210.7
050	Finishing	0.1	104.3	104.3	0.09	208.6
060	Semi-finishing	0.25	108.4	108.4	0.25	216.9
070	Semi-finishing	0.25	107.4	107.4	0.24	214.8
080	Semi-finishing	0.25	106.4	106.4	0.25	212.8
090	Semi-finishing	0.25	105.3	105.3	0.24	210.7
100	Semi-finishing	0.25	104.3	104.3	0.24	208.6
110	Roughing	0.5	108.5	108.5	0.50	217.0
120	Roughing	0.5	107.5	107.5	0.50	215.0
130	Roughing	0.5	106.5	106.5	0.50	212.9
140	Roughing	0.5	105.4	105.4	0.50	210.8
150	Roughing	0.5	104.4	104.3	0.49	208.7

As discussed within section 3.6, trials were conducted as 5 repeat grinding cuts in 3 different grinding regimes. The trial No. given in Table 8 is later referenced within this section to describe the trials which are studied as part of the AE repeatability study. The actual wheel diameter measurements given in Table 8 uses the Renishaw laser measurement system to record the pre and post radius measurement and averages the results to finalise the diameter of the grinding wheel during the grinding cut. 3 repeat measurements of the grinding wheel radius is completed before averaging to finalise the pre and post grinding wheel radius to improve the accuracy and precision. The actual depth of cut is given by measuring the height of the workpiece coupon pre and post grinding cut by probing as described within section 3.6.2.

Figure 48 shows the graph of the percentage of radial wear that the PGW witnesses during each parameter grind within the 3 different grinding regime. As the wheel radius decreases from 109 mm to 104 mm,

there is a noticeable variation in the percentage radial wear across the different grinding regimes but the % wear fluctuates between 0.005 % 0.025 % which are low numbers. The finishing regime shows a more consistent and lower wear pattern, maintaining wear around 0.01-0.015% throughout the trials. Roughing shows intermediate wear values with some fluctuations but remains relatively consistent around the 0.02-0.03% mark. The semi-finishing regime regime exhibits the most significant fluctuations in wear, starting around 0.015 % at 108.5 mm then rises to 0.02% as the grinding wheel radius drops to 106.5 mm but then drops to 0.01 % near 105.5 and has an outlier which peaks at 0.055 % at 104 mm grinding wheel radius. Overall, the radial wear is not consistent through the repeat grinding cycles, especially in the semi-finishing regime, where significant wear variation suggests possible instability or variability in grinding conditions or material properties. Although, the trends shows this fluctuation, it is important to note that these values are minute in comparison to the grinding wheel radius and further relations to the grinding force and acoustic emission data needs to be inferred to understand if there is consistency in the grinding process recorded.

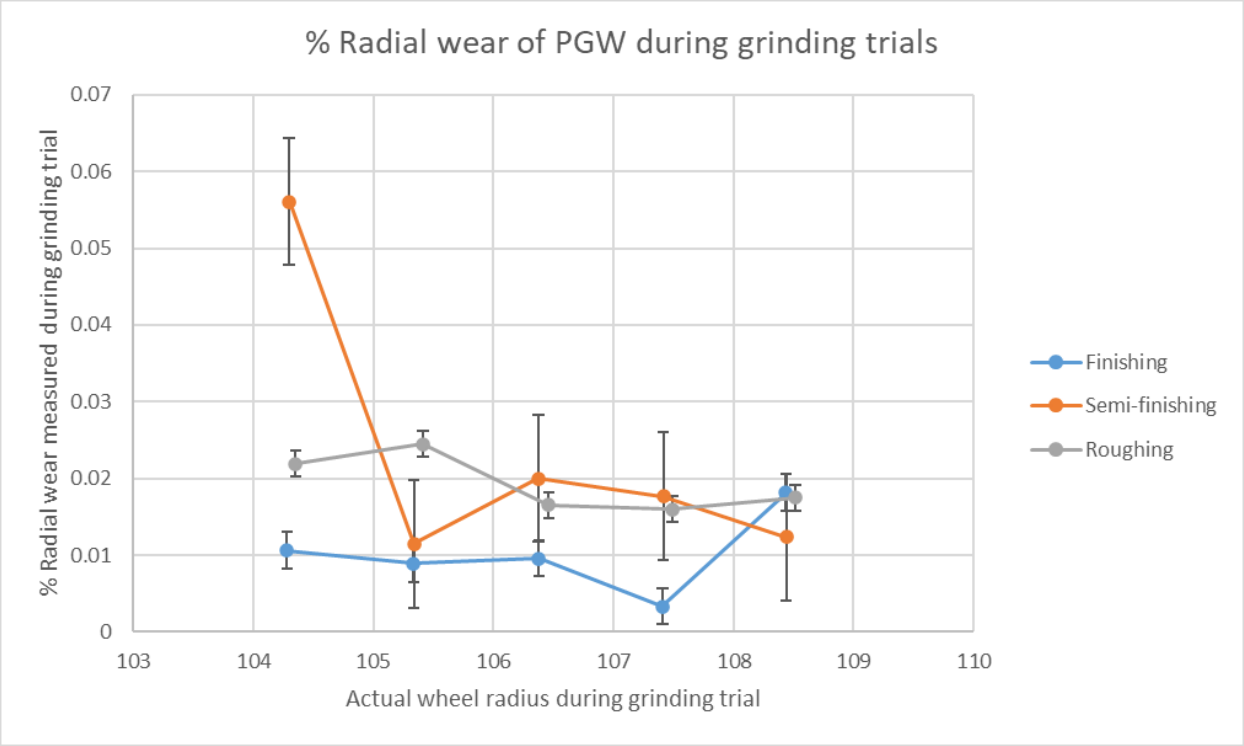

Figure 48 Graph showing the % wheel wear experienced by the PGW wheel after each grinding repeat and dressing cycle for the separate grinding regime investigated.

4.4 Effect of grinding wheel diameter progression

4.4.1 Grinding force

As discussed within section 3.7.3 and the literature review, the grinding normal force and instantaneous tangential force is solved from the vertical and horizontal grinding forces measured by the dynamometer. The statistics compared between the regimes of grinding cuts are the mean and range of the grinding cut recorded with the dynamometer. The grind being a straight cut, it is expected to observe a higher normal grinding force than tangential. Given the difference in grinding regimes, it is expected for the roughing regime to observe the highest grinding forces than the finishing regime i.e., vertical, horizontal, tangential and normal force. As grinding aggression increases during the grinding of I718, the grinding forces are expected to exhibit notable changes due to the interaction between the abrasive particles and the workpiece material. Increased grinding aggression means higher depths of cut, increased feed rates, or higher wheel speeds, all of which result in more substantial material removal rates but within this grinding trial only the depth of cut is increased. With increased aggression, the tangential (cutting) force is expected to rise significantly. This is because more material is being sheared off per unit time, requiring greater energy and force to maintain the material removal process. Consequently, the normal force will also increase as the wheel exerts more pressure to penetrate the workpiece surface with increased depth of cut. Figure 49 and Figure 50 shows the comparison of mean vertical and horizontal grinding forces which have been post-processed for the three grinding regimes. The error bars show the range of the grinding forces giving the minimum and max recording for the stable region of the grinding cuts. As expected, the roughing regime show the highest forces in comparison with the finishing regime (smaller depth of cut). Given the vertical and horizontal forces plot it is evident that there is a clear distinction between the different regimes and the force readings are repeatable given the straight line plots.

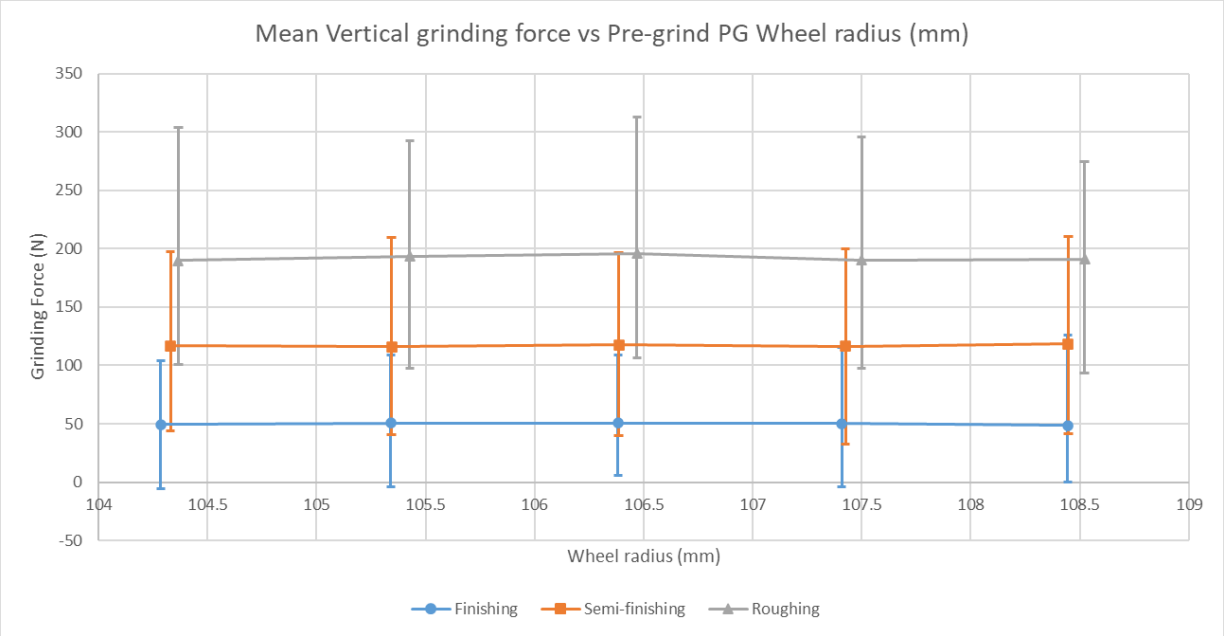

Figure 49 Graph showing mean vertical grinding force for the 5 repeats of grinding cuts of the three grinding regimes The error bars show the maximum and minimum peaks of the horizontal grinding force registered during the grinding cut.

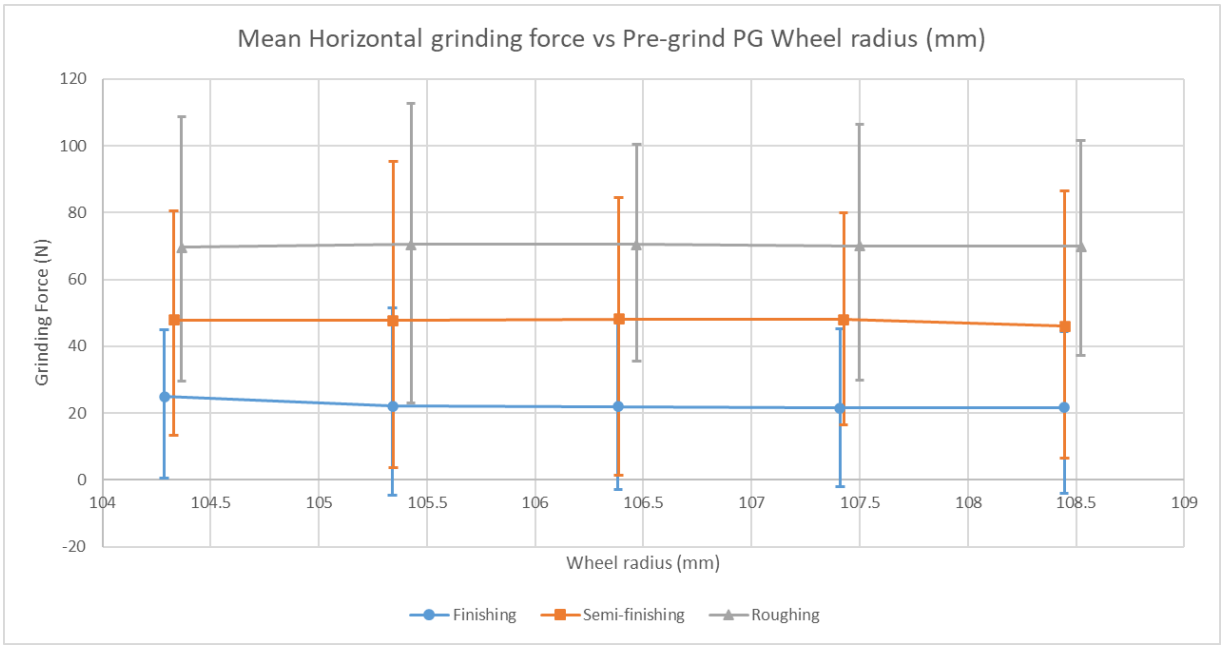

Figure 50 Graph showing mean horizontal grinding force for the 5 repeats of grinding cuts of the three grinding regimes The error bars show the maximum and minimum peaks of the horizontal grinding force registered during the grinding cut.

For the changing grinding wheel diameter for the 5 repeats, there has been no drastic change in the grinding tangential (Figure 52) and normal force (Figure 51) within the grinding regimes. As expected the grinding forces are higher for a larger depth of cut and higher aggression values. The straight lines within the graph shows that grinding force is stable as the grinding wheel diameter changes and therefore this behaviour should also transfer on as stable AE readings as grinding wheel changes. In comparison to the grinding wheel wear trend noted in section 4.3, the fluctuations in wheel wear has not instigated a drastic fluctuation in the grinding forces recorded. One primary reason for this observation could be the potential for the grinding system to reach a quasi-steady state condition, where the worn areas of the wheel become stabilized through repeated use. In this scenario, the abrasive grains on the wheel surface may undergo a self-sharpening effect, where dull grains break away, exposing new, sharp grains, thereby maintaining consistent cutting efficiency. Intermittent analysis of the grinding wheel surface in the future would have helped to monitor this in future testing. The standard deviation of the tangential force, calculated from the mean horizontal and vertical forces, is given as 1.42, 0.85, and 0.37 for the finishing, semi-finishing, and roughing grinding regimes, respectively. When expressed as a percentage of the mean tangential force, these standard deviations indicate the relative consistency of the grinding forces. For the finishing regime, with an average tangential force around 25 N, the standard deviation represents approximately 5.68%. In the semi-finishing regime, with an average tangential force around 50 N, the standard deviation corresponds to about 1.70%. In the roughing regime, where the average tangential force is around 75 N, the standard deviation accounts for roughly 0.49%. These percentages highlight that the roughing regime exhibits the most stable and repeatable grinding forces, followed by the semi-finishing regime, with the finishing regime showing the highest variability. This analysis suggests that despite the wheel wear fluctuations, the grinding forces remain relatively stable.

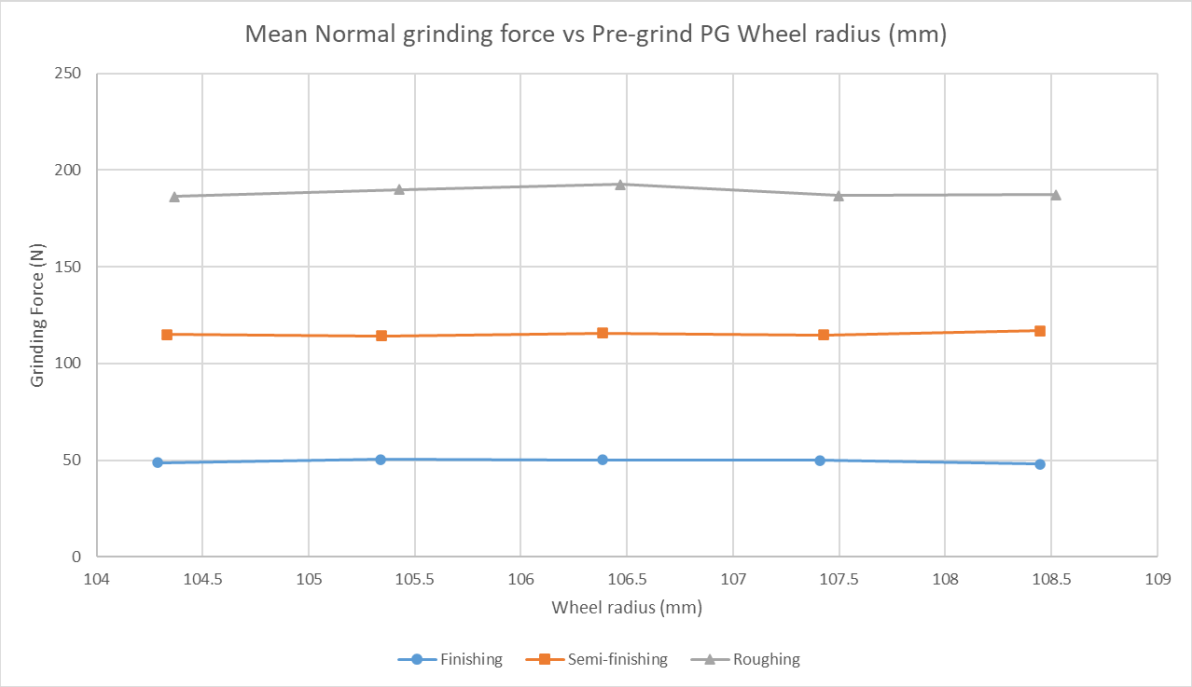

Figure 51 Graph showing the mean normal grinding force for the 5 repeats of grinding cuts of the three grinding regimes resolved from the horizontal and vertical forces measured on the dynamometer.

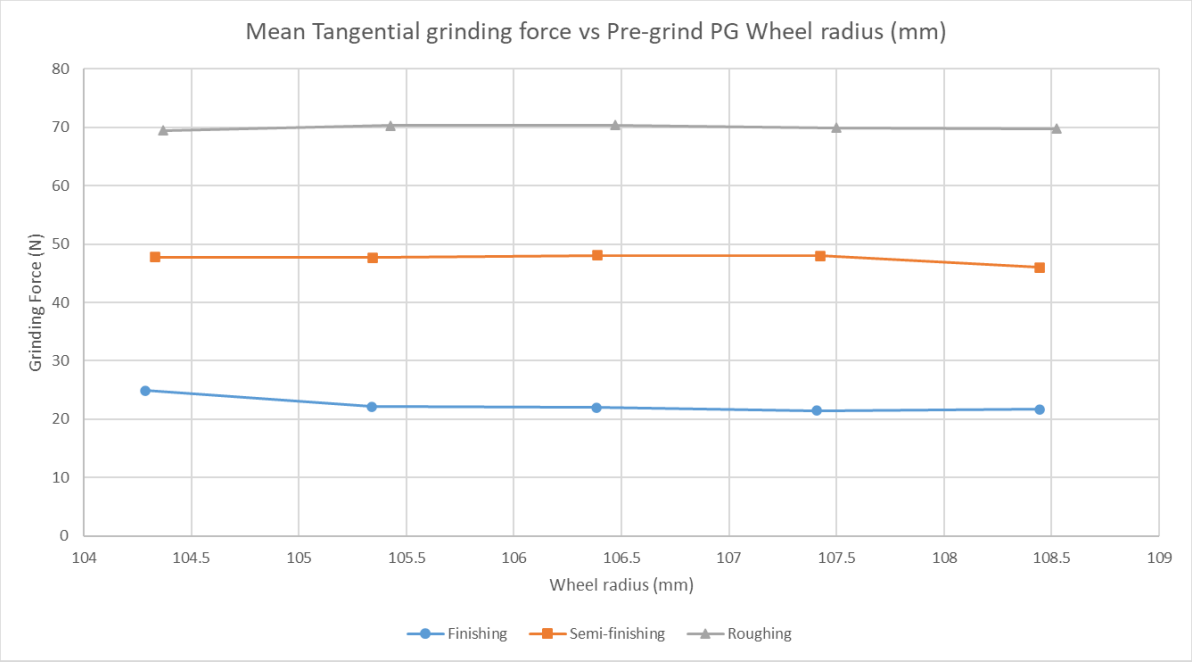

Figure 52 Graph showing the mean tangential grinding force for the 5 repeats of grinding cuts of the three grinding regimes resolved from the horizontal and vertical forces measured on the dynamometer.

4.4.2 Grinding power

Spindle power data recorded for the 5 repeats of the 3 grinding regimes were analysed to understand how the mean, maximum, RMS and skew changed with change in grinding wheel diameter progression.

From Figure 53 to Figure 55, it is evident that all the statistics explored for the spindle power recording show stability and does not seem to be affected by the changing grinding wheel diameter. The values for three different regimes differ in magnitude but this is expected considering the difference in aggression for the grinding cuts. A high spindle power is expected for the higher aggression values considering the increased material removal rate and vice versa. Error bars given in the mean values calculated for the spindle power shows the range for the mean value (maximum and minimum) for each grinding cut dataset evaluated. Evaluating the standard deviation of the 5 sample of repeats for each grinding regime gives 0.02, 0.01 and 0.04 for finishing, semi-finishing and roughing regimes respectively. Evaluating the standard deviation of the 5 samples of repeats for each grinding regime gives values of 0.02, 0.01, and 0.04 kW for the finishing, semi-finishing, and roughing regimes, respectively. When expressed as a percentage of the mean spindle power, these standard deviations provide insights into the consistency of the grinding power. For the finishing regime, with an average spindle power of approximately 0.7 kW, the standard deviation represents approximately 2.86%. In the semi-finishing regime, with an average spindle power of around 1.7 kW, the standard deviation corresponds to about 0.59%. In the roughing regime, where the average spindle power is around 2.75 kW, the standard deviation accounts for roughly 1.45%. These percentages indicate that the semi-finishing regime exhibits the most consistent spindle power, followed by the roughing regime, with the finishing regime showing the highest variability. These variation levels are very low numbers in comparison to overall mean of the spindle power suggesting that the grinding repeat cuts have been very stable in general even with reduction in grinding wheel radius/diameter. The RMS spindle power recordings shown in Figure 54 similar trends to the mean spindle power discussed previously. For the finishing regime, the RMS power remains around 0.7 kW with minimal variation, indicating stable power consumption during the grinding process. For the semi-finishing regime, the RMS power remains consistent around 1.7 kW, aligning well with the mean spindle power and demonstrating minimal fluctuation. The roughing regime shows the highest RMS power around 2.75 kW, consistent with the mean spindle power values, indicates relatively stable power usage despite the higher values involved. The skew of the spindle power provides information on the asymmetry of the power distribution during the grinding process. Figure 55 shows positive higher skew values which indicate a tendency for the power to have more frequent peaks, suggesting intermittent increases in load. In the finishing regime, the skew values hover around 4 to 5, indicating moderate asymmetry and the potential for occasional power spikes.

For the semi-finishing regime, the skew values are slightly lower, around 3.5 to 4, suggesting a more symmetric and stable power distribution. This low skew complements the minimal standard deviation in the mean and RMS power, confirming the consistency and control of the grinding process. The roughing regime exhibits the lowest skew values, around 2.5 to 3, indicating the most symmetric power distribution with fewer power spikes. Despite the higher mean and RMS power, the low skew suggests that the roughing regime maintains a relatively stable power profile without significant intermittent increases, ensuring a more controlled grinding process.

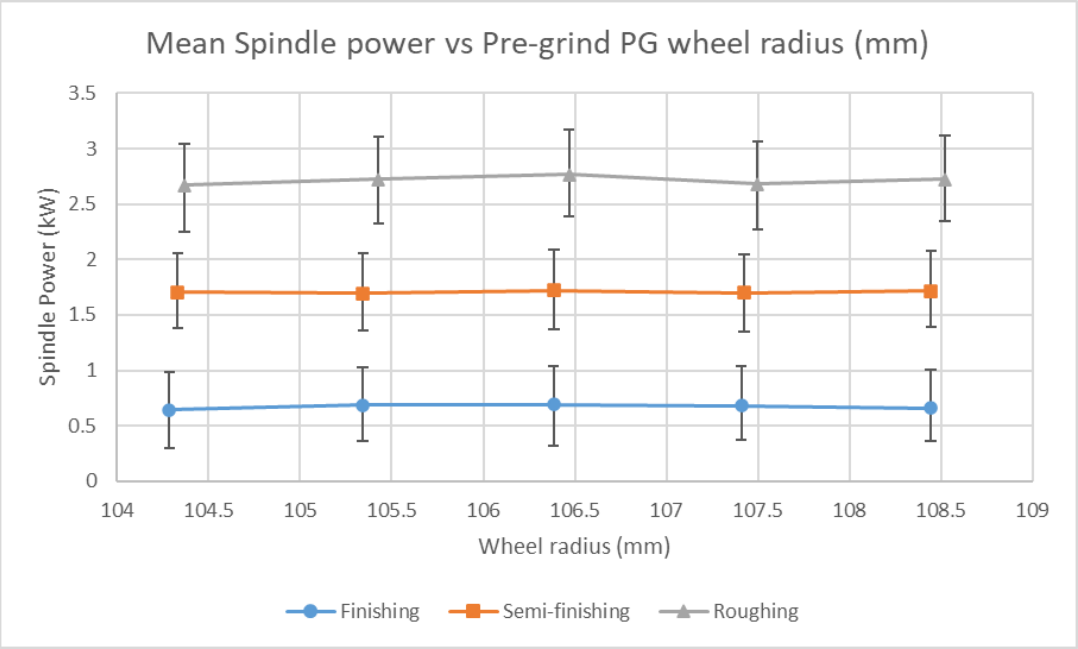

Figure 53 Mean of spindle power recording for the 5 repeats of grinding cuts conducted for the 3 grinding regimes. The error bar indicates the maximum and minimum power during a grinding cut that is recorded.

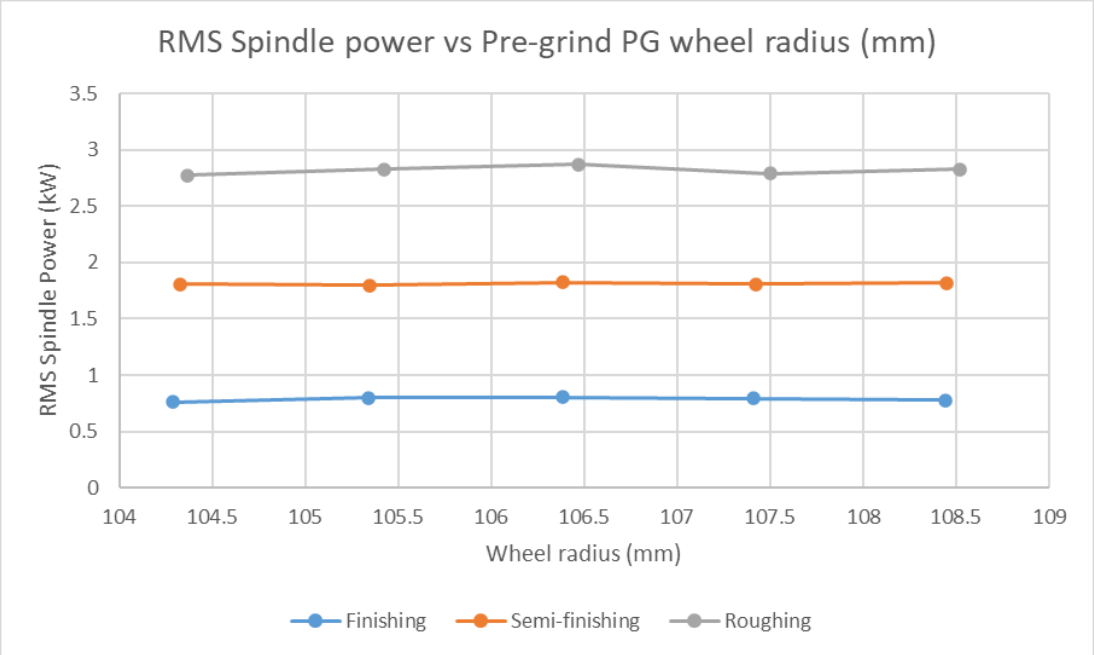

Figure 54 RMS of spindle power recording for the 5 repeats of grinding cuts conducted for the 3 grinding regimes

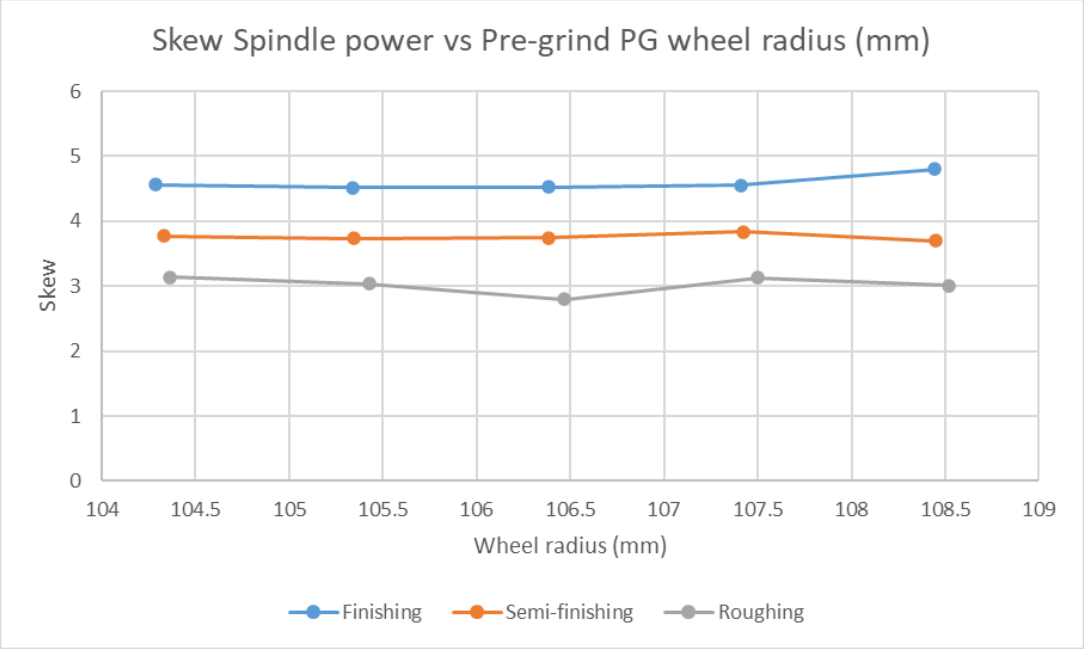

Figure 55 Skew of spindle power recording for the 5 repeats of grinding cuts conducted for the 3 grinding regimes.

4.5 Validation of grinding force and power results

The measurement taken for grinding force and power can be compared to understand their relationships.

Equation 4 in section 2.1.2 showed the relationship between tangential force and grinding power. This equation is used to see if there are differences in the measurement by comparing the two measurement approaches to evaluate grinding power.

Table 9 Grinding power evaluation using two measurement approaches to compare results

Trial	Type	Grinding Power calculated using Equation 4 (kW)	Net grinding power measured (kW)	% Difference in grinding power ((calculated – measured)/measured) (%)
010	Finishing	0.65	0.66	-1.60
020	Finishing	0.64	0.68	-5.42
030	Finishing	0.66	0.69	-4.87
040	Finishing	0.66	0.69	-3.63
050	Finishing	0.75	0.64	16.22
060	Semi-finishing	1.38	1.72	-19.51
070	Semi-finishing	1.44	1.70	-15.35
080	Semi-finishing	1.44	1.72	-16.20
090	Semi-finishing	1.43	1.70	-15.63
100	Semi-finishing	1.43	1.71	-15.96
110	Roughing	2.09	2.72	-23.09
120	Roughing	2.10	2.68	-21.81
130	Roughing	2.11	2.77	-23.67
140	Roughing	2.11	2.73	-22.61
150	Roughing	2.09	2.67	-21.87

From Table 9, it is evident there is a greater difference between the two measurement approaches for semi-finishing and roughing grinding regimes. When comparing against the physical methods of testing it can be apparent that there is increased noise factors that contribute to the measurement of grinding force compared to grinding power. In grinding operations, vibrations and oscillations can arise from multiple sources, including the machine structure, spindle bearings, and interactions between the wheel and the workpiece. Mechanical vibrations alter the normal and tangential forces acting on the wheel-workpiece interface. These fluctuations directly impact the measured grinding forces, introducing noise into the

grinding power calculation based on force measurements. Vibrations can cause periodic variations in force that are not captured in the average spindle power measurement, which integrates power over time and is less sensitive to high-frequency oscillations. Another noise factor that contributes to the difference is the dynamic force variations. As the grinding wheel engages with the workpiece, dynamic variations in force occur due to changes in contact conditions, material inhomogeneity, and wheel wear. These variations can lead to transient spikes and drops in the grinding forces. When calculating grinding power from these forces, the instantaneous changes can create a noisy signal, whereas spindle power measurement averages out these effects over time, providing a more stable reading. Another key factor that creates the difference is heat dissipation, spindle power records the energy provided to the spindle wheel to create the grinding cut but some of this heat escapes to the environment and even lost to the coolant. Some of this energy becomes friction and have a thermal effect on the workpiece and interaction between the grinding wheel and workpiece can be affected which cause fluctuations in the grinding force. This change in grinding force is recorded with the dynamometer but the energy lost through heat to the surrounding environment cannot be captured through the grinding force measurement. The calibration and sensitivity of force sensors can vary, leading to differences in the accuracy and precision of the measured forces. Force sensors can have inherent inaccuracies or drifts that introduce noise into the force measurements. It is important to note that drift and inaccuracies of the dynamometer signal has been catered for using signal processing which is discussed in seciton3.7.3. Additionally, the placement and alignment of sensors can affect the readings and within this thesis, it is considered that the workpiece fixture design and interaction should nullify the effect on this on the grinding force. Spindle power measurements, on the other hand, rely on power meters integrated into the spindle drive system, can offer more consistent and less noisy data.

Looking at the variation for grinding force it is apparent that the range of the error bars is much greater than grinding power showing less reliability in using this measurement. Investigation into the most stable grinding regime from this grinding trial, the roughing regime, will show that the percentage of error bar in relation to the mean signal is 55.7% in the horizontal grinding force measurements , 54.0 % in the vertical grinding force measurements while the percentage of error bar in relation to the grinding power signal is 14.7 %. The noise factors discussed in this section can be considered main contributors for this observation while also accepting the sensitivity of the force measurement is much greater than the power sensitivity.

The comparison of the percentage of standard deviation previously discussed (5.68%, 1.70%, and 0.49% for tangential grinding force, and 2.86%, 0.59%, and 1.45% for grinding power in the finishing, semi-finishing, and roughing regimes respectively) for the 5 repeats highlights a greater variation in the tangential grinding force measurements across all three regimes compared to the grinding power measurements. This indicates that the grinding force measurement approach is more susceptible to variations in repeated grinding cuts. Among the different grinding regimes, the finishing regime shows the most repeatable results, as evidenced by the lower percentage of standard deviation in both measurement approaches. This consistency suggests that the trends observed in the data collected from both methods can be reliably linked. For the rest of the project, it will be important to determine if similar conclusions can be drawn from the collected AE data.

4.6 Power spectral analysis of AE response: Repeatability

Power spectral analysis was conducted on the Acoustic Emission (AE) response recorded during the repeated grinding cuts across the different grinding regimes. This analysis provided an overview of the spectral distribution within the signals, enabling a high-level comparison and ensuring the repeatability of the frequency domain despite changes in grinding wheel diameter between repeats.

Initially, spectral analysis was performed separately on the different AE sensors and compared across the first trial for each of the three grinding regimes. A periodogram was used to analyse the spectral distribution of the full AE signal. The periodogram outputs a power spectral density estimate, which helps identify the dominant periods (or frequencies) within a time domain signal. This method ensures that the key frequency components of the AE signals are consistently captured and analysed, providing valuable insights into the grinding process.

For both AE sensors, as shown in Figure 56 and Figure 57, the trend of the frequency bands activated during the grinding process is similar across the finishing, semi-finishing, and roughing regimes. The power magnitude increases significantly as the grinding becomes more aggressive. This increase in power magnitude is largely due to the higher grinding forces involved and the increased number of interactions between the grinding wheel and the workpiece, which result in more pronounced acoustic emissions.

From a physics perspective, as grinding aggression increases, the contact area between the abrasive grains on the grinding wheel and the workpiece surface increases, leading to higher material removal rates. This increased contact area generates more friction and higher chances of mechanical interactions that

correlates to acoustic emission release, which in turn produce higher acoustic emissions in the same frequency regions. These emissions are captured as higher power magnitudes in the frequency spectrum.

The Mistras AE sensor exhibits a higher power magnitude compared to the Kistler AE sensor across all operational frequency bands. Several factors could contribute to this difference, including the relative distance of each sensor from the interaction point between the grinding wheel and the workpiece, the intrinsic quality and sensitivity of each AE sensor, and the amplification provided by their respective pre-amplifier systems. In this experiment, the relative distance of each sensor was kept consistent, with the sensor and workpiece fixture designed to be equidistant from the center of the grinding point. However, the orientation of the AE sensors relative to the grinding wheel direction differed. The intrinsic quality and sensitivity of each AE sensor can be a contributing factor, as both sensors operate at different frequencies with overlapping areas of the frequency domain. Despite these differences, it is noteworthy that the trends observed across the different grinding regimes are the same. The difference in signal amplification is expected given the performance characteristics of the AE sensors, as discussed in Section 4.2 during reproducibility tests.

The distance from the interaction point affects the signal strength due to attenuation, while the quality and sensitivity of the sensors influence their ability to detect and transmit acoustic signals accurately. Furthermore, differences in pre-amplifier systems can lead to variations in signal amplification and noise levels.

Given these complexities, it is challenging to pinpoint the exact reasons for the observed differences in power magnitude from these limited trials. Further investigation with controlled variables and additional trials would be necessary to isolate and understand the specific contributions of each factor to the overall sensor performance.

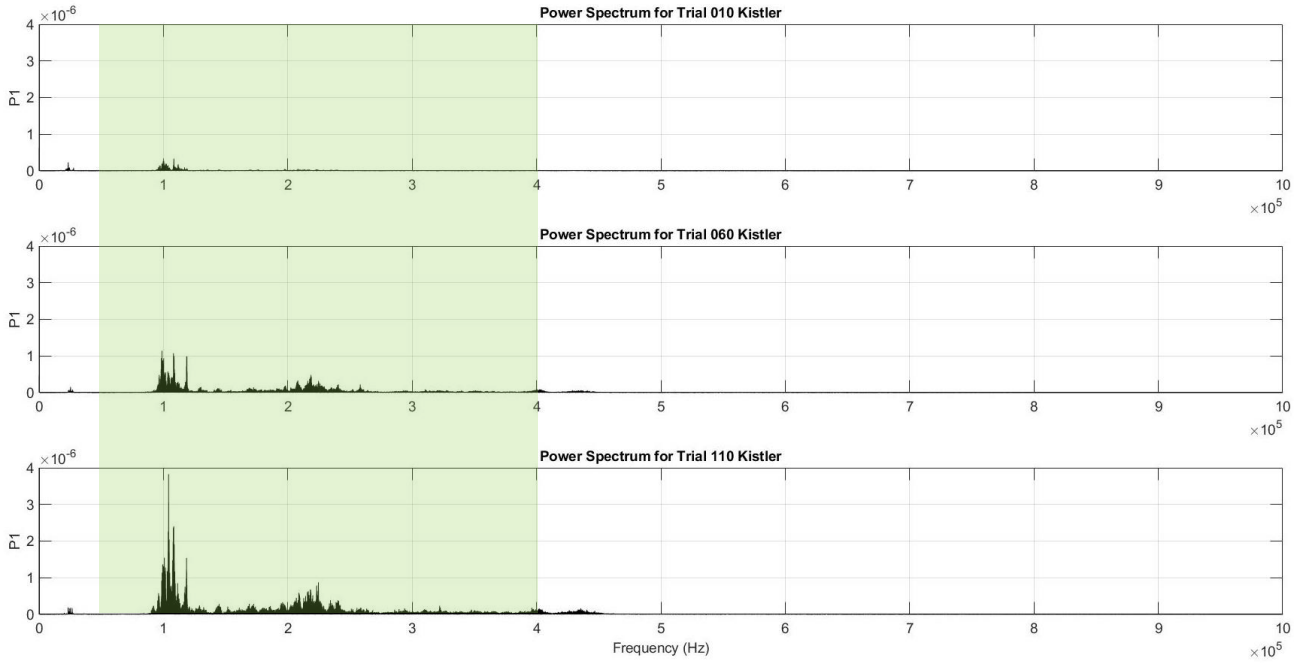

Figure 56 Power spectrum analysis for finishing grind (trial 010), semi-finishing grind (trial 060) and roughing grind (trial 110) using Kistel AE sensor data. Green shaded area shows the operating frequency range for the AE sensor.

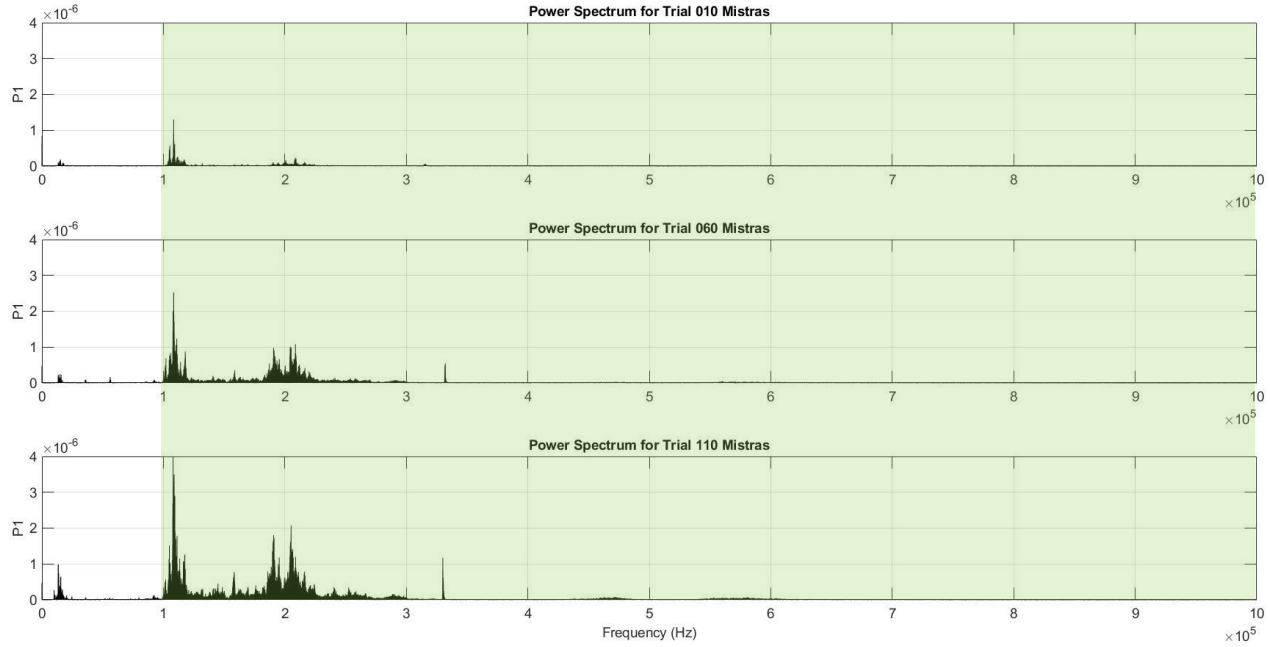

Figure 57 Power spectrum analysis for finishing grind (trial 010), semi-finishing grind (trial 060) and roughing grind (trial 110) using Mistras AE sensor data. Green shaded area shows the operating frequency range for the AE sensor.

With the Kistler AE sensor as shown in Figure 58, the trend in prominent peaks observed is consistent between the 5 trials while in the Mistas AE sensor, as shown in Figure 59, trial 040 and trial 050 which has lower grinding wheel diameter seems to have lost its power magnitude and does not follow the trend

closely. Considering the trend is observed on both AE sensors, it gives validation that the drop in acoustic emission is real especially in the frequency band of 100 – 125 kHz where the signal has been active in all grinding cuts. The grinding wheel diameter is the only measured change within the grinding mechanism and analysing the radial wheel wear (Figure 48) will show that the wheel is stable after trial 030. The grinding forces is consistent through trials 010 to 050 with a noticeable change of increased 12 % tangential force that was recorded on trial 050 while normal forces stayed stable. An increase in tangential force while the normal force remains constant generally indicates an increase in friction or shift towards less efficient material removal modes such as ploughing or rubbing. This could occur due to the wheel dulling in the process on trial 050 or increased material loading that was experienced towards the last trial. It could be the case that although the coolant supply and intermittent dressing was aimed at keeping the thermal conditions optimum and wheel surface controlled, there may have been build up that was not truly addressed before the last trial. This could have materialised to dampen the acoustic emission signals that are emitted during the last trials 040 and 050 as the material loaded and affected the interaction between the grains on the wheel and material surface. Further evaluation of the wheel surface would have been future steps to consider investigating into this hypothesis but beyond the scope of this thesis. Finishing parameters used have a low aggression this could mean that AE response could vary considerably and as previously discussed in section 4.4, there is significant variation noted during the finishing regime than the roughing regime. Low aggression values means less material being removed and hence given the lower contact length between the wheel and the material, the interactions between the abrasive grains and workpiece are less intense and can be more intermittent. This can results in the AE signals being less stable and more susceptible to variations due to minor inconsistencies in material or wheel surface. During the lead-in stage, as the wheel makes contact with the workpiece due to the low aggression levels, the grinding wheel may not maintain a constant, steady contact with the work piece. This inconsistent contact would mean that the energy released as acoustic emissions during the interaction between the grains and the workpiece surface will vary producing a signal with considerable variation. As discussed within the literature review regarding the grinding mechanisms that play a part of the grinding process, with low aggression values, a significant portion of energy would go into elastic deformation through the mechanism of rubbing and plouging [1] due to low depth of cut. Elastic deformation would generate a different acoustic emission compared to the plastic deformation during grinding and this maybe less predictable and variable as recorded within these grinding results. Finishing regime represents a lower cutting forces as recorded within the grinding force measurements, lower forces can cause the complex interaction between grains to engage and disengage more frequently

producing irregular AE signals and this can manifest itself as variability. The effect this variation in AE signal may have on repeatability can only be studied under the changes noted within exploring AE features for the different repeats.

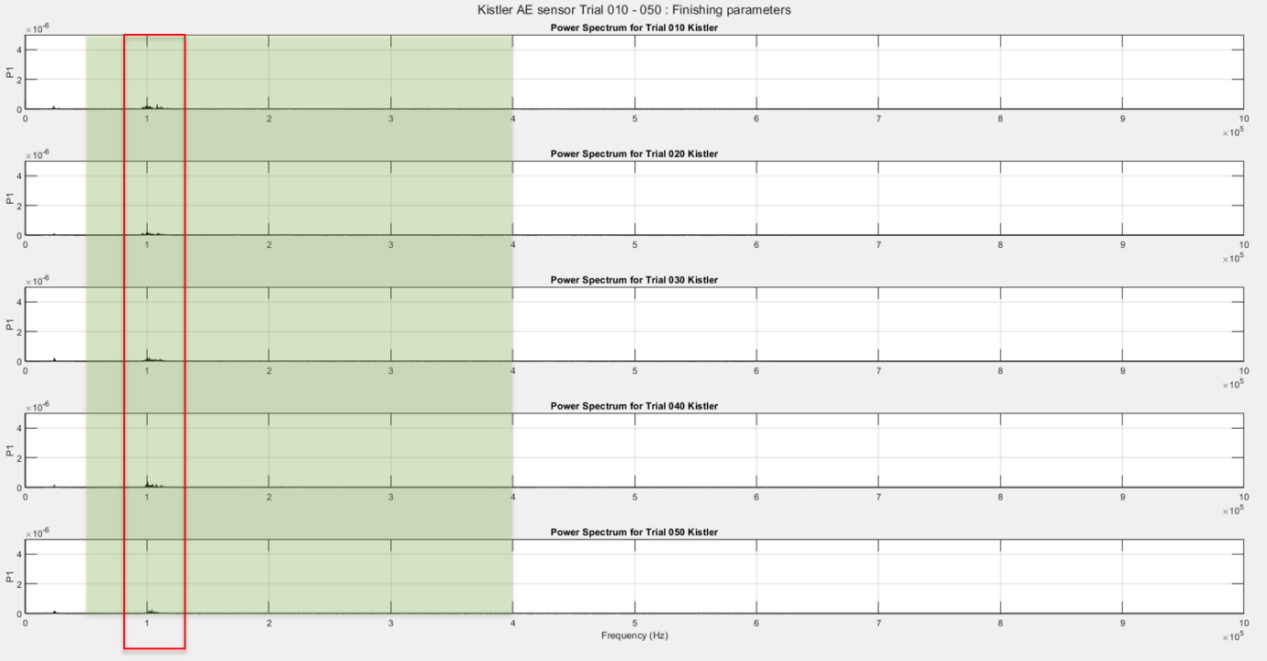

Figure 58 Kistler AE Power spectral distribution for the 5 repeats of finishing grinding regime with reducing grinding wheel diameter from trial 010 to trial 050.

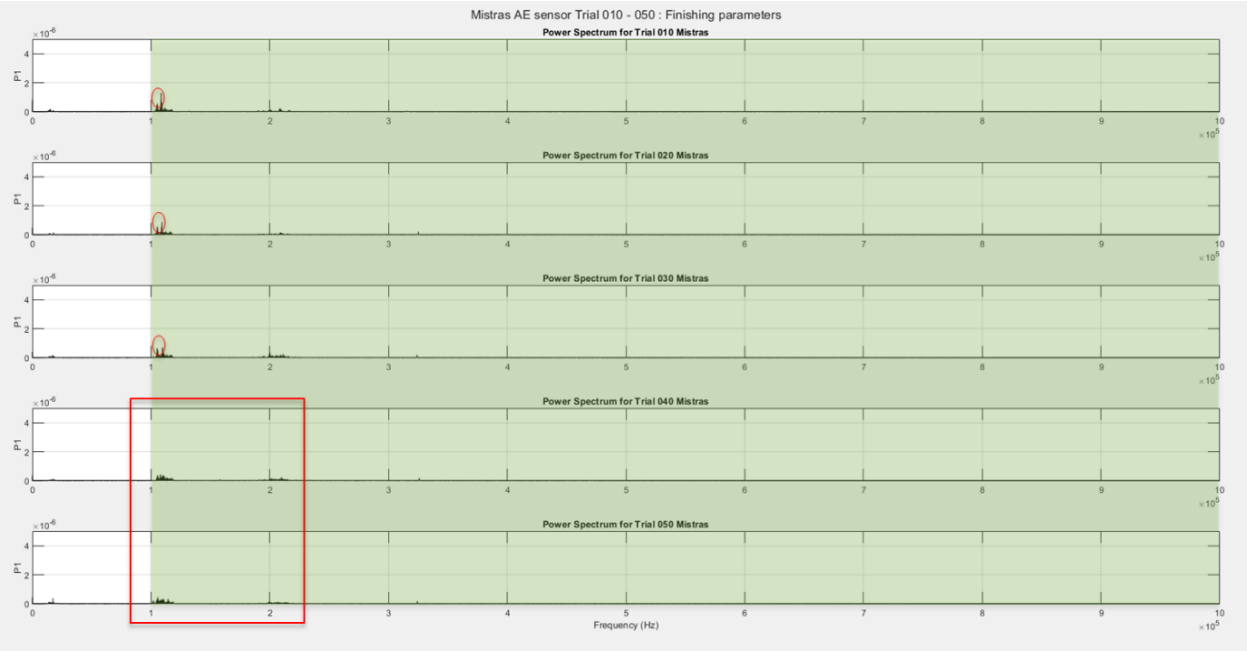

Figure 59 Mistras AE Power spectral distribution for the 5 repeats of finishing grinding regime with reducing grinding wheel diameter from trial 010 to trial 050.

The power spectral distribution within semi-finishing regime has not been consistent with the 5 repeats of changing grinding wheel diameter as shown in Figure 60 and Figure 61. The frequency bands which are activated within the 5 repeats are similar but the prominent peak behaviour differ between both AE sensors and reduction in the grinding wheel diameter. With the Kistler AE sensors, the prominent peaks are observed at 110 kHz and consistent between trial 080 and trial 100 while during trial 060 to 070 there are peaks arising at 100 kHz, 110 kHz and 120 kHz. Mistras AE sensor show consistency in the prominent peaks for trials 060 to trial 080 with peaks around 115kHz. Another interesting observation made is that the magnitude of acoustic emission power for the spectrum increases with decrease of the grinding wheel diameter which is contrary to the expectation that decrease in grinding wheel diameter would be linked with reduced contact between the wheel and the workpiece as a result reduced chance of acoustic emissions. Closer investigation against the wheel wear trace shown in Figure 48 indicates the trend of increased wheel wear with reduction in wheel diameter for the semi-finishing trials. This would give confidence in the observation made that higher wheel wear suggested evidence of greater interactions between wheel grains and workpiece which lead to higher acoustic emissions. Trial 090 is an outlier on the wheel wear graph where there is a sudden drop in wheel wear recorded, against the trend, before it picks up for trial 100. The drop in wheel wear for trial 090 also shows as a drop in the power magnitude of the AE signal across the whole frequency band that is detected in both Kistler and Mistras. Considering the observation is made on both AE sensors it can be considered real. Such a drop in wheel wear can be attributed to several factors even though these grind trials were conducted in a controlled experiment including a workpiece surface quality issue that may arise at the microstructural level at that depth of workpiece, an intermittent reduction in wheel loading that may have occurred during the dressing stage pior to the grinding cut and change in the wear pattern on the grinding wheel. Although a controlled dressing routine was implemented for the progression of wheel diameter, a post-experiment grinding wheel surface analysis would have benefitted in understanding this behaviour better.

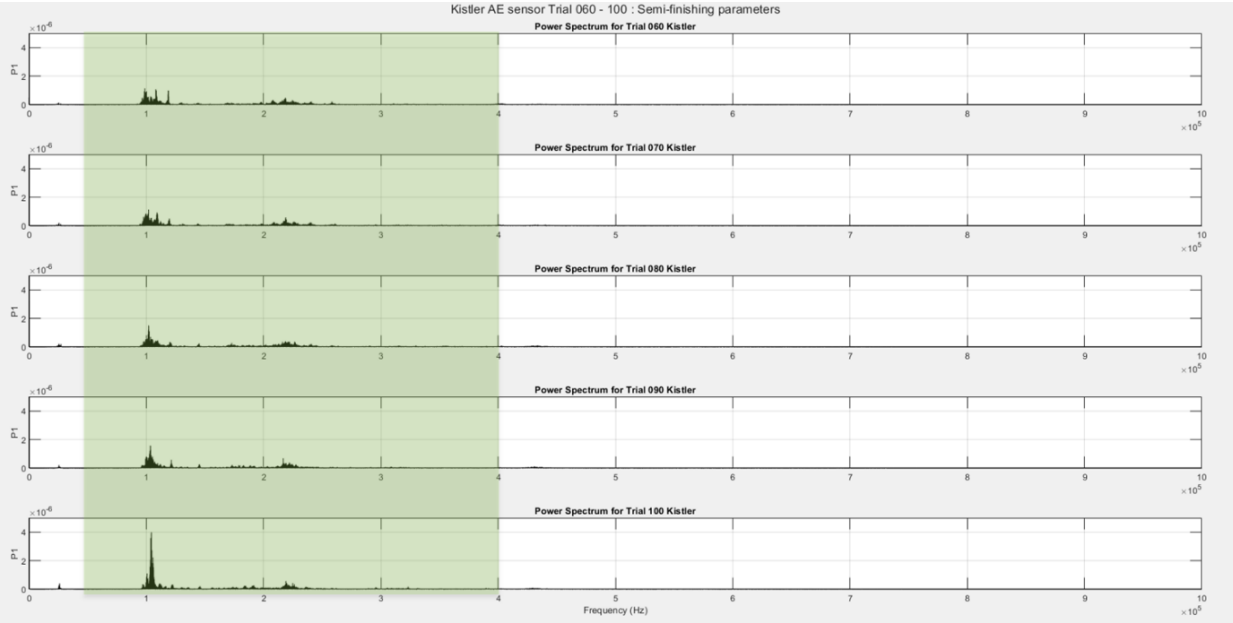

Figure 60 Kistler AE Power spectral distribution for the 5 repeats of semi-finishing grinding regime with reducing grinding wheel diameter from trial 060 to trial 100.

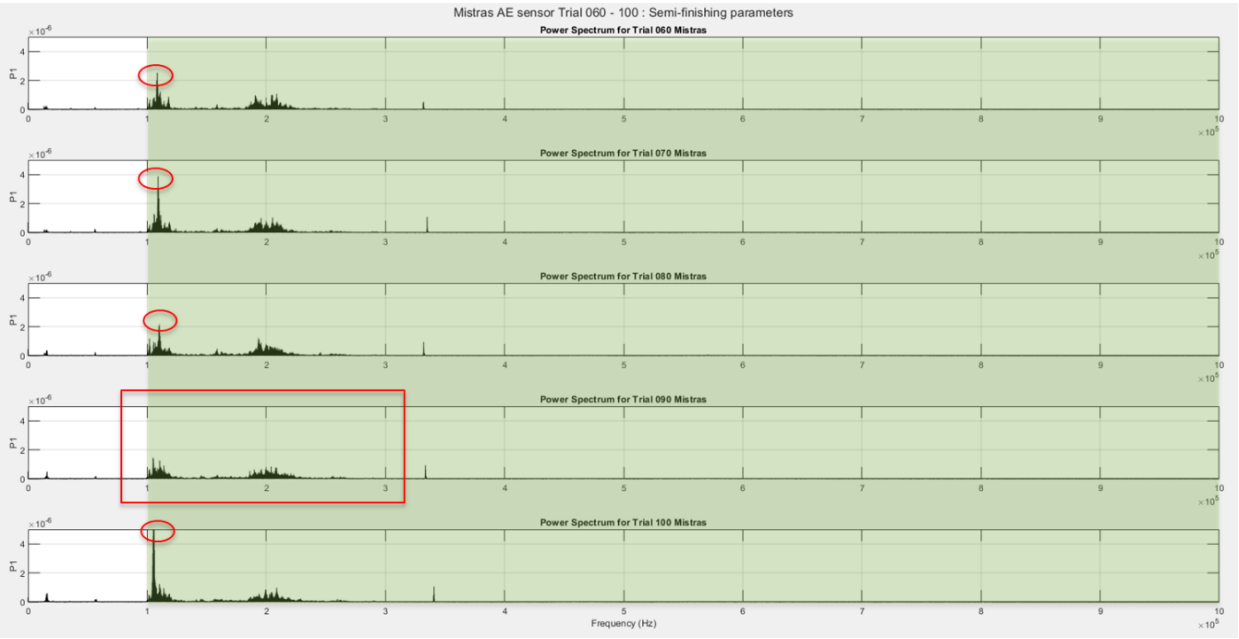

Figure 61 Mistras AE Power spectral distribution for the 5 repeats of semi-finishing grinding regime with reducing grinding wheel diameter from trial 060 to trial 100.

Figure 62 and Figure 63 shows how the spectral distribution changes for the 5 repeats of roughing regime. Previous discussion within grinding force (4.4.1) and grinding power(4.4.2) has shown how roughing regime trials gave stable signal with less variation compared to the rest of the grinding regimes investigated within this thesis. These spectral distribution show how the trends are also reflected within

the roughing regime with the consistency and repeatability in the frequency bands that are activated. Kistler AE sensor show a consistent trend with all trials where the prominent peaks (around 105 kHz) are consistent for the 5 repeats and the activated frequency bands are consistent between 100 – 120 kHz. The higher sensitive Mistras show more details within the prominent peaks, from Figure 63, it is evident how prominent peaks shown in trials 100 – 130 changes within trials 140 – 150. This change in prominent peaks have been marked by red boxed noted as (a) at 105 kHz and (b) at 110 kHz. Within boxed region (b), it is evident that the prominent peak in (a) still exists as a peak but with lower power magnitude and this may not have a big effect in understanding the repeatability of the AE response. To understand the impact of changes in prominent peaks, further investigation into the AE features analysis is necessary. This will help determine how much variation these changes may introduce in the output for fault diagnosis or process monitoring in the future. From, the analysis of all the different repeats, it is safe to conclude that the power spectral analysis does show consistency within the frequency bands activated during a grinding cut and therefore renders the experiment repeatable with further work using AE features required to understand how useful the AE response could be for process monitoring.

In summary, the power spectral analysis of the AE response for the different grinding regimes demonstrates consistent trends in frequency bands activated during grinding. However, variations in power magnitude between the Kistler and Mistras AE sensors suggest the need for further investigation into sensor performance characteristics. The repeatability of AE signals for the 5 repeats of grinding trials under different regimes is validated, with the finishing regime showing the most variation due to lower aggression values. Future discussion in this thesis should focus on the detailed AE features analysis to enhance fault diagnosis and process monitoring capabilities based on these findings.

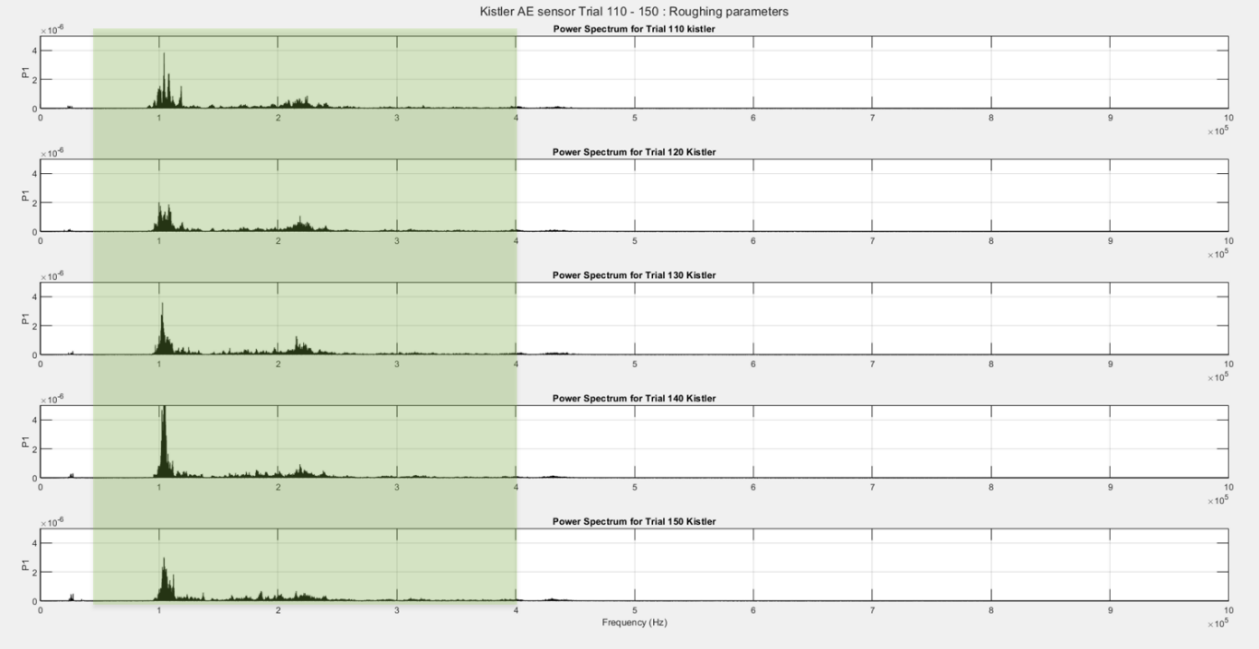

Figure 62 Kistler AE Power spectral distribution for the 5 repeats of roughing grinding regime with reducing grinding wheel diameter from trial 100 to trial 140.

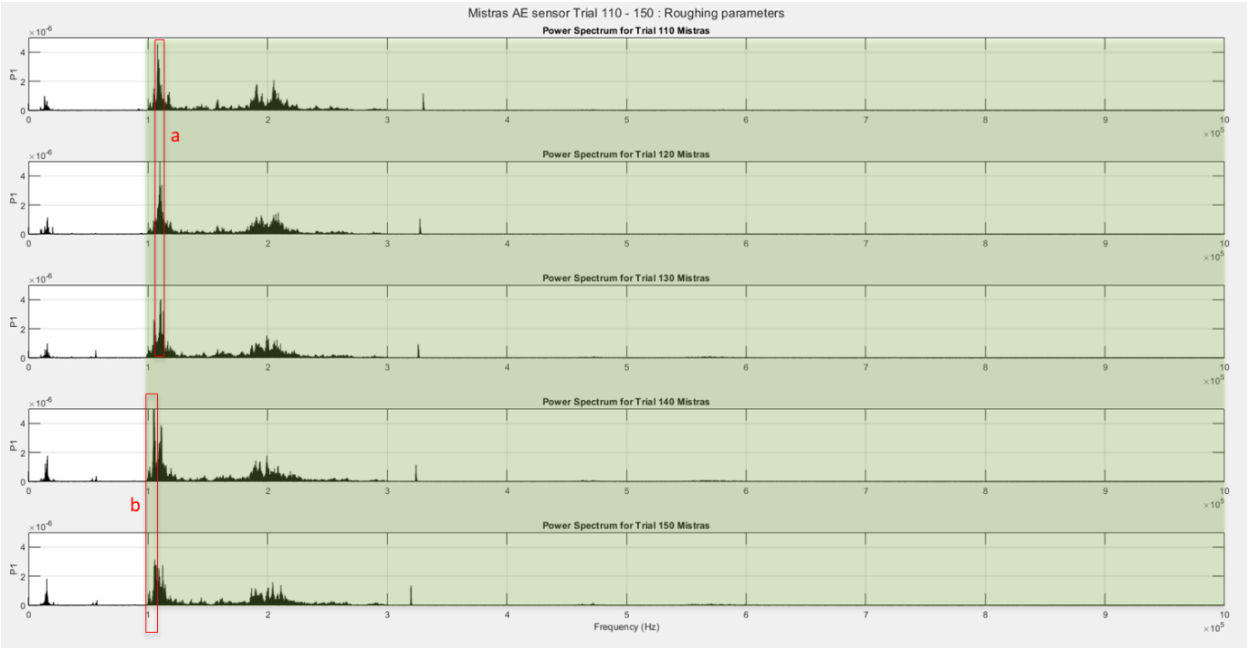

Figure 63 Mistras AE Power spectral distribution for the 5 repeats of roughing grinding regime with reducing grinding wheel diameter from trial 100 to trial 140.

4.7 Spectral Coherence and Cross spectral density of AE response: AE repeatability

Spectral coherence gives the detail in frequencies at which two signals most strongly covary using a linear model. For a spectral coherence graph, the value closer to 1 means there is high coherence between the two signals and vice versa. For the data gathered from both AE sensors, spectral coherence analysis has been compared using the first trial on each grinding regime comparing each other.

From Figure 64, it is evident that with Kistler AE sensor data, all signals show a steady value along all frequency bands above 0.5 and varying closer to 1. Therefore, it can be noted that the signals between all three grinding types have coherence. This gives more confidence that the AE response from different grinding regimes is reliable and are similar even with the different magnitude seen in power spectral analysis. The same trend can be noticed for Figure 65 which shows the Mistras AE sensor data.

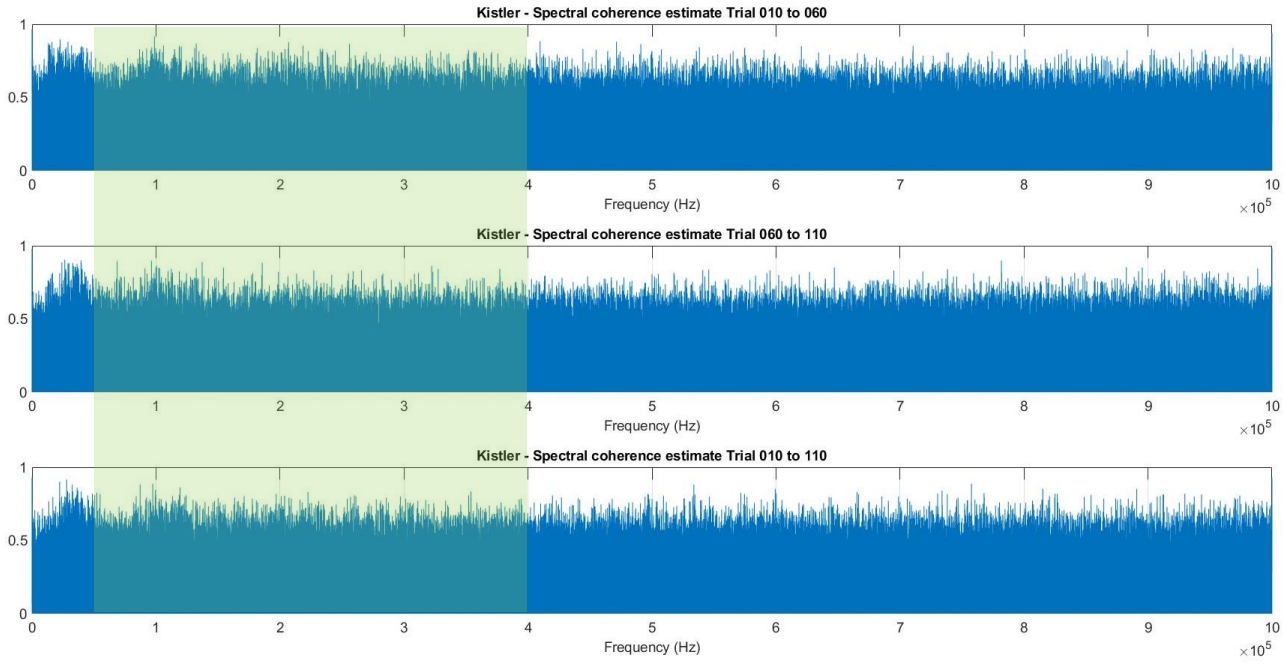

Figure 64 Spectral coherence estimate between pairs of the first grinding trial on each grinding regime using Kistler AE sensor data.

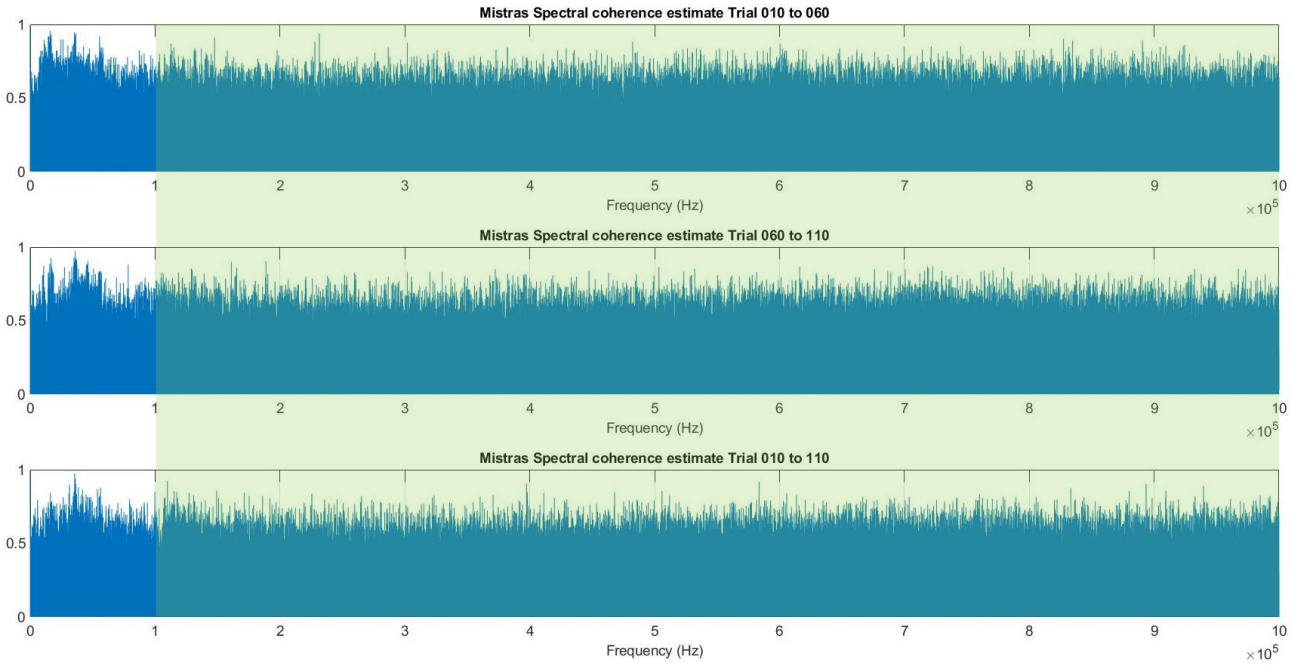

Figure 65 Spectral coherence estimate between pairs of the first grinding trial on each grinding regime using Mistras AE sensor data.

Another aspect of spectral analysis is including a cross spectral density (CSD) which shows the distribution of power for a pair of signal and it can determine the influence of signal in relation to another. Same analysis approach of comparing the first trial data from each grinding regime is used. Figure 66 and Figure 67 shows that the shapes of the CSD graph for each comparison are alike and therefore the pairs investigated in each graph have similar power distribution and related/statistically connected. The CSD analysis gives further assurance to the consistency in the activation of frequency bands noted in spectral analysis.

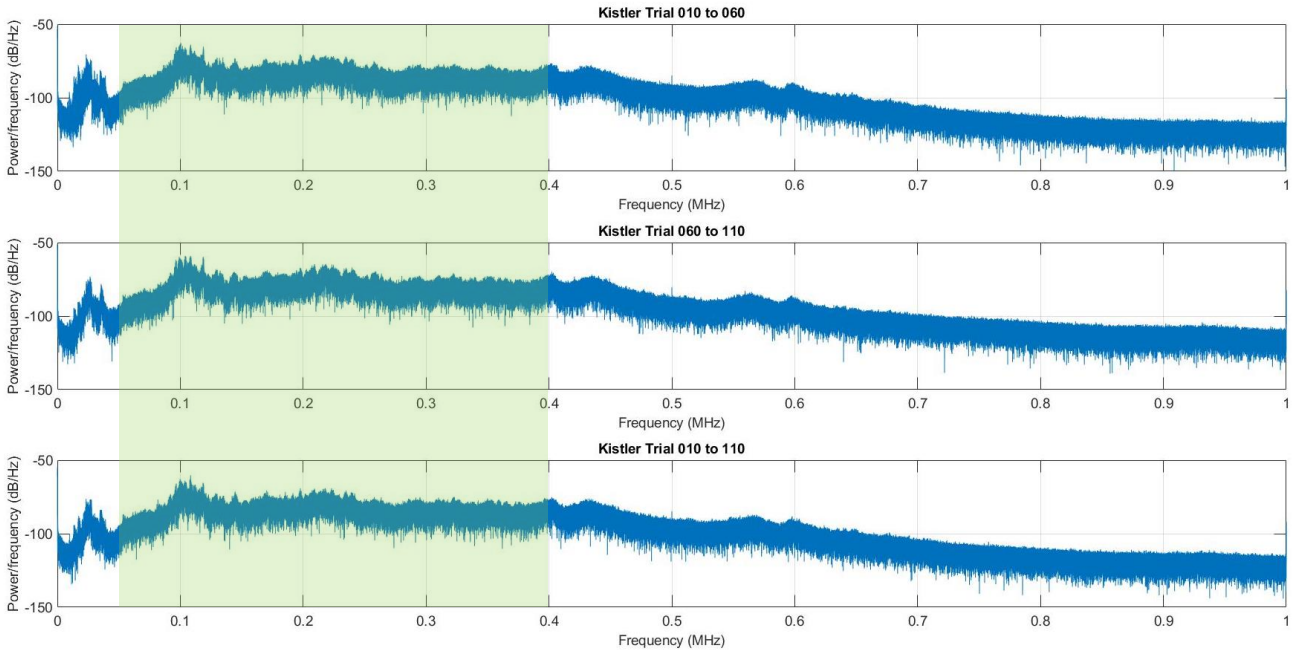

Figure 66 Cross power spectral density between pairs of the first grinding trial on each grinding regime using Kistler AE sensor data

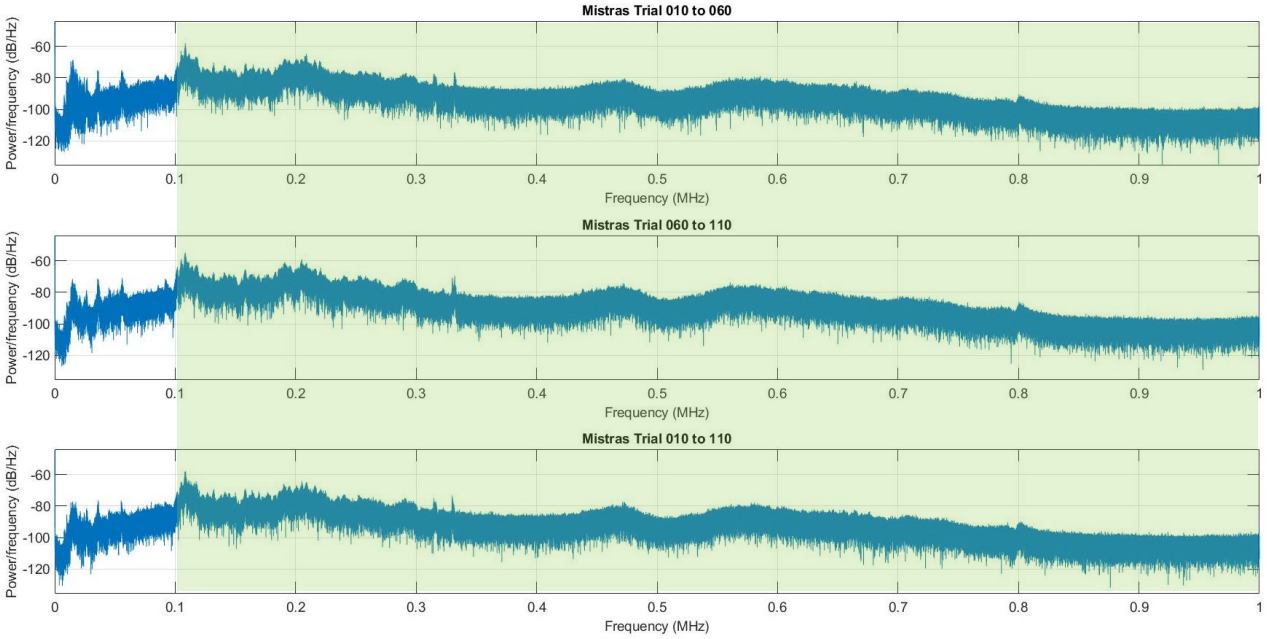

Figure 67 Cross power spectral density between pairs of the first grinding trial on each grinding regime using Mistras AE sensor data

4.8 Trends in AE features with roughing, semi-finishing and finishing parameters

This chapter delved into the analysis of Acoustic Emission (AE) features, as explored in the literature review, to understand their behavior across different grinding regimes: roughing, semi-finishing, and finishing. The primary objective was to investigate how these AE features were influenced by repeated grinding cuts and varying grinding wheel diameters. By examining data from both AE sensors, comparisons of the AE features across all three grinding regimes were made to assess their repeatability. This analysis was crucial for identifying the extent to which changes in wheel diameter impacted the AE features, thereby affecting the consistency and reliability of the grinding process. The AE features analyzed in this section included AE RMS, Skew, MVD, CFAR, and ROP. Understanding the trends in these AE features provided valuable insights into the grinding process and its stability under varying operational parameters

From Figure 68 and Figure 69, it is apparent that the average AE RMS value remains relatively constant, with minimal fluctuation, as the wheel radius changes and repeats are conducted. This consistency indicates good repeatability for this AE feature across the different grinding regimes. The different magnitudes observed between the grinding regimes are expected, as similar trends were noted with grinding force and spindle power measurements.

The AE RMS magnitude is higher in the roughing regime compared to the semi-finishing and finishing regimes. This increase in magnitude is due to the higher aggression values associated with roughing, which involves higher depth of cut and increased material removal rates. These conditions lead to more interactions due to the increased contact area between the wheel and the workpiece with increased depth of cut and intense interactions between the grinding wheel grains and the workpiece, generating stronger higher amplitude acoustic emissions. The increased grinding forces are also an effect of more aggressive grinding regimes, increased tangential force indicates the increase in friction between the grinding wheel and workpiece. Increased friction generates heat and stress waves, both of which can contribute to higher AE levels. Greater grinding forces result in higher localized stresses and strain within the workpiece material which propagates plastic deformation within the workpiece which all leads to increase AE signals. The semi-finishing and finishing regimes show lower AE RMS values, reflecting the less aggressive grinding conditions and lower material removal rates. In these regimes, the interactions between the abrasive grains and the workpiece are less intense, resulting in lower acoustic emission signals.

Both the Kistler and Mistras AE sensors exhibit similar trends in AE RMS values across the different grinding regimes, which enhances confidence in the repeatability and reliability of using this AE feature

for fault diagnosis and process monitoring. The consistency between the two sensors also suggests that the observed AE RMS values are robust and not significantly influenced by sensor-specific characteristics.

In summary, the analysis of AE RMS values from both sensors across the different grinding regimes demonstrates the feature's repeatability and its correlation with grinding aggression levels. This makes AE RMS a valuable tool for future applications in fault diagnosis and process monitoring.

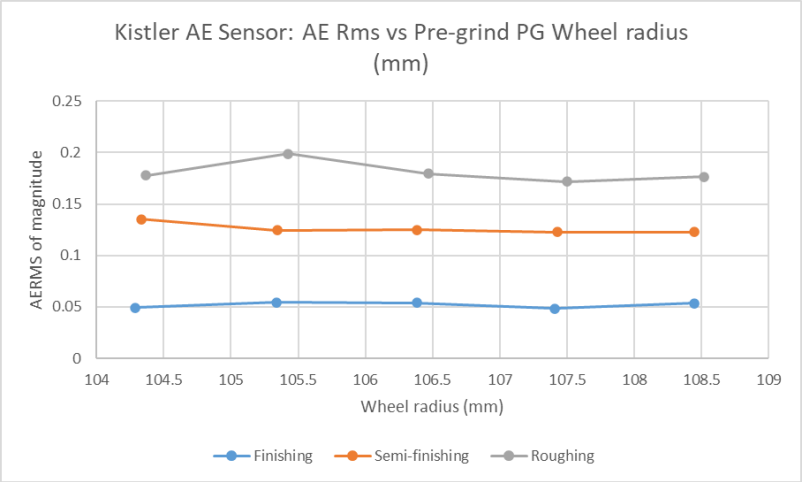

Figure 68 AE RMS graph for Kistler AE sensor for the three grinding regimes and 5 repeats with changing grinding wheel diameter

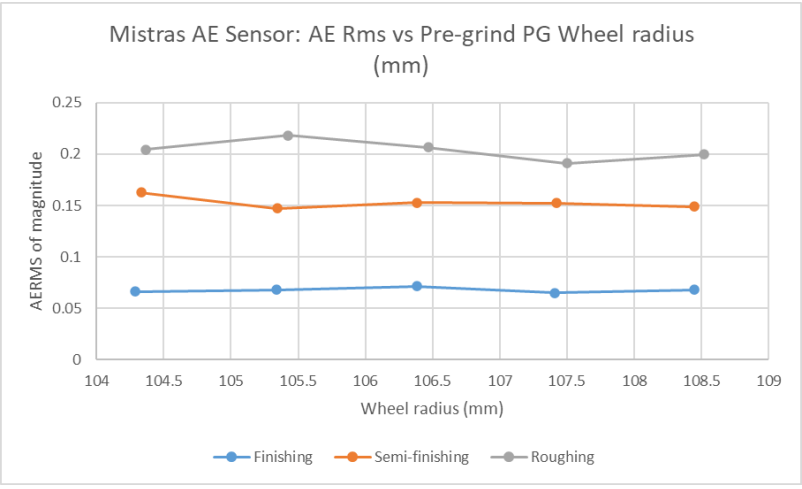

Figure 69 AE RMS graph for Mistras AE sensor for the three grinding regimes and 5 repeats with changing grinding wheel diameter

Skew is a statistical measure that indicates the asymmetry of the probability distribution of the AE signal data set, providing insights into the 'tail' behavior of the data relative to its mean. From Figure 70 and Figure 71, the results exhibit a consistent pattern for roughing and semi-finishing grinds, with relatively

stable skew values. However, for the finishing grind, there is a noticeable increase in skew as the grinding wheel diameter increases.

The increased skew in the finishing grind can be attributed to the lower magnitude of AE response in this regime. The finishing grind operates at lower aggression values, resulting in less material removal and lower overall acoustic emissions. Because the AE signals are weaker, any minor variations or noise in the signal can significantly affect the skew value, making it more sensitive and less repeatable compared to higher aggression grinds.

Additionally, the increased skew in the finishing grind may be influenced by the more intermittent contact between the grinding wheel and the workpiece. At lower depths of cut, the interactions between abrasive grains and the workpiece are less consistent, leading to sporadic spikes in the AE signal that contribute to a higher skew. This behavior is reflected in both the Kistler and Mistras AE sensors, with the Mistras sensor showing a more pronounced increase in skew as the wheel radius increases. Another noteworthy observation in the finishing regime is that the skew values are positive for larger grinding wheel diameters but shift towards the negative as the grinding wheel diameter decreases. Focusing on the grinding trials for the finishing regime, it appears that the grinding mechanism stabilizes as the wheel diameter reduces. This stabilization is evident from the consistent wheel wear observed and aligns with previous observations in the power spectral distribution. The reduction in material loading and the dulling of the wheel could have resulted in the dampening of acoustic emissions, thereby producing a more symmetrical AE signal as the instantaneous peak of signals are not generated to cause the asymmetry in signal data.

In summary, the skew of the AE signal is a valuable feature for characterizing the grinding process, particularly for roughing and semi-finishing grinds. However, its sensitivity to lower magnitude AE responses in finishing grinds indicates that it may be less reliable under these conditions. This analysis underscores the importance of considering the grinding regime and associated aggression values when utilizing skew as a diagnostic feature in process monitoring.

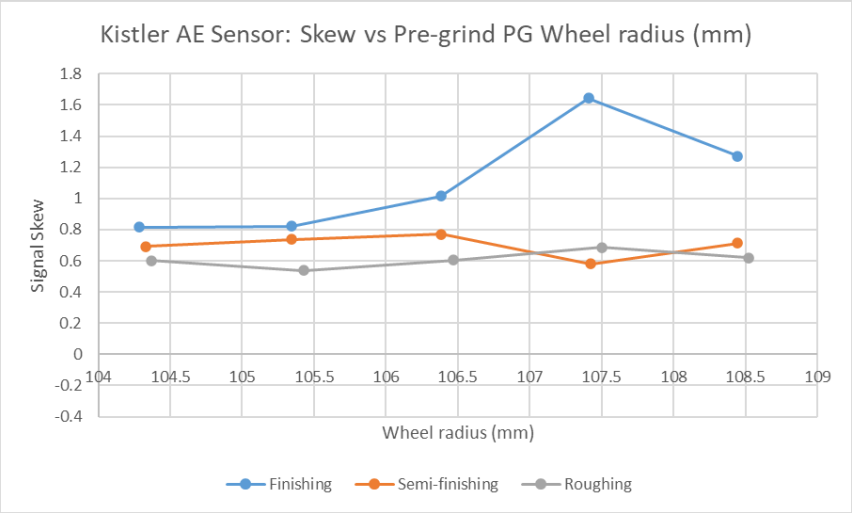

Figure 70 AE signal skew for Kistler AE sensor for the three grinding regimes and 5 repeats with changing grinding wheel diameter

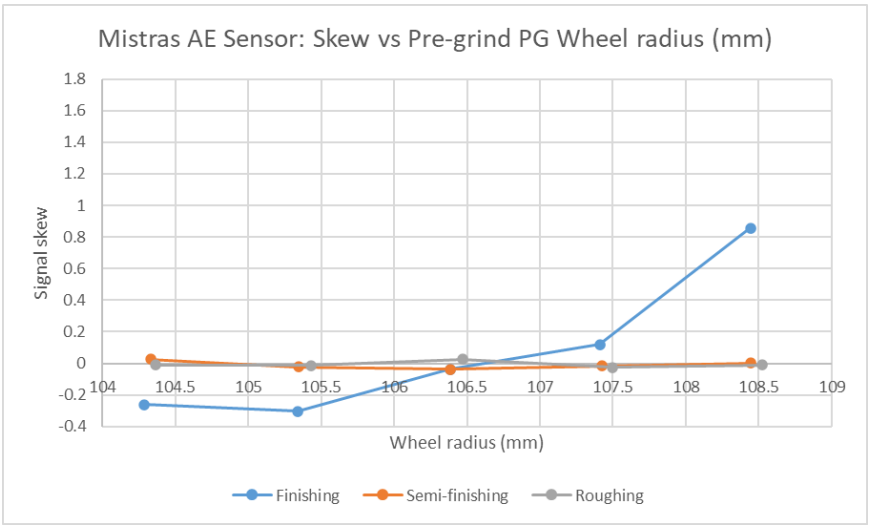

Figure 71 AE signal skew for Mistras AE sensor for the three grinding regimes and 5 repeats with changing grinding wheel diameter

MVD shows how dispersed the signal is from the mean value for a signal. Figure 72 which looks at the Kistler AE sensor data shows the MVD values for the roughing and semi-finishing regimes remain relatively stable across different wheel diameters, fluctuating slightly around a mean value. Figure 73 which looks at Mistras AE sensor show the MVD values for the roughing and semi-finishing regimes show minimal variation, indicating consistent AE signal characteristics. The MVD values for the finishing regime show slight fluctuation but generally remains consistent across wheel diameters on the Kistler AE sensors but exhibit more noticeable variation, with a peak around wheel radius of 105.5 mm, before stabilising on the Mistras AE sensor.

The observed stability in MVD values for the roughing and semi-finishing regimes suggests high repeatability of the AE feature under these grinding conditions. This can be attributed to the higher aggression values in these regimes, which result in more consistent material removal and interaction between the grinding wheel and the workpiece. The higher aggression levels ensure that the AE signals generated are robust and less susceptible to minor variations in the grinding process, leading to stable MVD values.

For the finishing regime, the variation in MVD, particularly observed in the Mistras AE sensor, can be explained by the lower aggression values characteristic of this regime. The finishing grind involves less material removal and lower forces, making the AE signals more sensitive to minor inconsistencies and noise. This sensitivity can lead to greater variability in the MVD values, as small changes in the grinding conditions or wheel surface condition including wheel loading can have a more pronounced effect on the AE signals.

The peak in MVD observed in the finishing regime with the Mistras AE sensor around a wheel radius of 105.5 mm may indicate a transitional phase in the grinding process, where the wheel's interaction with the workpiece undergoes subtle changes. This could be due to slight variations in wheel wear pattern or changes in the workpiece material properties at this specific depth of the workpiece which can have an effect in the deformation and grinding mechanisms witnessed on the contact length. Unfortunately, the investigation into wheel wear does not show the influence of irregular wear patterns unless the wheel surface was investigated, but this is beyond the scope of this thesis. As the wheel diameter continues to decrease, the process stabilizes during the finishing regime, and the MVD values return to a more consistent level.

The MVD of AE signals demonstrates high repeatability for the roughing and semi-finishing grinding regimes, with stable values across different wheel diameters. In the finishing regime, the MVD values show more variability, reflecting the sensitivity of AE signals to lower aggression grinding conditions but does not show any trend that is affected by the grinding wheel diameter change. These observations underscore the importance of considering grinding parameters and wheel condition when using AE features like MVD for process monitoring and fault diagnosis.

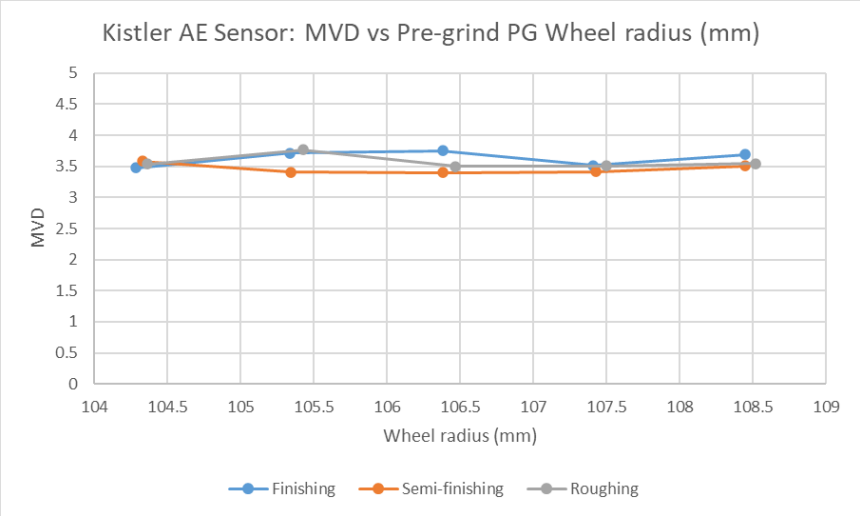

Figure 72 AE signal MVD for Kistler AE sensor for the three grinding regimes and 5 repeats with changing grinding wheel diameter

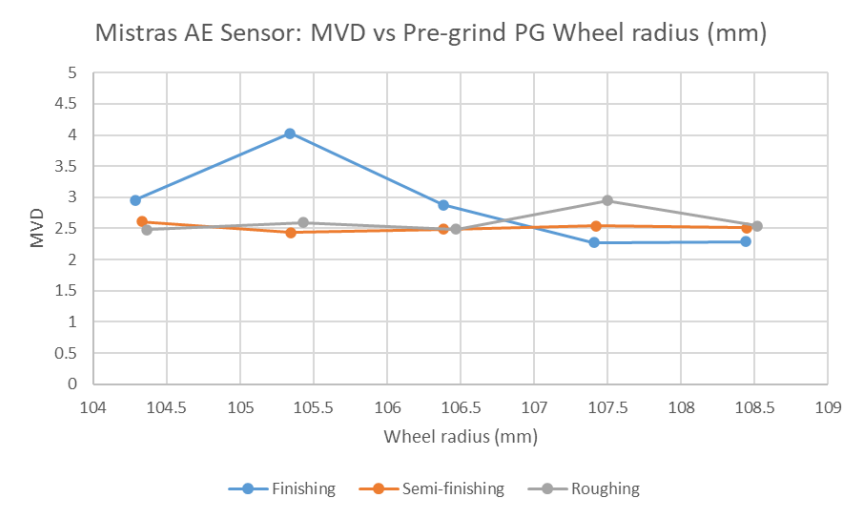

Figure 73 AE signal MVD for Mistras AE sensor for the three grinding regimes and 5 repeats with changing grinding wheel diameter

CFAR is a feature which picks out the number of events occurring in an AE signal. From Figure 74, it is evident for the Kistler AE sensor the CFAR values for all three grinding regimes exhibit minimal fluctuation as the grinding wheel diameter decreases. This indicates a high degree of repeatability in the AE feature across different trials. From Figure 75, it is evident for Mistras AE sensors the CFAR values remain consistent across different grinding wheel diameters, reinforcing the repeatability of this AE feature. Both sensors show a clear separation in CFAR values between the different grinding regimes. The roughing regime consistently shows the highest CFAR values, followed by the semi-finishing and finishing regimes. Across both sensors, the roughing regime has the highest CFAR values, indicating a greater number of AE

events during this grinding process. The CFAR values for the semi-finishing and finishing regimes show minimal variation, suggesting that the AE event frequency is stable under these grinding conditions.

The minimal fluctuation in CFAR values across different grinding wheel diameters for all three regimes indicates that this AE feature is highly repeatable and not correlated to a trend with changing grinding wheel diameter. This stability can be attributed to the controlled grinding parameters and consistent material removal processes during the grinding trials. The repeatability of CFAR is crucial for reliable fault diagnosis and process monitoring, as it reflects the frequency of AE events, which are indicative of interactions between the grinding wheel and the workpiece.

The higher CFAR values in the roughing regime can be explained by the increased material removal rates and more aggressive grinding conditions. These factors lead to more intense interactions between the abrasive grains and the workpiece, resulting in a higher frequency of AE events. This is consistent with the observed trends in other AE features, where the roughing regime typically exhibits higher magnitudes due to the greater forces and energy involved.

The clear separation in CFAR values between the different grinding regimes suggests that this feature can effectively differentiate between various grinding conditions. The semi-finishing and finishing regimes have lower CFAR values, reflecting the less aggressive nature of these processes. The consistent CFAR values in these regimes indicate stable grinding conditions with fewer AE events, likely due to the lower depth of cut and reduced material removal rates.

The slight peak in CFAR values around a wheel radius of 105.5 mm in both sensors for the roughing regime could be indicative of transitional effects in the grinding process. This may result from changes in wheel wear dynamics or slight variations in the workpiece material properties at this specific depth. Further investigation of wheel surface quality at this point of the investigation would have given further indication of this slight variation but currently this change in CFAR is correlated with the prominent peak change noted under the roughing regime as discussed in 4.6. As previously discussed, there is a shift in the prominent peak from 110 kHz to 105 kHz, which coincides with an increase in wheel wear. This observation correlates with the acoustic emission (AE) data but is independent of any trend related to the change in wheel diameter. Increased wheel wear suggests that the abrasive grains become dull, and the vitrified bond material starts interacting more with the workpiece. The dull grains and vitrified bond create more friction, making the grains less effective at cutting. Consequently, ploughing and rubbing

interactions increase, which can cause a rise in AE at different frequencies as the interactions between the wheel and the workpiece change.

Additionally, increased wheel wear implies a higher likelihood of grain breakage due to the open structure of the grinding wheel. This grain breakage contributes to changes in the AE signal pattern, as recognized in the spectral distribution and CFAR analysis. As the wheel diameter continues to decrease, the process stabilizes, and CFAR values return to consistent levels.

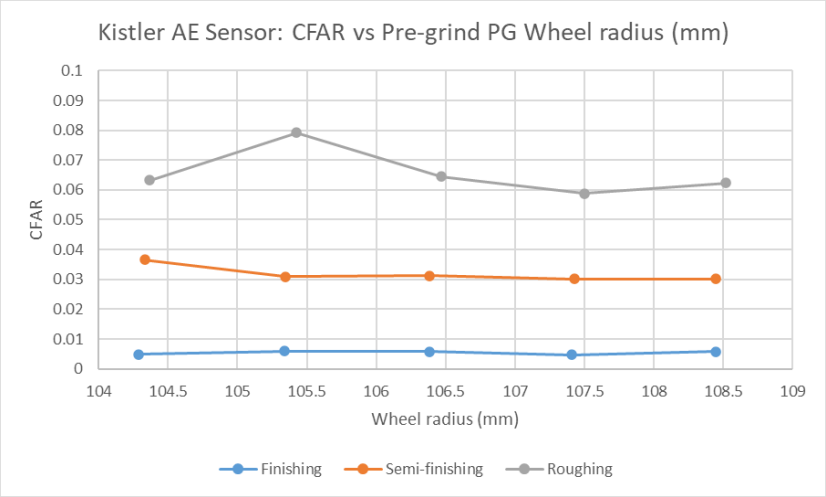

Figure 74 AE signal CFAR for Kistler and Mistras AE sensor for the three grinding regimes and 5 repeats with changing grinding wheel diameter

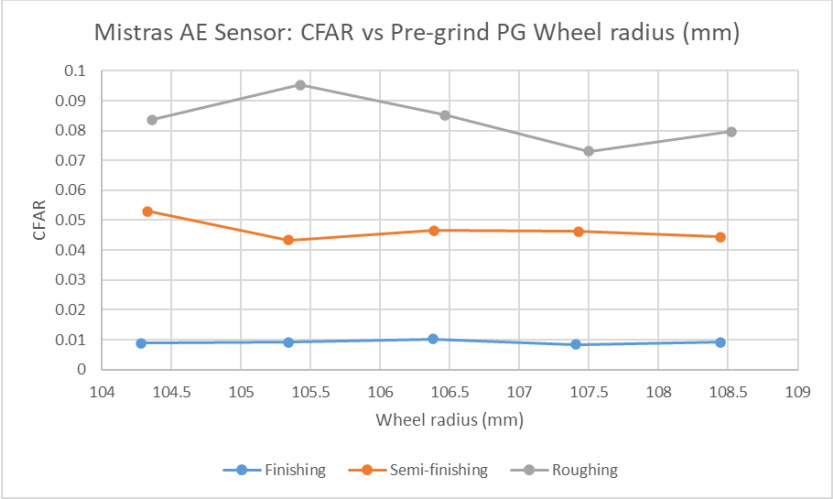

Figure 75 AE signal CFAR for Mistras AE sensor for the three grinding regimes and 5 repeats with changing grinding wheel diameter

The most prominent ROP frequency bands are in the 100–150 kHz range across all grinding regimes (Figure 76 to Figure 81) see , consistent with repeated grinding cuts and changes in grinding wheel diameter.

These trends in ROP align with observations made in the power spectral analysis of AE responses discussed in section 4.6. The Mistras AE sensors exhibit higher power magnitudes compared to the Kistler AE sensors, which can be attributed to their quality, sensitivity, and orientation during the experiments. Although further investigation is needed to fully understand the differences in AE power magnitude between the two sensors, the observed trends are consistent across both.

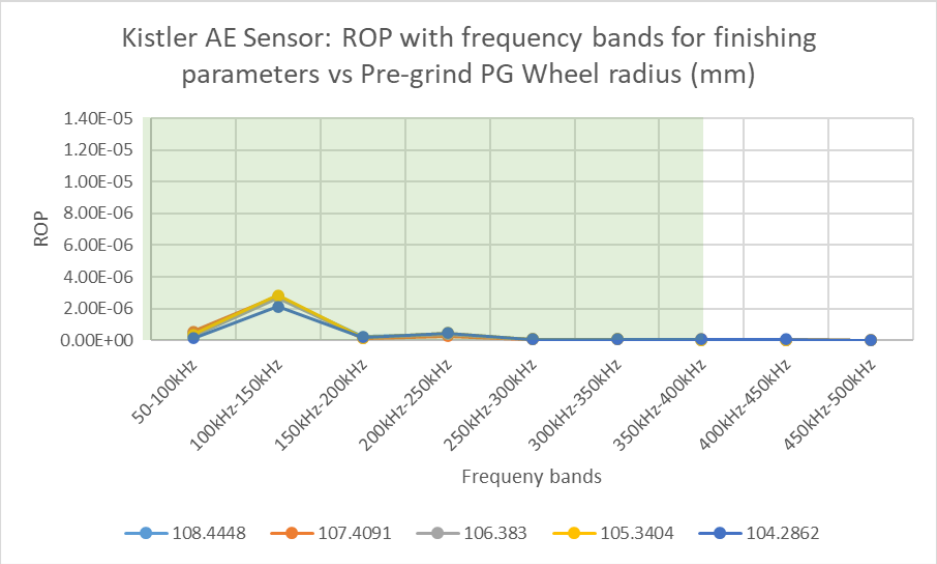

Figure 76Comparison of ROP for finishing parameter grinds with repeats of change in grinding wheel diameter for Kistler AE sensor. Green shaded area represents the operational frequency for the respective AE sensors.

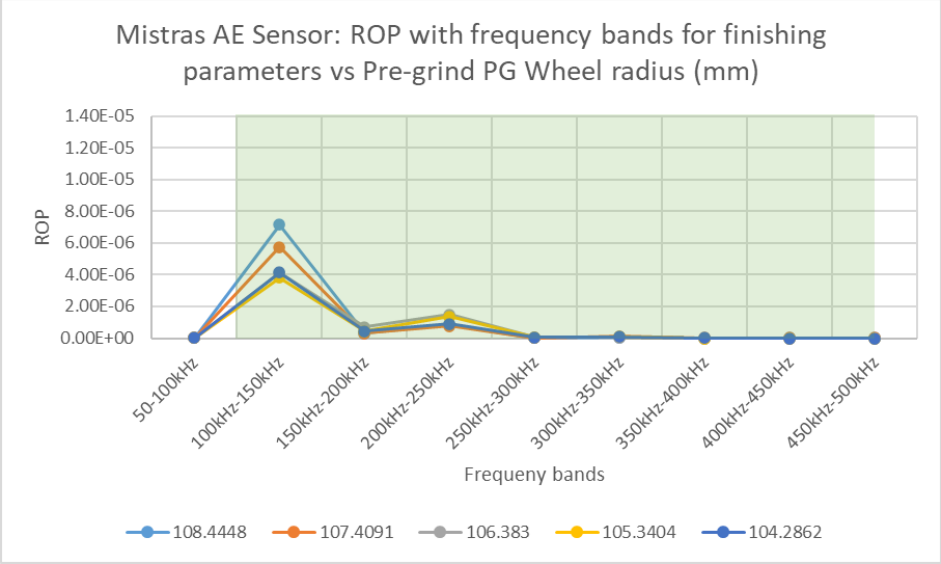

Figure 77 Comparison of ROP for finishing parameter grinds with repeats of change in grinding wheel diameter for Mistras AE sensor. Green shaded area represents the operational frequency for the respective AE sensors.

For instance, Figure 78 and Figure 79 illustrate that the peak ROP within the 100–150 kHz range for both sensors occurs when the grinding wheel radius is at its smallest, 104.331 mm, after five grinding repeats. This observation coincides with the highest wheel wear recorded in the semi-finishing grinding regime. This suggests that increased wheel wear, which leads to greater interaction between the grinding wheel and the workpiece, results in higher AE signals recorded by both sensors, thereby validating the data.

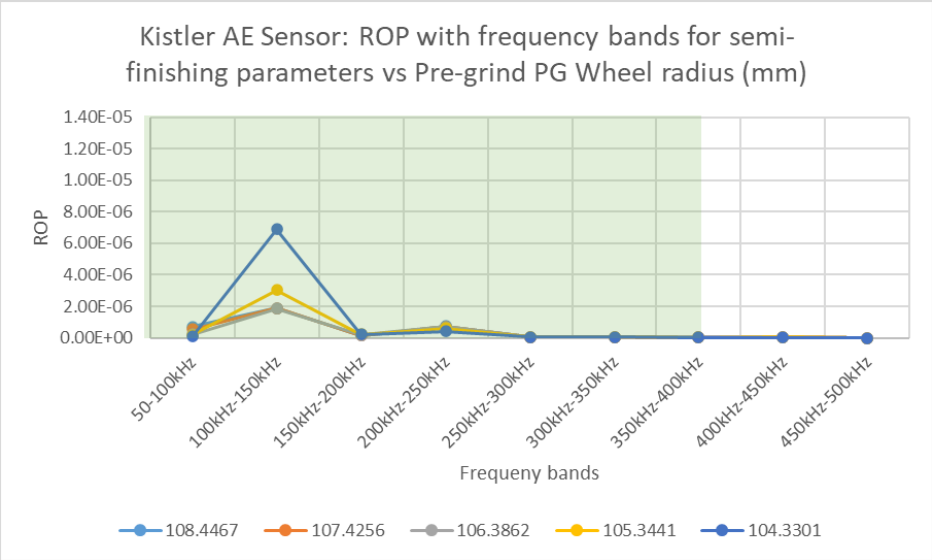

Figure 78 Comparison of ROP for semi-finishing parameter grinds with repeats of change in grinding wheel diameter for Kistler AE sensor. Green shaded area represents the operational frequency for the respective AE sensors.

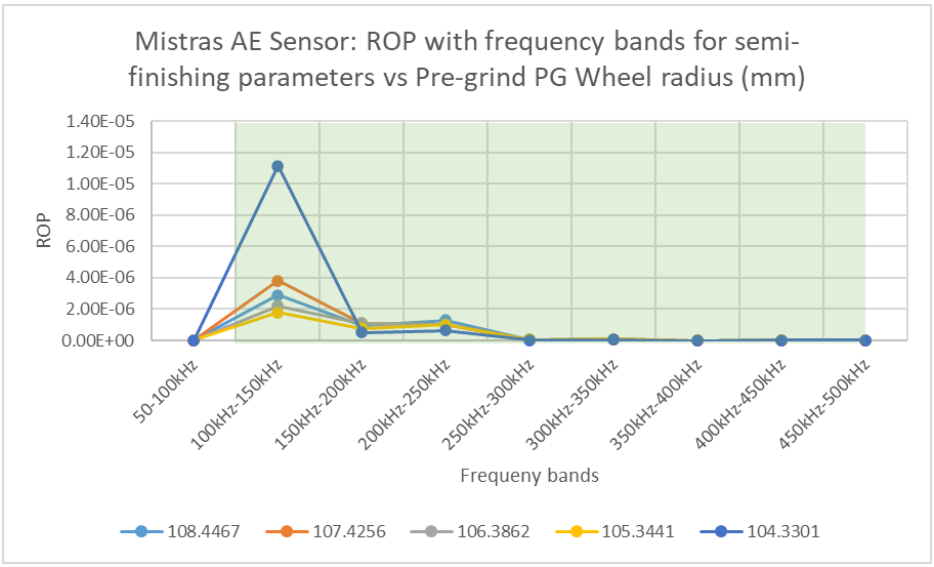

Figure 79 Comparison of ROP for semi-finishing parameter grinds with repeats of change in grinding wheel diameter for Mistras AE sensor. Green shaded area represents the operational frequency for the respective AE sensors.

Similarly, in the roughing regime (Figure 80 and Figure 81), trial 040 with a grinding wheel diameter of 105.427 mm also showed a peak in the ROP for the 100–150 kHz frequency band in both the Mistras and Kistler AE sensors. This trial also exhibited higher wheel wear, indicating more significant interactions between the grinding wheel and the workpiece during the grinding cut, which is reflected in the ROP frequency band (100–150 kHz).

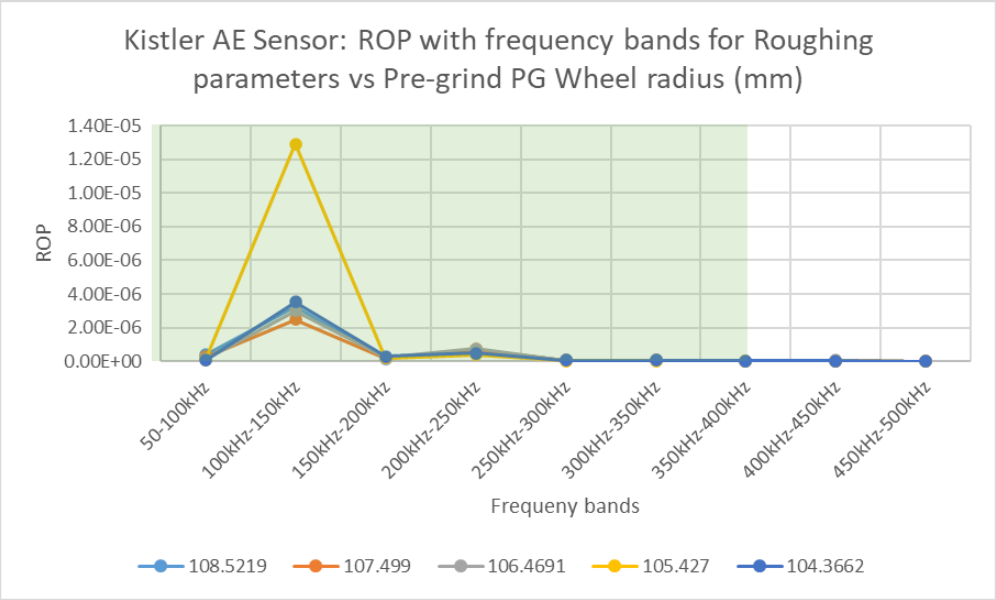

Figure 80 Comparison of ROP for Roughing parameter grinds with repeats of change in grinding wheel diameter for Kistler AE sensor. Green shaded area represents the operational frequency for the respective AE sensors.

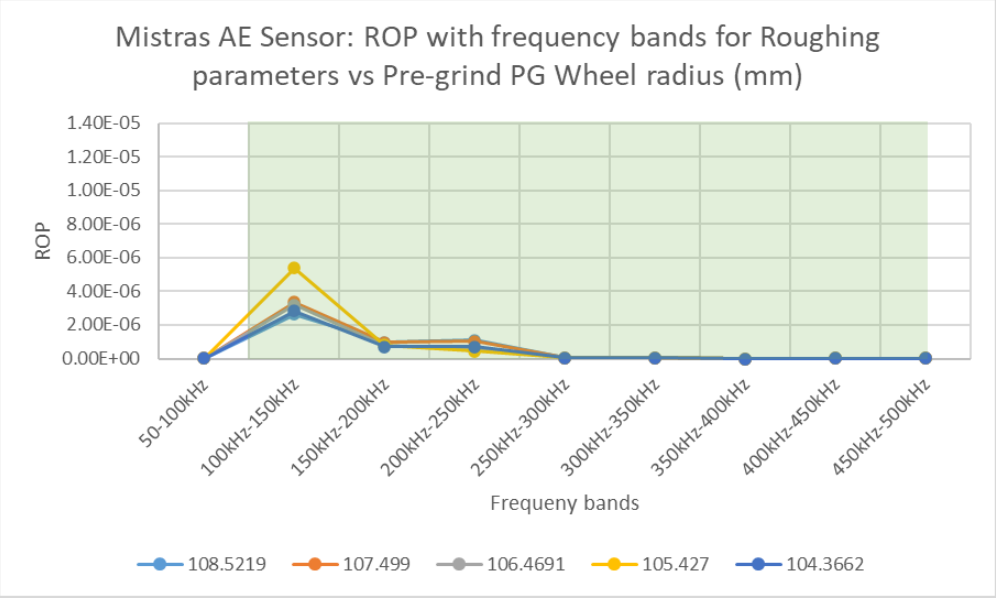

Figure 81 Comparison of ROP for Roughing parameter grinds with repeats of change in grinding wheel diameter for Mistras AE sensor. Green shaded area represents the operational frequency for the respective AE sensors.

The results indicate that most acoustic emission generated during the grinding of IN718 using alumina wheels is concentrated within the 100–150 kHz frequency band. Further investigation could explore why this specific frequency band is the most active. Previous literature indicated that a high-pass cut-off frequency of 90 kHz [35] was useful for removing machine noise and other environmental noise. This study highlights the importance of the 90–150 kHz region for AE signals.

The ROP values do not show a trend of increase or decrease with changes in grinding aggression, demonstrating that the frequency bands in which AE signals occur are consistent across grinding regimes. Apart from the outliers discussed in certain grinding cuts within the semi-finishing and roughing regimes, a stable grinding scenario always emits similar AE patterns. This consistency indicates that while the AE signal's power magnitude varies with grinding aggression, the frequency band remains constant. This opens opportunities for future pattern recognition work on the ROP to detect anomalies in the grinding mechanism.

Currently, there is a good correlation between ROP values and wheel wear trends discovered in this thesis. Further research could explore the potential to predict wheel wear values using ROP. Analyzing ROP values with respect to grinding wheel diameter shows negligible variation within each grinding regime, with similar and consistent trends observed across both AE sensors. Overall, it can be concluded that ROP results are repeatable even with changes in grinding wheel diameter.

Finally, the trends noticed in the AE features can be easily summarised into Table 10.

Table 10 Shows the summary of the observations made with AE features investigated and if they are repeatable with grinding wheel diameter progression.

AE feature	Observation/findings	Repeatable ?
AE RMS	▪ Demonstrated repeatability with changes in wheel diameter. ▪ Higher magnitudes observed in roughing parameters compared to finishing due to higher grinding forces and material removal rates. ▪ Consistent trends across both Kistler and Mistras AE sensors, enhancing confidence in the feature's reliability for fault diagnosis and process monitoring.	✓
Skew	▪ At finishing parameter conditions, larger wheel diameter resulted in higher skew values due to more intermittent and less consistent AE signals. ▪ Skew values shifted from positive for larger diameters to negative as the wheel diameter decreased.	✗

	▪ Other parameter conditions (roughing and semi-finishing) showed consistent and repeatable skew values. ▪ Sensitivity to lower magnitude AE responses in finishing grinds makes skew less reliable under these conditions.	
MVD	▪ Showed repeatability across all grinding parameter conditions. ▪ Stable values observed in roughing and semi-finishing regimes across different wheel diameters. ▪ Slight fluctuations in finishing regime, particularly in Mistras AE sensor, indicating sensitivity to minor inconsistencies and noise at lower aggression levels. ▪ Peaks in MVD during transitional phases of grinding suggest subtle changes in wheel-workpiece interactions.	✓
CFAR	▪ High CFAR values for roughing parameters compared to finishing and semi-finishing, indicating a greater number of AE events. ▪ Minimal fluctuation in CFAR values across different wheel diameters, demonstrating high repeatability. ▪ Clear separation in CFAR values between different grinding regimes, reflecting varying grinding conditions. ▪ Stability attributed to controlled grinding parameters and consistent material removal processes.	✓
ROP	▪ Most prominent frequency bands observed in the 100–150 kHz range across all grinding regimes. ▪ Higher power magnitudes in Mistras AE sensors compared to Kistler, attributed to sensor quality and sensitivity. ▪ Peaks in ROP values correlated with higher wheel wear and increased interactions between the grinding wheel and workpiece. ▪ Consistent frequency bands observed regardless of grinding aggression, with stable AE patterns indicating repeatability. ▪ Good correlation with wheel wear trends, suggesting potential for future predictive analysis using ROP.	✓

5 Conclusion

Work conducted within this thesis has been successful at meeting the objectives set out in the beginning and report findings which can supplement the existing body of knowledge. Literature review conducted explored the background of process monitoring during grinding and picked grinding wheel diameter as a parameter which was crucial to understanding repeatability of AE signal during trials. As a result, the experiment was designed to investigate changes in AE signals in terms of repeatability across different grinding regimes and varying grinding wheel diameters.

Signal pre-processing work for standardising wavelet de-noising has been conducted within this thesis to define the recommended de-noising method and selected parameters to remove background noise from coolant and machine environment for grinding AE signals.

The AE features analysed in this study included AE RMS, Skew, MVD, CFAR, and ROP. The results demonstrated that AE RMS and MVD values showed high repeatability across different grinding regimes and grinding wheel diameters, making them reliable features for fault diagnosis and process monitoring. The Skew feature, although consistent in roughing and semi-finishing regimes, showed variability in the finishing regime due to its sensitivity to lower magnitude AE responses. CFAR values remained stable across all grinding regimes, indicating consistent AE event frequency, which is crucial for reliable process monitoring.

Power spectral analysis of AE responses revealed consistent frequency bands across different grinding regimes, with increased power magnitude correlating with higher grinding aggression. The prominent frequency band of 100-150 kHz was identified as significant for AE signals during grinding, providing a focus for future studies on pattern recognition and anomaly detection. The study highlighted that increased wheel wear leads to higher AE signals due to more intense interactions between the grinding wheel and the workpiece. This correlation between AE features and wheel wear trends suggests potential for predictive analysis using AE data.

Overall, this thesis contributes to the understanding of AE signal behaviour during grinding, emphasizing the importance of grinding wheel diameter and aggression levels. The findings provide a foundation for future work on process monitoring and fault diagnosis in grinding operations, with implications for improving the consistency and reliability of manufacturing processes. Further investigation into AE feature analysis and sensor performance characteristics will enhance the practical applications of AE monitoring in industrial settings.

6 Future work

Work done within this thesis has set standards for working with AE sensors at AMRC and therefore further work needs to be focused on design of experiments which focus on fault detection. Different areas that the DOE can be focused to investigate the use of AE signals include detecting of nano hardness profile, residual stress, grain size profiling, depth of strain bands, white layer/grinding burn profile, cracks or swept grain. For this detection study, workpiece preparation and post-experiment analysis would be required to analyse and pin-point AE features which detect the above-mentioned surface integrity fault diagnosis within a workpiece. There has been research conducted within these fronts but none that have been substantial to show potential of industrial application but once successful, this initiative can save time and money from in-process failures for the high value manufacturing process in the aviation industry.

This thesis focused solely on the repeatability of AE signals with grinding wheel diameter progression but a 100% repeatability of signal may not be required for detecting any fault diagnosis while process monitoring. Depending on the fault diagnosis that needs to be investigated, there would be a threshold or pattern recognition threshold which can reliably predict any fault diagnosis. Therefore while conducting further work within process monitoring using AE signals, it is important to run an independent repeatability study with fault induced experiment runs with key variables which may affect repeatability. This approach is suitable for supervised learning form of machine learning to detect any faults using AE data and defining the threshold and it is rather difficult to define a threshold using unsupervised learning.

One key area for future research identified within research involves conducting additional grinding trials, particularly within the finishing grinding regime, to increase the data pool. This would help identify trends and improve the understanding of lower repeatability in less aggressive grinding conditions. Incorporating a wider range of grinding wheel diameter progression data points would provide a more comprehensive analysis, enabling a deeper understanding of AE signal behavior.

The scope of this thesis changed from an EngD to the MPhil thesis which meant that the surface analysis of workpiece after these grinding cuts had been beyond the scope of this experiment. The machine programme and setup was initially designed to cater for the pre/post analysis of workpiece surface and this is still the case. Therefore future work, could still look at using the same grinding programme and tool path to enhance any fault diagnosis study within grinding which can be supplemented by surface analysis pre/post grinding.

In conclusion, the continuation of this research will not only deepen the understanding of AE monitoring during grinding but also contribute to the development of more reliable and efficient manufacturing processes. By addressing the identified challenges and exploring the proposed future work, significant advancements can be made in process monitoring and fault diagnosis in the grinding industry.

7 Industrial implications

The findings from this thesis have significant implications for the industrial application of AE monitoring in grinding processes. The comprehensive analysis and insights gained from studying the AE features across different grinding regimes provide a robust foundation for enhancing process monitoring, fault diagnosis, and overall manufacturing efficiency in industrial settings.

The correlation between AE features and grinding wheel wear opens the potential for predictive maintenance. By analysing AE data, it is possible to forecast wheel wear and schedule maintenance activities proactively. This predictive approach reduces unexpected downtime and extends the lifespan of grinding wheels, resulting in cost savings and increased operational efficiency. Industries can plan maintenance schedules based on data-driven insights rather than relying on fixed intervals, thereby optimizing resource allocation. The study demonstrates that AE monitoring can effectively detect variations in grinding conditions, such as increased wheel wear or changes in material removal rates. This capability is crucial for fault diagnosis, as it allows for the early detection of anomalies that could lead to product defects or equipment damage. Implementing AE-based fault diagnosis systems can enhance the reliability of grinding operations and minimize the risk of producing defective parts, ultimately improving customer satisfaction and reducing waste. The consistent trends observed in AE features across different grinding regimes suggest that AE monitoring can be integrated into quality control processes. By establishing baseline AE signals for optimal grinding conditions, industries can compare real-time AE data to these baselines to ensure that each grinding operation meets quality standards. This integration can streamline quality assurance processes and provide a non-destructive method for verifying product integrity. The implementation of AE monitoring systems can lead to significant cost reductions by minimizing downtime, reducing wheel wear, and preventing defects. The increased efficiency and reliability of grinding operations translate to higher productivity and lower operational costs. Additionally, the ability to monitor and control grinding processes in real-time allows for the optimization of grinding parameters, leading to energy savings and more sustainable manufacturing practices.

The work conducted within this thesis has significantly enhanced the process monitoring capability at AMRC. An improved data acquisition system, capable of capturing synchronous signals from various sensors at high data sampling rates, was implemented as part of the investigation. The capabilities and limitations of the new system have been shared with AMRC personnel, ensuring that future work can build on the progress made in this thesis. An ASTM standardized AE sensor reproducibility test method was deployed to assess the reliability of AE signals from sensors before and after testing. This standardized

work documentation has been shared with the relevant teams at AMRC for future use. Additionally, a MATLAB app (included in the appendix) was designed and implemented to facilitate the determination of AE sensor signal reproducibility.

Learnings from this thesis on wavelet denoising have also been applied to other machining practices at AMRC for further research and development. The One-Way Assembly (OWA) project at AMRC trialed the wavelet denoising technique to reduce machine noise from AE signals recorded during the drilling of different material stacks. As part of this work, a MATLAB app (included in the appendix) was produced to help visualize and de-noise signals from four different types of materials investigated within the OWA project.

In conclusion, the findings from this thesis highlight the significant industrial implications of AE monitoring in grinding processes. The adoption of AE monitoring systems can lead to enhanced process control, predictive maintenance, improved fault diagnosis, and overall cost efficiency. By leveraging these insights, industries can achieve higher product quality, operational reliability, and competitiveness in the manufacturing sector. The continued research and development in this area will further solidify the role of AE monitoring as a critical tool for modern manufacturing.

8 References

[1] W. B. Rowe, *Principles of modern grinding technology*. 2013. doi: 10.1016/C2013-0-06952-6.

[2] S. Wee *et al.*, 'Review on mechanical thermal properties of superalloys and thermal barrier coating used in gas turbines', *Applied Sciences*, vol. 10, no. 16, p. 5476, 2020.

[3] M. K. Sinha, D. Setti, S. Ghosh, and P. V. Rao, 'An investigation on surface burn during grinding of Inconel 718', *J Manuf Process*, vol. 21, pp. 124–133, 2016.

[4] S. Malkin and C. Guo, *Grinding Technology Theory & Application of Machining with Abrasives*, vol. 2. 2008.

[5] A. Biro, J. Hagan, and B. Gustafson, 'Understanding Forces in Grinding for Reducing Costs and Improving Consistency Why Creepfeed Grinding ?', *NORTON : SAINT GOBAIN - white paper*, 2019.

[6] J. A. Badger, 'The Great Divide: Grinding in Academia and Production', *Sweedish Production Symposium*, 2011.

[7] M. E. Merchant, 'Mechanics of the metal cutting process. I. Orthogonal cutting and a type 2 chip', *J Appl Phys*, vol. 16, no. 5, pp. 267–275, 1945, doi: 10.1063/1.1707586.

[8] J. Badger, 'Practical application of aggressiveness and chip thickness in grinding', in *J. Badger. Annals of the CIRP 3rd International Conference High Performance Cutting (HPC), Dublin, Ireland*, 2008, pp. 599–606.

[9] M. K. Sinha, D. Setti, S. Ghosh, and P. Venkateswara Rao, 'An investigation on surface burn during grinding of Inconel 718', *J Manuf Process*, vol. 21, pp. 124–133, Jan. 2016, doi: 10.1016/j.jmapro.2015.12.004.

[10] S. Kohli, C. Guo, and S. Malkin, 'Energy partition to the workpiece for grinding with aluminum oxide and CBN abrasive wheels', 1995.

[11] P. L. Tso, 'Study on the grinding of Inconel 718', *Journal of Materials Processing Tech.*, vol. 55, no. 3–4, pp. 421–426, 1995, doi: 10.1016/0924-0136(95)02026-8.

[12] Z. Zhong, K. Ramesh, and S. H. Yeo, 'Grinding of nickel-based super-alloys and advanced ceramics', *Materials and Manufacturing Processes*, vol. 16, no. 2, pp. 195–207, Mar. 2001, doi: 10.1081/AMP-100104300.

[13] Q. Liu, X. Chen, and N. Gindy, 'Assessment of Al2O3 and superabrasive wheels in nickel-based alloy grinding', *International Journal of Advanced Manufacturing Technology*, vol. 33, no. 9–10, pp. 940–951, Jul. 2007, doi: 10.1007/s00170-006-0519-1.

[14] S. Huddedar, P. Chitalkar, A. Chavan, and R. S. Pawade, 'Effect of cooling environment on grinding performance of nickel based superalloy Inconel 718', *Journal of Applied Sciences*, vol. 12, no. 10, pp. 947–954, 2012, doi: 10.3923/JAS.2012.947.954.

[15] C. F. Yao, Q. C. Jin, X. C. Huang, D. X. Wu, J. X. Ren, and D. H. Zhang, 'Research on surface integrity of grinding inconel718', *International Journal of Advanced Manufacturing Technology*, vol. 65, no. 5–8, pp. 1019–1030, Mar. 2013, doi: 10.1007/s00170-012-4236-7.

[16] M. K. Sinha, D. Setti, S. Ghosh, and P. Venkateswara Rao, 'An investigation on surface burn during grinding of Inconel 718', *J Manuf Process*, vol. 21, pp. 124–133, Jan. 2016, doi: 10.1016/J.JMAPRO.2015.12.004.

[17] H. K. Tönshoff, T. Friemuth, and J. C. Becker, 'Process monitoring in grinding', *CIRP Ann Manuf Technol*, 2002, doi: 10.1016/S0007-8506(07)61700-4.

[18] B. Harbour, D. O. Harris, and C. A. Tatro, 'ACOUSTIC EMISSION A symposium presented at the December Committee Week AMERICAN SOCIETY FOR TESTING AND MATERIALS', 1972.

[19] 'Acoustic Emission - an overview | ScienceDirect Topics'. Accessed: Feb. 24, 2020. [Online]. Available: https://www.sciencedirect.com/topics/chemistry/acoustic-emission

[20] E. Govekar, J. Gradišek, and I. Grabec, 'Analysis of acoustic emission signals and monitoring of machining processes', *Ultrasonics*, vol. 38, no. 1, pp. 598–603, Mar. 2000, doi: 10.1016/S0041-624X(99)00126-2.

[21] M. Wevers and K. Lambrighs, 'Applications of Acoustic Emission for SHM: A Review', in *Encyclopedia of Structural Health Monitoring*, John Wiley & Sons, Ltd, 2008. doi: 10.1002/9780470061626.shm011.

[22] D. A. Roberts and D. L. Leete, 'Camshaft grinding burn detection by acoustic emission', *Sensor Review*, vol. 3, no. 2, pp. 72–74, 1983, doi: 10.1108/eb007591.

[23] Z. Wang, P. Willett, P. R. Deaguiar, and J. Webster, 'Neural network detection of grinding burn from acoustic emission', *Int J Mach Tools Manuf*, vol. 41, no. 2, pp. 283–309, 2001, doi: 10.1016/S0890-6955(00)00057-2.

[24] P. R. Aguiar, P. J. A. Serni, E. C. Bianchi, and F. R. L. Dotto, 'In-process grinding monitoring by acoustic emission', *ICASSP, IEEE International Conference on Acoustics, Speech and Signal Processing - Proceedings*, vol. 5, pp. V–405, 2004, doi: 10.1109/icassp.2004.1327133.

[25] Q. Liu, X. Chen, and N. Gindy, 'Fuzzy pattern recognition of AE signals for grinding burn', *Int J Mach Tools Manuf*, vol. 45, no. 7–8, pp. 811–818, 2005, doi: 10.1016/j.ijmachtools.2004.11.002.

[26] P. R. de Aguiar, E. Carlos, and R. Chinali, 'Monitoring of Grinding Burn by Acoustic Emission', *Acoustic Emission*, 2012, doi: 10.5772/31339.

[27] Z. Gao, J. Lin, X. Wang, and Y. Liao, 'Grinding Burn Detection Based on Cross Wavelet and Wavelet Coherence Analysis by Acoustic Emission Signal', *Chinese Journal of Mechanical Engineering (English Edition)*, 2019, doi: 10.1186/s10033-019-0384-0.

[28] Q. Liu, X. Chen, and N. Gindy, 'Investigation of acoustic emission signals under a simulative environment of grinding burn', *Int J Mach Tools Manuf*, vol. 46, no. 3–4, pp. 284–292, 2006, doi: 10.1016/j.ijmachtools.2005.05.017.

[29] X. Chen, A. Mohamed, and A. Oluwajobi, 'Investigation of AE features in grinding', *J Phys Conf Ser*, vol. 364, no. 1, 2012, doi: 10.1088/1742-6596/364/1/012090.

[30] Hamed Adibi, A. S. Ashtiani, and A. Rahimi, 'In-Process Monitoring of Nickel-Based Super Alloy Grinding Using the Acoustic Emission Method', *Russian Journal of Nondestructive Testing*, vol. 55, no. 12, pp. 909–917, Dec. 2019, doi: 10.1134/S1061830919120027.

[31] I. Yesilyurt, A. Dalkiran, O. Yesil, and O. Mustak, 'Scalogram-Based Instantaneous Features of Acoustic Emission in Grinding Burn Detection', *Journal of Dynamics, Monitoring and Diagnostics*, vol. 1, no. 1, pp. 19–28, Dec. 2021, doi: 10.37965/jdmd.2021.49.

[32] G. Yin, J. Wang, Y. Guan, D. Wang, and Y. Sun, 'The prediction model and experimental research of grinding surface roughness based on AE signal', *International Journal of Advanced Manufacturing Technology*, vol. 120, no. 9–10, pp. 6693–6705, Jun. 2022, doi: 10.1007/s00170-022-09135-x.

[33] D. González, J. Alvarez, J. A. Sánchez, L. Godino, and I. Pombo, 'Deep Learning-Based Feature Extraction of Acoustic Emission Signals for Monitoring Wear of Grinding Wheels', *Sensors*, vol. 22, no. 18, Sep. 2022, doi: 10.3390/s22186911.

[34] G. Bi, S. Liu, S. Su, and Z. Wang, 'Diamond grinding wheel condition monitoring based on acoustic emission signals', *Sensors (Switzerland)*, vol. 21, no. 4, pp. 1–17, Feb. 2021, doi: 10.3390/s21041054.

[35] Z. Yang and Z. Yu, 'Grinding wheel wear monitoring based on wavelet analysis and support vector machine', *International Journal of Advanced Manufacturing Technology*, vol. 62, no. 1–4, pp. 107–121, Sep. 2012, doi: 10.1007/s00170-011-3797-1.

[36] P. R. Aguiar, P. J. A. Serni, E. C. Bianchi, and F. R. L. Dotto, 'In-process grinding monitoring by acoustic emission', in *ICASSP, IEEE International Conference on Acoustics, Speech and Signal Processing - Proceedings*, 2004. doi: 10.1109/icassp.2004.1327133.

[37] V. Barat, Y. Borodin, and A. Kuzmin, 'Intelligent Ae Signal Filtering Methods', *J. Acoustic Emission*, vol. 28, pp. 109–119, 2010.

[38] C. S. Burrus and R. a Gopinath, 'Introduction to Wavelets and Wavelet Transformer', in *Prentice Hall*, 1998, p. 268.

[39] P. Wojtaszczyk, 'A Mathematical Introduction to Wavelets (London Mathematical Society Student Texts)', 1997.

[40] S. Talebi, 'The Wavelet Transform. An Introduction and Example | by Shawhin Talebi | Towards Data Science'. Accessed: Apr. 22, 2021. [Online]. Available: https://towardsdatascience.com/the-wavelet-transform-e9cfa85d7b34

[41] 'Orthogonal and Biorthogonal Filter Banks - MATLAB & Simulink'. Accessed: Apr. 26, 2021. [Online]. Available: https://www.mathworks.com/help/wavelet/orthogonal-and-biorthogonal-filter-banks.html

[42] A. C. H. Rowe and P. C. Abbott, 'Daubechies wavelets and Mathematica', *Computers in Physics*, vol. 9, no. 6, p. 635, Jun. 1995, doi: 10.1063/1.168556.

[43] Z. Yang and Z. Yu, 'Grinding wheel wear monitoring based on wavelet analysis and support vector machine', *International Journal of Advanced Manufacturing Technology*, vol. 62, no. 1–4, pp. 107–121, 2012, doi: 10.1007/s00170-011-3797-1.

[44] Mathworks, 'Multilevel 1-D wavelet decomposition - MATLAB wavedec - MathWorks United Kingdom'. Accessed: Sep. 24, 2022. [Online]. Available: https://uk.mathworks.com/help/wavelet/ref/wavedec.html

[45] Mathworks, 'Multilevel 1-D wavelet decomposition - MATLAB wavedec - MathWorks United Kingdom'. Accessed: Sep. 24, 2022. [Online]. Available: https://uk.mathworks.com/help/wavelet/ref/wavedec.html

[46] B. Ergen, 'Comparison of Wavelet Types and Thresholding Methods on Wavelet Based Denoising of Heart Sounds', *Journal of Signal and Information Processing*, vol. 04, no. 03, pp. 164–167, 2013, doi: 10.4236/jsip.2013.43b029.

[47] 'Threshold selection for denoising - MATLAB thselect'. Accessed: Sep. 26, 2022. [Online]. Available: https://www.mathworks.com/help/wavelet/ref/thselect.html#mw_3f5f07d2-c808-475a-9a3f-6a513c670891

[48] L. Jing-Yi, L. Hong, Y. Dong, and Z. Yan-Sheng, 'A New Wavelet Threshold Function and Denoising Application', *Math Probl Eng*, vol. 2016, 2016, doi: 10.1155/2016/3195492.

[49] L. Jing-Yi, L. Hong, Y. Dong, and Z. Yan-Sheng, 'A New Wavelet Threshold Function and Denoising Application', *Math Probl Eng*, vol. 2016, 2016, doi: 10.1155/2016/3195492.

[50] D. L. Donoho, 'De-Noising by Soft-Thresholding', *IEEE Trans Inf Theory*, vol. 41, no. 3, pp. 613–627, 1995, doi: 10.1109/18.382009.

[51] 'TRIM C272 - Description - Master Fluid Solutions'. Accessed: Sep. 25, 2022. [Online]. Available: https://www.masterfluids.com/eu/en/products/show-product-description.php?pid=C272

[52] 'Solutions : EROWA LTD'. Accessed: Oct. 14, 2022. [Online]. Available: https://www.erowa.com/en/solutions/sr/workpieceholding

[53] ‘Bolt Torque Calculator’. Accessed: Oct. 16, 2022. [Online]. Available: https://www.engineeringtoolbox.com/bolt-torque-load-calculator-d_2065.html

[54] R. de Souza Ruzzi, R. B. da Silva, L. R. R. da Silva, Á. R. Machado, M. J. Jackson, and A. Hassui, ‘Influence of grinding parameters on Inconel 625 surface grinding’, *J Manuf Process*, vol. 55, pp. 174–185, 2020.

[55] ‘Designation: A388/A388M − 23 Standard Practice for Ultrasonic Examination of Steel Forgings 1’, doi: 10.1520/A0388_A0388M-23.

[56] ASTM, ‘E2075/E2075M-10 Standard Practice for Verifying the Consistency of AE-Sensor Response Using an Acrylic Rod 1’, *ASTM Standards*, vol. i, no. Reapproved 2020, pp. 10–13, 2015, doi: 10.1520/E2075.

[57] ‘The scientist and engineer’s guide to digital signal processing statics,probability and Noise’.

[58] R. R. Devi and D. Pugazhenthi, ‘Ideal Sampling Rate to Reduce Distortion in Audio Steganography’, in *Procedia Computer Science*, Elsevier B.V., 2016, pp. 418–424. doi: 10.1016/j.procs.2016.05.185.

[59] H. M. Soe Naing, R. Hidayat, R. Hartanto, and Y. Miyanaga, ‘Discrete wavelet denoising into mfcc for noise suppressive in automatic speech recognition system’, *International Journal of Intelligent Engineering and Systems*, vol. 13, no. 2, pp. 74–82, 2020, doi: 10.22266/ijies2020.0430.08.

9 Appendix

9.1 AE wavelet de-noising app :

GUI screenshot :

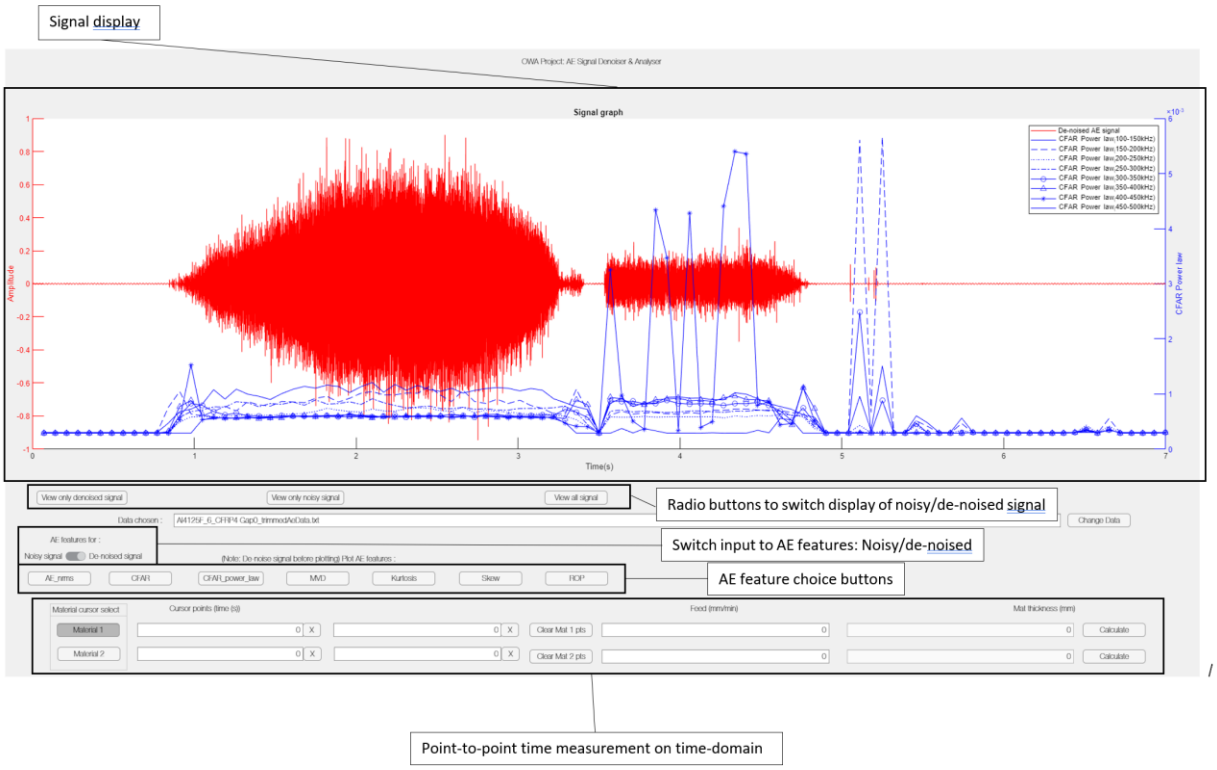

Script available on request.

9.2 Data analysis road map for thesis showing MATLAB files used :

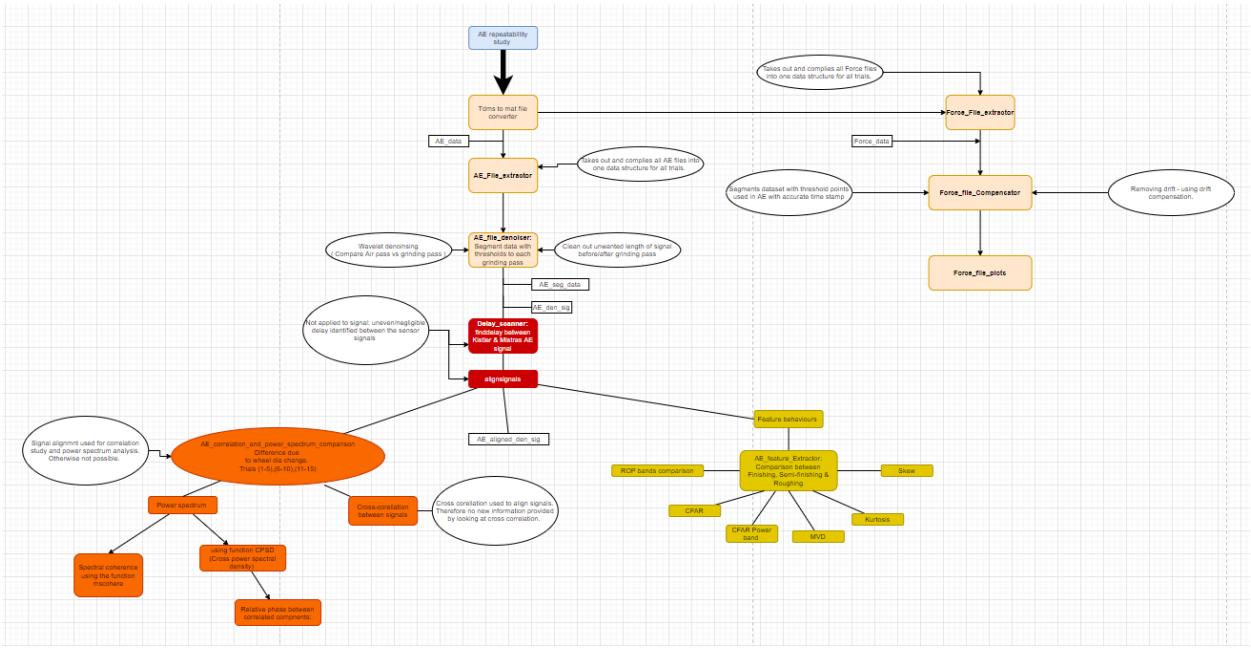

9.2.1 AE File extraction from dataset :

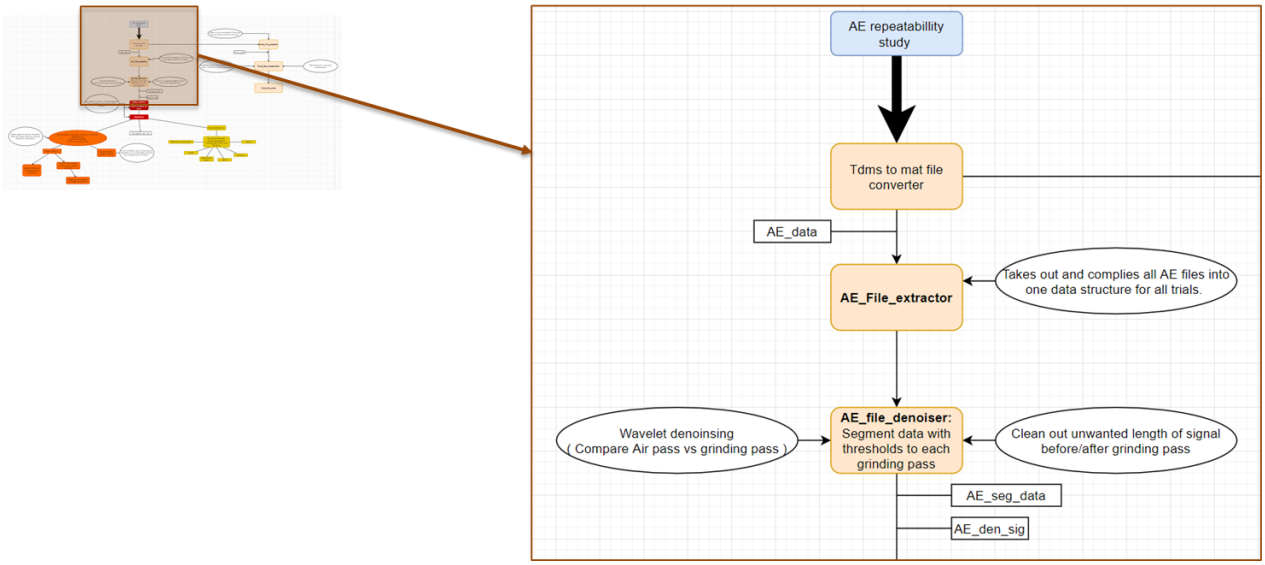

AE_file_extractor.mlx:

- Convert .tdms to .mat file
- Extracted AE files for each sensors separately

AE File extractor

```
% Prompt the user for the file
[filename_1,pathname]=uigetfile({'*.mat','All Files (*.tdms)'},'Choose the TDMS
Files', 'Multiselect' , 'on');

if isempty(filename_1)

   print("No files selected");

   return % No files selected, does not

end

filename_full=fullfile(pathname,filename_1);

num_mat_files=size(filename_full,2); % num

for num_struct=1:num_mat_files % looping through each trial no file

    clear ConvertedData

    load(filename_full{num_struct},'ConvertedData');

    for i=1:length((ConvertedData))

    if isempty(strfind(ConvertedData(i).FileName,'Parameter'))==0


AE_data(num_struct).trial_no=str2double(extractBetween(filename_1(num_struct),'Tr
ial_','.mat'));


AE_data(num_struct).AE_Mistras_data_PG=tall(ConvertedData(i).Data.MeasuredData(16
).Data); % extracting Mistras AE sensor data for Paramater grind


AE_data(num_struct).AE_Kistler_data_PG=tall(ConvertedData(i).Data.MeasuredData(15
).Data); % extracting Kistler AE Sensor data for Parameter grind

    elseif isempty(strfind(ConvertedData(i).FileName,'Airpass'))==0


AE_data(num_struct).AE_Mistras_data_AP=tall(ConvertedData(i).Data.MeasuredData(16
).Data); % extracting Mistras AE sensor data for Air pass


AE_data(num_struct).AE_Kistler_data_AP=tall(ConvertedData(i).Data.MeasuredData(15
).Data); % extracting Kistler AE Sensor data for Air pass

    end

    end

end
```

AE_file_denoiser.mlx:

Segmented grinding pass data:

- using threshold of 0.15 for Kistler AE sensor
- using threshold of 0.2 for Mistras AE sensor

Segmented air pass data:

- Using the first statistic RMS change point as thresholding start point.
- Each signal limited to 4 secs of data = 4000000 samples at 2Mhz

AE- file denoiser

Segment the data with thresholding to remove useless data points

```
Fs=2000000; % Sampling rate (2Mhhz for AE signals recorded)

% For kistler data :

for i= 1:length(AE_data)

    AE_signal_i=gather(AE_data(i).AE_Kistler_data_PG); % getting pre_data

    %Trimming for Kistler AE data

    threshold=0.15; % threshold for Kistler data

    threshold_point=find(AE_signal_i>(threshold),1,"first");

    AE_sig_trim_start=(threshold_point-(Fs*0.5)); % start the trim 0.5 seconds
before threshold point

    if threshold_point-(Fs*0.5)+((Fs*4)-1)>size(AE_signal_i,1)

        AE_sig_trim_start=AE_sig_trim_start-(threshold_point-(Fs*0.5)+((Fs*4)-1)-
size(AE_signal_i,1)); % Moving the trim start further back if the segment to be
cut out is longer than signal

    elseif AE_sig_trim_start<0

        AE_sig_trim_start=1; % If trimstart chosen is negative then it is made to
start from 1
```

```
    end

    AE_signal_i=AE_signal_i([AE_sig_trim_start:(AE_sig_trim_start+((Fs*4)-
1))],:); % segmenting the signal to gather the 4 sec signal of grinding pass.

    AE_seg_data(i).AE_kistler_data_PG=AE_signal_i; % adding the segmented data to
a new structure

end

% For Mistras data :

for i= 1:length(AE_data)

    AE_signal_i=gather(AE_data(i).AE_Mistras_data_PG); % getting the raw data

    %Trimming for Mistras AE data

    threshold=0.2; % threshold for Mistras data

    threshold_point=find(AE_signal_i>(threshold),1,"first");

    AE_sig_trim_start=(threshold_point-(Fs*0.5)); % start the trim 0.5 seconds
before threshold point

    if threshold_point-(Fs*0.5)+((Fs*4)-1)>size(AE_signal_i,1)

        AE_sig_trim_start=AE_sig_trim_start-(threshold_point-(Fs*0.5)+((Fs*4)-1)-
size(AE_signal_i,1)); % Moving the trim start further back if the segment to be
cut out is longer than signal

    elseif AE_sig_trim_start<0

        AE_sig_trim_start=1; % If trimstart chosen is negative then it is made to
start from 1

    end

    AE_signal_i=AE_signal_i([AE_sig_trim_start:(AE_sig_trim_start+((Fs*4)-
1))],:); % segmenting the signal to gather the 4 sec signal of grinding pass.

    AE_seg_data(i).AE_Mistras_data_PG=AE_signal_i; % adding the segmented data to
a new structure

end




figure
%plot(AE_signal_i);

plot(AE_seg_data(12).AE_kistler_data_PG);

hold on
```

```
plot(AE_seg_data(12).AE_Mistras_data_PG);



% Segment Airpass data to same length as a Parameter grind cut signal
% for Kistler data :

for i= 1:length(AE_seg_data)

    clear AE_signal_AP

    clear AE_signal_i

    AE_signal_AP=gather(AE_data(i).AE_Kistler_data_AP);

    rms_signal_AP=rms(AE_signal_AP,100000,1000,0);

    [idx]=findchangepts(rms_signal_AP,"Statistic","rms","MaxNumChanges",4);

    threshold_point=idx(1)*100000;

    AE_sig_trim_start=(threshold_point);  % start the trim 0.5 seconds before
threshold point

    if threshold_point+((Fs*4)-1)>size(AE_signal_AP,1)

        AE_sig_trim_start=AE_sig_trim_start-(threshold_point+((Fs*4)-1)-
size(AE_signal_AP,1)); % Moving the trim start further back if the segment to be
cut out is longer than signal

    elseif AE_sig_trim_start<0

        AE_sig_trim_start=1; % If trimstart chosen is negative then it is made to
start from 1

    end

    AE_signal_i=AE_signal_AP([AE_sig_trim_start:(AE_sig_trim_start+((Fs*4)-
1))],:); % segmenting the signal to gather the 4 sec signal of grinding pass.

    AE_seg_data(i).AE_kistler_data_AP=AE_signal_i; % adding the segmented data to
a new structure

end

% for Mistras data :

for i= 1:length(AE_seg_data)

    clear AE_signal_AP

    clear AE_signal_i

    AE_signal_AP=gather(AE_data(i).AE_Mistras_data_AP);

    rms_signal_AP=rms(AE_signal_AP,100000,1000,0);
```

```
    [idx]=findchangepts(rms_signal_AP,"Statistic","rms","MaxNumChanges",4);

    threshold_point=idx(1)*100000;

    AE_sig_trim_start=(threshold_point); % start the trim 0.5 seconds before
threshold point

    if threshold_point+((Fs*4)-1)>size(AE_signal_AP,1)

        AE_sig_trim_start=AE_sig_trim_start-(threshold_point+((Fs*4)-1)-
size(AE_signal_AP,1)); % Moving the trim start further back if the segment to be
cut out is longer than signal

    elseif AE_sig_trim_start<0

        AE_sig_trim_start=1; % If trimstart chosen is negative then it is made to
start from 1

    end

    AE_signal_i=AE_signal_AP([AE_sig_trim_start:(AE_sig_trim_start+((Fs*4)-
1))],:); % segmenting the signal to gather the 4 sec signal of grinding pass.

    AE_seg_data(i).AE_Mistras_data_AP=AE_signal_i; % adding the segmented data to
a new structure

end

% %plot(AE_signal_AP);

% %figure

% %plot(AE_signal_i);

% %figure

% %plot(rms_signal_AP);

% %plot(AE_data(12).AE_Mistras_data_PG)

% plot(AE_seg_data(15).AE_Mistras_data_AP);

% figure

% plot(AE_seg_data(15).AE_kistler_data_AP);

% figure
```

```
% Wavelet denoising signal
for i=1:length(AE_seg_data)% Kistler signal

    AP_signal=(AE_seg_data(i).AE_kistler_data_AP);
```

```
    PG_signal=(AE_seg_data(i).AE_kistler_data_PG);

    % Wavelet properties

    wname='coif5'; % wavelet chosen

    level=5; %decomposition level chosen

    sorh='s'; % soft thresholding chosen

    % % IDT Thresholding

    % nb_Int = 3;   % Number of intervals for thresholding.

    %
[den_IDT_PG_signal,coefs,thrParams,int_DepThr_Cell,BestNbofInt]=cmddenoise(PG_sig
nal,wname,level,sorh,nb_Int); % wavelet denoising done

    % %SNR1_IDT=10*log10(sum(PG_signal)/(sum(PG_signal-(den_IDT_PG_signal)')));

    %  SNR_OG=snr((PG_signal),AP_signal) % snr of denoisned signal divided by
airpass(noise) signal

    %  SNR2_IDT=snr((den_IDT_PG_signal)',AP_signal); % snr of denoisned signal
divided by airpass(noise) signal

    % SNR3_IDT=mean(den_IDT_PG_signal)/std(den_IDT_PG_signal); % mean of denoised
signal / std of denoised signal

    % Thresholding using Airpass information

    [c,l]=wavedec(AP_signal,level,wname);

    [cd1,cd2,cd3,cd4,cd5]=detcoef(c,l,[1 2 3 4 5]);

    thresholds=[max(abs(cd1))    max(abs(cd2))    max(abs(cd3))    max(abs(cd4))
max(abs(cd4)) max(abs(cd5))];

    den_PG_signal=cmddenoise(PG_signal,wname,level,sorh,NaN,thresholds);        %
wavelet denoising done

    %SNR1=10*log10(sum(PG_signal)/(sum(PG_signal-(den_PG_signal)')));

    SNR2=snr((den_PG_signal)',AP_signal) % snr of denoisned signal divided by
airpass(noise) signal

    SNR3=mean(den_PG_signal)/std(den_PG_signal) % mean of denoised signal / std of
denoised signal

    AE_den_sig(i).AE_kistler_data_PG=den_PG_signal;

end

for i=1:length(AE_seg_data)% Mistras signal

    AP_signal=(AE_seg_data(i).AE_Mistras_data_AP);
```

```
    PG_signal=(AE_seg_data(i).AE_Mistras_data_PG);

    % Wavelet properties

    wname='coif5'; % wavelet chosen

    level=5; %decomposition level chosen

    sorh='s'; % soft thresholding chosen

    % % IDT Thresholding

    % nb_Int = 3;   % Number of intervals for thresholding.

    %
[den_IDT_PG_signal,coefs,thrParams,int_DepThr_Cell,BestNbofInt]=cmddenoise(PG_sig
nal,wname,level,sorh,nb_Int); % wavelet denoising done

    % %SNR1_IDT=10*log10(sum(PG_signal)/(sum(PG_signal-(den_IDT_PG_signal)')));

    %  SNR_OG=snr((PG_signal),AP_signal) % snr of denoisned signal divided by
airpass(noise) signal

    %  SNR2_IDT=snr((den_IDT_PG_signal)',AP_signal); % snr of denoisned signal
divided by airpass(noise) signal

    % SNR3_IDT=mean(den_IDT_PG_signal)/std(den_IDT_PG_signal); % mean of denoised
signal / std of denoised signal

    % Thresholding using Airpass information

    [c,l]=wavedec(AP_signal,level,wname);

    [cd1,cd2,cd3,cd4,cd5]=detcoef(c,l,[1 2 3 4 5]);

    thresholds=[max(abs(cd1))    max(abs(cd2))    max(abs(cd3))    max(abs(cd4))
max(abs(cd4)) max(abs(cd5))];

    den_PG_signal=cmddenoise(PG_signal,wname,level,sorh,NaN,thresholds);        %
wavelet denoising done

    %SNR1=10*log10(sum(PG_signal)/(sum(PG_signal-(den_PG_signal)')));

    SNR2=snr((den_PG_signal)',AP_signal) % snr of denoisned signal divided by
airpass(noise) signal

    SNR3=mean(den_PG_signal)/std(den_PG_signal) % mean of denoised signal / std of
denoised signal

    AE_den_sig(i).AE_Mistras_data_PG=den_PG_signal;

end
```

9.2.2 Delaying and aligning signals

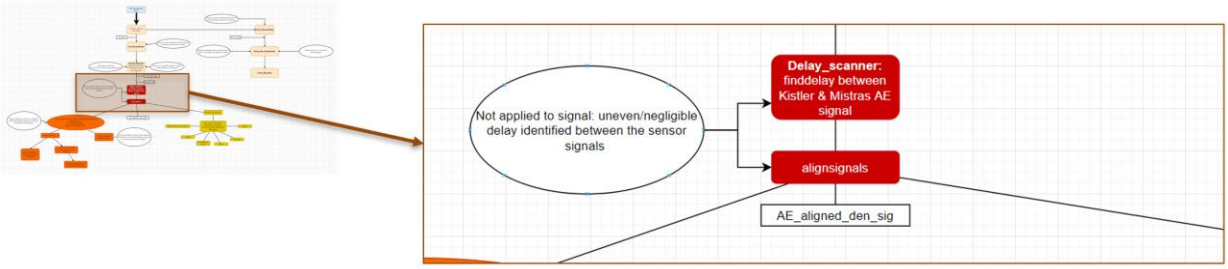

- Finddelay function was used between the Kistler and Mistras AE signal for the same trials.
- Finddelay uses cross-correlation between each pair of signals at all possible lags. The estimated delay is given by the negative of the lag for which normalised cross-correlation has the largest absolute value.
- The maximum delay that was noted from all trial signals was 9 milli seconds. In real space, the spacing distance between the AE sensors were about 10 – 15 mm, therefore taking into account speed of sound in air, the approx. delay in signal could be 90 samples i.e. 0.045 milli seconds.
- Considering the error that can occur from the noise in the signal, experimental setup and calculation of delay using cross-correlation, this minute delay is rather considered negligible and no further alignment of the signal is carried out.

Delay scanner and alignment of signals

```
% load AE_den_sig variable
for i=1:15
    Kistler_sig=AE_den_sig(i).AE_kistler_data_PG;
    Mistras_sig=AE_den_sig(i).AE_Mistras_data_PG;
    sig_delay(i)=finddelay(Kistler_sig,Mistras_sig); % find delay uses cross-
correlation between each pair of signals at all possible lags. The normalized

[aligned_Kistler_sig,aligned_Mistras_sig]=alignsignals(Kistler_sig,Mistras_sig);
    AE_aligned_den_sig(i).AE_kistler_data_PG=aligned_Kistler_sig;
    AE_aligned_den_sig(i).AE_Mistras_data_PG=aligned_Mistras_sig;
    %cross-correlation between each pair of signals is then calculated. The
    %estimated delay is given by the negative of the lag for which
```

```
    %normalised cross-correlation has the largest absolute value.
end


mean_sig_delay=mean(sig_delay)
average_time_delay=mean_sig_delay/2000000 % Number of samples/sampling rate, this
is the max calculated delay in each PG.
average_distance_delay=331*average_time_delay;
% Given as 9 micro seconds.
% speed of sound given as 331 m/s (approx), (any frequency changes means
% wavlength is changed)
% approx difference between the sensors calculated with this difference in
% sig delay
% signal delay to be



% In reality the spacing between the AE sensors were about 10 - 15 mm,
% therefore :
expected_time_delay=(15/1000)/330;
expected_sig_delay=expected_time_delay*2000000;
% expected sig delay should be 90 samples in delay between the sensors.
% This not what is seen using the 'finddelay' function. Considering the
% difference in signal is
```

9.2.3 Power spectrum and Cross-correlation analysis

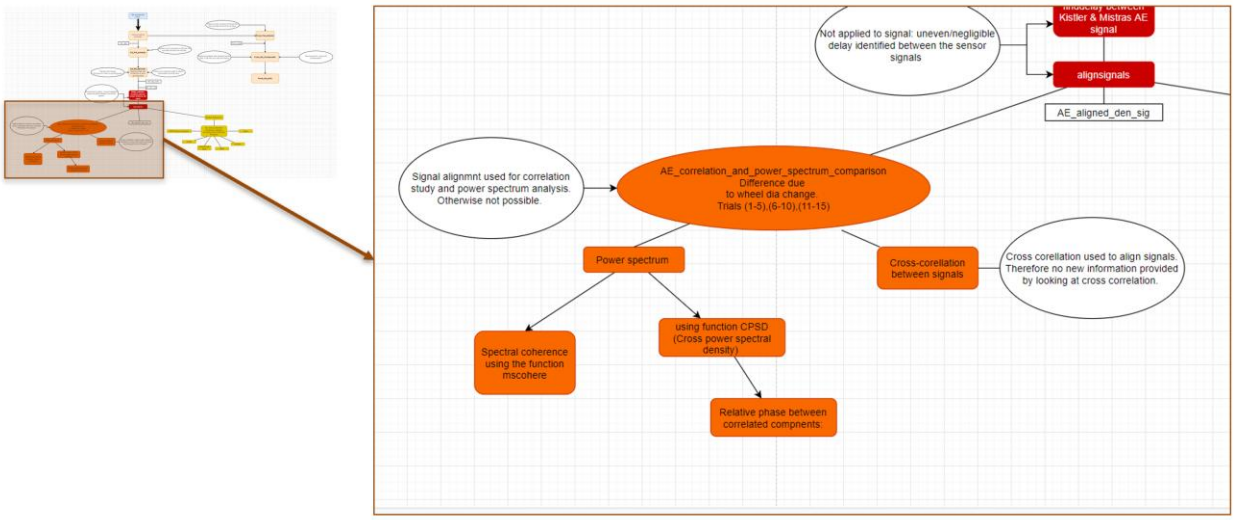

- Provide an overview of the spectral distribution within the signal.
- A high-level comparison between the signals and AE features will spend a more detailed exploration into the AE response with respect to frequency

Power spectrum analysis

```
% Power spectrum analyis between trial 010 / 060 /110

Fs=2000000;

sig1=AE_aligned_den_sig(1).AE_kistler_data_PG;

sig2=AE_aligned_den_sig(6).AE_kistler_data_PG;

sig3=AE_aligned_den_sig(11).AE_kistler_data_PG;

[P010,F010]=periodogram(sig1,[],[],Fs,'power');

[P060,F060]=periodogram(sig2,[],[],Fs,'power');

[P110,F110]=periodogram(sig3,[],[],Fs,'power');

P010(1)=0;

P060(1)=0;

P110(1)=0;


figure
tiledlayout(3,1)
```

```
ax1=nexttile;
plot(F010,P010,'k')
ylabel('P1')
grid on
axis tight
title('Power Spectrum for Trial 010 Kistler')
ax2=nexttile;
plot(F060,P060,'k')
ylabel('P1')
grid on
axis tight
title('Power Spectrum for Trial 060 Kistler')
ax3=nexttile;
plot(F110,P110,'k')
ylabel('P1')
grid on
axis tight
title('Power Spectrum for Trial 110 Kistler')
linkaxes([ax1,ax2,ax3]);
ax1.YLim=[0 4*10^-6];
xlabel('Frequency (Hz)');


%Spectral choerence
[Cxy1,f]=mscohere(sig1,sig2,[],[],[],Fs);
[Cxy2,f]=mscohere(sig2,sig3,[],[],[],Fs);
[Cxy3,f]=mscohere(sig1,sig3,[],[],[],Fs);


figure
n=tiledlayout(3,1);
nx1=nexttile;
```

```
plot(f,Cxy1,"DisplayName","Spectral coherence estimate Trial 010 to 060");
xlabel('Frequency (Hz)');
title('Kistler - Spectral coherence estimate Trial 010 to 060')
nx2=nexttile;
plot(f,Cxy2,"DisplayName","Spectral coherence estimate Trial 060 to 110");
xlabel('Frequency (Hz)');
grid on
title('Kistler - Spectral coherence estimate Trial 060 to 110')
nx3=nexttile;
plot(f,Cxy3,"DisplayName","Spectral coherence estimate Trial 010 to 110");
xlabel('Frequency (Hz)');
grid on
title('Kistler - Spectral coherence estimate Trial 010 to 110')
linkaxes([nx1,nx2,nx3]);
xlabel('Frequency (Hz)');


% Cross power spectral density
[Pxy1]=cpsd(sig1,sig2,[],[],[],Fs);
[Pxy2]=cpsd(sig2,sig3,[],[],[],Fs);
[Pxy3]=cpsd(sig1,sig3,[],[],[],Fs);
phase1=-angle(Pxy1)/pi*180;
phase2=-angle(Pxy2)/pi*180;
phase3=-angle(Pxy3)/pi*180;


% CPSD Plots
figure
o=tiledlayout(3,1);
ox1=nexttile;
cpsd(sig1,sig2,[],[],[],Fs);
title('Kistler Trial 010 to 060')
```

```
ox2=nexttile;
cpsd(sig2,sig3,[],[],[],Fs);
grid on
title('Kistler Trial 060 to 110')
ox3=nexttile;
cpsd(sig1,sig3,[],[],[],Fs);
grid on
title('Kistler Trial 010 to 110')
grid on
linkaxes([ox1,ox2,ox3]);
%
% % Cross-spectrum Phase (deg) Plots
% figure
% o=tiledlayout(3,1);
% ox1=nexttile;
% plot(f,phase1);
% xlabel('Frequency (Hz)');
% title('Cross-spectrum phase (Deg) Trial 010 to 060')
% ox2=nexttile;
% plot(f,phase2);
% grid on
% xlabel('Frequency (Hz)');
% title('Cross-spectrum phase (Deg) Trial 060 to 110')
% ox3=nexttile;
% plot(f,phase3);
% grid on
% xlabel('Frequency (Hz)');
% title('Cross-spectrum phase (Deg) Trial 010 to 110')
% linkaxes([ox1,ox2,ox3]);
```

```
% Power spectrum analyis between trial 010 / 060 /110
Fs=2000000;

sig1=AE_aligned_den_sig(1).AE_Mistras_data_PG;

sig2=AE_aligned_den_sig(6).AE_Mistras_data_PG;

sig3=AE_aligned_den_sig(11).AE_Mistras_data_PG;

[P010,F010]=periodogram(sig1,[],[],Fs,'power');

[P060,F060]=periodogram(sig2,[],[],Fs,'power');

[P110,F110]=periodogram(sig3,[],[],Fs,'power');

P010(1)=0;

P060(1)=0;

P110(1)=0;


figure
tiledlayout(3,1)

ax1=nexttile;

plot(F010,P010,'k')

ylabel('P1')

grid on

axis tight

title('Power Spectrum for Trial 010 Mistras')

ax2=nexttile;

plot(F060,P060,'k')

ylabel('P1')

grid on

axis tight

title('Power Spectrum for Trial 060 Mistras')

ax3=nexttile;

plot(F110,P110,'k')
```

```
ylabel('P1')
grid on
axis tight
title('Power Spectrum for Trial 110 Mistras')
linkaxes([ax1,ax2,ax3]);
ax1.YLim=[0 4*10^-6];
xlabel('Frequency (Hz)');


%Spectral choerence
[Cxy1,f]=mscohere(sig1,sig2,[],[],[],Fs);
[Cxy2,f]=mscohere(sig2,sig3,[],[],[],Fs);
[Cxy3,f]=mscohere(sig1,sig3,[],[],[],Fs);


figure
n=tiledlayout(3,1);
nx1=nexttile;
plot(f,Cxy1,"DisplayName","Mistras Spectral coherence estimate Trial 010 to 060");
xlabel('Frequency (Hz)');
title('Mistras Spectral coherence estimate Trial 010 to 060')
nx2=nexttile;
plot(f,Cxy2,"DisplayName","Mistras Spectral coherence estimate Trial 060 to 110");
xlabel('Frequency (Hz)');
grid on
title('Mistras Spectral coherence estimate Trial 060 to 110')
nx3=nexttile;
plot(f,Cxy3,"DisplayName","Mistras Spectral coherence estimate Trial 010 to 110");
xlabel('Frequency (Hz)');
grid on
title('Mistras Spectral coherence estimate Trial 010 to 110')
linkaxes([nx1,nx2,nx3]);
```

```
xlabel('Frequency (Hz)');


% Cross power spectral density
[Pxy1]=cpsd(sig1,sig2,[],[],[],Fs);
[Pxy2]=cpsd(sig2,sig3,[],[],[],Fs);
[Pxy3]=cpsd(sig1,sig3,[],[],[],Fs);
phase1=-angle(Pxy1)/pi*180;
phase2=-angle(Pxy2)/pi*180;
phase3=-angle(Pxy3)/pi*180;


% CPSD Plots
figure
o=tiledlayout(3,1);
ox1=nexttile;
cpsd(sig1,sig2,[],[],[],Fs);
title('Mistras Trial 010 to 060')
ox2=nexttile;
cpsd(sig2,sig3,[],[],[],Fs);
grid on
title('Mistras Trial 060 to 110')
ox3=nexttile;
cpsd(sig1,sig3,[],[],[],Fs);
grid on
title('Mistras Trial 010 to 110')
grid on
linkaxes([ox1,ox2,ox3]);


% Power spectrum analyis between trial 010-050 (Finishing grinding parameter)
Fs=2000000;
```

```
sig1=AE_aligned_den_sig(1).AE_Mistras_data_PG;

sig2=AE_aligned_den_sig(2).AE_Mistras_data_PG;

sig3=AE_aligned_den_sig(3).AE_Mistras_data_PG;

sig4=AE_aligned_den_sig(4).AE_Mistras_data_PG;

sig5=AE_aligned_den_sig(5).AE_Mistras_data_PG;




[P010,F010]=periodogram(sig1,[],[],Fs,'power');
[P020,F020]=periodogram(sig2,[],[],Fs,'power');

[P030,F030]=periodogram(sig3,[],[],Fs,'power');

[P040,F040]=periodogram(sig4,[],[],Fs,'power');

[P050,F050]=periodogram(sig5,[],[],Fs,'power');


P010(1)=0;
P020(1)=0;

P030(1)=0;

P040(1)=0;

P050(1)=0;


figure
m=tiledlayout(5,1)

ax1=nexttile;

plot(F010,P010,'k')

ylabel('P1')

grid on

axis tight

title('Power Spectrum for Trial 010 Mistras')

ax2=nexttile;

plot(F020,P020,'k')

ylabel('P1')
```

```
grid on
axis tight
title('Power Spectrum for Trial 020 Mistras')
ax3=nexttile;
plot(F030,P030,'k')
ylabel('P1')
grid on
axis tight
title('Power Spectrum for Trial 030 Mistras')
ax4=nexttile;
plot(F040,P040,'k')
ylabel('P1')
grid on
axis tight
title('Power Spectrum for Trial 040 Mistras')
ax5=nexttile;
plot(F050,P050,'k')
ylabel('P1')
grid on
axis tight
title('Power Spectrum for Trial 050 Mistras')
linkaxes([ax1,ax2,ax3,ax4,ax5]);
ax1.YLim=[0 5*10^-6];
xlabel('Frequency (Hz)');
title(m,'Mistras AE sensor Trial 010 - 050 : Finishing parameters')
```

```
% Power spectrum analyis between trial 060-100 (Semi-finishing grinding parameter)
Fs=2000000;
```

```
sig1=AE_aligned_den_sig(6).AE_Mistras_data_PG;

sig2=AE_aligned_den_sig(7).AE_Mistras_data_PG;

sig3=AE_aligned_den_sig(8).AE_Mistras_data_PG;

sig4=AE_aligned_den_sig(9).AE_Mistras_data_PG;

sig5=AE_aligned_den_sig(10).AE_Mistras_data_PG;




[P010,F010]=periodogram(sig1,[],[],Fs,'power');
[P020,F020]=periodogram(sig2,[],[],Fs,'power');

[P030,F030]=periodogram(sig3,[],[],Fs,'power');

[P040,F040]=periodogram(sig4,[],[],Fs,'power');

[P050,F050]=periodogram(sig5,[],[],Fs,'power');


P010(1)=0;
P020(1)=0;

P030(1)=0;

P040(1)=0;

P050(1)=0;


figure
m=tiledlayout(5,1)

ax1=nexttile;

plot(F010,P010,'k')

ylabel('P1')

grid on

axis tight

title('Power Spectrum for Trial 060 Mistras')

ax2=nexttile;

plot(F020,P020,'k')

ylabel('P1')
```

```
grid on
axis tight
title('Power Spectrum for Trial 070 Mistras')
ax3=nexttile;
plot(F030,P030,'k')
ylabel('P1')
grid on
axis tight
title('Power Spectrum for Trial 080 Mistras')
ax4=nexttile;
plot(F040,P040,'k')
ylabel('P1')
grid on
axis tight
title('Power Spectrum for Trial 090 Mistras')
ax5=nexttile;
plot(F050,P050,'k')
ylabel('P1')
grid on
axis tight
title('Power Spectrum for Trial 100 Mistras')
linkaxes([ax1,ax2,ax3,ax4,ax5]);
ax1.YLim=[0 5*10^-6];
xlabel('Frequency (Hz)');
title(m,'Mistras AE sensor Trial 060 - 100 : Semi-finishing parameters')
```

```
% Power spectrum analyis between trial 110-150 (Roughing grinding parameter)
Fs=2000000;
sig1=AE_aligned_den_sig(11).AE_Mistras_data_PG;
```

```
sig2=AE_aligned_den_sig(12).AE_Mistras_data_PG;

sig3=AE_aligned_den_sig(13).AE_Mistras_data_PG;

sig4=AE_aligned_den_sig(14).AE_Mistras_data_PG;

sig5=AE_aligned_den_sig(15).AE_Mistras_data_PG;




[P010,F010]=periodogram(sig1,[],[],Fs,'power');
[P020,F020]=periodogram(sig2,[],[],Fs,'power');

[P030,F030]=periodogram(sig3,[],[],Fs,'power');

[P040,F040]=periodogram(sig4,[],[],Fs,'power');

[P050,F050]=periodogram(sig5,[],[],Fs,'power');



P010(1)=0;
P020(1)=0;

P030(1)=0;

P040(1)=0;

P050(1)=0;



figure
m=tiledlayout(5,1)

ax1=nexttile;

plot(F010,P010,'k')

ylabel('P1')

grid on

axis tight

title('Power Spectrum for Trial 110 Mistras')

ax2=nexttile;

plot(F020,P020,'k')

ylabel('P1')

grid on
```

```
axis tight
title('Power Spectrum for Trial 120 Mistras')
ax3=nexttile;
plot(F030,P030,'k')
ylabel('P1')
grid on
axis tight
title('Power Spectrum for Trial 130 Mistras')
ax4=nexttile;
plot(F040,P040,'k')
ylabel('P1')
grid on
axis tight
title('Power Spectrum for Trial 140 Mistras')
ax5=nexttile;
plot(F050,P050,'k')
ylabel('P1')
grid on
axis tight
title('Power Spectrum for Trial 150 Mistras')
linkaxes([ax1,ax2,ax3,ax4,ax5]);
ax1.YLim=[0 5*10^-6];
xlabel('Frequency (Hz)');
title(m,'Mistras AE sensor Trial 110 - 150 : Roughing parameters')
```

```
% Power spectrum analyis between trial 010-050 (Finishing grinding parameter)
Fs=2000000;
sig1=AE_aligned_den_sig(1).AE_kistler_data_PG;
sig2=AE_aligned_den_sig(2).AE_kistler_data_PG;
```

```
sig3=AE_aligned_den_sig(3).AE_kistler_data_PG;

sig4=AE_aligned_den_sig(4).AE_kistler_data_PG;

sig5=AE_aligned_den_sig(5).AE_kistler_data_PG;




[P010,F010]=periodogram(sig1,[],[],Fs,'power');
[P020,F020]=periodogram(sig2,[],[],Fs,'power');

[P030,F030]=periodogram(sig3,[],[],Fs,'power');

[P040,F040]=periodogram(sig4,[],[],Fs,'power');

[P050,F050]=periodogram(sig5,[],[],Fs,'power');



P010(1)=0;
P020(1)=0;

P030(1)=0;

P040(1)=0;

P050(1)=0;



figure
m=tiledlayout(5,1)

ax1=nexttile;

plot(F010,P010,'k')

ylabel('P1')

grid on

axis tight

title('Power Spectrum for Trial 010 Kistler')

ax2=nexttile;

plot(F020,P020,'k')

ylabel('P1')

grid on

axis tight
```

```
title('Power Spectrum for Trial 020 Kistler')
ax3=nexttile;
plot(F030,P030,'k')
ylabel('P1')
grid on
axis tight
title('Power Spectrum for Trial 030 Kistler')
ax4=nexttile;
plot(F040,P040,'k')
ylabel('P1')
grid on
axis tight
title('Power Spectrum for Trial 040 Kistler')
ax5=nexttile;
plot(F050,P050,'k')
ylabel('P1')
grid on
axis tight
title('Power Spectrum for Trial 050 Kistler')
linkaxes([ax1,ax2,ax3,ax4,ax5]);
ax1.YLim=[0 5*10^-6];
xlabel('Frequency (Hz)');
title(m,'Kistler AE sensor Trial 010 - 050 : Finishing parameters')
```

```
% Power spectrum analyis between trial 060-100 (Semi-finishing grinding parameter)
Fs=2000000;
sig1=AE_aligned_den_sig(6).AE_kistler_data_PG;
sig2=AE_aligned_den_sig(7).AE_kistler_data_PG;
```

```
sig3=AE_aligned_den_sig(8).AE_kistler_data_PG;

sig4=AE_aligned_den_sig(9).AE_kistler_data_PG;

sig5=AE_aligned_den_sig(10).AE_kistler_data_PG;




[P010,F010]=periodogram(sig1,[],[],Fs,'power');
[P020,F020]=periodogram(sig2,[],[],Fs,'power');

[P030,F030]=periodogram(sig3,[],[],Fs,'power');

[P040,F040]=periodogram(sig4,[],[],Fs,'power');

[P050,F050]=periodogram(sig5,[],[],Fs,'power');



P010(1)=0;
P020(1)=0;

P030(1)=0;

P040(1)=0;

P050(1)=0;



figure
m=tiledlayout(5,1)

ax1=nexttile;

plot(F010,P010,'k')

ylabel('P1')

grid on

axis tight

title('Power Spectrum for Trial 060 Kistler')

ax2=nexttile;

plot(F020,P020,'k')

ylabel('P1')

grid on

axis tight
```

```
title('Power Spectrum for Trial 070 Kistler')
ax3=nexttile;
plot(F030,P030,'k')
ylabel('P1')
grid on
axis tight
title('Power Spectrum for Trial 080 Kistler')
ax4=nexttile;
plot(F040,P040,'k')
ylabel('P1')
grid on
axis tight
title('Power Spectrum for Trial 090 Kistler')
ax5=nexttile;
plot(F050,P050,'k')
ylabel('P1')
grid on
axis tight
title('Power Spectrum for Trial 100 Kistler')
linkaxes([ax1,ax2,ax3,ax4,ax5]);
ax1.YLim=[0 5*10^-6];
xlabel('Frequency (Hz)');
title(m,'Kistler AE sensor Trial 060 - 100 : Semi-finishing parameters')
```

```
% Power spectrum analyis between trial 110-150 (Roughing grinding parameter)
Fs=2000000;
sig1=AE_aligned_den_sig(11).AE_kistler_data_PG;
sig2=AE_aligned_den_sig(12).AE_kistler_data_PG;
sig3=AE_aligned_den_sig(13).AE_kistler_data_PG;
```

```
sig4=AE_aligned_den_sig(14).AE_kistler_data_PG;

sig5=AE_aligned_den_sig(15).AE_kistler_data_PG;




[P010,F010]=periodogram(sig1,[],[],Fs,'power');
[P020,F020]=periodogram(sig2,[],[],Fs,'power');

[P030,F030]=periodogram(sig3,[],[],Fs,'power');

[P040,F040]=periodogram(sig4,[],[],Fs,'power');

[P050,F050]=periodogram(sig5,[],[],Fs,'power');



P010(1)=0;
P020(1)=0;

P030(1)=0;

P040(1)=0;

P050(1)=0;



figure
m=tiledlayout(5,1)

ax1=nexttile;

plot(F010,P010,'k')

ylabel('P1')

grid on

axis tight

title('Power Spectrum for Trial 110 kistler')

ax2=nexttile;

plot(F020,P020,'k')

ylabel('P1')

grid on

axis tight

title('Power Spectrum for Trial 120 Kistler')
```

```
ax3=nexttile;
plot(F030,P030,'k')
ylabel('P1')
grid on
axis tight
title('Power Spectrum for Trial 130 Kistler')
ax4=nexttile;
plot(F040,P040,'k')
ylabel('P1')
grid on
axis tight
title('Power Spectrum for Trial 140 Kistler')
ax5=nexttile;
plot(F050,P050,'k')
ylabel('P1')
grid on
axis tight
title('Power Spectrum for Trial 150 Kistler')
linkaxes([ax1,ax2,ax3,ax4,ax5]);
ax1.YLim=[0 5*10^-6];
xlabel('Frequency (Hz)');
title(m,'Kistler AE sensor Trial 110 - 150 : Roughing parameters')
```

9.2.4 AE Feature extraction and analysis

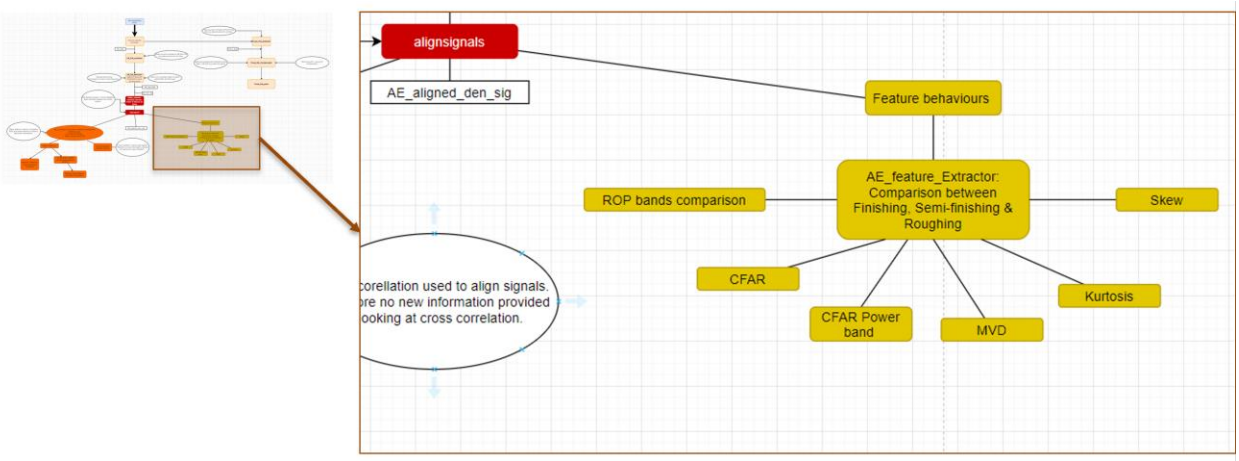

- To conduct a deeper investigation into the AE frequency response
- Detailed exploration within AE features which are used in process monitoring of grinding.
- Drawing conclusions on how much changes in AE features are affected with wheel dia change.

AE Feature extractor

```
Fs=2000000; % sampling frequency
block_num=8000000;% samples in a singal set


denm=((block_num/2)/(Fs/2)); % calcs for normalizing to the fft scale
freq_range=[50000*denm 100000*denm 150000*denm 200000*denm 250000*denm 300000*denm
350000*denm 400000*denm 450000*denm 500000*denm]; % frequency ranges for ROP calc

%freq range as 100kHz 200kHz 300kHz 400kHz 500kHz 600kHz 700kHz 800kHz 900kHz
1000kHz

block_n=length(AE_aligned_den_sig);

ROP=zeros(block_n,8); % ROP matrix initiation

CFAR_power_law=zeros(block_n,8); % initiating the CFAR Power law

AE_rms=zeros(block_n,1);

CFAR=zeros(block_n,1);

MVD=zeros(block_n,1);

Kurtosis=zeros(block_n,1);
```

```
Skew=zeros(block_n,1);
```

```
%AE Kistler feature extraction
for n=1:block_n
    block_signal=(AE_aligned_den_sig(n).AE_kistler_data_PG)';
    mean_block_signal=mean(block_signal);
    block_norm_signal=block_signal-mean_block_signal;
    fft_blocks_data=fft(block_signal);
    P2_block = abs(fft_blocks_data/block_num);
    P1_block = P2_block(1:(block_num/2));
    P1_block(2:end-1) = 2*P1_block(2:end-1);
    P1_block_squared=(P1_block.*P1_block);
    f=Fs*(0:(block_num/2)-1)/block_num;
    M=numel(P1_block);
    mean_block_signal=mean(block_signal);
    std_block_signal=std(block_signal);

    fft_blocks_norm_data=fft(block_norm_signal);
    P2_block_norm = abs(fft_blocks_norm_data/block_num);
    P1_block_norm = P2_block_norm(1:(block_num/2));
    P1_block_norm(2:end-1) = 2*P1_block_norm(2:end-1);
    P1_block_squared_norm=(P1_block_norm.*P1_block_norm);
    f=Fs*(0:(block_num/2)-1)/block_num;
    M=numel(P1_block_norm);
    mean_block_norm_signal=mean(block_norm_signal);
    std_block_norm_signal=std(block_norm_signal);

    % AE RMS
    AE_rms(n)=sqrt(sum((block_signal).^2)/block_num); %  root mean square
```

```
    %CFAR
    CFAR(n)=sum((P1_block).^2); % v given as 2

    % CFAR Power law
    for i=1:numel(freq_range)-1
        band_freq_data=P1_block(freq_range(i)+1:freq_range(i+1),1);
        CFAR_power_law(n,i)=(sum(band_freq_data.^2))/((sum(band_freq_data)).^2);
    end

    % Mean value dispersion (MVD)
    mean_P1_block_squared=mean(P1_block_squared);
    MVD(n)=(sum(log(mean_P1_block_squared./P1_block_squared)))/(M);

    % Kurtosis
    Kurtosis(n)=sum((((block_signal-
mean_block_signal).^4)/(M*(std_block_signal)^4))-3); % FOR A GAUSSIAN SIGNAL is
always three


    % Skew
    Skew(n)=sum(((block_signal-mean_block_signal).^3)/(M*(std_block_signal)^4));

    %ROP (For three parts of the AE frequency range from the AE block)
    for i=1:numel(freq_range)-1
        band_freq_data=P1_block_squared(freq_range(i):freq_range(i+1),1);
        ROP(n,i)=sum((band_freq_data.^2)/(sum(P1_block_squared).^2));
    end
    AE_kistler_features(n).AE_rms=AE_rms(n);
    AE_kistler_features(n).CFAR=CFAR(n);
    AE_kistler_features(n).CFAR_power_law=CFAR_power_law(n,:)';
```

```
    AE_kistler_features(n).MVD=MVD(n);
    AE_kistler_features(n).Kurtosis=Kurtosis(n);
    AE_kistler_features(n).Skew=Skew(n);
    AE_kistler_features(n).ROP=ROP(n,:)';
    AE_kistler_features(n).fft=P1_block;
    AE_kistler_features(n).f=f;
end
```

```
%AE Mistras feature extraction
for n=1:block_n
    block_signal=(AE_aligned_den_sig(n).AE_Mistras_data_PG)';
    mean_block_signal=mean(block_signal);
    block_norm_signal=block_signal-mean_block_signal;
    fft_blocks_data=fft(block_signal);
    P2_block = abs(fft_blocks_data/block_num);
    P1_block = P2_block(1:(block_num/2));
    P1_block(2:end-1) = 2*P1_block(2:end-1);
    P1_block_squared=(P1_block.*P1_block);
    f=Fs*(0:(block_num/2)-1)/block_num;
    M=numel(P1_block);
    mean_block_signal=mean(block_signal);
    std_block_signal=std(block_signal);

    fft_blocks_norm_data=fft(block_norm_signal);
    P2_block_norm = abs(fft_blocks_norm_data/block_num);
    P1_block_norm = P2_block_norm(1:(block_num/2));
    P1_block_norm(2:end-1) = 2*P1_block_norm(2:end-1);
    P1_block_squared_norm=(P1_block_norm.*P1_block_norm);
    f=Fs*(0:(block_num/2)-1)/block_num;
```

```
    M=numel(P1_block_norm);
    mean_block_norm_signal=mean(block_norm_signal);
    std_block_norm_signal=std(block_norm_signal);

    % AE RMS
    AE_rms(n)=sqrt(sum((block_signal).^2)/block_num); %  root mean square

    %CFAR
    CFAR(n)=sum((P1_block).^2); % v given as 2

    % CFAR Power law
    for i=1:numel(freq_range)-1
        band_freq_data=P1_block(freq_range(i)+1:freq_range(i+1),1);
        CFAR_power_law(n,i)=(sum(band_freq_data.^2))/((sum(band_freq_data)).^2);
    end

    % Mean value dispersion (MVD)
    mean_P1_block_squared=mean(P1_block_squared);
    MVD(n)=(sum(log(mean_P1_block_squared./P1_block_squared)))/(M);

    % Kurtosis
    Kurtosis(n)=sum((((block_signal-
mean_block_signal).^4)/(M*(std_block_signal)^4))-3); % FOR A GAUSSIAN SIGNAL is
always three


    % Skew
    Skew(n)=sum(((block_signal-mean_block_signal).^3)/(M*(std_block_signal)^4));

    %ROP (For three parts of the AE frequency range from the AE block)
    for i=1:numel(freq_range)-1
```

```
        band_freq_data=P1_block_squared(freq_range(i):freq_range(i+1),1);
        ROP(n,i)=sum((band_freq_data.^2)/(sum(P1_block_squared).^2));
    end
    AE_Mistras_features(n).AE_rms=AE_rms(n);
    AE_Mistras_features(n).CFAR=CFAR(n);
    AE_Mistras_features(n).CFAR_power_law=CFAR_power_law(n,:)';
    AE_Mistras_features(n).MVD=MVD(n);
    AE_Mistras_features(n).Kurtosis=Kurtosis(n);
    AE_Mistras_features(n).Skew=Skew(n);
    AE_Mistras_features(n).ROP=ROP(n,:)';
    AE_Mistras_features(n).fft=P1_block;
    AE_Mistras_features(n).f=f;
end


figure
plot(AE_Mistras_features(11).f,AE_Mistras_features(11).fft);
```

9.3 Force file extractor and data compensator for drift

Force extractor

```
% Prompt the user for the file
[filename_1,pathname]=uigetfile({'*.mat','All Files (*.tdms)'},'Choose the TDMS
Files', 'Multiselect' , 'on');
if isempty(filename_1)
   print("No files selected");
   return % No files selected, does not
end
filename_full=fullfile(pathname,filename_1);
num_mat_files=size(filename_full,2); % num
for num_struct=1:num_mat_files % looping through each trial no file
    clear ConvertedData
```

```
    load(filename_full{num_struct},'ConvertedData');
    for i=1:length((ConvertedData))
    if isempty(strfind(ConvertedData(i).FileName,'Parameter'))==0

Force_data(num_struct).trial_no=str2double(extractBetween(filename_1(num_struct),
'Trial_','.mat'));

Force_data(num_struct).PG_Fx_12=tall(ConvertedData(i).Data.MeasuredData(7).Data);

Force_data(num_struct).PG_Fx_34=tall(ConvertedData(i).Data.MeasuredData(8).Data);

Force_data(num_struct).PG_Fy_14=tall(ConvertedData(i).Data.MeasuredData(9).Data);

Force_data(num_struct).PG_Fy_23=tall(ConvertedData(i).Data.MeasuredData(10).Data)
;

Force_data(num_struct).PG_Fz_1=tall(ConvertedData(i).Data.MeasuredData(11).Data);

Force_data(num_struct).PG_Fz_2=tall(ConvertedData(i).Data.MeasuredData(12).Data);

Force_data(num_struct).PG_Fz_3=tall(ConvertedData(i).Data.MeasuredData(13).Data);

Force_data(num_struct).PG_Fz_4=tall(ConvertedData(i).Data.MeasuredData(14).Data);
    elseif isempty(strfind(ConvertedData(i).FileName,'Airpass'))==0

Force_data(num_struct).AP_Fx_12=tall(ConvertedData(i).Data.MeasuredData(7).Data);

Force_data(num_struct).AP_Fx_34=tall(ConvertedData(i).Data.MeasuredData(8).Data);

Force_data(num_struct).AP_Fy_14=tall(ConvertedData(i).Data.MeasuredData(9).Data);

Force_data(num_struct).AP_Fy_23=tall(ConvertedData(i).Data.MeasuredData(10).Data)
;

Force_data(num_struct).AP_Fz_1=tall(ConvertedData(i).Data.MeasuredData(11).Data);

Force_data(num_struct).AP_Fz_2=tall(ConvertedData(i).Data.MeasuredData(12).Data);
```

```
Force_data(num_struct).AP_Fz_3=tall(ConvertedData(i).Data.MeasuredData(13).Data);

Force_data(num_struct).AP_Fz_4=tall(ConvertedData(i).Data.MeasuredData(14).Data);
    end
    end
end
```

Force Drift compensation & Segmenting

```
% Collecting the threshold points from AE data
% need to load AE_Data
Fs_AE=2000000; % Sampling rate (2Mhhz for AE signals recorded)
Fs_force=51200; % Sampling rate for force (51.2kHz)
for i= 1:length(AE_data)
    %For PG dataset
    AE_signal_i=gather(AE_data(i).AE_Kistler_data_PG); % getting pre_data
    %Trimming for Kistler AE data
    threshold=0.15; % threshold for Kistler data
    threshold_point_PG(i,1)=find(AE_signal_i>(threshold),1,"first");  % threshold point for Kistler in Column 1
    AE_signal_i=gather(AE_data(i).AE_Mistras_data_PG); % getting the raw data
    %Trimming for Mistras AE data
    threshold=0.2; % threshold for Mistras data
    threshold_point_PG(i,2)=find(AE_signal_i>(threshold),1,"first");  % threshold point for Mistras in Column 2
    % Finding the threshold point in Force data for PG:
    t_stamp_Fs_AE=[0:(1/Fs_AE):15]; % creating time stamp vector for AE
    t_stamp_Fs_Force=[0:(1/Fs_force):15]; % creating time stamp vector for Force
    t_threshold_point_PG=t_stamp_Fs_AE(threshold_point_PG(i,2)); % find time stamp of threshold for AE Mistras
```

```
    [minD, IndexofMin]=min(abs(t_stamp_Fs_Force-t_threshold_point_PG)); % finding
equivalent index of threshold point in force vector

    Force_threshold_idx(i,1)=IndexofMin; % Threshold index to be used for force


    % For AP dataset

    clear AE_signal_i

    AE_signal_AP=gather(AE_data(i).AE_Mistras_data_AP);

    rms_signal_AP=rms(AE_signal_AP,100000,1000,0);

    [idx]=findchangepts(rms_signal_AP,"Statistic","rms","MaxNumChanges",4);

    threshold_point_AP(i,1)=idx(1)*100000;

    AE_signal_AP=gather(AE_data(i).AE_Mistras_data_AP);

    rms_signal_AP=rms(AE_signal_AP,100000,1000,0);

    [idx]=findchangepts(rms_signal_AP,"Statistic","rms","MaxNumChanges",4);

    threshold_point_AP(i,2)=idx(1)*100000;

    % Finding the threshold point in Force data for AP:

    t_stamp_Fs_AE=[0:(1/Fs_AE):15]; % creating time stamp vector for AE

    t_stamp_Fs_Force=[0:(1/Fs_force):15]; % creating time stamp vector for Force

    t_threshold_point_AP=t_stamp_Fs_AE(threshold_point_AP(i,2)); % find time stamp
of threshold for AE Mistras

    [minD, IndexofMin]=min(abs(t_stamp_Fs_Force-t_threshold_point_AP)); % finding
equivalent index of threshold point in force vector

    Force_threshold_idx(i,2)=IndexofMin; % Threshold index to be used for force

end
```

```
%% Drift compensation work:
for i=1:length(Force_data)

    %offsets to calulate drift regions

    DriftOffset1=1*Fs_force; %sec Offest Before Cut (Default=1)

    DriftOffset2=0.5*Fs_force; %sec Offest Before Cut  (Default=0.5)

    DriftOffset3=0.5*Fs_force;        %sec        Offest        After        Cut
(DefaultAT1=3.3)(DefaultAT2=7)
```

```
    DriftOffset4=1*Fs_force;       %sec       Offest       After       Cut       2
(DefaultAT1=4.3)(DefaultAT2=8)

    % Sum of Channels


Force_data(i).XForce_PG=gather(Force_data(i).PG_Fx_12(1:450000))+gather(Force_dat
a(i).PG_Fx_34(1:450000));


Force_data(i).YForce_PG=gather(Force_data(i).PG_Fy_14(1:450000))+gather(Force_dat
a(i).PG_Fy_23(1:450000));


Force_data(i).ZForce_PG=gather(Force_data(i).PG_Fz_1(1:450000))+gather(Force_data
(i).PG_Fz_2(1:450000))+gather(Force_data(i).PG_Fz_3(1:450000))+gather(Force_data(
i).PG_Fz_4(1:450000));


Force_data(i).XForce_AP=gather(Force_data(i).AP_Fx_12(1:415000))+gather(Force_dat
a(i).AP_Fx_34(1:415000));


Force_data(i).YForce_AP=gather(Force_data(i).AP_Fy_14(1:415000))+gather(Force_dat
a(i).AP_Fy_23(1:415000));


Force_data(i).ZForce_AP=gather(Force_data(i).AP_Fz_1(1:415000))+gather(Force_data
(i).AP_Fz_2(1:415000))+gather(Force_data(i).AP_Fz_3(1:415000))+gather(Force_data(
i).AP_Fz_4(1:415000));

    %drift compensation for PG

    % find points

    % find drift points before each cut

    CutStarts=Force_threshold_idx(i,1);

    CutEnds=CutStarts+(4*Fs_force);% Cut ends at 4 but using 5sec to clear end of
cut

    DriftBeforeStart=(CutStarts-DriftOffset1);

    DriftBeforeEnd=(CutStarts-DriftOffset2);

    Drifts(1,:)=mean(Force_data(i).XForce_PG(DriftBeforeStart:DriftBeforeEnd));

    Drifts(2,:)=mean(Force_data(i).YForce_PG(DriftBeforeStart:DriftBeforeEnd));

    Drifts(3,:)=mean(Force_data(i).ZForce_PG(DriftBeforeStart:DriftBeforeEnd));

    DriftAfterStart=(CutEnds+DriftOffset3);

    DriftAfterEnd=(CutEnds+DriftOffset4);
```

```
    if DriftAfterEnd>450000
        DriftAfterEnd=450000;
    end
    if DriftAfterStart>450000
        DriftAfterStart=450000;
    end
    Drifts_end(1,:)=mean(Force_data(i).XForce_PG(DriftAfterStart:DriftAfterEnd));
    Drifts_end(2,:)=mean(Force_data(i).YForce_PG(DriftAfterStart:DriftAfterEnd));
    Drifts_end(3,:)=mean(Force_data(i).ZForce_PG(DriftAfterStart:DriftAfterEnd));
    % Find drift points at very start and end of each data file
    DriftAtStart(1,:)=mean(Force_data(i).XForce_PG(1:0.25*Fs_force));
    DriftAtStart(2,:)=mean(Force_data(i).YForce_PG(1:0.25*Fs_force));
    DriftAtStart(3,:)=mean(Force_data(i).ZForce_PG(1:0.25*Fs_force));
    DriftAtFinish(1,:)=mean(Force_data(i).XForce_PG(end-0.25*Fs_force:end));
    DriftAtFinish(2,:)=mean(Force_data(i).YForce_PG(end-0.25*Fs_force:end));
    DriftAtFinish(3,:)=mean(Force_data(i).ZForce_PG(end-0.25*Fs_force:end));

    %Assembling drift curve
    DriftCurveX=linspace(DriftAtStart(1,:),Drifts(1,:),(CutStarts-DriftOffset1));
    DriftCurveY=linspace(DriftAtStart(2,:),Drifts(2,:),(CutStarts-DriftOffset1));
    DriftCurveZ=linspace(DriftAtStart(3,:),Drifts(3,:),(CutStarts-DriftOffset1));


DriftCurveX=[DriftCurveX,linspace(Drifts(1,:),Drifts_end(1,:),(DriftAfterStart-
DriftBeforeStart)),linspace(Drifts_end(1,:),DriftAtFinish(1,:),(DriftAfterEnd-
DriftAfterStart))];

DriftCurveY=[DriftCurveY,linspace(Drifts(2,:),Drifts_end(2,:),(DriftAfterStart-
DriftBeforeStart)),linspace(Drifts_end(2,:),DriftAtFinish(2,:),(DriftAfterEnd-
DriftAfterStart))];

DriftCurveZ=[DriftCurveZ,linspace(Drifts(3,:),Drifts_end(3,:),(DriftAfterStart-
```

```
DriftBeforeStart)),linspace(Drifts_end(3,:),DriftAtFinish(3,:),(DriftAfterEnd-
DriftAfterStart))];


    Force_data(i).comp_XForce_PG=Force_data(i).XForce_PG(1:DriftAfterEnd)-
DriftCurveX';
    Force_data(i).comp_YForce_PG=Force_data(i).YForce_PG(1:DriftAfterEnd)-
DriftCurveY';
    Force_data(i).comp_ZForce_PG=Force_data(i).ZForce_PG(1:DriftAfterEnd)-
DriftCurveZ';


    %drift compensation for AP
    % find points
    % find drift points before each cut
    CutStarts=Force_threshold_idx(i,2);
    CutEnds=CutStarts+(4*Fs_force);% Cut ends at 4 but using 5sec to clear end of
cut
    DriftBeforeStart=(CutStarts-DriftOffset1);
    DriftBeforeEnd=(CutStarts-DriftOffset2);
    Drifts(1,:)=mean(Force_data(i).XForce_AP(DriftBeforeStart:DriftBeforeEnd));
    Drifts(2,:)=mean(Force_data(i).YForce_AP(DriftBeforeStart:DriftBeforeEnd));
    Drifts(3,:)=mean(Force_data(i).ZForce_AP(DriftBeforeStart:DriftBeforeEnd));
    DriftAfterStart=(CutEnds+DriftOffset3);
    DriftAfterEnd=(CutEnds+DriftOffset4);
    if DriftAfterEnd>415000
        DriftAfterEnd=415000;
    end
    if DriftAfterStart>415000
        DriftAfterStart=415000;
    end
    Drifts_end(1,:)=mean(Force_data(i).XForce_AP(DriftAfterStart:DriftAfterEnd));
    Drifts_end(2,:)=mean(Force_data(i).YForce_AP(DriftAfterStart:DriftAfterEnd));
    Drifts_end(3,:)=mean(Force_data(i).ZForce_AP(DriftAfterStart:DriftAfterEnd));
```

```
    % Find drift points at very start and end of each data file
    DriftAtStart(1,:)=mean(Force_data(i).XForce_AP(1:0.25*Fs_force));
    DriftAtStart(2,:)=mean(Force_data(i).YForce_AP(1:0.25*Fs_force));
    DriftAtStart(3,:)=mean(Force_data(i).ZForce_AP(1:0.25*Fs_force));
    DriftAtFinish(1,:)=mean(Force_data(i).XForce_AP(end-0.25*Fs_force:end));
    DriftAtFinish(2,:)=mean(Force_data(i).YForce_AP(end-0.25*Fs_force:end));
    DriftAtFinish(3,:)=mean(Force_data(i).ZForce_AP(end-0.25*Fs_force:end));

    %Assembling drift curve
    clear DriftCurveX
    clear DriftCurveY
    clear DriftCurveZ

    DriftCurveX=linspace(DriftAtStart(1,:),Drifts(1,:),(CutStarts-DriftOffset1));
    DriftCurveY=linspace(DriftAtStart(2,:),Drifts(2,:),(CutStarts-DriftOffset1));
    DriftCurveZ=linspace(DriftAtStart(3,:),Drifts(3,:),(CutStarts-DriftOffset1));


DriftCurveX=[DriftCurveX,linspace(Drifts(1,:),Drifts_end(1,:),(DriftAfterStart-
DriftBeforeStart)),linspace(Drifts_end(1,:),DriftAtFinish(1,:),(DriftAfterEnd-
DriftAfterStart))];

DriftCurveY=[DriftCurveY,linspace(Drifts(2,:),Drifts_end(2,:),(DriftAfterStart-
DriftBeforeStart)),linspace(Drifts_end(2,:),DriftAtFinish(2,:),(DriftAfterEnd-
DriftAfterStart))];

DriftCurveZ=[DriftCurveZ,linspace(Drifts(3,:),Drifts_end(3,:),(DriftAfterStart-
DriftBeforeStart)),linspace(Drifts_end(3,:),DriftAtFinish(3,:),(DriftAfterEnd-
DriftAfterStart))];


    Force_data(i).comp_XForce_AP=Force_data(i).XForce_AP(1:DriftAfterEnd)-
DriftCurveX';
    Force_data(i).comp_YForce_AP=Force_data(i).YForce_AP(1:DriftAfterEnd)-
DriftCurveY';
```

```
    Force_data(i).comp_ZForce_AP=Force_data(i).ZForce_AP(1:DriftAfterEnd)-
DriftCurveZ';


end


%%Segmenting data with thresholds - Segmenting without lead-in & lead-out
%%taken out
fields=fieldnames(Force_data); % making an array of the fieldnames for looping
through
for i=1:length(Force_data)
    for k=24:26 % looping through the force channels of PG signal
        Force_signal_i=gather(Force_data(i).(fields{k})); % Picking all the force
channels
        Force_threshold=Force_threshold_idx(i,1);
        Force_sig_trim_start=(Force_threshold+(Fs_force*1)); % start the trim 0.5
sampling rate after threshold point
         if Force_threshold-(Fs_force*0.5)+((Fs_force*4)-
1)>size(Force_signal_i,1)
             Force_sig_trim_start=Force_sig_trim_start-(Force_threshold-
(Fs_force*0.5)+((Fs_force*4)-1)-size(Force_signal_i,1)); % Moving the trim start
further back if the segment to be cut out is longer than signal
         elseif Force_sig_trim_start<0
             Force_sig_trim_start=1; % If trimstart chosen is negative then it is
made to start from 1
         end

Force_signal_i=Force_signal_i([Force_sig_trim_start:(Force_sig_trim_start+((Fs_fo
rce*1)-1))],:); % segmenting the signal to gather the 4 sec signal of grinding
pass.
         Force_seg_data(i).(fields{k})=Force_signal_i; % adding the segmented
data to a new structure
    end
    for k=27:29 % looping through the force channels of AP signal
        Force_signal_i=gather(Force_data(i).(fields{k})); % Picking all the force
channels
        Force_threshold=Force_threshold_idx(i,2);
        Force_sig_trim_start=(Force_threshold-(Fs_force*1)); % start the trim 0.5
seconds before threshold point
         if Force_threshold-(Fs_force*0.5)+((Fs_force*4)-
1)>size(Force_signal_i,1)
             Force_sig_trim_start=Force_sig_trim_start-(Force_threshold-
(Fs_force*0.5)+((Fs_force*4)-1)-size(Force_signal_i,1)); % Moving the trim start
further back if the segment to be cut out is longer than signal
         elseif Force_sig_trim_start<0
```

```
            Force_sig_trim_start=1; % If trimstart chosen is negative then it is
made to start from 1
        end

Force_signal_i=Force_signal_i([Force_sig_trim_start:(Force_sig_trim_start+((Fs_fo
rce*1)-1))],:); % segmenting the signal to gather the 4 sec signal of grinding
pass.
        Force_seg_data(i).(fields{k})=Force_signal_i; % adding the segmented
data to a new structure
    end
end
```

9.4 Power signal data extractor and segmentation

Spindle power file data extractor

```
% Prompt the user for the file

[filename_1,pathname]=uigetfile({'*.mat','All Files (*.tdms)'},'Choose the TDMS
Files', 'Multiselect' , 'on');

if isempty(filename_1)

   print("No files selected");

   return % No files selected, does not

end

filename_full=fullfile(pathname,filename_1);

num_mat_files=size(filename_full,2); % num

for num_struct=1:num_mat_files % looping through each trial no file

    clear ConvertedData

    load(filename_full{num_struct},'ConvertedData');

    for i=1:length((ConvertedData))

    if isempty(strfind(ConvertedData(i).FileName,'Parameter'))==0


Power_data(num_struct).trial_no=str2double(extractBetween(filename_1(num_struct),
'Trial_','.mat'));


Power_data(num_struct).PG_Spindle_Power=tall(ConvertedData(i).Data.MeasuredData(1
7).Data);

    elseif isempty(strfind(ConvertedData(i).FileName,'Airpass'))==0
```

```
Power_data(num_struct).AP_Spindle_Power=tall(ConvertedData(i).Data.MeasuredData(17).Data);
    end
    end
end
```

Power segmentation

```
% Gathering the thresholding points from AE segmentation
Fs_AE=2000000; % Sampling rate (2Mhhz for AE signals recorded)
Fs_Power=51200; % Sampling rate for force (51.2kHz)
for i= 1:length(AE_data)
    %For PG dataset
    AE_signal_i=gather(AE_data(i).AE_Kistler_data_PG); % getting pre_data
    %Trimming for Kistler AE data
    threshold=0.15; % threshold for Kistler data
    threshold_point_PG(i,1)=find(AE_signal_i>(threshold),1,"first");  % threshold point for Kistler in Column 1
    AE_signal_i=gather(AE_data(i).AE_Mistras_data_PG); % getting the raw data
    %Trimming for Mistras AE data
    threshold=0.2; % threshold for Mistras data
    threshold_point_PG(i,2)=find(AE_signal_i>(threshold),1,"first");  % threshold point for Mistras in Column 2
    % Finding the threshold point in Force data for PG:
    t_stamp_Fs_AE=[0:(1/Fs_AE):15]; % creating time stamp vector for AE
    t_stamp_Fs_Force=[0:(1/Fs_Power):15]; % creating time stamp vector for Force
    t_threshold_point_PG=t_stamp_Fs_AE(threshold_point_PG(i,2)); % find time stamp of threshold for AE Mistras
    [minD, IndexofMin]=min(abs(t_stamp_Fs_Force-t_threshold_point_PG)); % finding equivalent index of threshold point in force vector
    Force_threshold_idx(i,1)=IndexofMin; % Threshold index to be used for force
```

```
    % For AP dataset
    clear AE_signal_i
    AE_signal_AP=gather(AE_data(i).AE_Mistras_data_AP);
    rms_signal_AP=rms(AE_signal_AP,100000,1000,0);
    [idx]=findchangepts(rms_signal_AP,"Statistic","rms","MaxNumChanges",4);
    threshold_point_AP(i,1)=idx(1)*100000;
    AE_signal_AP=gather(AE_data(i).AE_Mistras_data_AP);
    rms_signal_AP=rms(AE_signal_AP,100000,1000,0);
    [idx]=findchangepts(rms_signal_AP,"Statistic","rms","MaxNumChanges",4);
    threshold_point_AP(i,2)=idx(1)*100000;
    % Finding the threshold point in Force data for AP:
    t_stamp_Fs_AE=[0:(1/Fs_AE):15]; % creating time stamp vector for AE
    t_stamp_Fs_Force=[0:(1/Fs_Power):15]; % creating time stamp vector for Force
    t_threshold_point_AP=t_stamp_Fs_AE(threshold_point_AP(i,2)); % find time stamp
of threshold for AE Mistras
    [minD, IndexofMin]=min(abs(t_stamp_Fs_Force-t_threshold_point_AP)); % finding
equivalent index of threshold point in force vector
    Force_threshold_idx(i,2)=IndexofMin; % Threshold index to be used for force
end
```

```
% %%Segmenting data with thresholds
% fields=fieldnames(Power_data); % making an array of the fieldnames for looping
through
% for i=1:length(Power_data)
%     % looping through the Power data for PG signal
%     k=3;
%      Power_signal_i=gather(Power_data(i).(fields{k})); % Picking all the Power
data for PG signal
%     Power_threshold=Force_threshold_idx(i,1);
```

```
%     Power_sig_trim_start=(Power_threshold-(Fs_Power*0.5)); % start the trim 0.5
seconds before threshold point

%     if Power_threshold-(Fs_Power*0.5)+((Fs_Power*4)-1)>size(Power_signal_i,1)

%                     Power_sig_trim_start=Power_sig_trim_start-(Power_threshold-
(Fs_Power*0.5)+((Fs_Power*4)-1)-size(Power_signal_i,1)); % Moving the trim start
further back if the segment to be cut out is longer than signal

%     elseif Power_sig_trim_start<0

%           Power_sig_trim_start=1; % If trimstart chosen is negative then it is
made to start from 1

%     end

%
Power_signal_i=Power_signal_i([Power_sig_trim_start:(Power_sig_trim_start+((Fs_Po
wer*4)-1))],:); % segmenting the signal to gather the 4 sec signal of grinding
pass.

%    Power_seg_data(i).(fields{k})=Power_signal_i; % adding the segmented data to
a new structure

%     k=1;

%      Power_signal_i=gather(Power_data(i).(fields{k})); % Picking all the force
channels

%     Power_threshold=Force_threshold_idx(i,2);

%     Power_sig_trim_start=(Power_threshold-(Fs_Power*0.5)); % start the trim 0.5
seconds before threshold point

%     if Power_threshold-(Fs_Power*0.5)+((Fs_Power*4)-1)>size(Power_signal_i,1)

%                     Power_sig_trim_start=Power_sig_trim_start-(Power_threshold-
(Fs_Power*0.5)+((Fs_Power*4)-1)-size(Power_signal_i,1)); % Moving the trim start
further back if the segment to be cut out is longer than signal

%     elseif Power_sig_trim_start<0

%           Power_sig_trim_start=1; % If trimstart chosen is negative then it is
made to start from 1

%     end

%
Power_signal_i=Power_signal_i([Power_sig_trim_start:(Power_sig_trim_start+((Fs_Po
wer*4)-1))],:); % segmenting the signal to gather the 4 sec signal of grinding
pass.

%    Power_seg_data(i).(fields{k})=Power_signal_i; % adding the segmented data to
a new structure
```

```
% end



%Segmenting data with thresholds. Removing the lead-in and lead out signal.
fields=fieldnames(Power_data); % making an array of the fieldnames for looping
through

for i=1:length(Power_data)

    % looping through the Power data for PG signal

    k=3;

    Power_signal_i=gather(Power_data(i).(fields{k})); % Picking all the Power data
for PG signal

    Power_threshold=Force_threshold_idx(i,1);

    Power_sig_trim_start=(Power_threshold+(Fs_Power*1)); % start the trim 0.5
seconds before threshold point

    if Power_threshold-(Fs_Power*0.5)+((Fs_Power*4)-1)>size(Power_signal_i,1)

        Power_sig_trim_start=Power_sig_trim_start-(Power_threshold-
(Fs_Power*0.5)+((Fs_Power*4)-1)-size(Power_signal_i,1)); % Moving the trim start
further back if the segment to be cut out is longer than signal

    elseif Power_sig_trim_start<0

        Power_sig_trim_start=1; % If trimstart chosen is negative then it is made
to start from 1

    end


Power_signal_i=Power_signal_i([Power_sig_trim_start:(Power_sig_trim_start+((Fs_Po
wer*1)-1))],:); % segmenting the signal to gather the 4 sec signal of grinding
pass.

    Power_seg_data(i).(fields{k})=Power_signal_i; % adding the segmented data to
a new structure

    k=1;

    Power_signal_i=gather(Power_data(i).(fields{k})); % Picking all the force
channels

    Power_threshold=Force_threshold_idx(i,2);

    Power_sig_trim_start=(Power_threshold+(Fs_Power*1)); % start the trim 0.5
seconds before threshold point

    if Power_threshold-(Fs_Power*0.5)+((Fs_Power*4)-1)>size(Power_signal_i,1)
```

```
        Power_sig_trim_start=Power_sig_trim_start-(Power_threshold-
(Fs_Power*0.5)+((Fs_Power*4)-1)-size(Power_signal_i,1)); % Moving the trim start
further back if the segment to be cut out is longer than signal

    elseif Power_sig_trim_start<0

        Power_sig_trim_start=1; % If trimstart chosen is negative then it is made
to start from 1

    end


Power_signal_i=Power_signal_i([Power_sig_trim_start:(Power_sig_trim_start+((Fs_Po
wer*1)-1))],:); % segmenting the signal to gather the 4 sec signal of grinding
pass.

    Power_seg_data(i).(fields{k})=Power_signal_i; % adding the segmented data to
a new structure

end
```